

4



MARINE PHYSICAL LABORATORY

SCRIPPS INSTITUTION OF OCEANOGRAPHY

San Diego, California 92152

AD-A220 158

DTIC FILE COPY

**IN SITU INVESTIGATION OF SEA SURFACE NOISE
FROM A DEPTH OF ONE METER**

Garr Edward Updegraff

DTIC
ELECTE
APR 6 1990
S B D

SIO REFERENCE 89-21

MPL-U-78/89
December 1989

Approved for public release; distribution unlimited.

90 24 158 050

REPORT DOCUMENTATION PAGE				Form Approved OMB No. 0704-0188	
1a. REPORT SECURITY CLASSIFICATION UNCLASSIFIED		1b. RESTRICTIVE MARKINGS			
2a. SECURITY CLASSIFICATION AUTHORITY		3. DISTRIBUTION / AVAILABILITY OF REPORT Approved for public release; distribution unlimited.			
2b. DECLASSIFICATION / DOWNGRADING SCHEDULE					
4. PERFORMING ORGANIZATION REPORT NUMBER(S) SIO REFERENCE 89-21 [MPL-U-78/89]		5. MONITORING ORGANIZATION REPORT NUMBER(S)			
6a. NAME OF PERFORMING ORGANIZATION University of California, San Diego		6b. OFFICE SYMBOL (if applicable) MPL	7a. NAME OF MONITORING ORGANIZATION Office of Naval Research Department of the Navy		
6c. ADDRESS (City, State, and ZIP Code) Marine Physical Laboratory Scripps Institution of Oceanography San Diego, California 92152		7b. ADDRESS (City, State, and ZIP Code) 800 North Quincy Street Arlington, VA 22217-5000			
8a. NAME OF FUNDING / SPONSORING ORGANIZATION Office of Naval Research		8b. OFFICE SYMBOL (if applicable) ONR	9. PROCUREMENT INSTRUMENT IDENTIFICATION NUMBER N00014-87-K-0010		
8c. ADDRESS (City, State, and ZIP Code) 800 North Quincy Street Arlington, VA 22217-5000		10. SOURCE OF FUNDING NUMBERS			
		PROGRAM ELEMENT NO.	PROJECT NO.	TASK NO.	WORK UNIT ACCESSION NO.
11. TITLE (Include Security Classification) IN SITU INVESTIGATION OF SEA SURFACE NOISE FROM A DEPTH OF ONE METER					
12. PERSONAL AUTHOR(S) Garr Edward Updegraff					
13a. TYPE OF REPORT summary		13b. TIME COVERED FROM _____ TO _____		14. DATE OF REPORT (Year, Month, Day) December 1989	15. PAGE COUNT 214
16. SUPPLEMENTARY NOTATION					
17. COSATI CODES			18. SUBJECT TERMS (Continue on reverse if necessary and identify by block number)		
FIELD	GROUP	SUB-GROUP	sea surface noise, environmental time series, acoustic time series, Synoptic Surface Noise Instrument		
19. ABSTRACT The mechanism responsible for audible underwater surface noise, particularly at low wind speeds, is not well understood. Because most surface noise recording instruments are deployed at depths of tens to thousands of meters, they can only characterize the behavior of a population of noise sources, rather than individual noise mechanisms. For this reason, an instrument has been built and deployed at a depth of 1 meter to record the sounds and images of the sea surface during light winds. This self-suspending instrument contains an upward looking video camera, four hydrophones digitized at 20 kHz each, and positional sensors. A surface buoy, tethered 30 meters from the submerged instrument, continuously supplies the wind speed and direction. Recordings from the instrument indicate that surface noise produced during light winds is generated by small wavelet spills which have no correlation with the amplitude or phase of long period swells moving faster than prevailing winds. The averaged acoustic spectra from a single energetic spill showed a slope of -5 dB per octave, matching the spectral slope first reported by Knudsen, Alford, & Emiling in 1948 for wind generated surface noise. The sound generated by these small spills is composed of distinct transient sinusoids, each of which usually starts impulsively and then decays exponentially within milliseconds. This behavior matches the millimeter sized bubble signatures described by Strassberg [1956] and Medwin & Beaky [1989]. The unique frequency for each oscillation within a wavelet spill indicates that bubbles are "rung" during entrainment, die out, and then no longer contribute actively to the acoustic recording. The peak pressures of these oscillations range up to 1.2 Pascals, with little apparent dependence on frequency over the 300 to 8,000 Hz range of the instrument. Analysis of the acoustic energy generated by a number of bubbles versus frequency suggests that the -5 dB per octave slope is caused by the shorter lifetimes of high frequency bubbles, rather than significantly lower peak pressures.					
20. DISTRIBUTION / AVAILABILITY OF ABSTRACT <input type="checkbox"/> UNCLASSIFIED/UNLIMITED <input type="checkbox"/> SAME AS RPT. <input type="checkbox"/> DTIC USERS			21. ABSTRACT SECURITY CLASSIFICATION UNCLASSIFIED		
22a. NAME OF RESPONSIBLE INDIVIDUAL V. C. Anderson			22b. TELEPHONE (Include Area Code) (619) 534-1793	22c. OFFICE SYMBOL MPL	



In Situ Investigation of
Sea Surface Noise
from a Depth of One Meter

A dissertation submitted in partial satisfaction of the

requirements for the degree Doctor of Philosophy

in Oceanography

by

Garr Edward Updegraff

Committee in charge:

Professor Victor C. Anderson, Chairperson

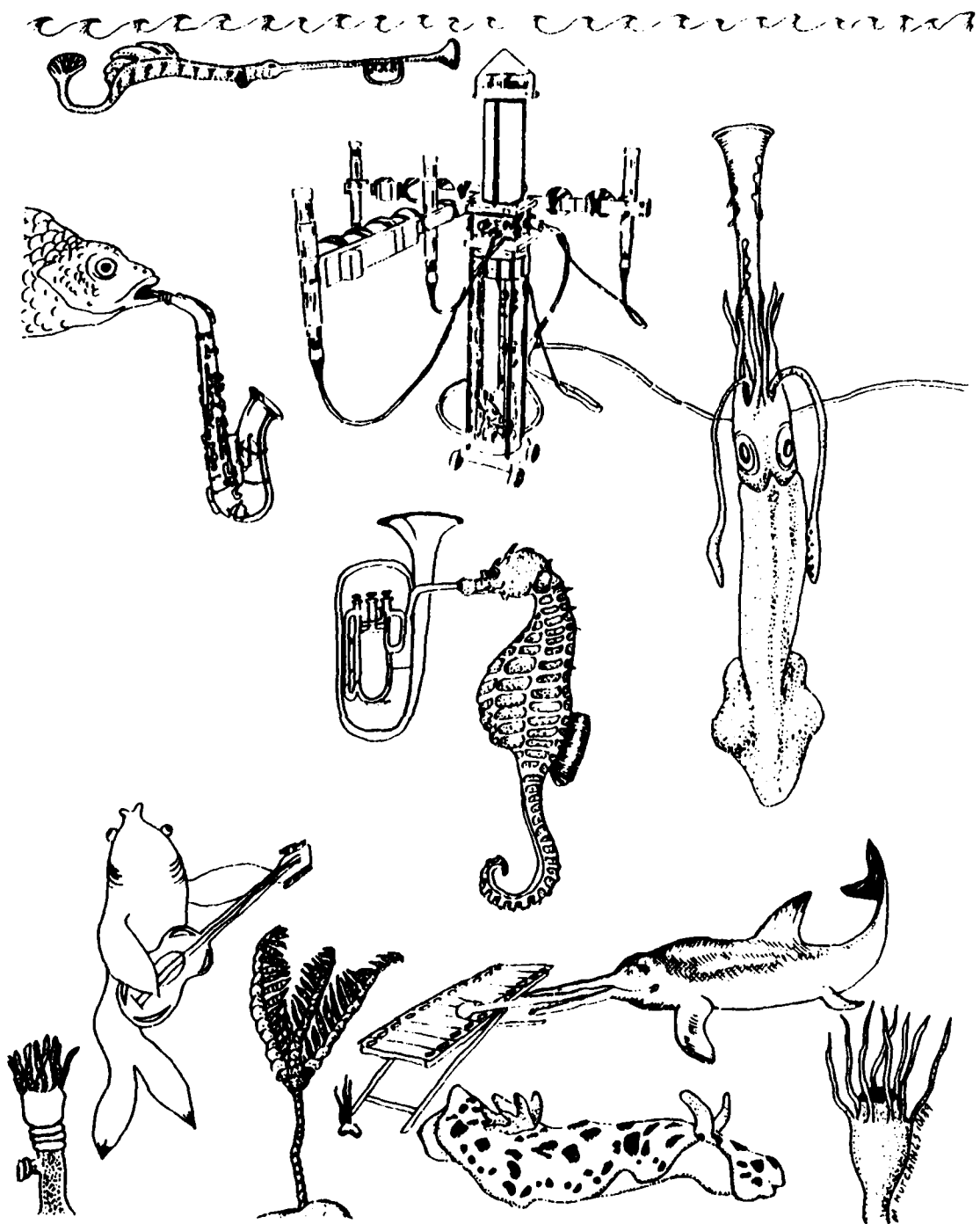
Professor William Hodgkiss

Professor Clinton D. Winant

Professor Carl H. Gibson

Professor Ken L. Smith

SIO REFERENCE 89-21



Beneath the Ocean Surface is a Completely Different Acoustical Environment

Table of Contents

Frontispiece	iv
Table of Contents	v
List of Figures	viii
Acknowledgements	xii
Vita	xiii
Abstract	xiv
1. Background for the Synoptic Surface Noise Instrument	1
Introduction	1
I. A Brief Survey of Audible Noise Mechanism Proposals	2
A. Bubble Breathing Mode Oscillation and Decay	2
B. Alternate Bubble Mechanisms	6
C. Non-Bubble Mechanisms	7
II. Early SSNI Design Considerations	10
Conclusion	11
List of References in Chapter 1	12
2. An Instrument for the In Situ Measurement of Sea Surface Noise from a Depth of One Meter Under Low Wind Conditions	15
Abstract	15
Introduction	15
I. Instrument History	17
II. SSNI Description	21
A. SSNI Video	21

B. SSNI Hydrophones	37
C. Slow Sensors	42
D. Buoyancy Control	45
III. Initial Results	45
Conclusion	55
List of References in Chapter 2	56
3. Bubble Noise and Wavelet Spills Recorded One Meter Below the Ocean Surface	59
Abstract	59
Introduction	60
I. Time Series Samples	62
II. Spectral Analysis of Time Series	63
III. Individual Oscillation Statistics	94
IV. Environmental Observations	101
Conclusion	112
List of References in Chapter 3	114
Appendix A: 30-Minute Environmental Time Series	115
I. Environmental Record from June 30, 1988	116
II. Environmental Record from July 1, 1988	117
III. Environmental Record 5 from July 2, 1988	127
IV. Environmental Record 8 from July 2, 1988	137
V. Environmental Record from July 4, 1988	147
VI. Environmental Record 2 from Feb 20, 1989	157
VII. Environmental Record 4 from Feb 20, 1989	167
Appendix B: Acoustic Time Series Samples from Feb 20, 1988, Record 2	177

G.E. Updegraff -- SIO Reference 89-21

I. Wavelet Break at Video Frame 7890 178

II. Wavelet Break at Video Frame 13140 184

III. Wavelet Break at Video Frame 14500 193

IV. Wavelet Break at Video Frame 22250 197

V. Wavelet Break at Video Frame 29370 203



Accession For	
NTIS GRA&I	<input checked="" type="checkbox"/>
DTIC TAB	<input type="checkbox"/>
Unannounced	<input type="checkbox"/>
Justification _____	
By _____	
Distribution/ _____	
Availability Codes	
Dist	Avail and/or Special
A-1	

List of Figures in Chapter 1

Chapter 1, Figure 1 [from Strasberg, 1956]: 3
Oscillogram of the sound pulse from an individual gas bubble leaving a nozzle, with synchronized high-speed photographs of the bubble itself. The horizontal location of each bubble photograph is chosen so that the time each photograph was taken corresponds to the point on the oscillogram below the center of the bubble.

Chapter 1, Figure 2: 5
Relationship between bubble size near the surface and resonant frequency.

Chapter 1, Figure 3 [from Kerman, 1984, based on Plesset, 1949]: 8
Variation of sound pressure and cavitating bubble radius as the response to changing external pressure.

Chapter 1, Figure 4 [from Franz, 1959]: 9
The typical shape of the sound pressure pulse radiated into the water by the vertical impact of a water droplet (V is the speed of the drop of radius a . r is the distance from the surface to an underwater observer at an angle θ from vertical. ρ is the density of the fluid, and p is the resulting pressure at time t).

List of Figures in Chapter 2

Chapter 2, Figure 1 [from Knudsen, Alford, and Emling, 1948]: 16
Ambient noise level spectra for sounds generated at the sea surface at different wind speeds. (Taken from Knudsen, Alford, and Emling [1948], figure 4).

Chapter 2, Figure 2: 18
Drawing of the SSNI submerged package.

Chapter 2, Figure 3: 19
Drawing of the SSNI wind-sensing buoy.

Chapter 2, Figure 4: 20
Shang and Anderson waterfall plot showing distinct surface noise sources at low wind speed (see text).

Chapter 2, Figure 5: 22
Drawing of the SSNI's deployment configuration.

Chapter 2, Figure 6: 23
SSNI and shipboard equipment block diagram.

Chapter 2, Figures 7a to 7l: 24-36
Sequence of video frames from 24377 to 24389 showing a small water break during deployment on July 1, 1988. The upper left corner of each screen identifies the sequential count.

Chapter 2, Figure 8: 38
 SSNI hydrophone locations as viewed from above.

Chapter 2, Figure 9: 39
 Close-up of acoustic traces for four hydrophones. The arrival time differences of the oscillating source at the hydrophones is used to calculate the noise source location.

Chapter 2, Figure 10: 40
 Signal and data flow for the SSNI submerged instrument.

Chapter 2, Figure 11: 41
 SSNI audio frequency response curves, with and without the pre-whitening filter.

Chapter 2, Figure 12: 43
 Plot showing 4 minutes of instrument depth, roll, and wind speed, with sampled values averaged over 1 second intervals.

Chapter 2, Figure 13: 44
 Shipboard computer monitor display.

Chapter 2, Figures 14a-14g: 46-53
 Acoustic traces for Hydrophone B (with pre-whitening filter) matching video frames in Figure 7. Each page contains four consecutive video frames of 1/30 second each.

Chapter 2, Figure 15: 54
 Close-up of oscillation in Frame 24371 from Chapter 2, Figure 14c.

List of Figures in Chapter 3

Chapter 3, Figure 1: 61
 SSNI Submerged Package -- Video Camera views surface from underneath thru clear top plate from a depth of 1 to 2 meters; four Clevite Hydrophones, each sampled at 20 kHz, allows recording and finding the relative position of surface noises; compass, pitch, roll, and depth sensors, sampled each second, allows monitoring the instruments environment.

Chapter 3, Figures 2a to 2i: 64-73
 Hydrophone B time series of approximately one second of a small wave break recorded on Feb 20, 1989. Each page contains four 1/30 second frames of data, and is numbered with a frame count offset. Individual oscillations within each plot are labeled according to their frequency f_o , location relative to Hydrophone B, and angle θ from vertical over Hydrophone B.

Chapter 3, Figures 3a to 3k: 74-85
 Energetic spill recorded one minute after Chapter 3, Figure 2.

Chapter 3, Figures 4a to 4e: 86-91
 Waterfall plot consisting of peaks from individual FFT's of time-series shown in Figure 3.

Chapter 3, Figure 5: 92
Average of FFT's taken from energetic part of Figure 3. SSNI filters attenuated frequencies below 500 and above 800 Hertz. The dashed reference line represents -5 dB per octave.

Chapter 3, Figure 6 [from Urick, 1983]: 93
Average deep water ambient ocean noise spectra.

Chapter 3, Figure 7: 95
Scatter plot of oscillation decay rates versus frequency. The dashed reference line is based on Strasberg's [1955] empirical formulas.

Chapter 3, Figure 8: 96
Scatter plot of the peak oscillation pressures from 81 bubble oscillations recorded during over 14 small wave breaks. Oscillation locations have been used to calculate the peak pressures at a distance of 1 meter based on spherical spreading losses.

Chapter 3, Figure 9: 98
Scatter plot in which the square pressure has been integrated over the life of each oscillation. The dashed reference line represents -5 dB per octave.

Chapter 3, Figure 10: 99
Solid line -- Integrated square pressure over life of bubble modelled as simple exponentially decaying sinusoid plotted against resonant frequency. Dashed line -- same -5 dB per octave reference line used in Figure 9.

Chapter 3, Figure 11: 100
Logarithmic histogram of bubble frequency distributions. Outer distributions have been affected by both the SSNI filters, which attenuated frequencies below 500 Hertz and above 8,000 Hertz, and by the rejection of overlapping oscillations, which occurred mostly for frequencies below 1,000 Hertz.

Chapter 3, Figure 12a to 12i: 102-111
30 minute time series of instrument environment during deployment on June 30, 1988, at 12:55 p.m. Instrument depth and roll tilt is plotted, followed by the speed and direction of winds measured 1.5 meters over the oceans surface with the SSNI Surface Buoy. A time scale is plotted at the bottom. Vertical dashed lines mark wavelet breaks determined from audio playback of videotape.

List of Figures in Appendix A

Appendix A, Figures 1a to 1i: 118-126
30 minute time series of instrument environment during deployment on July 1, 1988, at 1:57 pm, PST. See page 133 for details.

Appendix A, Figures 2a to 2i: 128-136
30 minute time series of instrument environment during deployment on July 2, 1988, at 4:57 pm, PST. See page 143 for details.

Appendix A, Figures 3a to 3i: 138-146
30 minute time series of instrument environment during deployment on July 2, 1988, at 6:27 pm, PST. See page 153 for details.

Appendix A, Figures 4a to 4i: 148-156
30 minute time series of instrument environment during deployment on July 4, 1988, at 8:54 pm, PST. See page 163 for details.

Appendix A, Figures 5a to 5i: 158-166
30 minute time series of instrument environment during deployment on February 20, 1989, at 10:41 am, PST. See page 173 for details.

Appendix A, Figures 6a to 6i: 168-176
30 minute time series of instrument environment during deployment on February 20, 1989, at 11:59 am, PST. See page 183 for details.

List of Figures in Appendix B

Appendix B, Figures 1a to 1e: 179-183
Wavelet break recorded by Hydrophone B on February 20, 1989, starting at Frame 7890. Sample rate is 20 kHz. Frequency range is 500 to 8000 Hz.

Appendix B, Figures 2a to 2h: 185-192
Wavelet break recorded by Hydrophone B on February 20, 1989, starting at Frame 13140. Sample rate is 20 kHz. Frequency range is 500 to 8000 Hz.

Appendix B, Figures 3a to 3c: 194-196
Wavelet break recorded by Hydrophone B on February 20, 1989, starting at Frame 14500. Sample rate is 20 kHz. Frequency range is 500 to 8000 Hz.

Appendix B, Figures 4a to 4e: 198-202
Wavelet break recorded by Hydrophone B on February 20, 1989, starting at Frame 22250. Sample rate is 20 kHz. Frequency range is 500 to 8000 Hz.

Appendix B, Figures 5a to 5c: 204-206
Wavelet break recorded by Hydrophone B on February 20, 1989, starting at Frame 29370. Sample rate is 20 kHz. Frequency range is 500 to 8000 Hz.

Acknowledgements

First, of course, I would like to thank my advisor, Professor Vic Anderson, who conceived and obtained funding for this entire project and offered it to me during my first year. It is very rare for a graduate student to be given the chance to build and deploy an oceanographic instrument from scratch. At the same time, with a background limited to Electrical Engineering, I never would have finished building this device without the talented assistance of Vic Anderson's Benthic Lab at Scripps: Ron Horn, who designed the dramatic, non-corroding, clear plastic housing of the instrument and programmed the microprocessor and shipboard computer; Fred Uhlman, who built the instrument housing and mechanical devices; and Gerry Denny, who built and wired the instrument power supplies and positional sensors.

In spending so many years building a complicated instrument, it is surprisingly easy to bury oneself in the minutiae of technical details and lose focus of the ultimate goal. Thus, I will be forever indebted to Jim Rohr, of the Naval Ocean Systems Center in San Diego, for his guidance and discussion concerning related literature and my instrument's results. While my investigation concerned the source of underwater sea surface noise, Jim has been working on the related theme of how such noise is suppressed by surface slicks. He provided considerable assistance during a number of ocean deployments, and supplied much needed sea time and encouragement to continue during the Dark Days when I was still trying to record Good Data after five years of work on the instrument.

I would also like to thank Michael Longuet-Higgins of the University of Cambridge, currently at the Center for Studies of Nonlinear Dynamics, in La Jolla, California, for taking the time to personally discuss his theories of surface noise mechanisms, and to suggest some strategies for analyzing my results.

Finally, having little native artistic talent, I am grateful to Molly Hutchings for the Frontispiece on page iv, and to Phil Rapp at the U.C. San Diego Marine Physical Lab for the excellent drawings of my instrument in Chapter 2, Figures 2, 3, and 5.

ABSTRACT OF THE DISSERTATION

In Situ Investigation of Sea Surface Noise
from a Depth of One Meter

by

Garr Edward Updegraff
Doctor of Philosophy in Oceanography
University of California, San Diego, 1989
Professor Victor C. Anderson, Chairperson

The mechanism responsible for audible underwater surface noise, particularly at low wind speeds, is not well understood. Because most surface noise recording instruments are deployed at depths of tens to thousands of meters, they can only characterize the behavior of a population of noise sources, rather than individual noise mechanisms. For this reason, an instrument has been built and deployed at a depth of 1 meter to record the sounds and images of the sea surface during light winds. This self-suspending instrument contains an upward looking video camera, four hydrophones digitized at 20 kHz each, and positional sensors. A surface buoy, tethered 30 meters from the submerged instrument, continuously supplies the wind speed and direction. Recordings from the instrument indicate that surface noise produced during light winds is generated by small wavelet spills which have no correlation with the amplitude or phase of long period swells moving faster than prevailing winds. The averaged acoustic spectra from a single energetic spill showed a slope of -5 dB per octave, matching the spectral slope first reported by Knudsen, Alford, & Emling in 1948 for wind generated surface noise. The sound generated by these small spills is composed of distinct transient sinusoids, each of which usually starts impulsively and then decays exponentially within milliseconds. This behavior matches the millimeter sized bubble signatures described by Strasberg [1956] and Medwin & Beaky [1989]. The unique frequency for each oscillation within a wavelet spill indicates that bubbles are "rung" during entrainment, die out, and then no longer contribute actively to the acoustic record. The peak pressures of these oscillations range up to 1.2 Pascals, with little apparent dependence on frequency over the 500 to 8,000 Hz range of the instrument. Analysis of the acoustic energy generated by a number of bubbles versus frequency suggests that the -5 dB per octave slope is caused by the shorter lifetimes of high frequency bubbles, rather than significantly lower peak pressures.

Chapter 1:

Background for the Synoptic Surface Noise Instrument

INTRODUCTION

Audible noise generated at the ocean surface in high winds is clearly linked with whitecap breaking. But what is the cause of noise generated at the sea surface when winds are too low to generate whitecapping?

There is no conclusive answer to this question in the literature. In an effort to learn more, Professor Anderson deployed ADA [Anderson, 1980; Shang and Anderson, 1986], a huge underwater acoustical array, fifty meters from the ocean surface during light winds. The array detected brief bursts of acoustic activity, but was still unable to identify the mechanism that generated the sounds. Anderson decided that a new instrument package was needed, one specifically designed to answer this basic mystery. Where other devices had been deployed at depths of tens to thousands of meters to record and analyze surface noise, the Synoptic Surface Noise Instrument (SSNI) would be self-suspended one meter from the ocean's surface and isolated from support ship noise by a horizontal, one-kilometer coaxial tether. Where other devices had recorded a *population* of noise sources, yielding noise population statistics which generally confirmed the frequency and wind-dependent characteristics first published by Knudsen, Alford, & Emling in 1948, the SSNI would be equipped with a video camera and four hydrophones for recording both the surface environment and the acoustical signatures of *individual* noise events.

However, when I agreed back in 1983 to build and deploy the SSNI (Chapter 2, Figures 2 and 3), and then analyze the resulting data for my thesis, neither Anderson nor I knew the sorts of sounds to expect. In order to record distinct, non-overlapping noise events, the SSNI would probably require mild wind conditions. Both the "Knudsen Curves" (Chapter 2, Figure 1) and ADA showed noises produced in winds as low as 1.8 meters per second. But until very recently, the noise mechanisms proposed in the literature -- although predicting the trademark of the Knudsen Curves: a spectral slope of -5 dB per octave from about 200 to 20,000 Hz, with a broadband increase in spectral energy to match rising winds -- were predicated on much higher wind speeds. What was the source of surface noise at low wind speeds? Was it different than at high wind speeds? In order to fulfil its mission, the SSNI had to be capable of differentiating between the various possible mechanisms.

I. A BRIEF SURVEY OF AUDIBLE NOISE MECHANISM PROPOSALS

Publication of the Knudsen Curves created a mystery: What was the surface noise mechanism that caused the deep water spectral slope of -5 dB per octave? In the four decades since then, the lack of conclusive oceanic data has resulted in a multitude of proposals. This section provides a short summary of these ideas for the benefit of the casual reader who may be unfamiliar with the subject. A familiarity with the area is important for understanding the design of the instrument and interpreting its results.

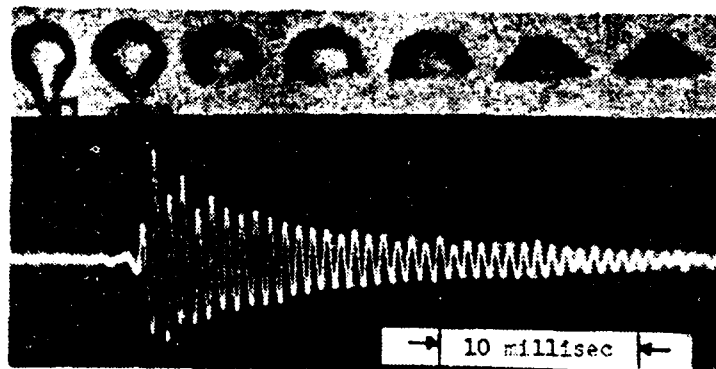
A. Bubble Breathing Mode Oscillation and Decay

One of the earliest proposals to explain the source of audible surface noise suggested that it was caused by oscillating air bubbles or cavitation (water vapor bubbles created by vacuum which collapse rapidly). In a 1962 overview, Wenz concluded that "air bubbles and cavitation produced at or near the surface, as a result of the action of the wind, could very well be a source of the wind-dependent ambient noise at frequencies between 50 and 10,000 Hertz." Although air bubbles continue to be popular in the literature, cavitation has largely fallen out of favor; the strong negative pressure required to initiate cavitation is highly unlikely in the open ocean [Prosperetti, 1988].

What, then, would the SSNI expect to record for noise produced by bubbles? One of the researchers upon whom Wenz based his report was Minnaert [1933], who first attributed the noise from gas bubbles to volume pulsations (the periodic and simultaneous expansion and contraction of the radius over the entire bubble), commonly called the zero-order or breathing mode oscillations of a bubble. Using various glass tubes to inject gas at a steady rate into a pail of water, Minnaert was able to determine, by ear, the pitches produced by the resulting bubbles to within a half tone. This was plotted against their air volume, which he calculated by capturing each bubble in an inverted funnel and channelling it into a capillary tube for lengthwise measurement. Minnaert found he obtained good agreement with his experimental results by modelling an oscillating bubble as a weight bouncing up and down at the end of a spring, "the surrounding water being the inert mass which is set in vibration, while the elasticity is due to the air of the bubble." With the spring-and-mass analogy, Minnaert was able to derive equations for both the resonant frequencies of bubbles and the resulting pressures in the surrounding liquid.

Strasberg [1956] repeated and expanded Minnaert's experiment, recording oscillogram traces of the pressures produced by bubbles as they detached from the air injection apparatus. In Figure 1, copied from Strasberg's paper, oscillations begin as the bubble detaches and then immediately decay exponentially. In a 1988 review of the physical processes involving bubbles in clean water, Prosperetti attributed this decay to three factors: 1) viscosity of the surrounding liquid, especially for bubbles smaller than 3 μm ; 2) thermal radiation, which dominates bubbles from about 3 μm to 3 mm; and 3) acoustic radiation, which is the chief cause of damping for bubbles larger than 3 millimeters. Thus, for bubbles that are initially "rung" and then left alone in fresh water, those larger than a millimeter might be expected to produce the loudest sounds. In ocean water, however, bubbles are known to rapidly form a biogenous coating at their surface which acts to preserve bubbles of approximately 10 μm from immediate dissolution [Johnson & Cooke, 1981]. It is not known what effect, if any, this surfactant contributes to bubble damping.

Minnaert showed that the resonant frequency of a bubble is directly correlated with its size. Worked out by Strasberg, the resonant frequency for a bubble of mean radius R_0 , in a liquid of density ρ and static pressure p_s , is



Chapter 1, Figure 1 [from Strasberg, 1956]: Oscillogram of the sound pulse from an individual gas bubble leaving a nozzle, with synchronized high-speed photographs of the bubble itself. The horizontal location of each bubble photograph is chosen so that the time each photograph was taken corresponds to the point on the oscillogram below the center of the bubble.

$$f_0 = \frac{1}{2\pi R_0} (3\gamma p_s / \rho)^{1/2},$$

where γ is the ratio of specific heats for the gas in the bubble. For an air bubble in water at atmospheric pressure, this simplifies to

$$f_0 R_0 = 3300 \text{ millimeters / sec.} \quad (1)$$

Figure 2 shows a plot of this relationship.

The amplitude of the radiated pressure in the liquid at a distance d from the center of the oscillating bubble, due to the radius changing by an increment r_0 , is

$$p_0 = \frac{3\gamma p_s r_0}{d}.$$

At a distance of one meter, this simplifies to

$$p_0 / r_0 = 270 \text{ Pa / millimeter} \quad (2)$$

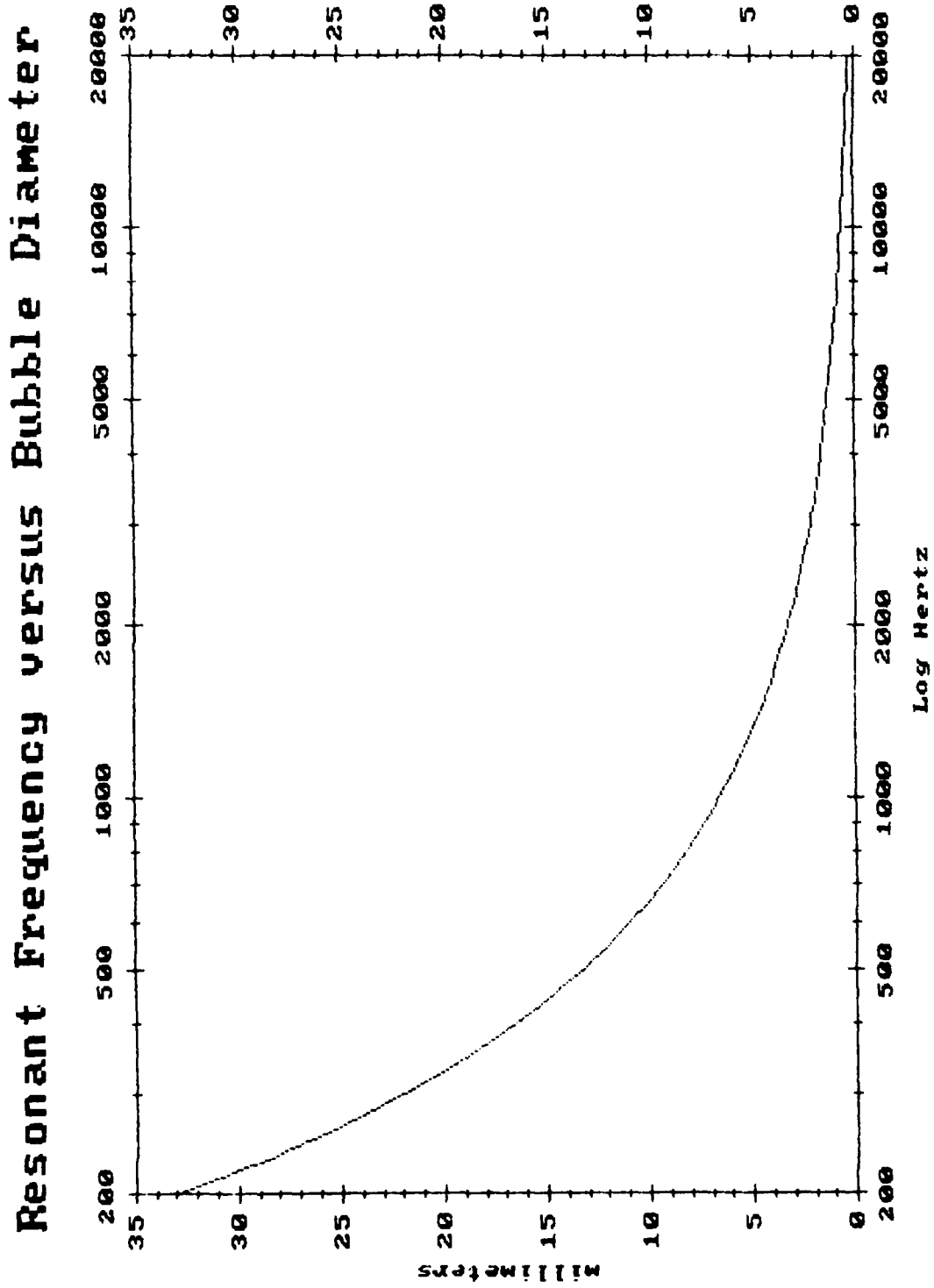
The exponential decay of the pressure envelope for free standing oscillating bubbles can be gauged by the decay constant τ_e , which is the time for the envelope to shrink by a factor of $1/e$. τ_e can be calculated for a given resonant frequency f_0 , specified in Hertz, based on the following formula (derived from Strasberg):

$$\tau_e(f) = \frac{91,000}{\pi f(f + 1300)} \text{ seconds.} \quad (3)$$

This equation is plotted with a dashed line in Figure 7 of Chapter 3.

From these equations (1) and (3), we can see that a bubble resonating at 500 Hz (the approximate frequency below which shipping noise begins to dominate surface noise) has a radius of 6.6 mm and a time constant of 33 ms, while a 10,000 Hz bubble has a radius of 0.33 mm and a time constant of 0.26 ms. Such small lifetimes shed new perspective on Minnaert's feat of calculating bubble frequencies by ear!

What these sizes mean to the SSNI video camera is that bubbles that are capable of resonating in the frequencies of interest are essentially invisible. This does not mean, however, that their position cannot be determined. The difference in time that it takes an acoustic signal, travelling at approximately 1,500 meters per second, to reach each of the four hydrophones can be used to determine the signal's location during later analysis. Knowing its position, relative to the SSNI submerged package, can help determine



Chapter 1, Figure 2: Relationship between bubble size near the surface and resonant frequency.

whether a noise is associated with a wavelet at the surface or with some more mysterious mechanism beneath the surface.

What sort of sound pressures might be expected from resonating bubbles? A calculation by Wenz using equation (2), based on a bubble oscillating near the surface with a mean radius $R_0 = 3.3$ mm and a radial amplitude of one-tenth this value, showed a peak pressure of 89 Pascals (160 dB re $1 \mu\text{Pa}$), measured from a distance of one meter! While this may seem to be an extreme pressure, Strasberg recorded peak pressures of up to 22 Pascals for bubbles injected into water with glass tubes. Clearly, properly excited bubbles are capable of generating very high pressure oscillations indeed.

The problem with attributing ocean surface noise to this classic bubble ringing has been the lack of both solid experimental evidence and convincing theories to explain the initiation of oscillations in the first place. Strasberg had noted in the lab that bubbles rang when they split or coalesced, with peak pressures of about 0.1 Pa from a distance of 1 meter, but it was not clear how such information was to be applied to the ocean's surface.

Recent laboratory experiments, however, have shed new light on bubble noise mechanisms. Banner and Cato [1988] used a high-speed movie camera to record the entrainment and agitation of bubbles formed in a water flume. They observed that, in general, bubbles rang when first formed, after splitting, or after coalescing. Bubble contortions caused by turbulence in the flume eddies did not produce significant noise, nor did bursting bubbles. In another experiment, Medwin & Beaky [1989] generated artificial breaking waves in a windless laboratory environment and detected significant Strasberg-like pressure oscillations, with peak pressures from 0.1 to 1 Pascals. Such a windless environment may not differ appreciably from the ocean's surface in light winds.

Recently, Longuet-Higgins [1989] has proposed a mechanism in which breathing mode oscillations are triggered by the distortion a bubble suffers during its initial entrainment and formation. He has estimated that peak pressures of roughly 0.5 Pascals would be typical for the bubble sizes of interest, and has predicted that the mechanism should be identifiable by oscillation energy peaks at certain frequencies.

B. Alternate Bubble Mechanisms

Since the bubbles of interest are more or less invisible, we must consider whether the behavior of Strasberg's bubbles is typical for all bubble mechanisms, or whether a different acoustical signature might be expected in other cases.

In proposing bubbles as a source of noise, Wenz suggested that rising bubbles might begin to oscillate under the effects of surface turbulence. But in a later paper, Crighton and Williams [1969] stated that a resonant response by bubbles due to turbulence alone was impossible because "the length scale over which the pressure field remains coherent at the resonance frequency is found to be very small compared with the bubble frequency." A similar idea was proposed by Kerman [1984], in which bubbles entrained in the turbulence of a white cap would be forced to oscillate at a non-resonant frequency. Kerman [1988] suggests that the frequency spectrum produced by such a mechanism should be related to the turbulent spectrum, although the details of this spectrum are not well understood in the ocean. At the least, one might expect a relatively smooth power spectrum during the life of the white cap and acoustical signatures considerably different than Strasberg's damped sinusoids. Prosperetti [1988] has indicated that the frequencies produced by Kerman's mechanism would be limited to a few tens of Hertz at the most, placing this mechanism's contributions beyond the range of the SSNI.

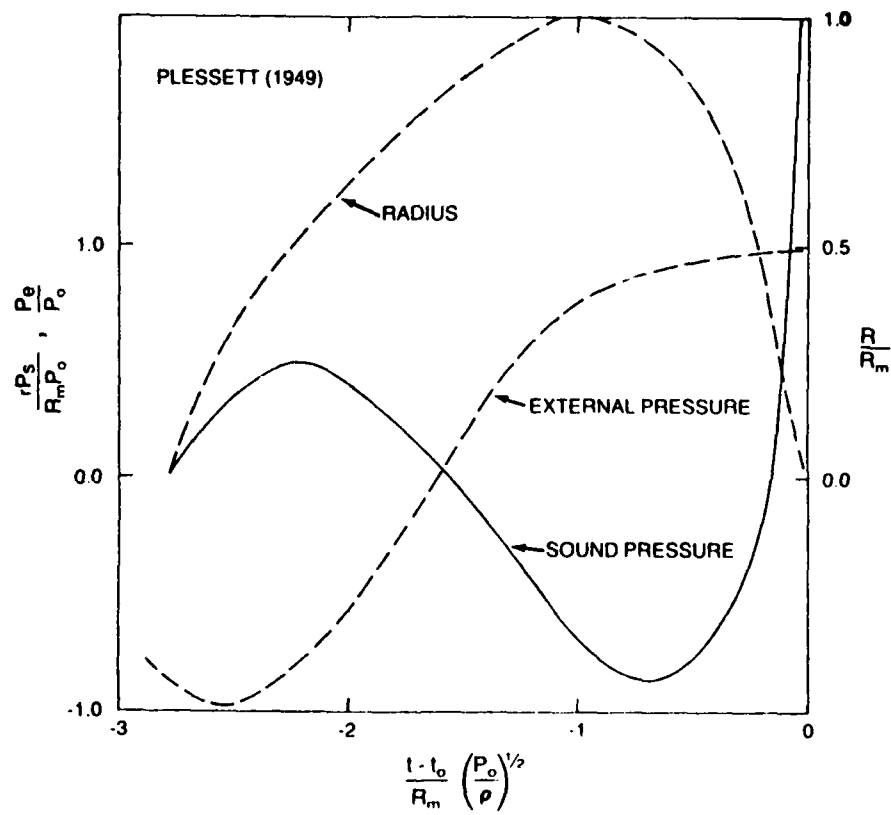
Both Wenz [1962] and Shang & Anderson [1986] suggested that bursting bubbles might produce substantial noise. However, the observed sounds due to bursting bubbles in laboratory experiments by G. J. Franz [1959], and later by Banner and Cato [1988] using an air-entraining water flume, have been negligible compared to bubble ringing.

Another possible noise mechanism is suggested by the presence of enormous numbers of microbubbles near the ocean surface [Medwin, 1977]. In clean water, the pressure inside a bubble is higher than the static surrounding pressure because of the surface tension T at the bubble's surface, which contributes a pressure equal to $2T/R_0$. Because this pressure is inversely proportional to the bubble's radius, a shrinking bubble will experience increasing internal pressure. This tends to force the enclosed air to dissolve into the surrounding water, which allows the bubble to shrink still smaller and experience more pressure in a system of positive feedback which causes rapid collapse and the pressure pulse shown in Figure 3. In sea water, however, Johnson & Cooke [1981] observed in a laboratory experiment that, after injecting 0.1 millimeter bubbles into seawater, some bubbles avoided collapse by adsorbing a biogenous coating onto their surfaces. These bubbles shrank and stabilized to sizes ranging from 1 to 15 μm . Increasing the external pressure to an effective depth of 1 or 2 meters of water resulted in the collapse of all such bubbles, while those left at atmospheric pressure lasted more than a day. These stabilized microbubbles are generally presumed to account for the bubble population estimates made acoustically by Medwin [1977], who calculated that a cubic meter of ocean surface water easily contained hundreds of thousands of bubbles of radii less than 50 μm . Bubbles of this size are essentially neutrally buoyant and will drift with the mildest of currents. Eventually, they must either dissolve on their own or be carried to a depth that forces collapse, which could result in an acoustic pulse. While the enormous pulse produced by a cavitation or vacuum enlarged bubble has been measured [Harrison, 1952], it is not clear whether the collapse of micrometer sized, coated bubbles is acoustically significant, even given the contributions of huge numbers. Certainly, higher winds can be expected to cause more bubbles to collapse as increasing turbulence carries them deeper. But the noise recorded by the SSNI, which would depend upon the speed of bubble collapse and the numbers involved, could conceivably range anywhere from a continuous background hiss to weak versions of the "sharp cracks" described by Harrison for collapsing vapor/air bubbles.

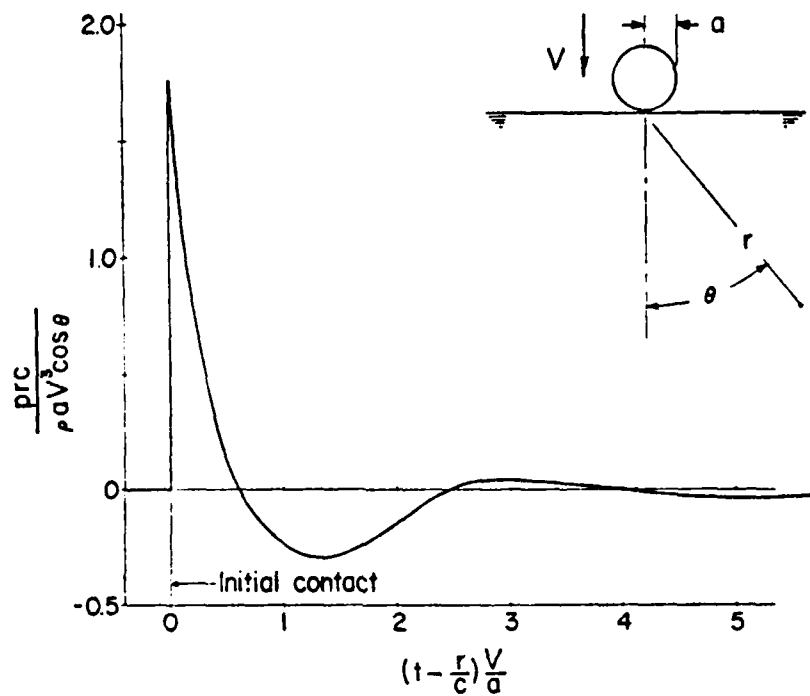
C. Non-Bubble Mechanisms

Sea spray impact at high winds has been proposed by Wilson [1980] to account for surface noise frequencies below 1,000 Hertz, based on the experimental results of Franz [1959] for drop impact noise. Although the SSNI is intended for light wind deployments where spray would be unlikely, the pressure trace produced by such impacts is quite distinct, as shown in Figure 4, copied from Franz.

In addition to the initial impact pulse, some water drop impacts have been shown to radiate sounds that are considerably louder. In a recent paper on the sound produced by water drops, Pumphrey & Crum [1988] showed that within a specific range of speed and size, which includes a significant fraction of rain drops, water drops entrain small bubbles that radiate in the frequency range of 14 to 16 kHz. The droplets capable of producing this noise range from roughly 1 to 4 mm, with matching impact velocities ranging from 4 to 1 meters/sec. Such drops would not seem to be unusual at the wind speeds associated with extensive white capping. Unfortunately, the data acquisition rate of the SSNI for four hydrophones limits each hydrophone to frequencies below 10 kHz, well below the expected frequency range for bubbles generated by this mechanism. Thus, the SSNI, which was built before Pumphrey & Crum's results were published, is incapable of detecting this mechanism. If I were to redesign the instrument, I would alter the SSNI hardware to allow a shipboard operator to send commands to switch from sampling four hydrophones



Chapter 1, Figure 3 [from Kerman, 1984, based on Plesset, 1949]: Variation of sound pressure and cavitating bubble radius as the response to changing external pressure.



Chapter 1, Figure 4 [from Franz, 1959]: The typical shape of the sound pressure pulse radiated into the water by the vertical impact of a water droplet (V is the speed of the drop of radius a . r is the distance from the surface to an underwater observer at an angle θ from vertical. ρ is the density of the fluid, and p is the resulting pressure at time t).

simultaneously to sampling a single hydrophone four times as fast. Although the ability to locate noise sources would be lost in the single hydrophone mode, the instrument would be able to record frequencies of up to 40 kHz.

II. EARLY SSNI DESIGN CONSIDERATIONS

The SSNI was built to identify surface noise mechanisms. As with any such system, this entailed trade-offs between various requirements and limitations. On the one hand, the acoustical identification of noise mechanism signatures required a high signal-to-noise ratio and the capability of recording high frequencies. On the other hand were hard limits on how quickly and how much information could be stored on the recording system. Facing sound sources of unknown dynamic range, the SSNI was built to digitize all hydrophones and sensors at a resolution of 12 bits per sample. On a relative scale, this is equivalent to being able to measure a signal from 1 Pascal down to half a milliPascal. Once digitized, the signals become immune to transmission and recording distortion, and can be analyzed immediately by a shipboard computer.

In addition to just recognizing an acoustical signature, however, knowing its location relative to the instrument and the surface was deemed equally important to understanding its mechanism. For example, an oscillating bubble trace might indicate air entrainment at the surface, a subsurface bubble splitting due to turbulence, or just trapped air slowly leaking from part of the instrument. Or, depending on its location, a pressure impulse might indicate a collapsing bubble, bad sound proofing of the instrument's tether attachment, or perhaps some sort of electronic noise. But calculating the location of a noise source acoustically, based on the different arrival times by an acoustic pulse at each hydrophone, requires at least four hydrophones. Since there is a limit on how fast data can be stored, there is a direct trade-off between digital sampling speed and the number of hydrophones: Each of four hydrophones can only be recorded at one-quarter the frequency of a single hydrophone by itself.

Adding yet more complexity was a concern over the role of subsurface turbulence in creating noise. Shang & Anderson [1986] favored a mechanism proposed by Furdujev [1966], cavitation bubbles created by turbulence, as the mechanism behind the surface noise they observed in their data. In order to measure some portion of the turbulent spectrum above the instrument, I designed the SSNI data stream to accommodate the future installation of a doppler sonar system. Thus, two more channels were added to the four hydrophone channels. Although the doppler sonar has yet to be added to the SSNI, it now seems that a simple surface-pointed echo sounder would be more useful. This would allow small swells over the instrument to be recorded and correlated against prevailing winds and surface spills.

Digitizing four hydrophone and two doppler channels at 12 bits per sample in the audible frequency range entails transmitting and recording an enormous amount of data. A Megatape MT-500 streaming tape drive, attached to a somewhat portable PDP-11/23 computer, was selected for storing this information. Capable of recording 180,000 bytes per second on 30-minute cartridges, the MT-500 allows each channel to be sampled at 20 kHz. After input signals are filtered against anti-aliasing effects, this allows frequencies of up to 8 kHz to be recorded. While a glance at the ambient noise spectrum in Figure 6 of Chapter 3 shows that this does not cover the entire surface noise spectrum, it still encompasses well over half of the expected logarithmic frequency range.

While Anderson's acoustical array ADA, mentioned at the beginning of this chapter, had associated transient sounds with the ocean surface, it was not clear what aspect of surface conditions caused the sounds. Were the sounds due to microbreaks? Whitecap spray? Collapsing bubbles? Rising

bubbles caught in turbulence? Were they associated with the phase, period, or amplitude of swells? Clearly the SSNI required additional sensors in order to resolve such questions.

A video camera was included in the SSNI so that surface conditions could be monitored and associated with noise events. A television time-channel electronic chip is used in the instrument to allow the microprocessor to write unique frame counts onto each 1/30 second video frame (see Figure 7 of Chapter 2 for examples). In this manner, a swell washing over the instrument could be analyzed one video frame at a time and correlated with the digitized hydrophone data. In addition, recording the reconstructed analog signals from two hydrophones onto videotape has allowed real-time audio playback. This has proven invaluable for rapidly locating noise events within a 30-minute deployment, and recognizing extraneous sounds such as ship noise or submarine sonars.

In order to determine the role of swells in surface noise, tilt, roll, and acceleration meters were added to the SSNI submerged package. While small, 1-meter swells are undetectable by such sensors for an instrument submerged one or two meters beneath the surface, long swells with wavelengths of tens of meters can be accurately recorded.

Since wind speed is known to affect surface noise, the surface buoy shown in Figure 3 of Chapter 2 was added to the system. The surface buoy, attached 30 meters from the submerged package, contains two calibrated, magnetically coupled, perpendicular propellers and an electronic compass, so that wind speed and direction can be recorded.

CONCLUSION

This chapter presents short histories of both the surface noise mystery and the SSNI.

In Chapter 2, which has been written for journal publication, I describe the technical aspects of the SSNI in more detail, along with some initial deployment data. This data indicates that surface noise in light winds is caused by small surface wave spills and breaks which are composed of distinct oscillations. The oscillations, which strongly resemble the bubble oscillations described by Strasberg [1956], decay within milliseconds.

In Chapter 3, also written for journal publication, I present and analyze additional data in more detail in order to characterize these bubble oscillations.

As these chapters cover only a small subset of the data recorded by the SSNI, the interested reader will find supplementary data plots in the appendices of this dissertation. These plots show data taken over a variety of surface conditions.

LIST OF REFERENCES IN CHAPTER 1

- Anderson, V. C., 1980. "Nonstationary and Nonuniform Oceanic Background in a High-Gain Acoustic Array", *J. Acoust. Soc. Amer.* **67**(4), 1170-1179.
- Banner, M. L. and D. H. Cato, 1988. "Physical Mechanisms of Noise Generation by Breaking Waves -- A Laboratory Study", from *Sea Surface Sound*, 429-436, Kluwer Academic Publishers, edited by B. R. Kerman.
- Crighton, D. G. and J. E. Ffowcs Williams, 1969. "Sound Generation by Turbulent Two-Phase Flow", *J. Fluid Mech.* **36**(3), 585-603.
- Franz, G. J., 1959. "Splashes as Sources of Sound in Liquids", *J. Acoust. Soc. Amer.* **31**(8), 1080-1096.
- Furduev, A.V., 1966. "Undersurface Cavitation as a Source of Noise in the Ocean", *Atmos. Oceanic Phys.* **2**(5), 314-320.
- Harrison, M., 1952. "An Experimental Study of Single Bubble Cavitation Noise", *J. Acoust. Soc. Amer.* **24**(6), 776-782.
- Johnson, B. D. and R. C. Cooke, 1981. "Generation of Stabilized Microbubbles in Seawater", *Science* **213**, 209-211.
- Kerman, B. R., 1984. "Underwater Sound Generation by Breaking Wind Waves", *J. Acoust. Soc. Amer.* **75**(1), 149-165.
- Knudsen, V. O., R. S. Alford, and J. W. Emling, 1948. "Underwater Ambient Noise", *J. Mar. Res.* **7**, 410-429.
- Longuet-Higgins, M. S., 1989. "Monopole Emission of Sound by Asymmetric Bubble Oscillations", *J. Fluid Mech.* **201**, 525-565.
- Minnaert, M., 1933. "On Musical Air-Bubbles and the Sounds of Running Water", *Phil. Mag.* **16**, 235-248.
- Medwin, H., 1977. "In Situ Acoustic Measurements of Microbubbles at Sea", *J. Geophys. Res.* **82**(6), 971-976.
- Medwin, H. and M. M. Beaky, 1989. "Bubble Sources of the Knudsen Sea Noise Spectra", *J. Acoust. Soc. Amer.* **86**(3), 1124-1130.
- Plesset, M. S., 1949. "The Dynamics of Cavitation Bubbles", *J. Applied Mech.* **16**, 277-282.
- Prosperetti, A., 1988. "Bubble Dynamics in Oceanic Ambient Noise", from *Sea Surface Sound*, Kluwer Academic Publishers, edited by B. R. Kerman.
- Pumphrey, H. C., L. A. Crum, L. Bjorno, 1988. "Underwater Sound Produced by individual Drop Impacts and Rainfall", *J. Acoust. Soc. Amer.* **85**(4), 1518-1526.
- Shang, E. C. and V. C. Anderson, 1986. "Surface Generated Noise Under Low Wind Speed at Kilohertz Frequencies", *J. Acoust. Soc. Amer.* **79**(4), 964-971.

- Strasberg, M. 1956. "Gas Bubbles as Sources of Sound in Liquids", *J. Acoust. Soc. Amer.* 28(1), 20-26.
- Urick, R. J., 1985. *Ambient Noise In The Sea* (1st edition), Peninsula Publishing, Los Altos, CA.
- Wenz, G. M., 1962. "Acoustic Ambient Noise in the Ocean: Spectra and Sources", *J. Acoust. Soc. Amer.* 34(12), 1936-1956.
- Wilson, J. H., 1980. "Low Frequency Wind-Generated Noise Produced by the Impact of Spray with the Ocean's Surface", *J. Acoust. Soc. Amer.* 68(3), 952-956.

Chapter 2:

An Instrument for the In Situ
Measurement of Sea Surface Noise
from a Depth of One Meter
Under Low Wind Conditions

(submitted to the Journal of the Acoustical Society of America
as a joint paper by G. E. Updegraff and V. C. Anderson)

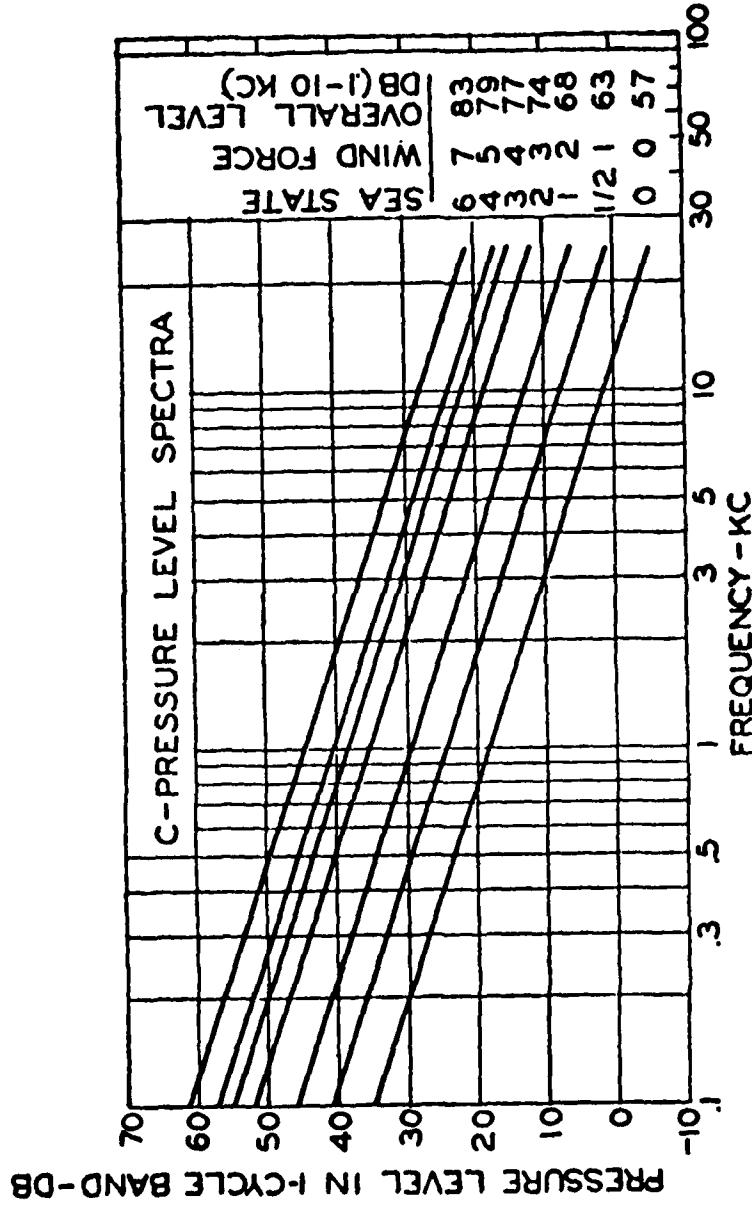
ABSTRACT

An underwater package has been developed and deployed to determine the cause of surface noise generated at low wind speeds. The self-suspending instrument, tethered one kilometer from a support ship, contains a video camera and four hydrophones, as well as orientation sensors. The signal from each hydrophone is filtered and digitized to cover a frequency range of 500 to 8,000 Hertz. Data recorded from a depth of 1 to 2 meters indicates that considerable noise is generated by tiny surface spills. The sound from each spill is composed of distinct decaying oscillations which last only for a few milliseconds. These oscillations match the resonant bubble signatures described by Strasberg [1956] and Medwin & Beaky [1989].

INTRODUCTION

What makes the audible underwater noise that comes from the surface of the ocean in light winds?

As simple and fundamental as this question seems, the mechanism behind the noise has yet to be satisfactorily identified based on ocean data. In the years since Knudsen, Alford and Emling published the



Chapter 2, Figure 1 [from Knudsen, Alford, and Emling, 1948]: Ambient noise level spectra for sounds generated at the sea surface at different wind speeds. (Taken from Knudsen, Alford, and Emling [1948], figure 4).

"Knudsen Curves" (Figure 1) in 1948, several experimenters have confirmed that audible noise above 500 Hertz is generated at or near the surface, and tends to be closely correlated with sea state and wind speed, with a spectral slope of -5 to -6 dB per octave (see Urick [1986], pages 2-18 to 2-27 for a general summary of the field).

Unfortunately, these studies have not been able to identify the actual mechanism behind the noise. Most of the published in situ measurements have been conducted using hydrophone arrays mounted or tethered to the ocean bottom at depths ranging from 6 to 4,000 meters. While this avoids the self noise generated by waves slapping against a surface suspended hydrophone structure, such arrays are measuring a large simultaneous population of noise sources, rather than isolated mechanisms. This has led to a rich and varied body of literature over possible source mechanisms generating spectral slopes of -5 to -6 dB per octave [Wenz, 1962; Wilson, 1980; Marsh, 1963; Kuo, 1968; Kerman, 1984; Shang and Anderson, 1986; Furduev, 1966; Hollett and Heitmeyer, 1988; and Longuet-Higgins, 1989], covering such possibilities as: drop impact from whitecap spray, capillary wave interaction, air bubbles entrained in turbulent fluctuations, air bubbles bursting at the surface, cavitating bubbles, bubbles oscillating after initial formation due to initial distortion, bubbles oscillating due to an abrupt depth increase during entrainment, and bubbles oscillating due to the initial momentum of the surrounding water following the bubble as it closes.

The Synoptic Surface Noise Instrument (SSNI) described in this paper has been designed to help resolve these possibilities for ocean noise generated at low wind speeds. It is a self-suspending, horizontally tethered package containing a variety of sensors, including a video camera and four hydrophones (Figure 2). The instrument adjusts its buoyancy to stay within 2 meters of the surface so that individual noise sources can be isolated and recorded for later analysis. Each hydrophone is digitally recorded to cover a frequency band ranging from roughly 500 to 9,000 Hertz. The horizontal tether, a 75-ohm, foam dielectric coaxial cable, allows the transmission of power and telemetry between the instrument and a support ship; at one kilometer, the cable is long enough to isolate the instrument from noise generated by the support ship. A surface buoy, attached to the coax tether 30 meters from the instrument, transmits continuous wind speed data to the submerged instrument (Figure 3).

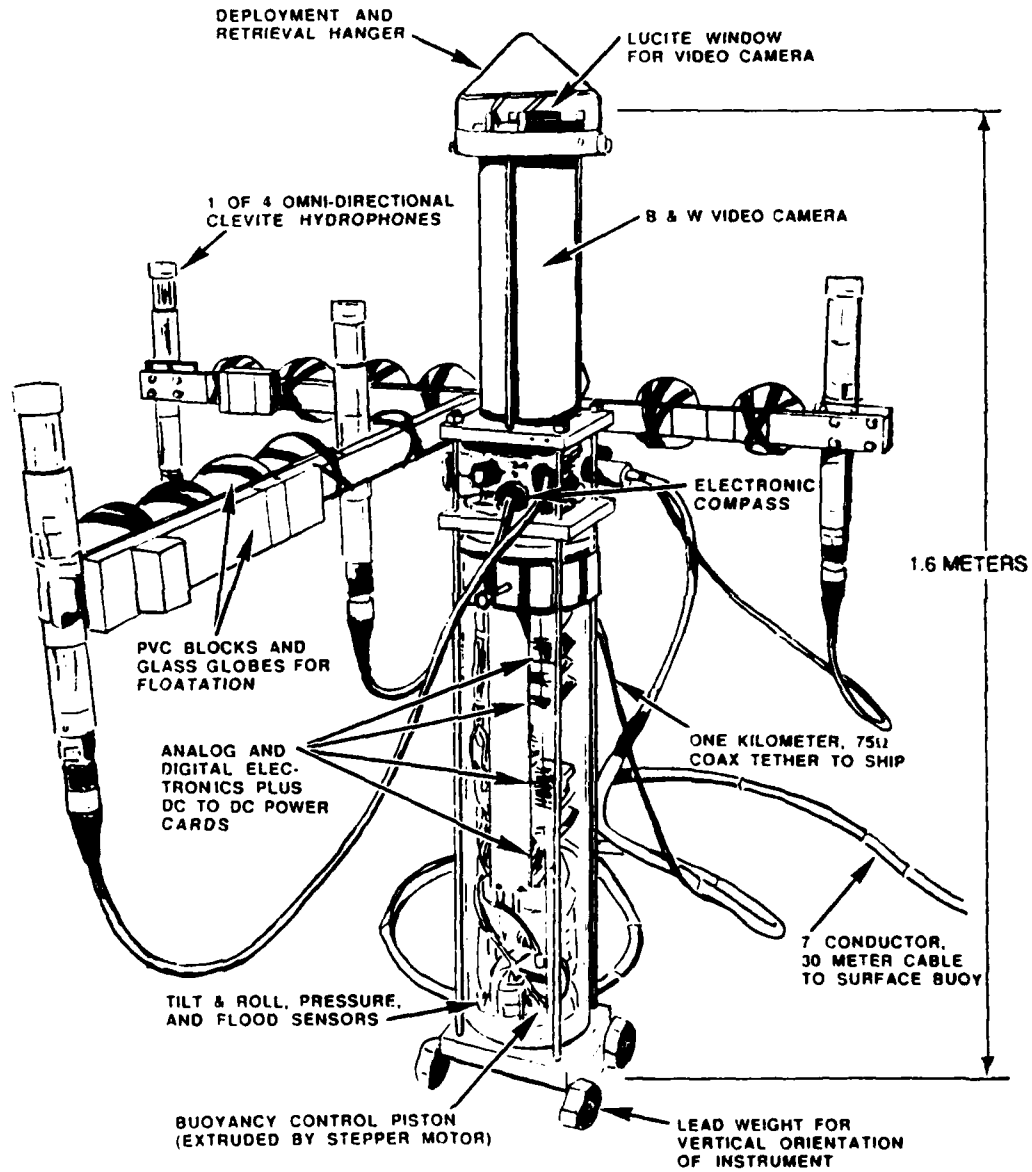
I. INSTRUMENT HISTORY

The construction of the SSNI was suggested by the results of Shang and Anderson [1986], which were based on deployment of a huge underwater array 50 meters from the ocean surface in deep water. Certain data showed evidence of discrete noise events occurring under wind conditions (1.8 meters/sec on an uncalibrated anemometer 10 meters above the sea surface) which were too low to generate the whitecapping generally associated with surface noise.

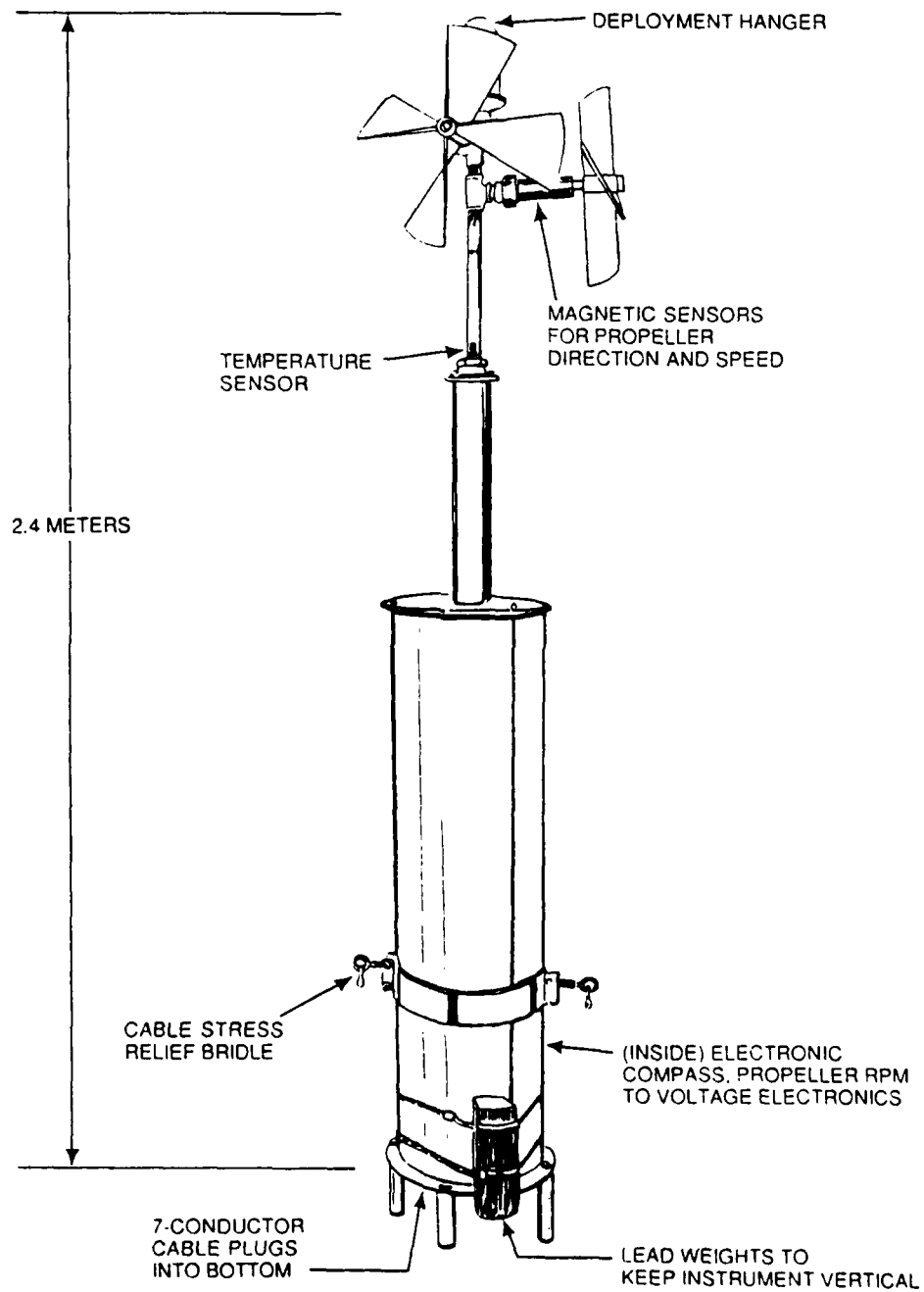
The data from their paper is shown in Figure 4: Two waterfall plots of acoustic power taken from an annular sector over the array. Each horizontal line in the plots represents a 50 millisecond average of a set of rectified beam outputs; moving up past each line represents a 50 millisecond advance in time. The greatest focus and sensitivity lies along the vertical center of the plots.

The right half of Figure 4 shows data recorded when the wind speed was 3.6 meters/sec. Notice that the noise episodes tend to last across a one-second sequence of lines. This is most likely due to wave breaks associated with the tops of passing swells (the exact surface condition, such as the angle of the dominant swells and wind with respect to ADA, was not recorded). According to Wille & Geyer [JASA, 1984], such breaking can occur in winds as low as 2.5 meters/sec, given sufficiently steep swells.

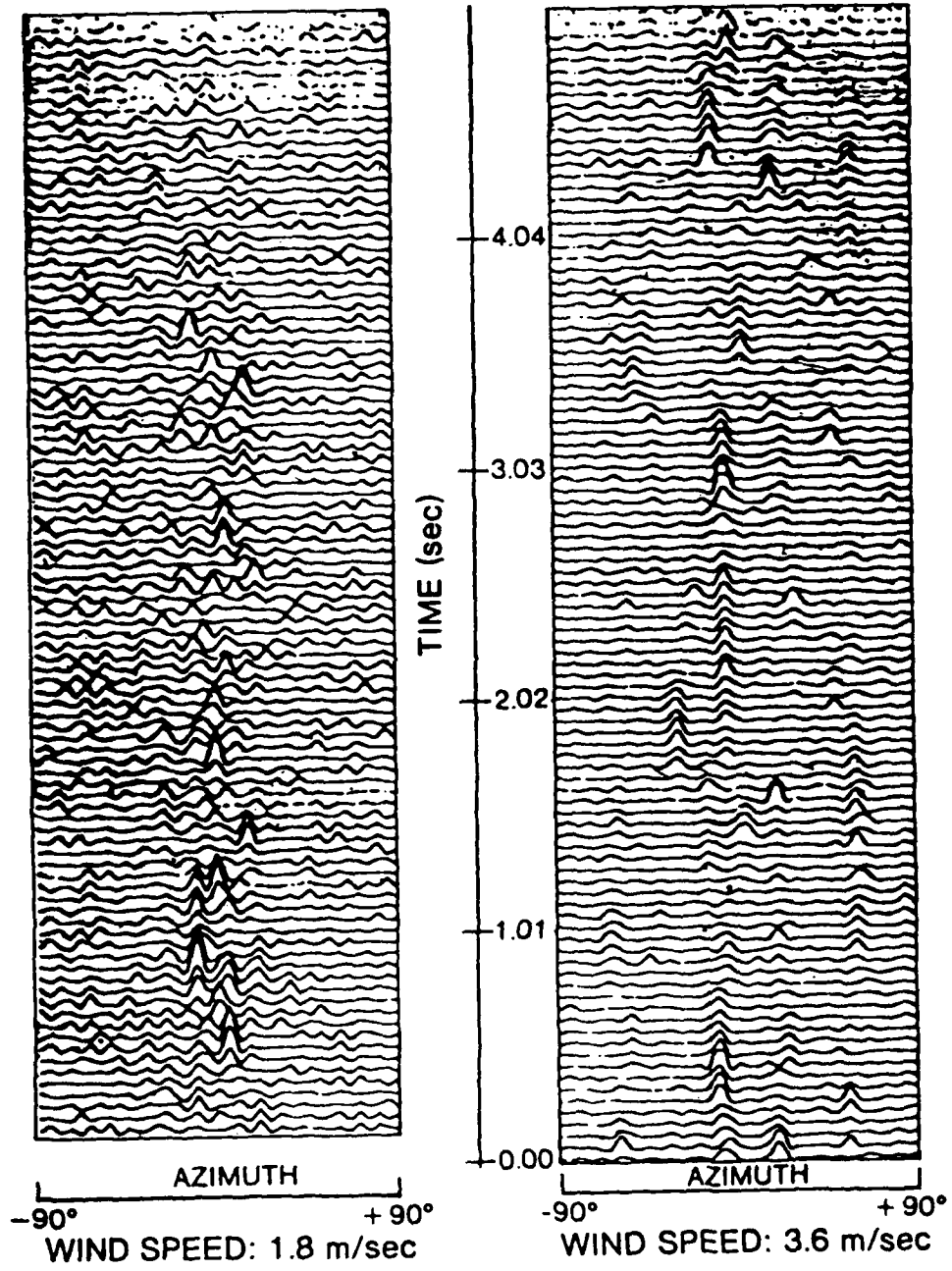
SSNI SUBMERGED PACKAGE



Chapter 2, Figure 2: Drawing of the SSNI submerged package.



Chapter 2, Figure 3: Drawing of the SSNI wind-sensing buoy.



Chapter 2, Figure 4: Shang and Anderson waterfall plot showing distinct surface noise sources at low wind speed (see text).

On the left half of Figure 4 is a plot for data recorded when the wind speed, measured one kilometer from the array, was 1.8 meters/sec. The noise events appear to be confined to episodes within 50 to 150 milliseconds (50 milliseconds was the temporal resolution of the recorded data). Although the gain in these plots, which was automatically adjusted based on average noise levels, was not recorded, it seems that the noise events have intensities at least three times higher than the surrounding noise bumps, which represent background noise. Shang and Anderson concluded that this might be evidence of a unique noise mechanism audible only at low wind speeds, and that close range acoustic measurements would be required to determine the characteristics of the source.

With this goal in mind, we began construction of the SSNI in 1983.

II. SSNI DESCRIPTION

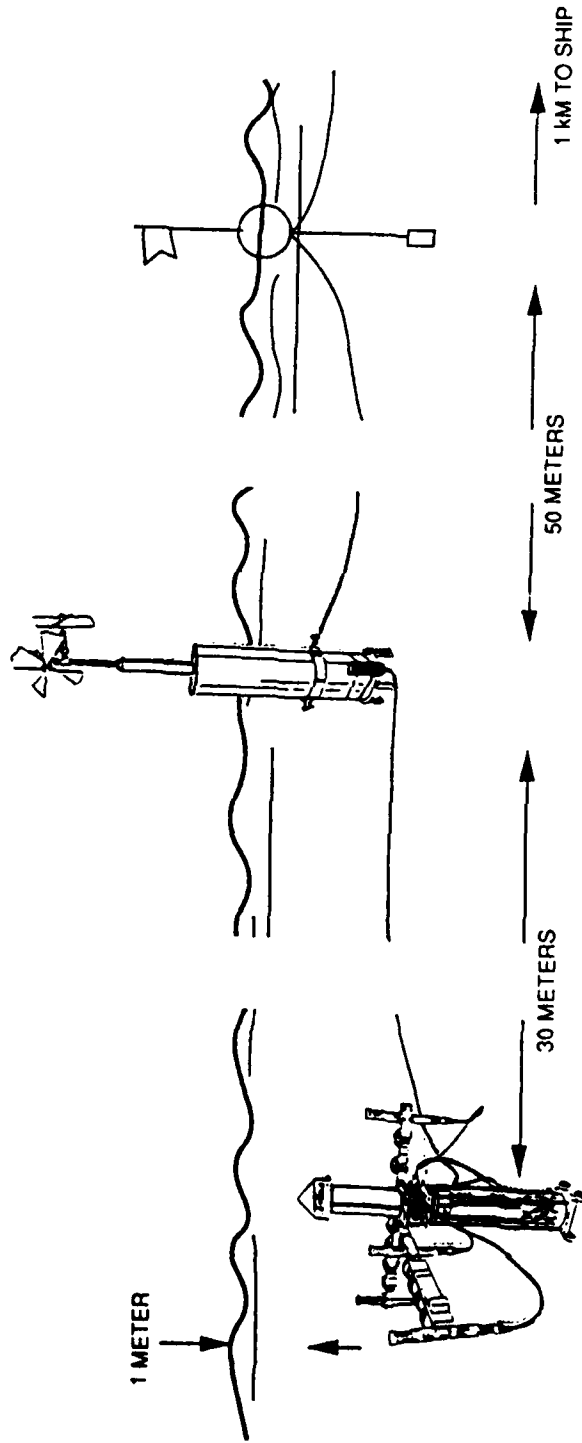
Figure 5 shows how the submerged instrument and surface buoy are deployed, while figures 2 and 3 show the various parts of these packages, which are described below. Figure 6 shows a block diagram of the SSNI and the equipment on shipboard.

A. SSNI Video

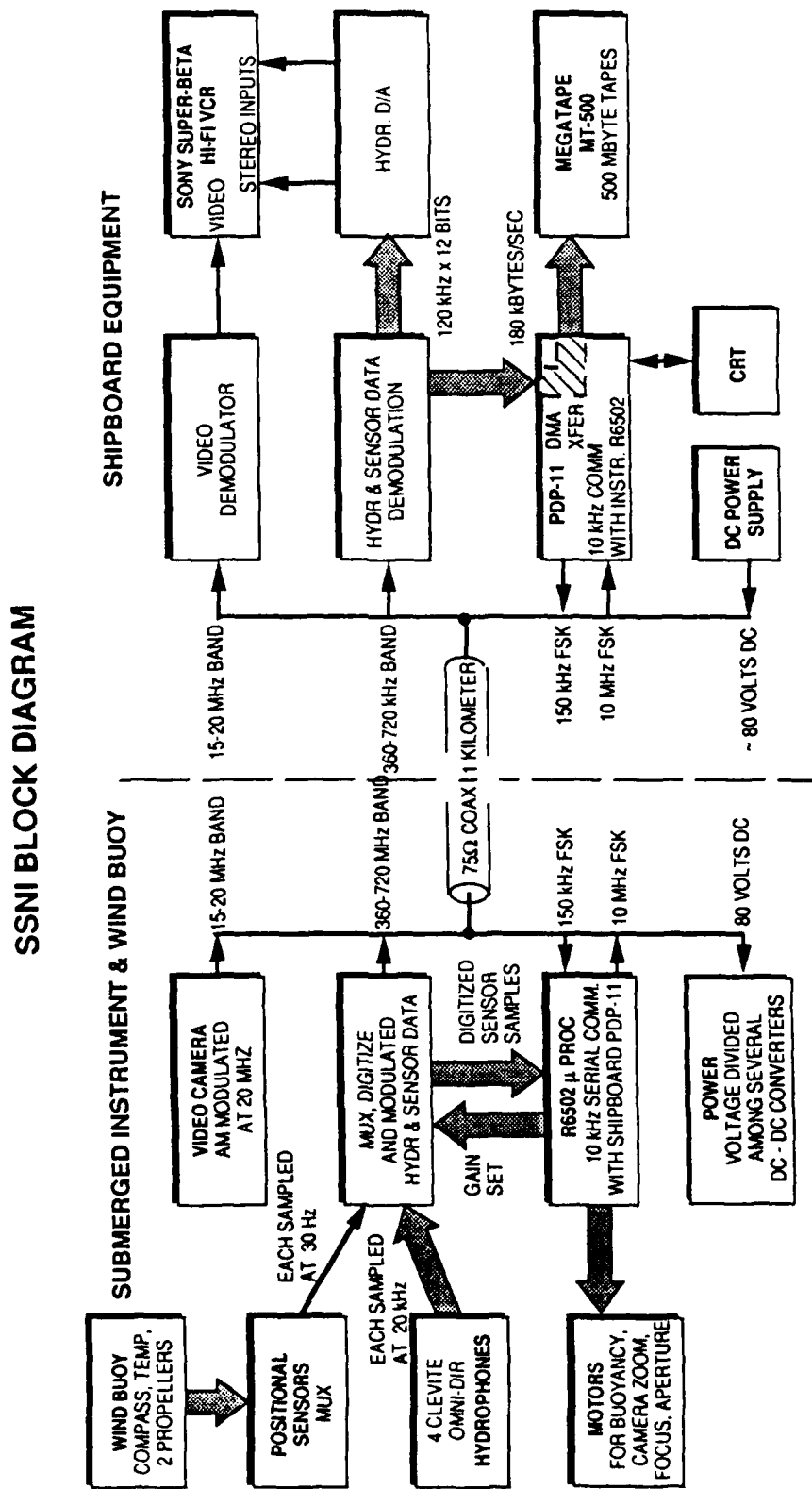
An RCA TC2011U Black & White Ultricon Closed Circuit Video Camera is used within the submerged instrument to record surface conditions. The camera's outer case and power supply module have been removed to mount the camera within the aluminum upper tube of the instrument. 24 Volts DC is supplied in place of the camera's power module. Three small 6 volt DC motors, controlled by the instrument's microprocessor, allow remote control of the camera's zoom, focus, and aperture lenses. The camera looks thru a clear, flat, half-inch thick lucite plate mounted to the top of the instrument. After a few initial deployments, a dark green optical filter was fitted beneath the lucite window to dim the brightness experienced by the camera looking skyward from just beneath the surface.

The video signal is blended electronically with the output of a National Semiconductor MM5840 TV Channel and Time Display chip. By writing sequential frame count numbers into the time field of the chip, the microprocessor can uniquely label each 1/30 second video frame. This allows an easy correlation later between individual frames stored on video tape and blocks of digitized hydrophone/sensor data stored on magnetic tape. The chip's Channel Number field is set remotely thru the microprocessor to identify successive deployment runs. Figure 7 shows a sequence of video frames during a small break.

The video signal is transmitted over the kilometer-long coaxial tether by amplitude-modulating a 20 MHz carrier. At shipboard, the video signal is demodulated and stored on a Sony Super Beta Hi-Fi Stereo VCR. The 20 MHz modulation frequency was selected as a compromise between the signal attenuation which would have resulted over the coaxial tether at a higher frequency, and the picture degradation which would have occurred at lower frequencies. The stereo tracks on the VCR are used to record any two of the four hydrophones, which allows real time audio-visual playback. This has proved to be invaluable for screening out sources of acoustic contamination such as dolphins, birds, and distant ships.



Chapter 2, Figure 5: Drawing of the SSNI's deployment configuration.



Chapter 2, Figure 6: SSNI and shipboard equipment block diagram.

Chapter 2, Figures 7a to 7i: Sequence of video frames from 24377 to 24389 showing a small water break during deployment on July 1, 1988. The upper left corner of each screen identifies the sequential count.



Chapter 2, Figure 7a



Chapter 2, Figure 7b



Chapter 2, Figure 7c



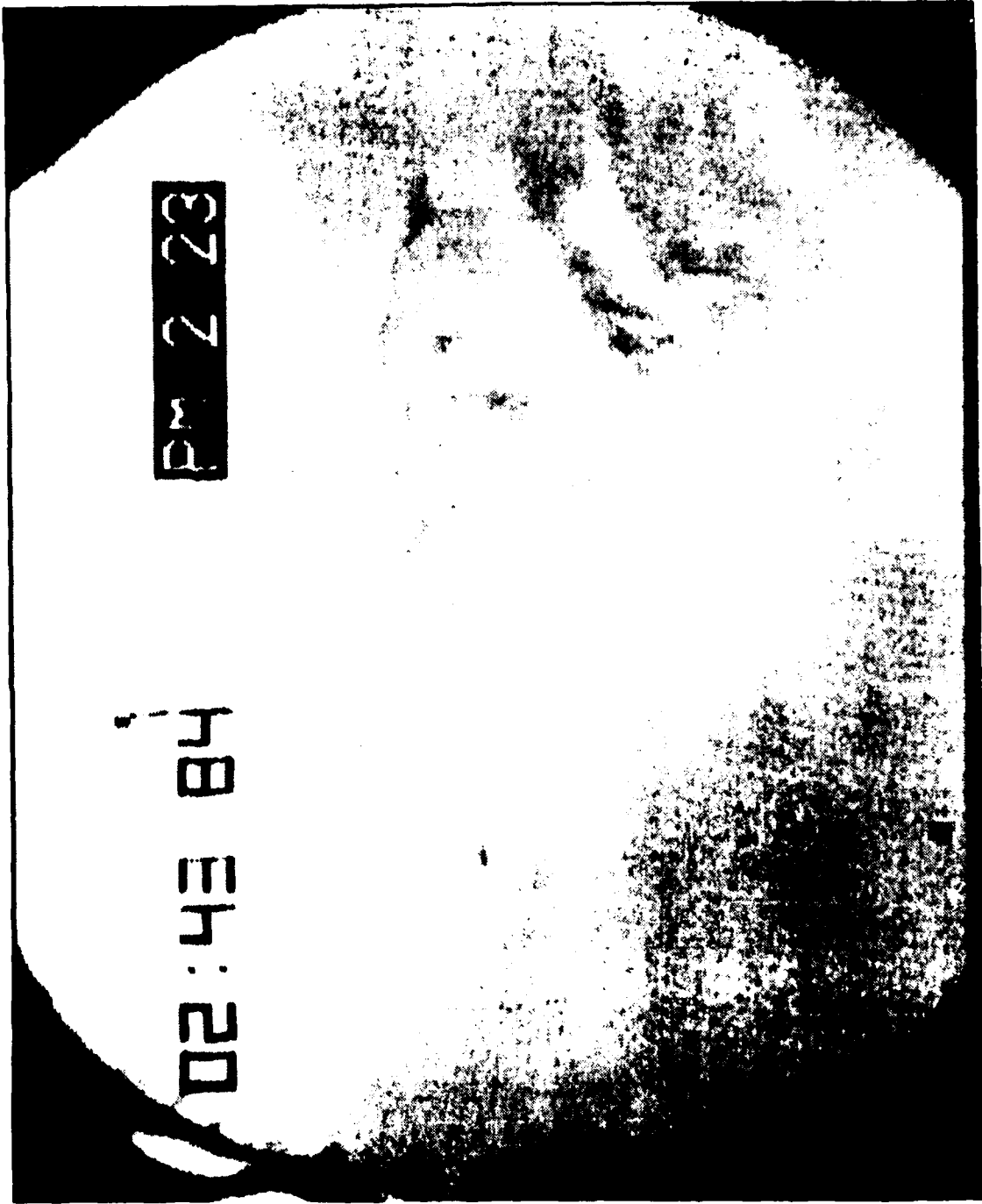
Chapter 2, Figure 7d



Chapter 2, Figure 7e



Chapter 2, Figure 7f



Chapter 2, Figure 7g



Chapter 2, Figure 7h



Chapter 2, Figure 7i



Chapter 2, Figure 7j



Chapter 2, Figure 7k



Chapter 2, Figure 71

B. SSNI Hydrophones

The submerged instrument uses four omni-directional Clevite Hydrophones, each with a sensitivity of -160 dB re 1 volt/ μ Pa and spectrally flat to 50 kHz. Figure 8 specifies the hydrophone locations, looking down on the instrument. The distance to a noise source is iteratively calculated from recorded data based on how the arrival times for a single noise event differ at each of the four hydrophones. An example of this variance is shown in Figure 9, a close up of a typical noise source recorded by the four hydrophone.

Figure 10 shows a block diagram of the instrument's signal and digital data flow. In early deployments, each audio signal was passed thru the attenuating skirt of a simple RC high pass filter ($f_c = 10$ kHz). The 6 dB per octave skirt acted as a pre-whitening filter against the expected -5 dB per octave spectrum shown in the Knudsen Curves. The idea was to prevent the high-energy low frequencies from swamping the low-energy high frequencies over the limited dynamic range of the digitized data. In the most recent deployments this filter has been removed. Our data shows that peak noise amplitude for a single source does not vary extensively over the audible frequencies. Rather, it is the energy due to the longer duration of each low frequency source which contributes to the observed -5 dB per octave curves of the literature.

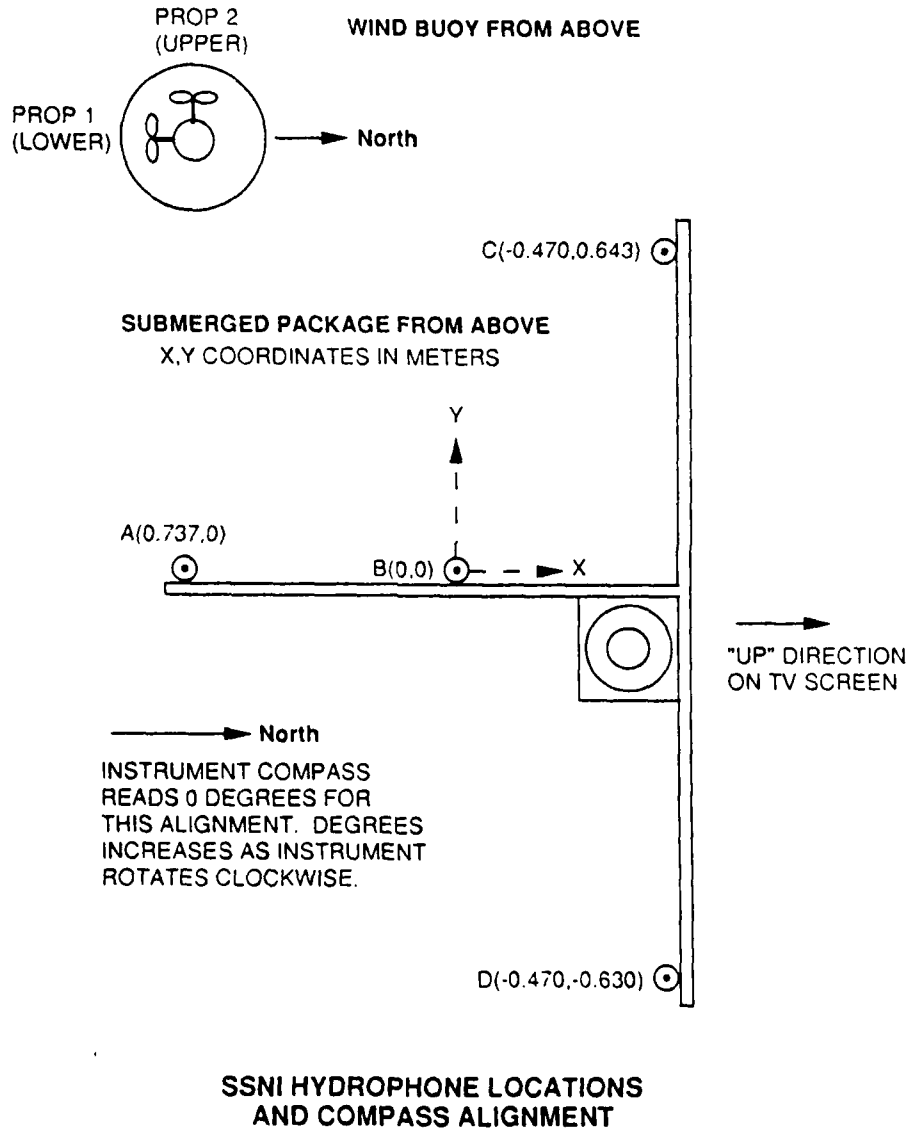
The signal from each hydrophone is passed thru RC filters to cut off frequencies below 100 Hertz, while an anti-aliasing, low-pass, 5-pole active filter suppresses frequencies above 10 kHz. Figure 11 shows the frequency response curves for the hydrophone filter both with and without the pre-whitening filter.

An 8-bit multiplying D/A, settable by the microprocessor, allows a shipboard operator to vary the gain by factors of 1/256 to 255/256.

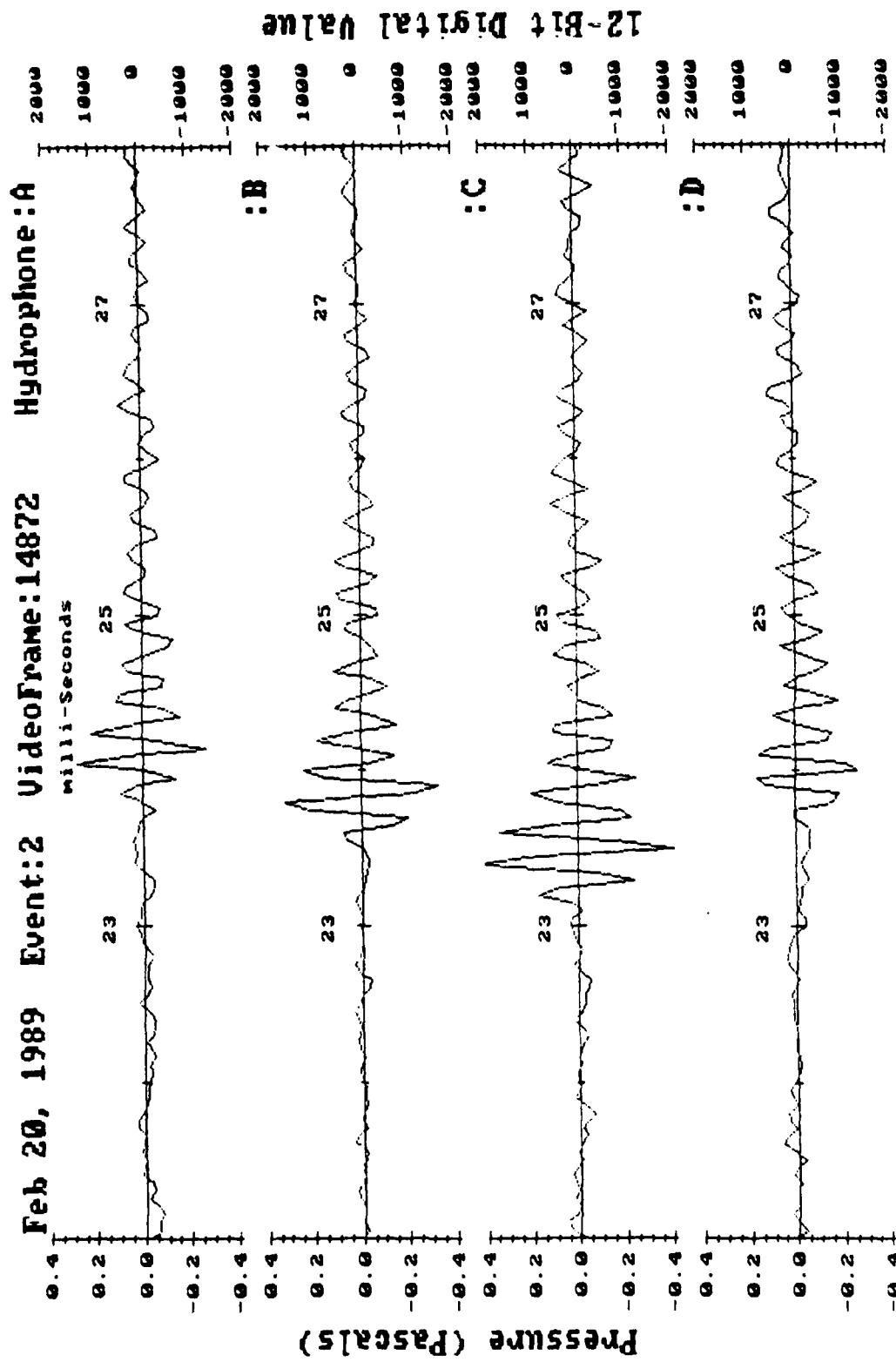
As shown in Figure 10, the hydrophones constitute four of six channels fed to a single 12-bit A/D chip through an analog multiplexer. The hydrophones are sampled-and-held simultaneously while the A/D converts the two extra channels, which are in turn sampled-and-held while the A/D digitizes the four hydrophones. Each channel is individually sampled at 20 kHz.

The designed gain at 7,500 Hertz (the peak gain point after all of the filtering) was calculated from the data of Shang & Anderson shown in Figure 4, which shows noise events approximately 3 times higher than the background noise levels. Anderson's instrument, ADA, had a directivity index which amplified the noise events by about 25 dB. Although this gain is lost for the non-directional Clevite hydrophones of the SSNI, it is more than compensated by the instrument's close proximity to the individual noise sources. The difference in intensity between distances of 100 meters (ADA) and 1 meter (SSNI) represents a gain of about 40 dB. Therefore the SSNI was designed with the expectation that individual noise events would be approximately 15 dB above the background noise level across 10,000 Hertz. This led to a designed voltage gain of 65 dB at 7500 Hertz. By implementing this gain with the multiplying A/D set at 16/255, the geometric middle of its range, a shipboard operator is free to adjust the gain by a factor of 16 in either direction to compensate for changing conditions.

The serial data stream produced by the 12-bit A/D chip consists of successive digitized samples from each of the four hydrophones and two extra channels. The 20 kHz sample rate for each channel leads to a serial bit rate of 1.44 mega-bits per second. This is transmitted over the one-kilometer coaxial tether

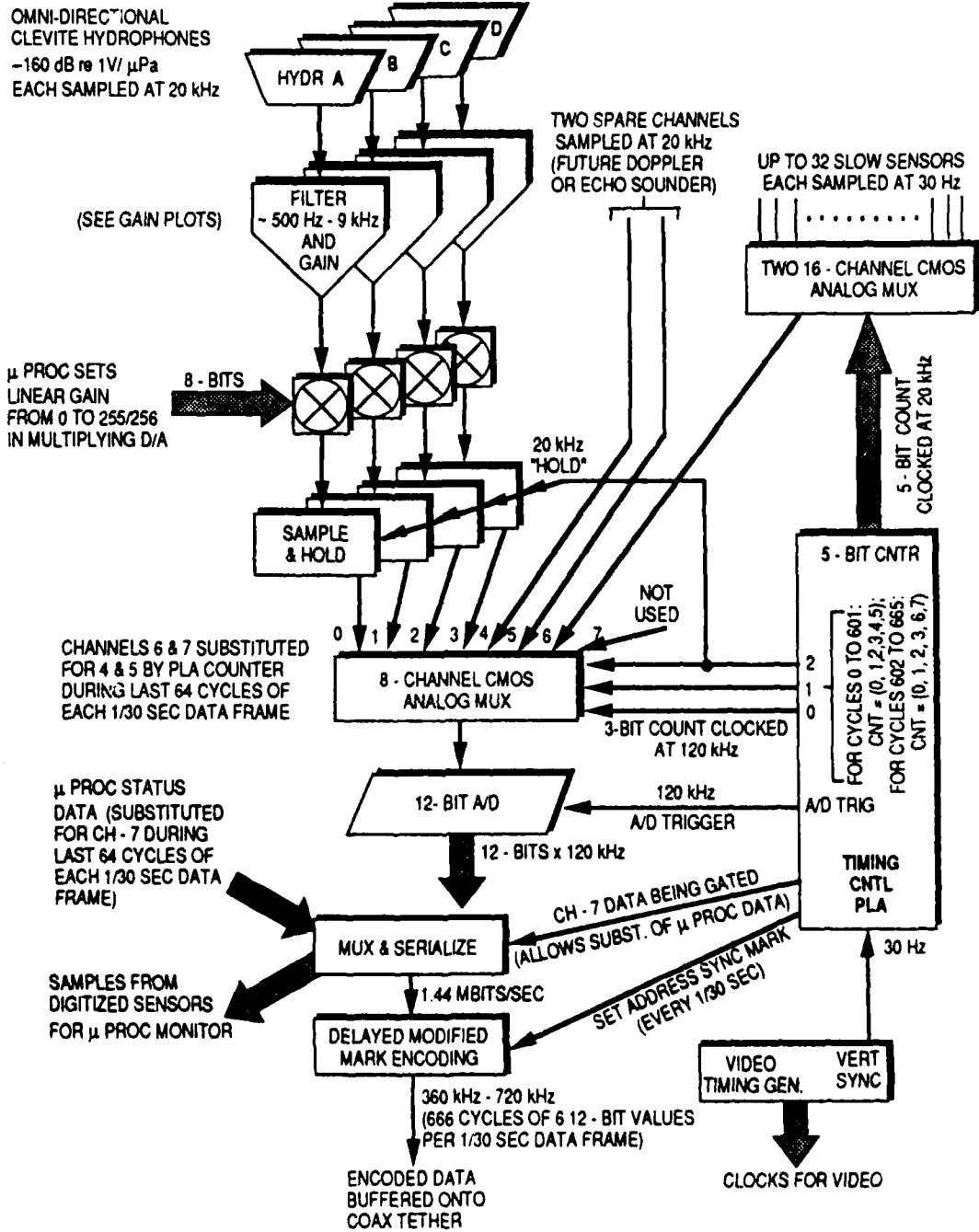


Chapter 2, Figure 8: SSNI hydrophone locations as viewed from above.



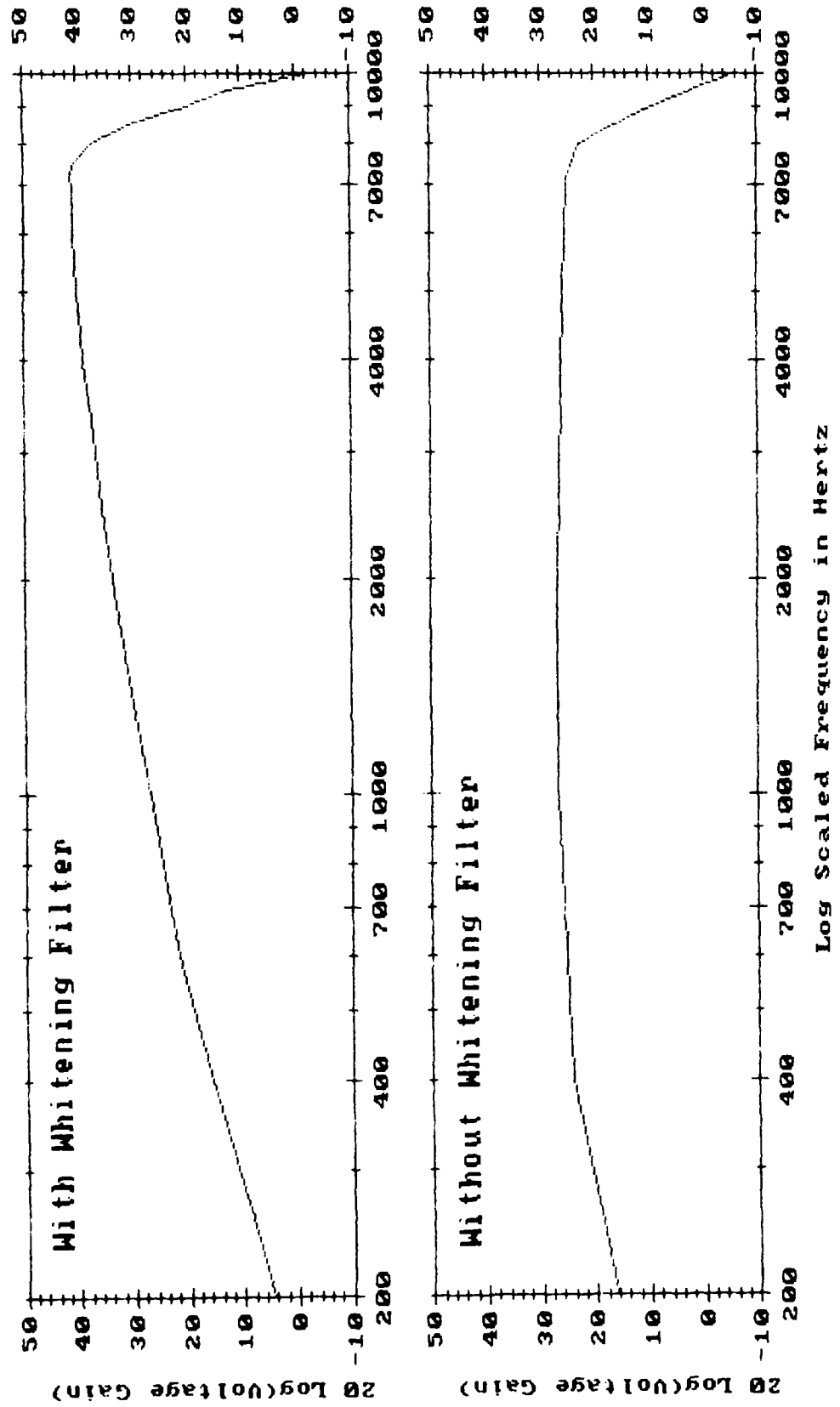
Chapter 2, Figure 9: Close-up of acoustic traces for four hydrophones. The arrival time differences of the oscillating source at the hydrophones is used to calculate the noise source location.

HYDROPHONE AND SENSOR DATA FLOW WITHIN SUBMERGED INSTRUMENT



Chapter 2, Figure 10: Signal and data flow for the SSNI submerged instrument.

SSNI Voltage Gain Between Hydrophone And D/A



Chapter 2, Figure 11: SSNI audio frequency response curves, with and without the pre-whitening filter.

thru the use of Delayed Modulation Mark (Miller) encoding, which converts the signal to a frequency band ranging from approximately 360 kHz to 720 kHz. (In practice, filtering out a lower frequency 150 kHz FSK signal from the microprocessor disrupted the phase encoding sufficiently at the receiving end that the microprocessor signal was remodulated to 10 MHz). The digitized data is sent continuously, but is resynchronized every 1/30 second to match the video frames. Each "frame" of digitized data is identified by the unique frame count number placed on each video frame by the microprocessor. The frame number is also placed near the end of one of the two additional digitized channels.

At shipboard, the digital frames are recovered and stored on MegaTape MT-500 tape cartridges. Approximately 30 minutes of data can be stored on a single 500 megabyte cartridge. Two selectable hydrophone signals are also reconverted to analog for simultaneous recording on the videotape stereo channels.

C. Slow Sensors

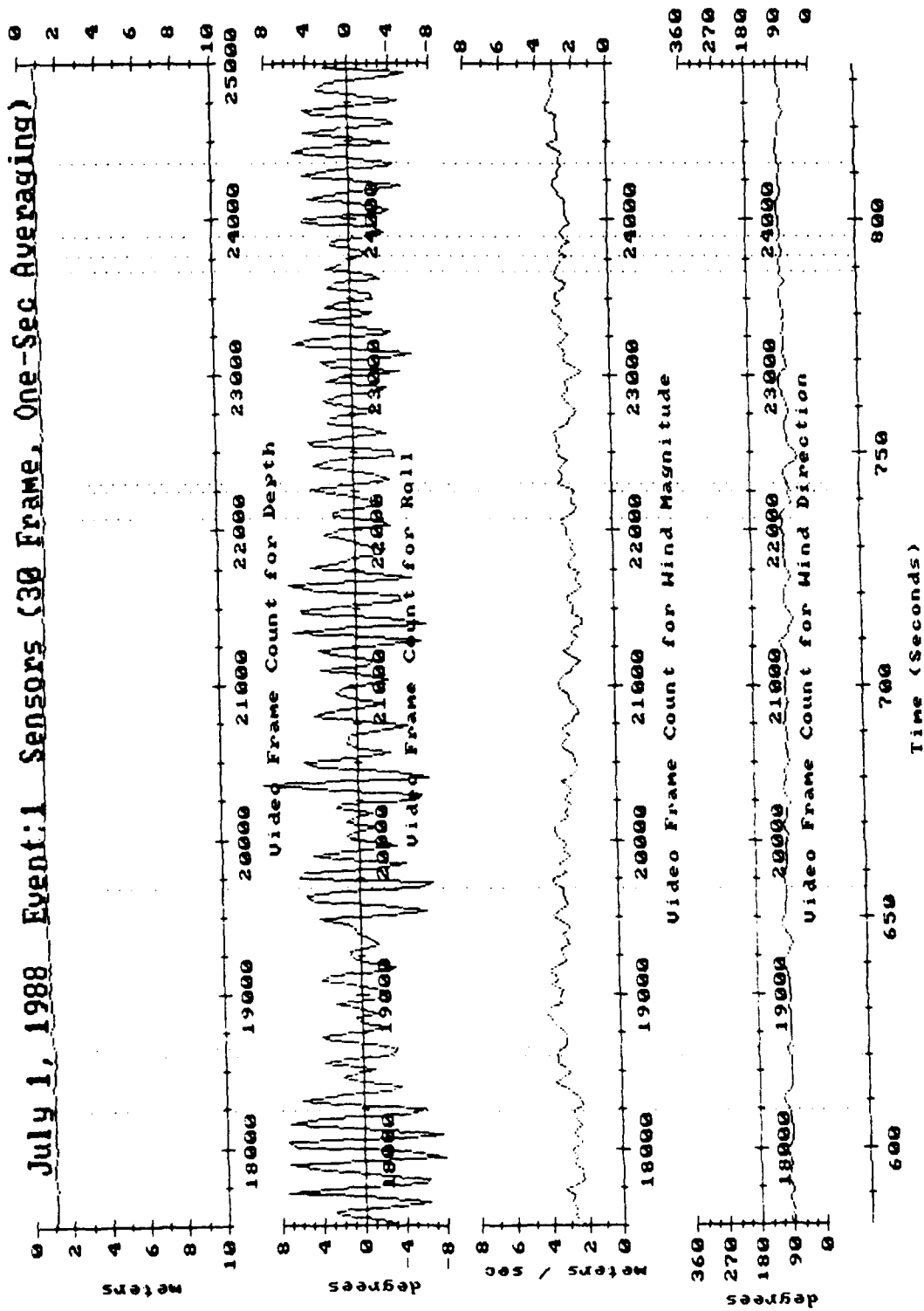
As mentioned in the previous section, there are two spare channels being sampled at 20 kHz in addition to the four hydrophone channels (numbered 0 to 3). One of these spares, Channel 4, is used to store values from a variety of slowly varying analog sensors. As described above, the digitized data stream is organized into blocks of data corresponding to the 1/30-second video frames. By swiftly switching each of the various sensors thru analog multiplexors, Channel 4 can easily contain one sample from each sensor near the end of each "frame" of data. By placing this data at the end of the frame, Channel 4 (and Channel 5) is kept mostly free for adding a new signal in the future.

Among the slow sensors are a set which specify the orientation of the submerged instrument. Vertical tilt of the instrument due to swell is measured by pitch and roll sensors (in practice, only the roll sensor has been useful in tracking swells because the instrument's pitch is affected by the pull of the tether). Vertical acceleration is measured by an accelerometer, although this sensor has not proved sensitive enough to track swell motion. A compass sensor not only gives direction to the pitch and roll sensors, but also indicates the direction of pull by the prevailing current on the passively drifting instrument. A depth reading is provided by a pressure transducer, while instrument overheating is checked by two temperature sensors at the top and bottom of the case.

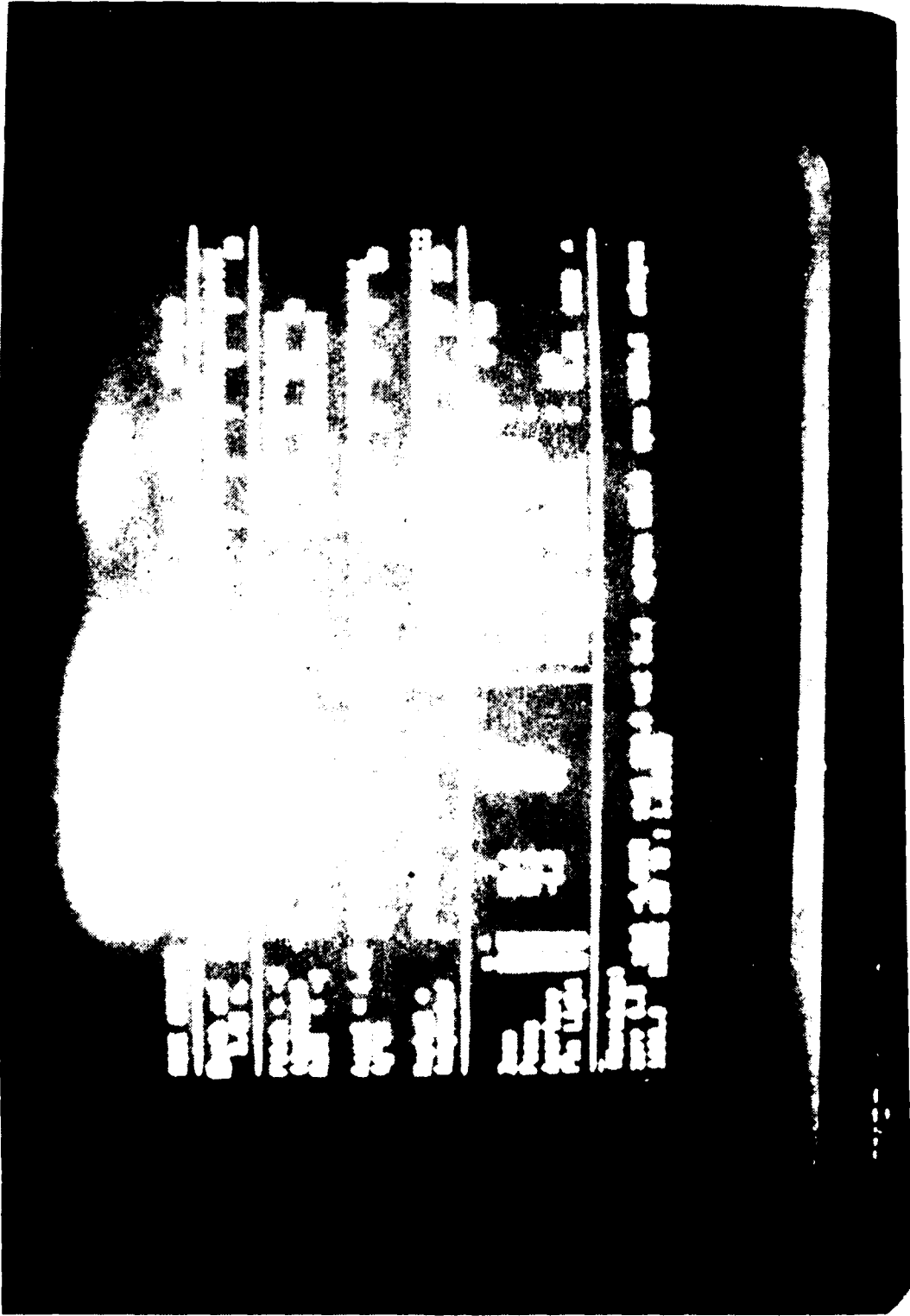
The surface buoy, tethered 30 meters from the submerged instrument, also supplies slow sensor signals. A compass and two calibrated perpendicular propellers specify horizontal wind speed and direction. Another sensor specifies the air temperature at the surface buoy.

In addition to the analog sensors, the microprocessor intercepts the digitized stream from Channel 5 near the end of each frame and inserts about 40 values. These include the frame count (incremented every 1/30 second to correspond with the number inserted into each video frame picture), the starting date and time for each deployment, the multiplying A/D gain for the hydrophones (set by the remote user), and the deployment number (written onto the video screen in the "Channel" field via the Time/Channel chip).

Figure 12 shows some typical sensor results, averaged into 1 second time periods, for 5 minutes of data. The dashed vertical lines represent wavelet breaks determined from careful listening of the matching videotape record. Figure 13 shows the computer monitor used to display real-time sensor information for the shipboard operator.



Chapter 2, Figure 12: Four minutes of instrument depth, roll, and wind speed, with sampled values averaged over 1 second intervals.



Chapter 2, Figure 13: Shipboard computer monitor display.

D. Buoyancy Control

The submerged instrument's depth is adjustable by using a stepper motor and worm gear to extrude or retract a brass piston at the base of the instrument. Although the original plan was to adjust the piston continuously based on a target depth transmitted to the instrument's microprocessor, in practice the stepper motor clicking is loud enough that the instrument depth is adjusted only while changing digital recording cartridges. The piston, sealed to the instrument with a rubber boot, has a length of 5 cm and a diameter of 12 cm. This has not proven to be a large enough displacement to do more than modify the depth of the instrument, particularly when it has been deployed from an anchored barge. Under strong currents, the submerged instrument has acted like an underwater kite, with its depth determined largely by current speed.

III. INITIAL RESULTS

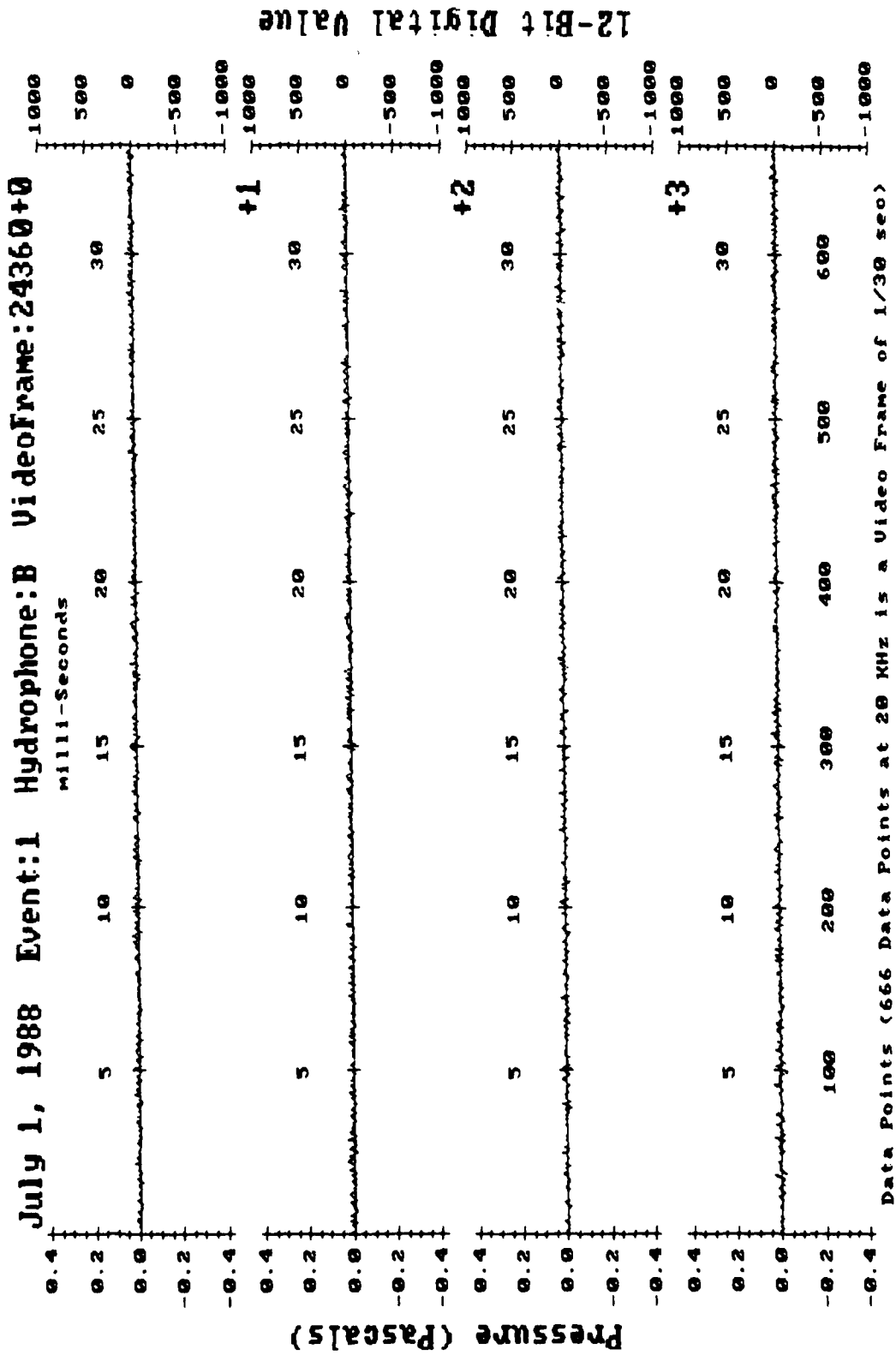
The purpose of this instrument is to identify noise producing mechanisms. In reviewing videotapes produced by the instrument, small wavelet spills are the most obvious source of surface noise at low wind speeds. However, while the centimeter resolution of the SSNI's video can easily discern small waves and spills, it is insufficient to observe, say, the millimeter sized bubbles capable of generating noise in the kilohertz frequency range.

Fortunately, different sonic signatures are expected for most of the noise mechanisms proposed in the literature. Strasberg [1956] showed that air bubbles which have split or detached from an air tube will result in abrupt pressure oscillations which decay exponentially within milliseconds. Bubbles somehow activated by turbulence alone, such as suggested by Wenz [1962] but later discounted by Crighton and Williams [1969], would neither start as abruptly nor decay in the same way as Strasberg's bubbles. The growth and collapse of a cavitation bubble, which was suggested by Furduiev [1966] but later discounted by Prosperetti [1988] for the open ocean, is known to result in an acoustic impulse when produced mechanically (Kerman [1984] provides a good overview of some of these mechanisms). Water drop impact, such as that due to spray or rain, has been studied most recently by Pumphrey, Crum, and Bjorno [1988]. Their laboratory work has shown that non-air entraining drops produce only an impact sound pulse, while drops within a specific size and speed range also entrain a bubble with much higher pressure oscillations. Their recent work has also indicated, corroborated by the laboratory work of Banner and Cato [1988], that the sound produced by small bubbles bursting at the surface is negligible.

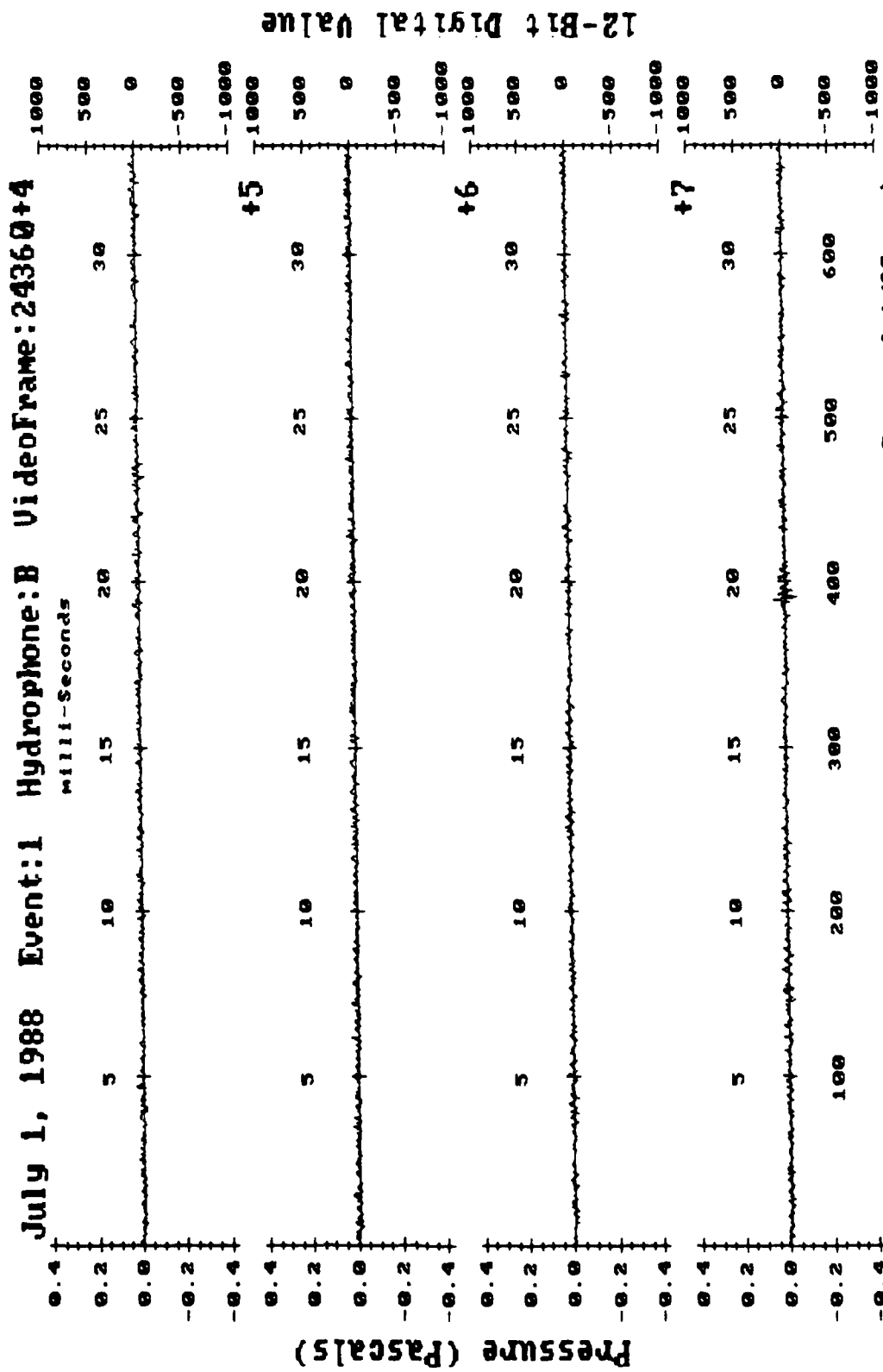
Figure 14, which is typical of the data recorded by the SSNI, contains continuous plots of the audio signal received by Hydrophone B during the small spill pictured in Figure 7. Figure 15 shows a close-up of the oscillation from Frame 24371 in Figure 14c. This data was taken during an early deployment using the pre-whitening filter, so the low frequencies are somewhat attenuated. With few exceptions, the plots show the distinct decaying sinusoids associated with Strasberg's ringing bubbles. Although the agitation in the video pictures of Figure 7 suggest possible capillary interaction, the audio record shows no noise produced as a result. The plots of Figure 14 show that most of the generated noise has taken place before the spill has even entered the camera's view. Although this might lead one to speculate about noise production during the lifetime of a spill, the capture of entire surface breaks by the SSNI's video has been so rare that we have not been able to make any generalizations.

Given that the oscillations pictured in Figure 14 are bubbles, the obvious question is then: What causes them to ring? The video record can provide few direct clues, since the millimeter bubble sizes associated with these frequencies are invisible to the SSNI. However, the small size of the spill would

Chapter 2, Figures 14a-14g: Acoustic traces for Hydrophone B (with pre-whitening filter) matching video frames in Figure 7. Each page contains four consecutive video frames of 1/30 second each.

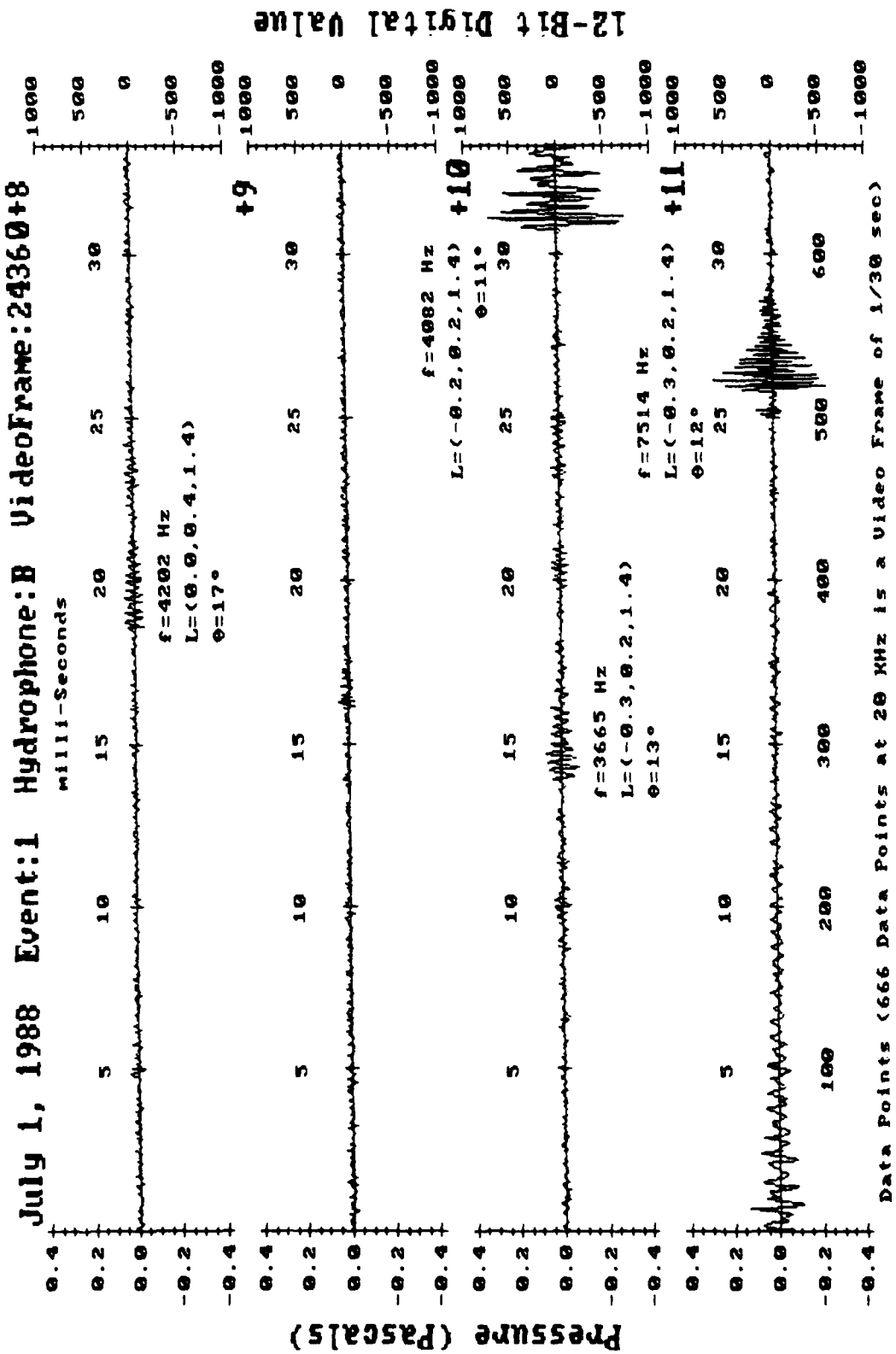


Chapter 2, Figure 14a: Video Frames 24360 to 24363.

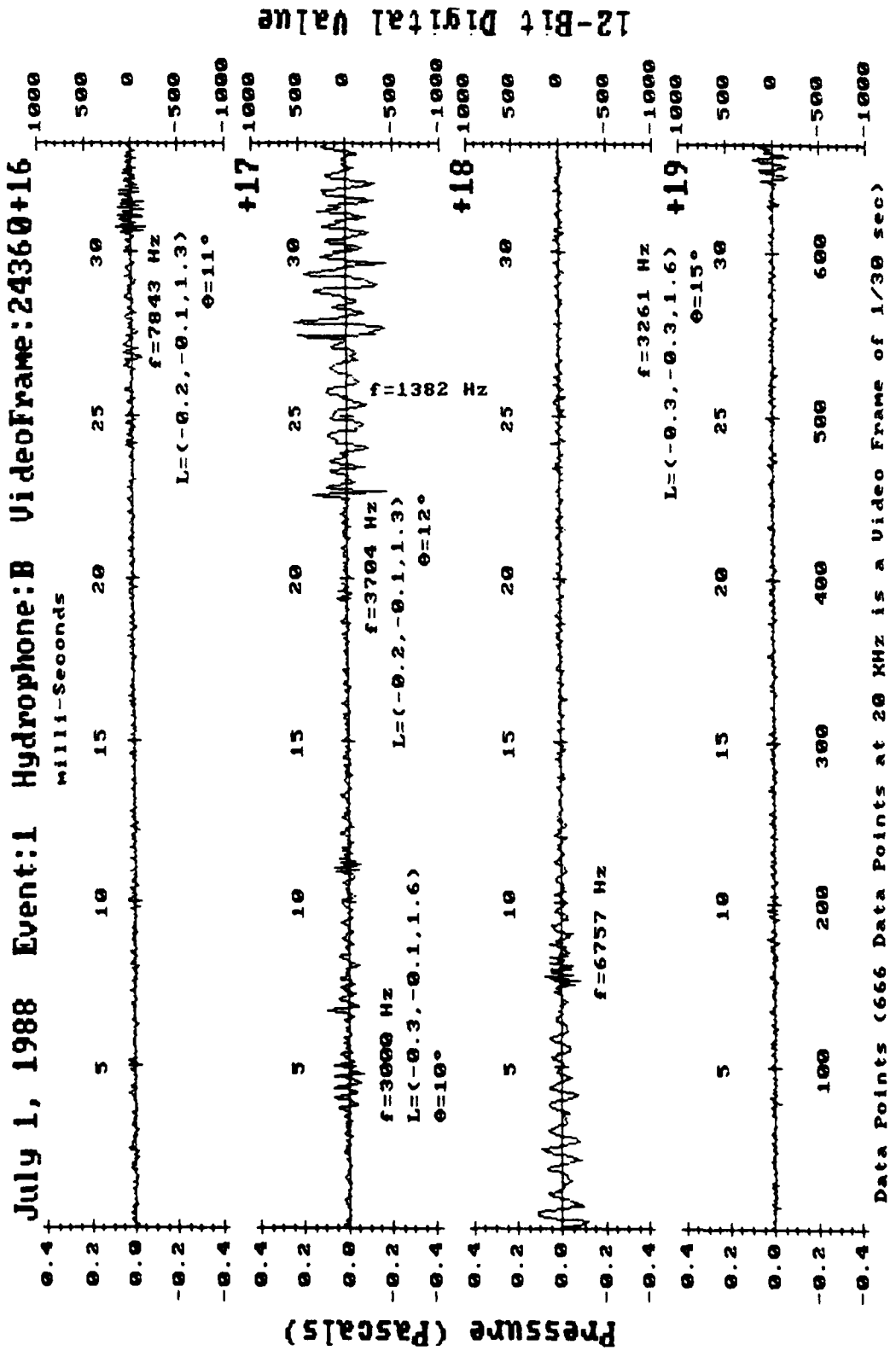


Data Points (666 Data Points at 20 KHz is a Video Frame of 1/30 sec)

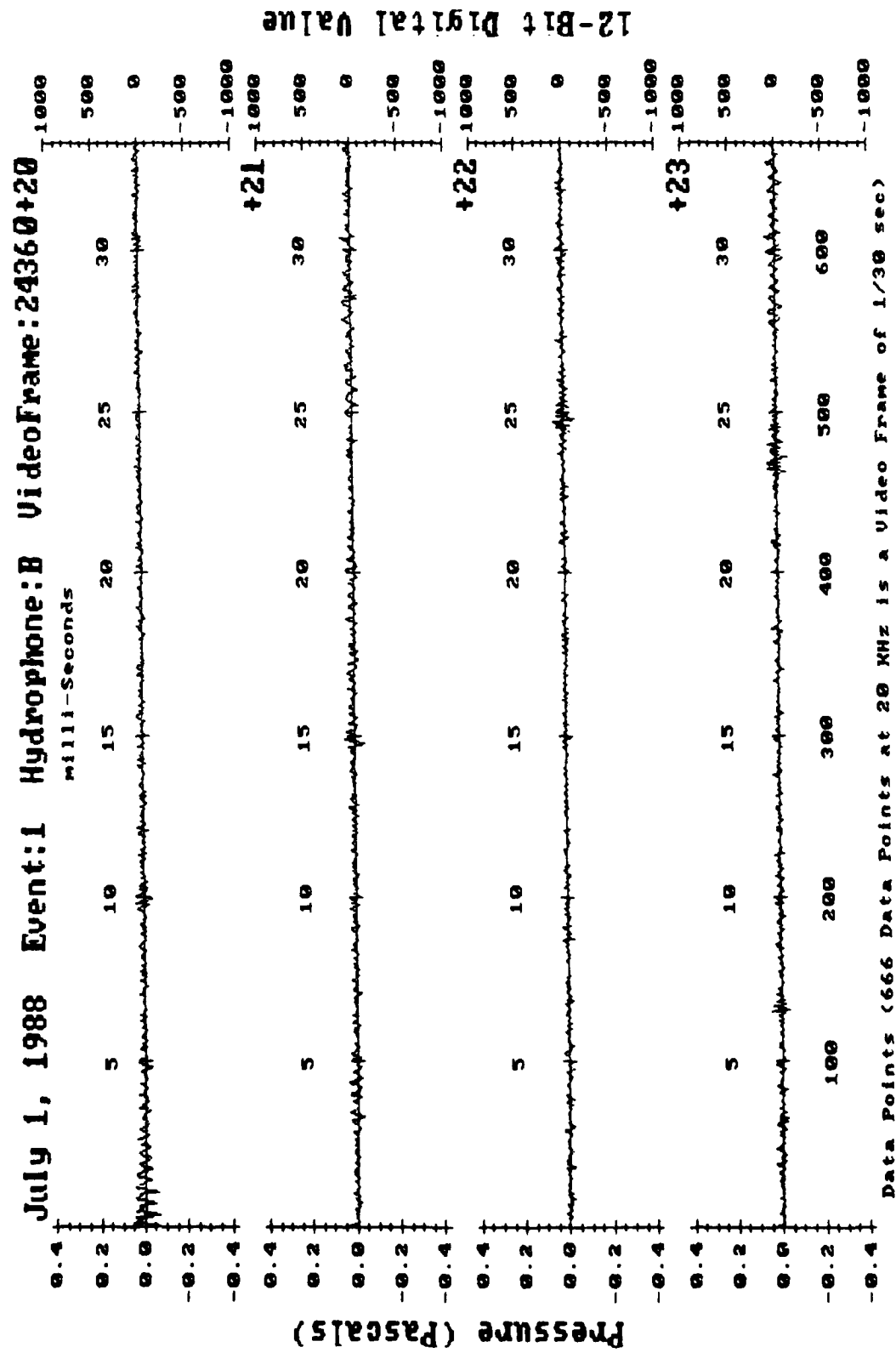
Chapter 2, Figure 14b: Video Frames 24364 to 24367.



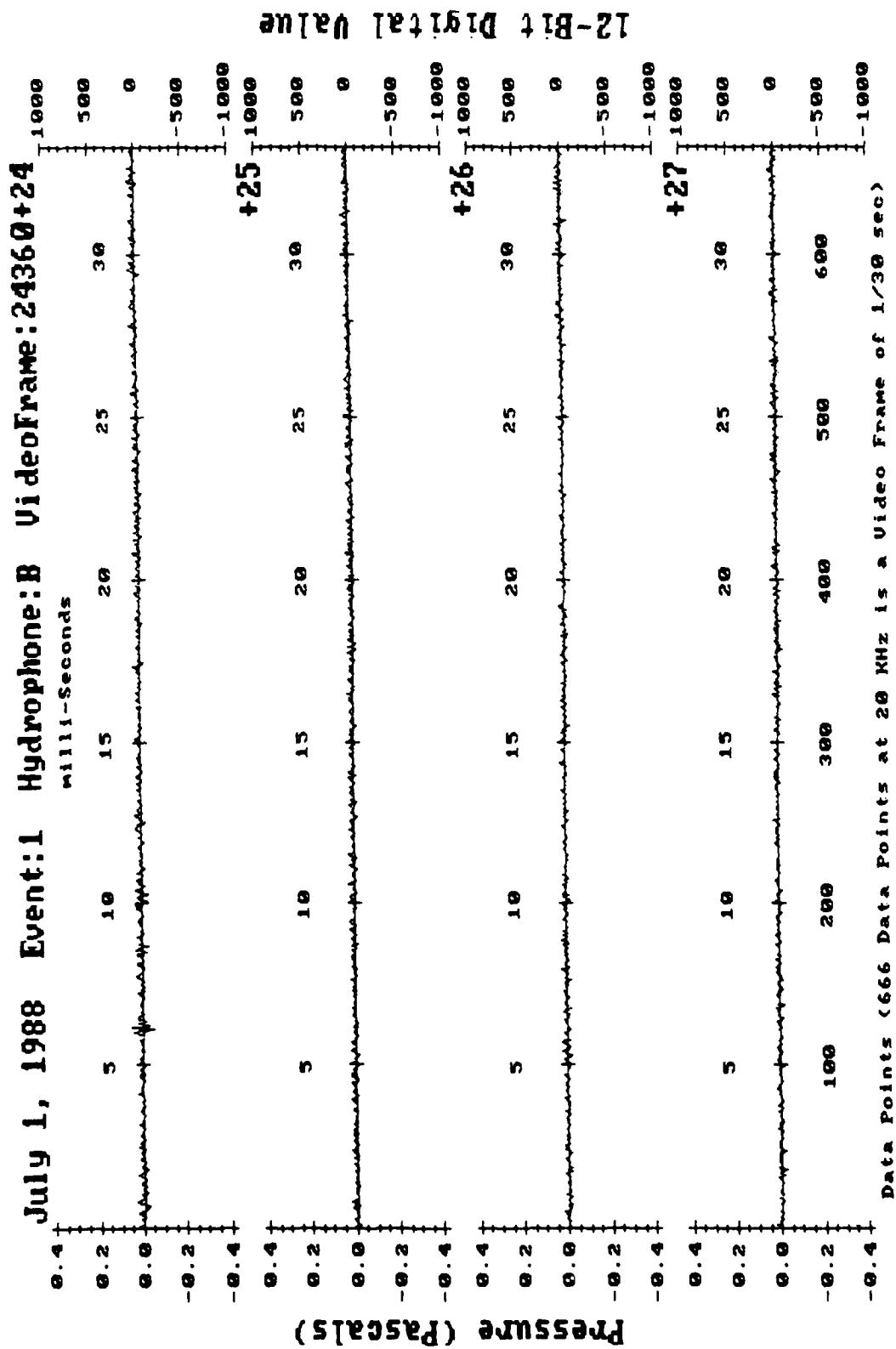
Chapter 2, Figure 14c: Video Frames 24368 to 24371.



Chapter 2, Figure 14e: Video Frames 24376 to 24379.

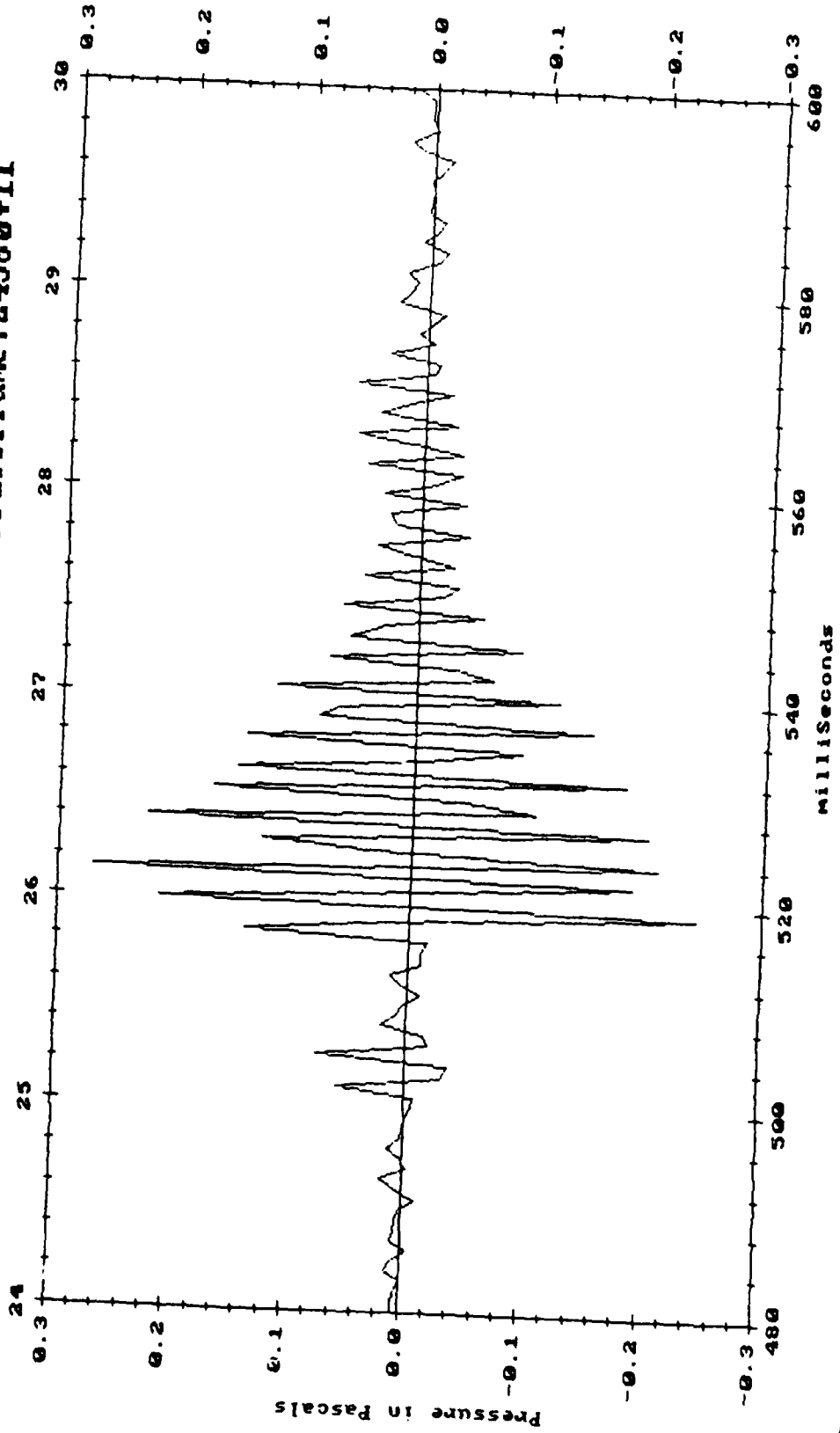


Chapter 2, Figure 14f: Video Frames 24380 to 24383.



Chapter 2, Figure 14g: Video Frames 24384 to 24387.

July 1, 1988 Event:1 Hydrophone:B VideoFrame:24360+11



Chapter 2, Figure 15: Close-up of oscillation in Frame 24371 from Chapter 2, Figure 14c.

seem to rule out the possibility of bubbles experiencing sudden pressure changes due to abrupt depth changes. Also, bubbles do not appear to be recycled: once a bubble has decayed over a few milliseconds, its identifying frequency is absent from the later audio records. Thus, a given bubble apparently oscillates and decays only once, presumably during formation. This is consistent with the observations of Banner and Cato [1988], who recorded the entrainment of bubbles in a laboratory water flume with a high speed camera. Their slow-motion movie shows bubbles ringing as they initially form or split, but making little noise while bursting or being distorted by turbulence.

The acoustic data recorded by the SSNI is strikingly similar to the recent results of Medwin and Beaky [1989], who recorded the sounds produced by artificially generated windless wave breaks in the laboratory. They also have recorded distinct bubble oscillations with rather high peak pressure amplitudes, which typically decay within a few milliseconds.

CONCLUSION

The data records generated by the SSNI indicate that the surface noise generated under light winds is due to distinct bubble oscillations occurring as bubbles are entrained in small spills. The bubbles, which generally oscillate and decay in a manner similar to those described by Strasberg [1956], are rung once and then disappear from the acoustic record. The oscillation lifetimes of a few milliseconds are well within the 50-millisecond resolution of the Shang and Anderson data of figure 4, making it likely that the bumps in their data were caused by the brief ringing of individual bubbles.

In another paper we will present a more detailed characterization of the surface noise and conditions recorded by the SSNI. The acoustic records from a number of surface breaks are presented in the appendices of Updegraff [1989].

This project was supported under Office of Naval Research Contract Number N00014-87-K-0010.

LIST OF REFERENCES IN CHAPTER 2

- Banner, M. L. and D. H. Cato, 1988. "Physical Mechanisms of Noise Generation by Breaking Waves -- A Laboratory Study", from *Sea Surface Sound*, 429-436, Kluwer Academic Publishers, edited by B. R. Kerman.
- Crighton, D. G. and J. E. Ffowcs Williams, 1969. "Sound Generation by Turbulent Two-Phase Flow", *J. Fluid Mech.* **36**(3), 585-603.
- Furduiev, A.V., 1966. "Undersurface Cavitation as a Source of Noise in the Ocean", *Atmos. Oceanic Phys.* **2**(5), 314-320.
- Hollett, R. and R. Heitmeyer, 1988. "Noise Generation by Bubbles Formed in Breaking Waves", from *Sea Surface Sound*, Kluwer Academic Publishers, edited by B. R. Kerman.
- Kerman, B. R., 1984. "Underwater Sound Generation by Breaking Wind Waves", *J. Acoust. Soc. Amer.* **75**(1), 149-165.
- Knudsen, V. O., R. S. Alford, and J. W. Emling, 1948. "Underwater Ambient Noise", *J. Mar. Res.* **7**, 410-429.
- Kuo, E.Y.T., 1968. "Deep Sea Noise Due to Surface Motion", *J. Acoust. Soc. Amer.* **43**(5), 1017-1024.
- Longuet-Higgins, M. S., 1989. "Monopole Emission of Sound by Asymmetric Bubble Oscillations", *J. Fluid Mech.* **201**, 525-565.
- Marsh, H. W., 1963. "Origin of the Knudsen Spectra", *J. Acoust. Soc. Amer.* **35**, 410.
- Medwin, H. and M. M. Beaky, 1989. "Bubble Sources of the Knudsen Sea Noise Spectra", *J. Acoust. Soc. Amer.* **86**(3), 1124-1130.
- Prosperetti, A., 1988. "Bubble Dynamics in Oceanic Ambient Noise", from *Sea Surface Sound*, Kluwer Academic Publishers, edited by B. R. Kerman.
- Pumphrey, H. C., L. A. Crum, L. Bjorno, 1988. "Underwater Sound Produced by Individual Drop Impacts and Rainfall", *J. Acoust. Soc. Amer.* **85**(4), 1518-1526.
- Shang, E. C. and V. C. Anderson, 1986. "Surface Generated Noise Under Low Wind Speed at Kilohertz Frequencies", *J. Acoust. Soc. Amer.* **79**(4), 964-971.
- Strasberg, M. 1956. "Gas Bubbles as Sources of Sound in Liquids", *J. Acoust. Soc. Amer.* **28**(1), 20-26.
- Urick, R. J., 1985. *Ambient Noise In The Sea* (1st edition), Peninsula Publishing, Los Altos, CA.
- Urick, R. J., 1983. *Principles of Underwater Sound for Engineers*, (3rd edition), McGraw-Hill, New York.
- Updegraff, G. E., 1989. "In Situ Investigation of Sea Surface Noise From a Depth of One Meter", Ph.D. dissertation at Scripps Institution of Oceanography, U.C. San Diego, CA 92093.
- Wenz, G. M., 1962. "Acoustic Ambient Noise in the Ocean: Spectra and Sources", *J. Acoust. Soc. Amer.* **34**(12), 1936-1956.

- Wille, P. C. and D. Geyer, 1984. "Measurements on the Origin of the Wind-Dependent Ambient Noise Variability in Shallow Water", *J. Acoust. Soc. Amer.* **75**(1), 173-185.
- Wilson, J. H., 1980. "Low Frequency Wind-Generated Noise Produced by the Impact of Spray with the Ocean's Surface", *J. Acoust. Soc. Amer.* **68**(3), 952-956.

Chapter 3:
Bubble Noise and
Wavelet Spills
Recorded One Meter Below
the Ocean Surface

(submitted to the Journal of the Acoustical Society of America
as a joint paper by G. E. Updegraff and V. C. Anderson)

ABSTRACT

A remote instrument has been used to record the sound and environment of small surface spills in light winds from a depth of approximately one meter in the open ocean. Recordings from the instrument indicate that these small breaks have no correlation with the amplitude or phase of long period swells moving faster than prevailing winds. The sound from the spills, which is composed of a number of distinct resonant bubble oscillations, is very similar to that described by Medwin & Beaky [1989] for windless artificial wave breaks. Peak oscillation source pressures range up to 1.2 Pascals. The average of several acoustic spectra from a single energetic spill has shown a slope of -5 dB per octave over the frequency range of the instrument, roughly 800 to 8,000 Hertz. The unique frequency for each oscillating bubble within a spill indicates that bubbles are "rung" as they are formed during entrainment, die out exponentially within milliseconds, and then no longer contribute actively to the acoustic record. Analysis of the acoustic energy generated by a number of bubbles versus frequency suggests that the -5 dB per octave wind-dependent ambient noise slopes of the Knudsen curves [1948] are caused by the shorter lifetimes of high frequency bubbles, rather than significantly lower peak pressures.

INTRODUCTION

What is the nature of the noise produced in light winds by small spills?

In the years since Knudsen, Alford and Emling [1948] published the "Knudsen Curves", which first characterized the vertical directionality and wind dependence of surface noise, there has been a sense that air bubbles played an important role in the noise mechanism. Strasberg [1956] and Franz [1959] showed experimentally that bubbles were individually capable of significant acoustic pressures when oscillating at resonance. Later, in an overview of ambient noise in the ocean, Wenz [1962] strongly suggested that noise over the 500 to 20,000 Hertz frequency band was due to bubble oscillations or cavitation noise.

A difficulty with confirming the bubble theory has been both the lack of direct ocean measurements capable of resolving individual noise characteristics, and the lack of a plausible mechanism for generating the required breathing mode oscillation pressures in bubbles. Wenz had suggested that oscillations were initiated as bubbles underwent turbulence while rising to the surface. But this mechanism was ruled out by Crighton & Williams [1969], who noted that bubbles could not be excited to a resonant response by turbulent pressure fields alone since such pressures did not remain coherent in space, at the high resonant frequency of a given bubble, over length scales as large as the bubble radius. There have been other theories since then, but the lack of physical evidence has forced a good deal of speculation. Recent lab work, however, has begun to shed new light on the characteristics of entrained air bubbles.

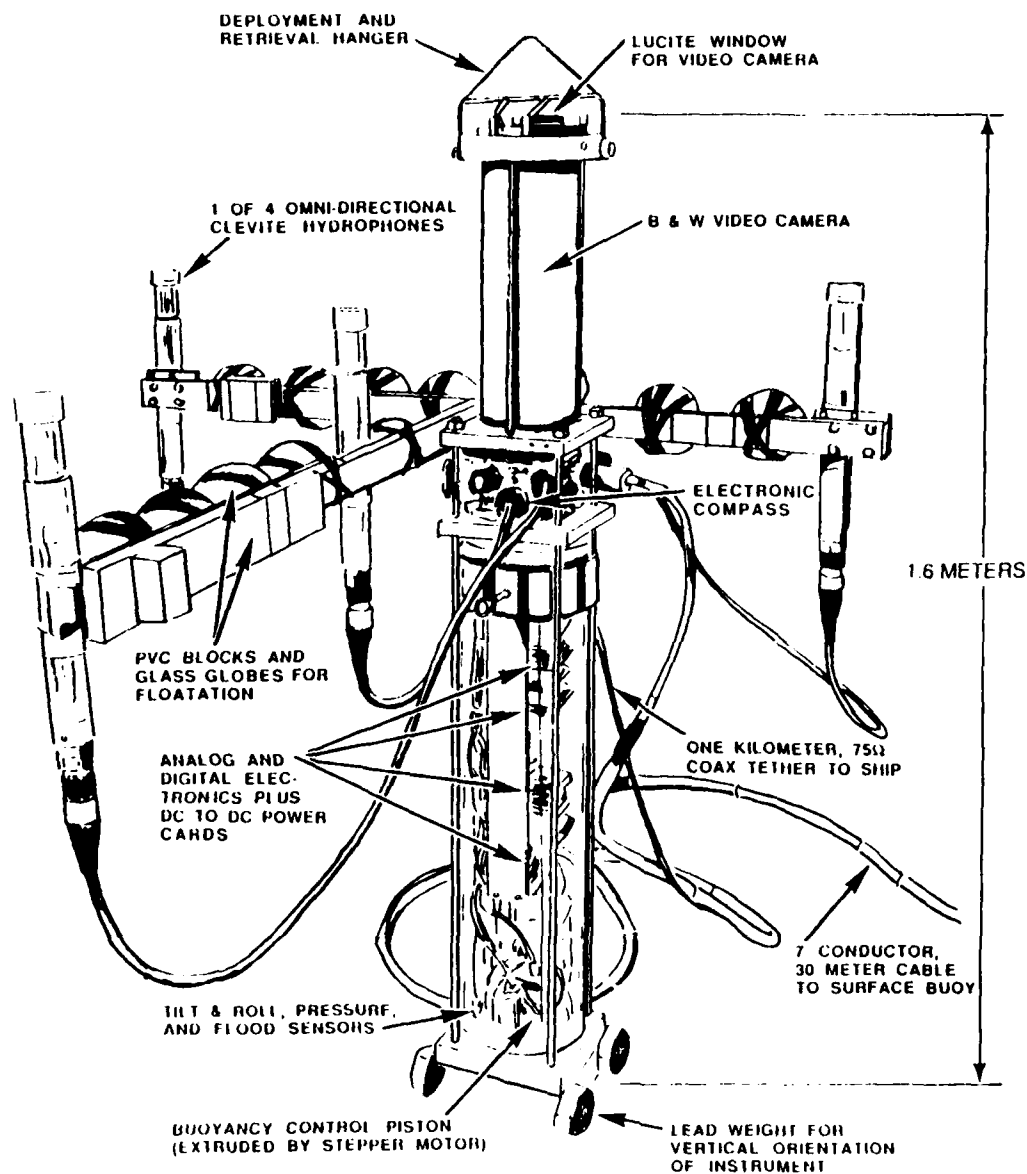
Banner & Cato [1988] constructed an air-entraining water flume and used a high-speed video system to record the entrainment of bubbles. An important result of their experiment was that, observed in slow motion, bubbles rang as they initially formed, split, or coalesced; bubble sounds due to turbulence or popping at the surface appeared to be negligible. Ringing sounds faded immediately even as the bubbles were still being distorted by turbulence.

Pumphrey, Crum, and Bjorno [1988] conducted drop impact experiments that showed impact energy dwarfed by bubble oscillation energy in those cases where a single bubble was entrained. Like Banner & Cato, no sound was observed by popping bubbles. Given that the ocean conditions capable of creating a significant amount of spray would also create innumerable bubbles, this suggests that spray impact may be a very limited noise mechanism in the ocean.

More recently, a study has been conducted by Medwin and Beaky [1989] which shows the nature of sounds produced by bubbles entrained in small wave spills. They constructed a long wave tank that generated small spills, in the absence of wind, as waves moved into a larger tank containing high frequency hydrophones. Their results showed individual bubble oscillations of high amplitude (peak pressures in the vicinity of 1 Pascal at a distance of 1 meter), with exponential damping that was non-constant in some cases. Medwin and Beaky concluded that these oscillations were caused mostly by the initial formation of bubbles, and possibly by bubble splitting.

In a previous paper [1989] we described a device that we have constructed and deployed, the Synoptic Surface Noise Instrument (SSNI), for investigating surface noise mechanisms from a depth of one meter under low wind conditions in the open ocean. The device is a self-suspending, horizontally tethered package containing a variety of sensors, including a video camera and four hydrophones (Figure 1). The digitally recorded frequency range covers roughly 500 to 9,000 Hertz. The instrument is designed to hold itself within 2 meters of the surface in the open ocean -- close enough that individual noise sources can be isolated and analyzed. The one-kilometer horizontal telemetry cable provides isolation from ship noise,

SSNI SUBMERGED PACKAGE



Chapter 3, Figure 1: SSNI Submerged Package -- Video Camera views surface from underneath thru clear top plate from a depth of 1 to 2 meters; four Clevite Hydrophones, each sampled at 20 kHz, allows recording and finding the relative position of surface noises; compass, pitch, roll, and depth sensors, sampled each second, allows monitoring the instruments environment.

while a surface buoy, attached 30 meters from the submerged instrument, supplies continuous wind measurements 1.5 meters over the ocean's surface.

In this paper, we will describe and summarize data recorded with this instrument. In general, the acoustic data we have recorded from the ocean has shown a remarkable similarity to Medwin and Beaky's windless lab results.

I. TIME SERIES SAMPLES

Figure 2 shows the sound recorded by one hydrophone for the life of a typical small spill, during an SSNI deployment in the Gulf of California on February 20, 1989. The water depth was over 1,000 meters, while the instrument's depth was about two meters. The SSNI wind buoy, taking measurements 1.5 meters over the water, gauged the wind speed at 1.5 to 1.8 meters per second. The predominant long-period swells, with periods of 3.8 seconds, were negligible. Unlike previous deployments, no pre-whitening filter was used to attenuate low frequencies during this run. The frequency response of the instrument was therefore fairly flat from 500 to 8,000 Hertz. The background noise level was slightly higher than normal, however, because the SSNI was only tethered 500 meters from the support ship. The plots in Figure 2 start with "frame" 11300, where each frame represents one-thirtieth of a second of data and corresponds to one video frame picture recorded on videotape (like most of the spills recorded by the SSNI, this spill was not in the camera's view). The plots are contiguous and numbered successively with "+1", "+2", etc., and referenced to the initial frame number of the spill, 11300 (therefore, dividing a frame number by 30 frames per second gives the number of seconds into the deployment recording: $11300 + 30 = 377$ seconds).

Most of the sound plotted in Figure 2 is produced by distinct, transient oscillations, much like those reported by Medwin and Beaky, and are assumed to be bubbles. Where possible, the frequencies and locations -- in Cartesian coordinates relative to Hydrophone B and calculated from the different arrival times of the noise signatures between the four SSNI hydrophones -- of the oscillations have been marked on the plot. θ measures the angle at Hydrophone B between the noise source and vertical. Note that each frequency is unique within the record; this indicates that the corresponding bubbles are likewise unique. In the records we have taken so far, similar observations indicate that bubbles are not recycled intact for further audible oscillations within a spill.

Figure 3 shows a particularly energetic spill which occurred about one minute after the spill in Figure 2. As the wavelet breaks, we see a few distinct bubble oscillations between frames 12861 to 12870. By frame 12873, individual oscillations are overlapping so frequently that they can no longer be distinguished. By frame 12878, the bubble peak pressures appear to have increased, with some unfortunate clipping occurring in frame 12880. The oscillations begin to die out by frame 12887, lasting another third-to-half-second. Curiously, the oscillations in this latter section are not nearly so distinct and well formed as at the beginning. This may be because the initial bubbles were entrained in relatively "clean" water, that is, water containing few millimeter sized bubbles that would resonate at the same frequencies, while sounds produced by bubbles entrained at the end are subject to the scattering and distorting effects of previously entrained bubbles.

The apparent increase in peak pressures during the most energetic part of Figure 3 may be an indication that these bubbles were thrust deeper as they formed. Longuet-Higgins [1989b] has suggested that the acoustic radiation from a bubble oscillating close to the surface will be partly cancelled by radiation from its image, forming a vertical dipole whose strength is proportional to the distance of the bubble from the surface. Thus, bubbles formed at greater depth by more energetic wave breaks should generate higher peak pressures than bubbles formed by small spills close to the ocean surface. Longuet-

Higgins further suggests that this reduction in acoustic damping for bubbles formed close to the surface should result in their having slightly longer lifetimes.

II. SPECTRAL ANALYSIS OF TIME SERIES

While most of the wavelet breaks recorded on February 20, 1989, resemble Figure 2, where distinct oscillations are readily apparent, the overlapping oscillations of Figure 3 are much more complicated. For this reason, we have performed a spectral analysis of Figure 3 in order to characterize the spill. Since bubble oscillations are short lived (time constants of 33 ms at 500 Hz, 0.3 ms at 9,000 Hz, according to Strasberg), correspondingly short (6.4 ms) 128-point FFT's have been used to generate the waterfall plots of Figure 4, where frequency is plotted on the vertical axis. Nine overlapping FFT's were generated per frame (1/30 second) of data, with each frame offset marked on the bottom axis. Moving right, successive small tic marks represent successive FFT's, taken 3.7 ms apart, as labeled on the top axis. Only spectral values exceeding 65 dB re 1 μ Pa-squared per Hz for each FFT are plotted, with higher intensity increasing to the left for a given FFT peak. Small tic marks to the left of a given FFT represent increases of 5 dB over the 65 dB minimum threshold for that FFT. A Kaiser-Bessel window, such as described by Harris [1978], with $\alpha = 3.0$, was used on the input data to smooth FFT edge effects. It should be noted that frequencies below 500 Hertz and above 8,000 Hertz are attenuated by SSNI filters; within this range the gain is close to flat.

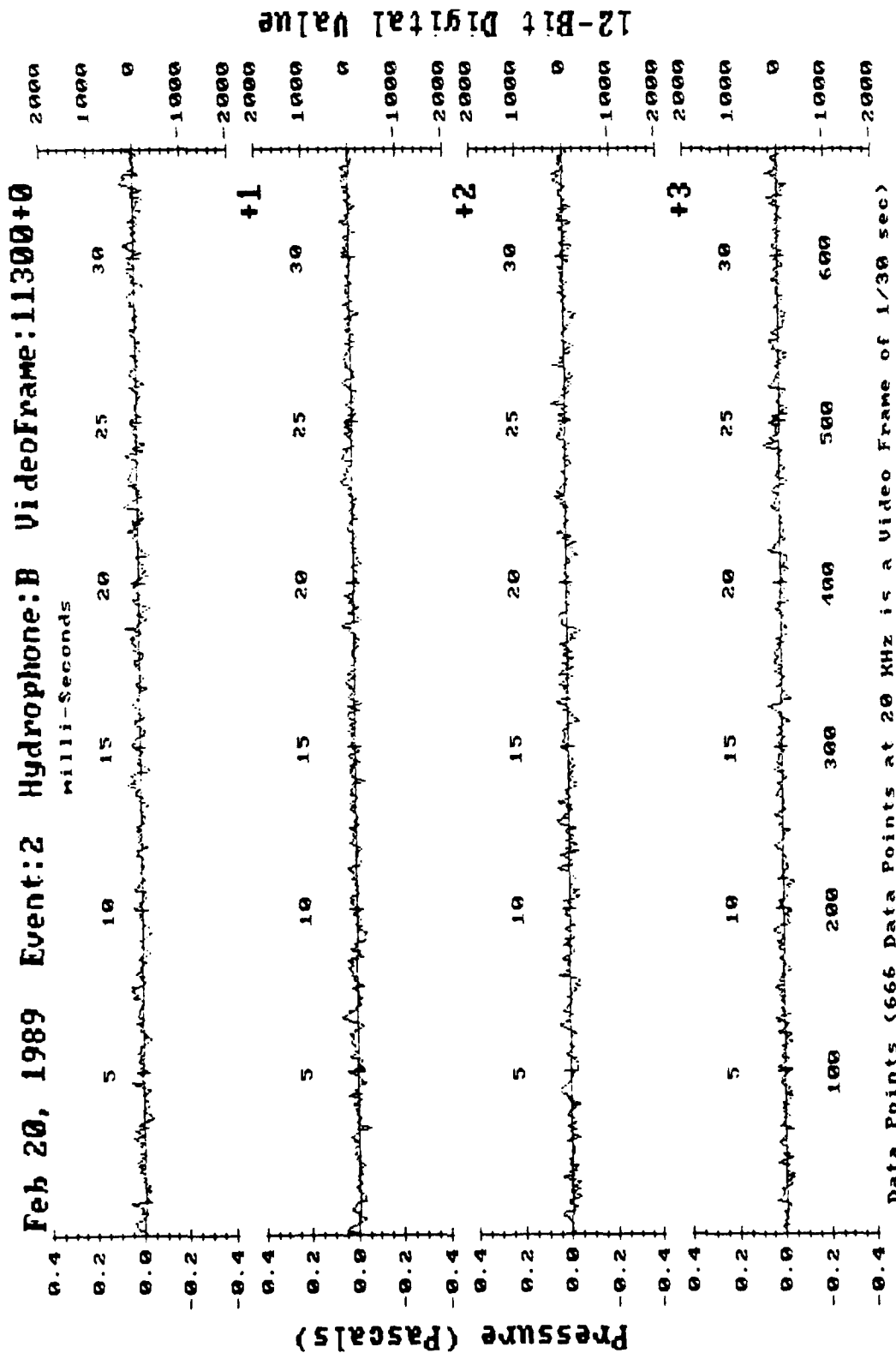
The plots of Figure 4 confirm that the complicated time series of Figure 3 is mostly composed of brief, highly tonal oscillations. The low frequencies tend to be overemphasized in these plots because their longer lifetimes allow them to oscillate over a number of FFT's. Intriguingly, there is a noticeable paucity of oscillation peaks between 4,000 and 5,000 Hertz over the most energetic part of Figure 4. It is not clear whether this represents a lack of oscillations within this band, a lack of energy for oscillations within this band, or some other frequency dependent effect.

The continuous oscillations of Figure 3, which are much higher than the background noise, provide an opportunity to determine an average spectrum over time for the wavelet break. The FFT's from the most energetic part of Figure 2, from frames 12876 to 12888, have been averaged and plotted logarithmically in Figure 5. The match between the plot and the -5 dB per octave dashed line provides strong evidence that small, bubble-entraining breaks such as this are responsible for the -5 dB per octave Knudsen curves. Although the dB scale of this spectral average, measured from a distance of 2.5 to 3 meters, corresponds to a sea state of 4 to 5 according to Urick's ambient noise summation in Figure 6, it is clear that its noise contribution to large depths must be averaged with part of the quiet surrounding ocean surface. Indeed, if the spectral level had been 20 dB lower, such an infrequent sound source would not have been capable of contributing to the sound levels recorded at great depths.

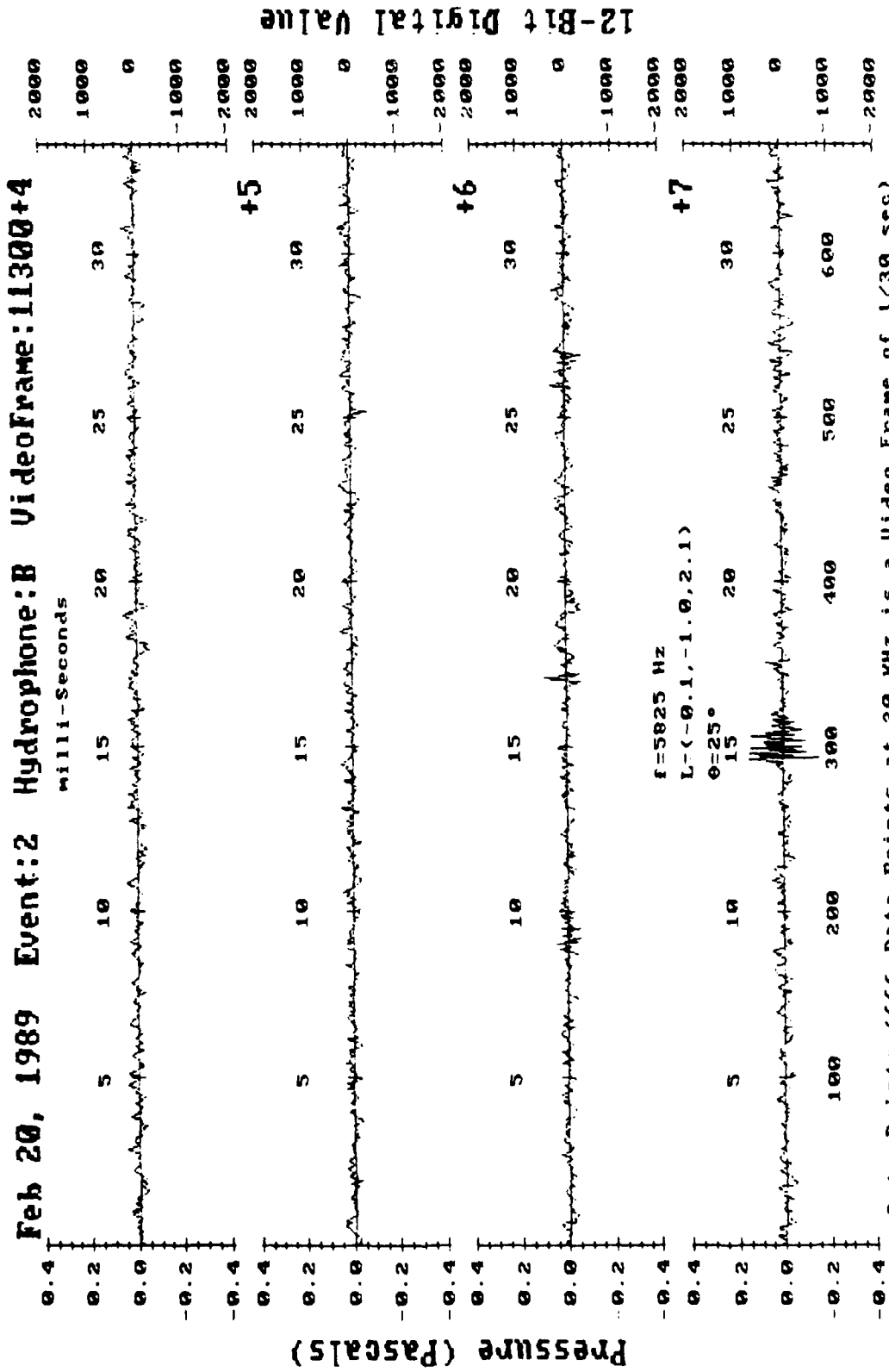
The dip in the spectrum of Figure 5, between 4,000 and 5,000 Hertz, corresponds to the already noted lack of oscillation peaks within this range in the waterfall plots of Figure 4. Note, though, that this dip is followed by a peak at 5,800 Hz.

One explanation for this behavior is that the bubbles we have recorded may have been ringing at depths of 11 centimeters or so, which would cause a close observer to witness acoustic cancelling or reinforcement between a bubble and its surface-reflected image within narrow audible frequency bands, dependent upon the observer's distance and angle from the bubble. Such an explanation could also explain the fact that certain bubbles do not reach their peak pressure during the first cycle. The oscillation in Figure 3c, 5 ms into Frame 12860+10, shows an initial positive half-cycle followed by a much larger

Chapter 3, Figures 2a to 2i: Hydrophone B time series of approximately one second of a small wave break recorded on Feb 20, 1989. Each page contains four 1/30 second frames of data, and is numbered with a frame count offset. Individual oscillations within each plot are labeled according to their frequency f_o , location relative to Hydrophone B, and angle θ from vertical over Hydrophone B.

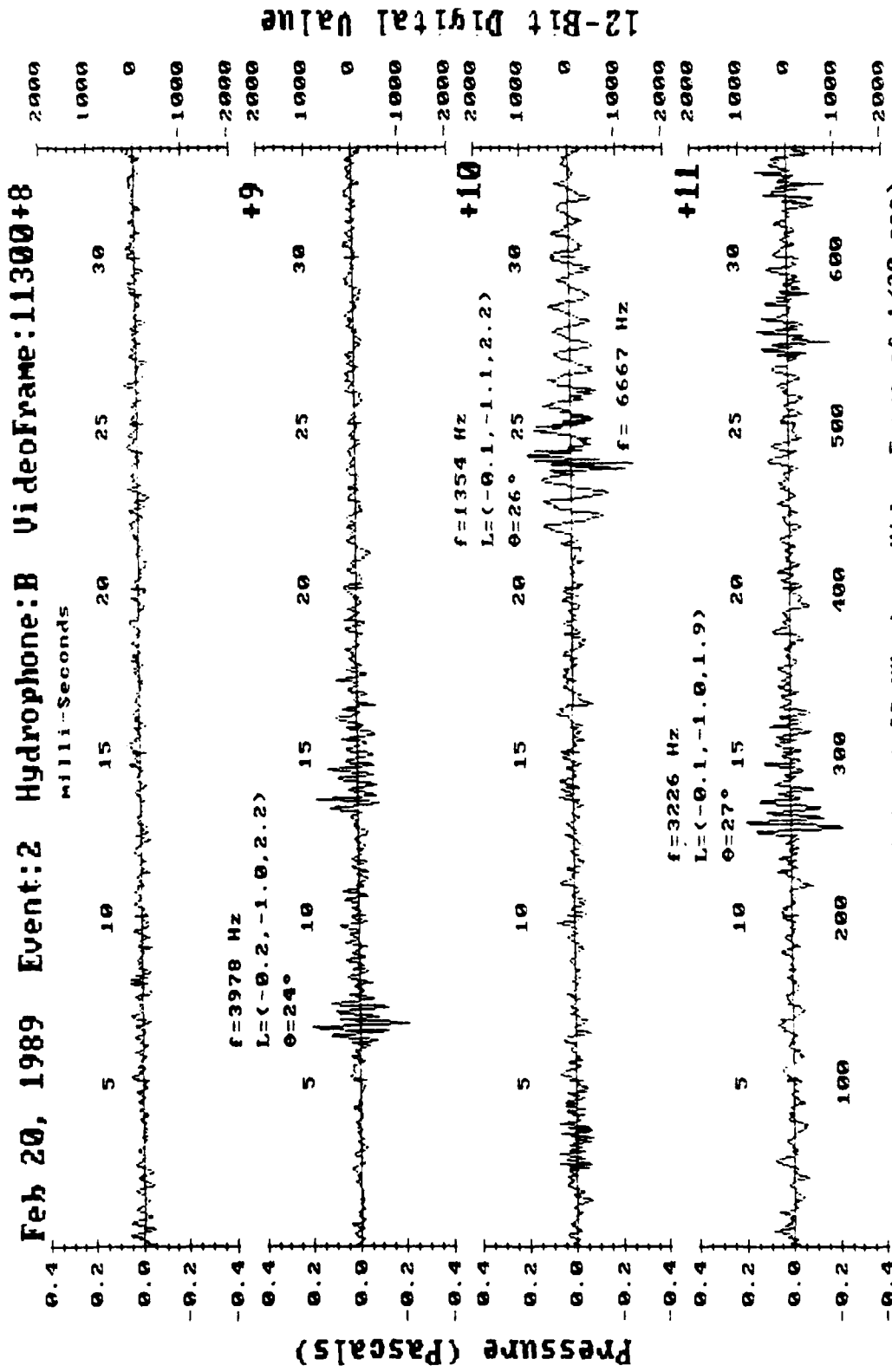


Chapter 3, Figure 2a: Video Frames 11300 to 11303.

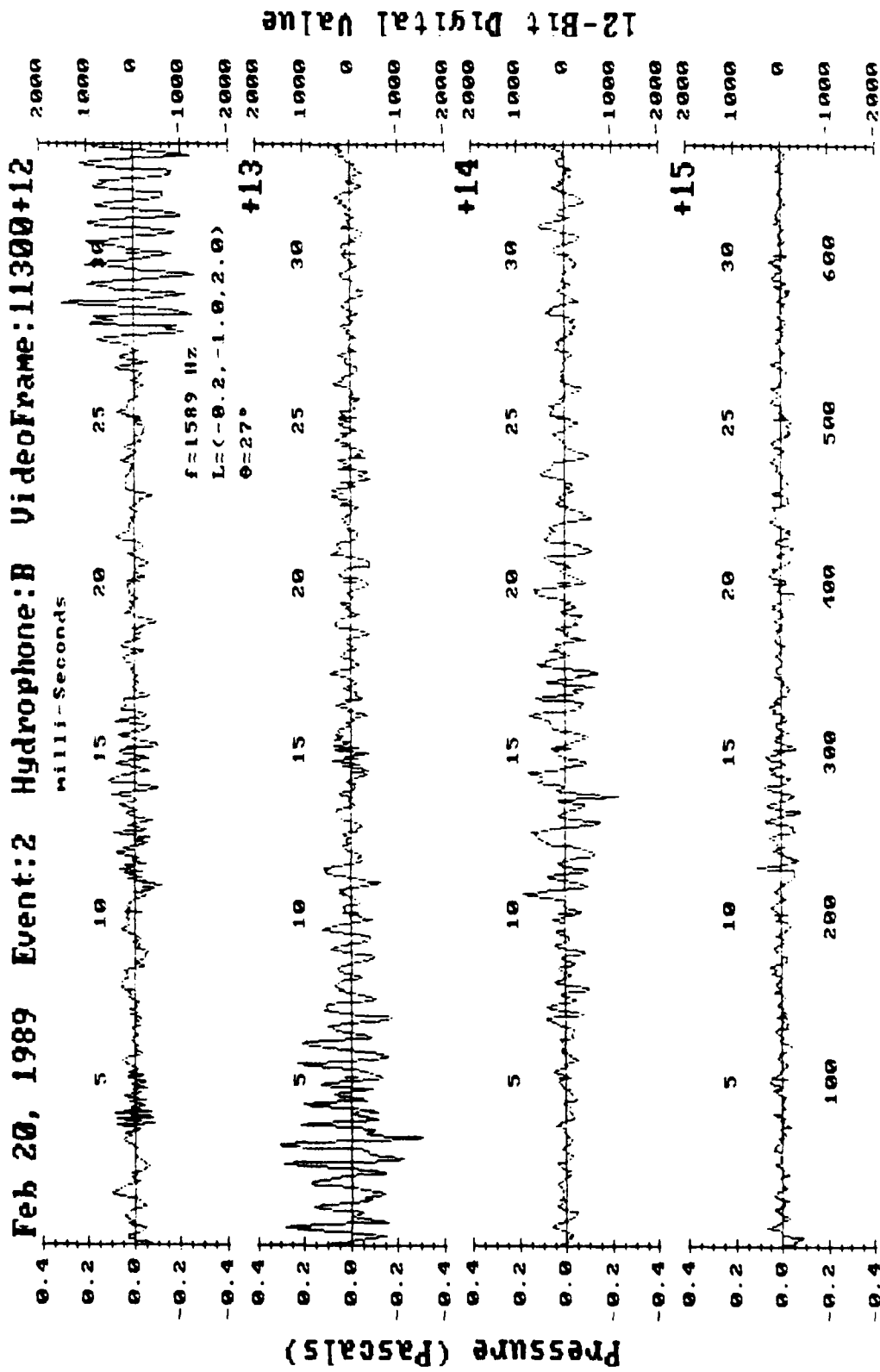


Data Points (666 Data Points at 20 KHz is a Video Frame of 1/30 sec)

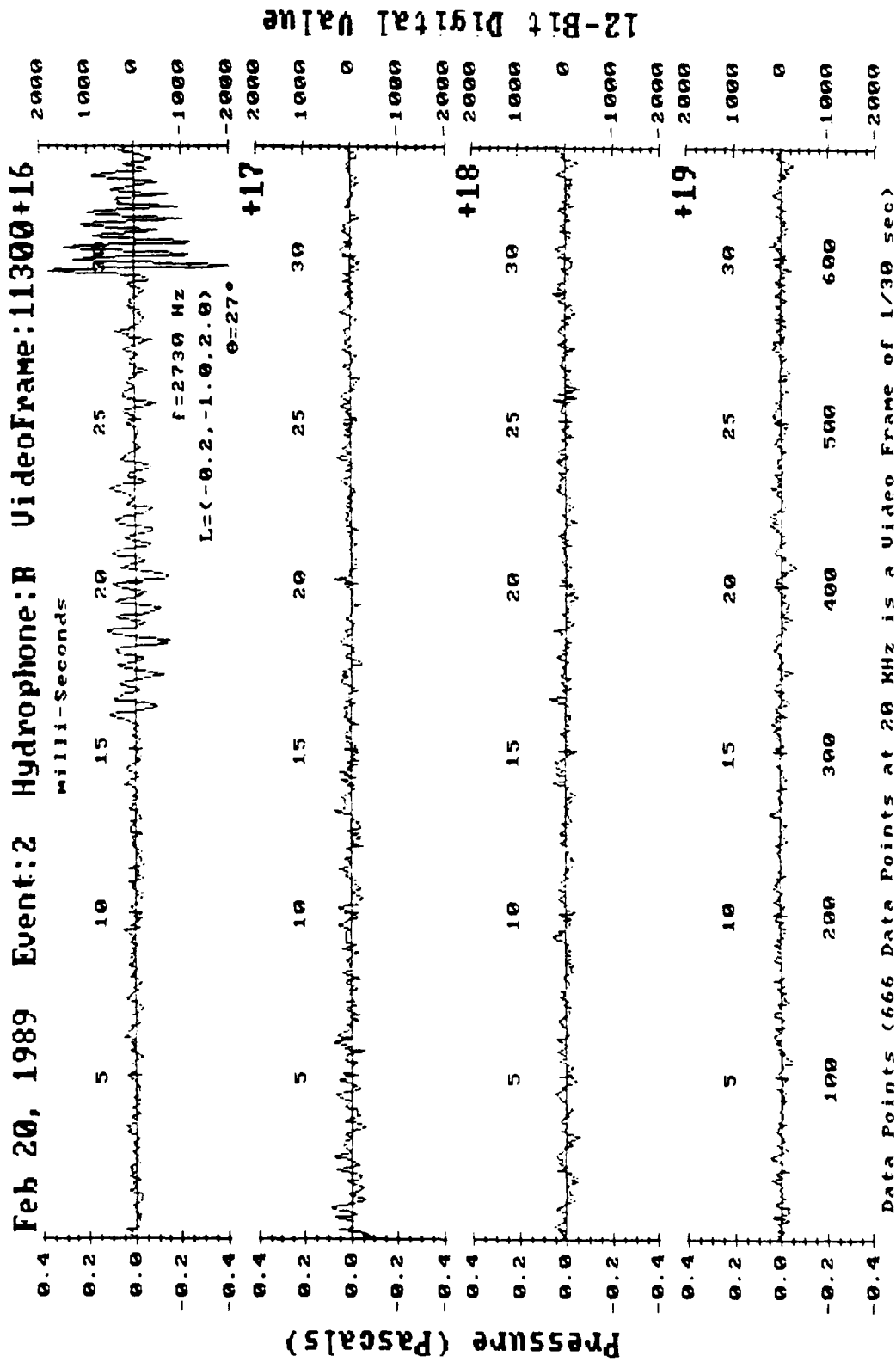
Chapter 3. Figure 2b: Video Frames 11304 to 11307.



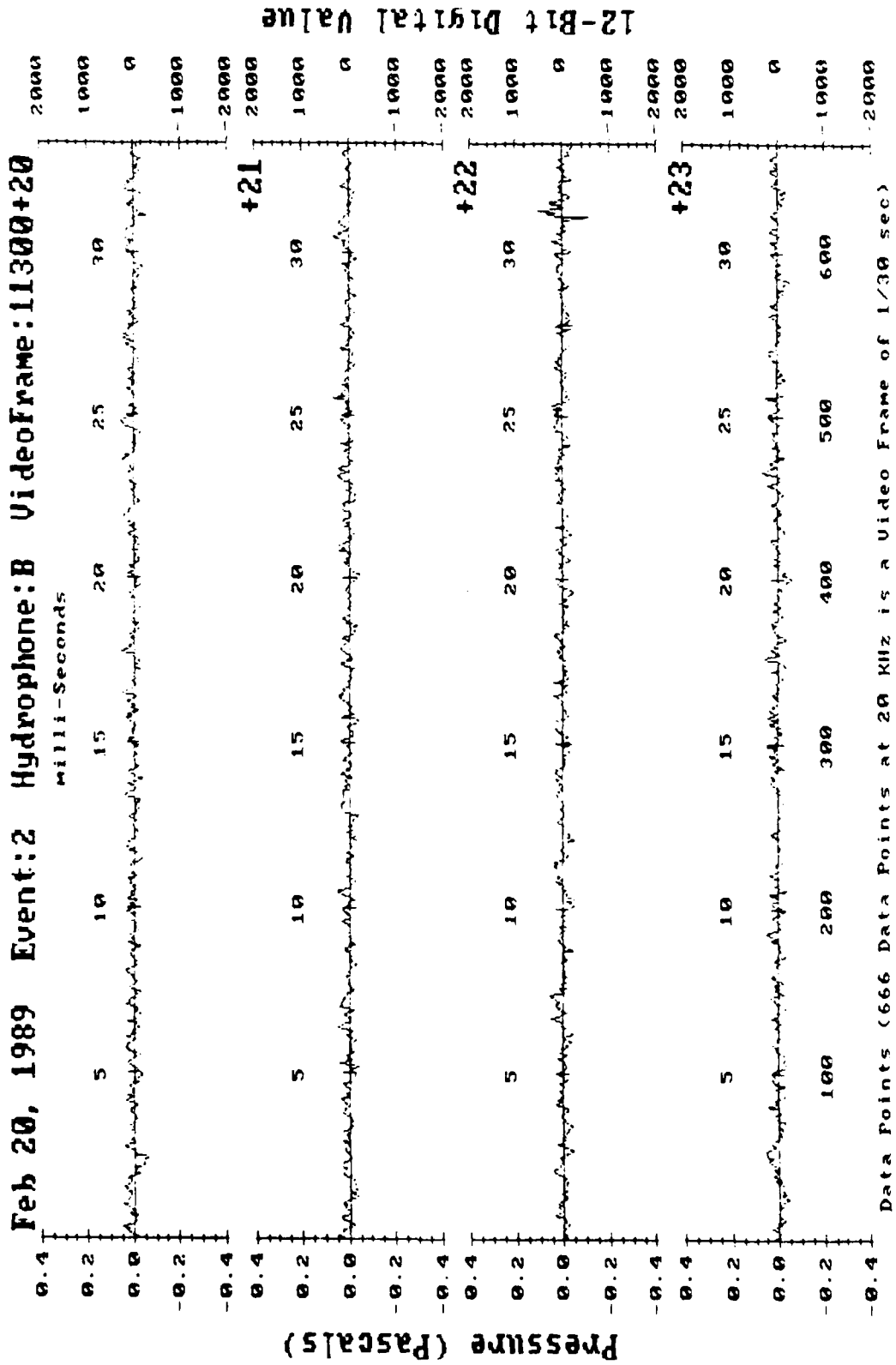
Chapter 3, Figure 2c: Video Frames 11308 to 11311.



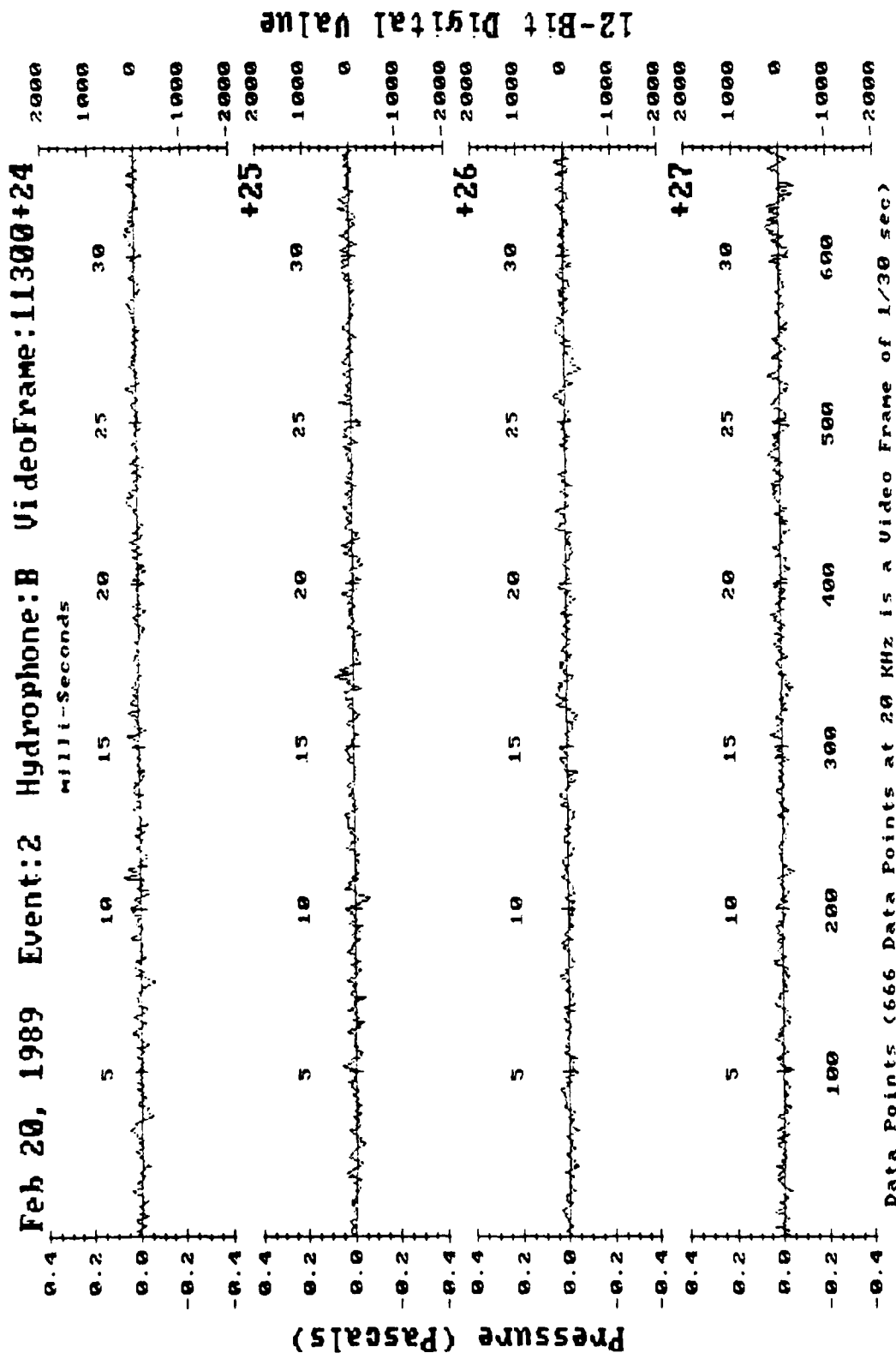
Chapter 3, Figure 2d: Video Frames 11312 to 11315.



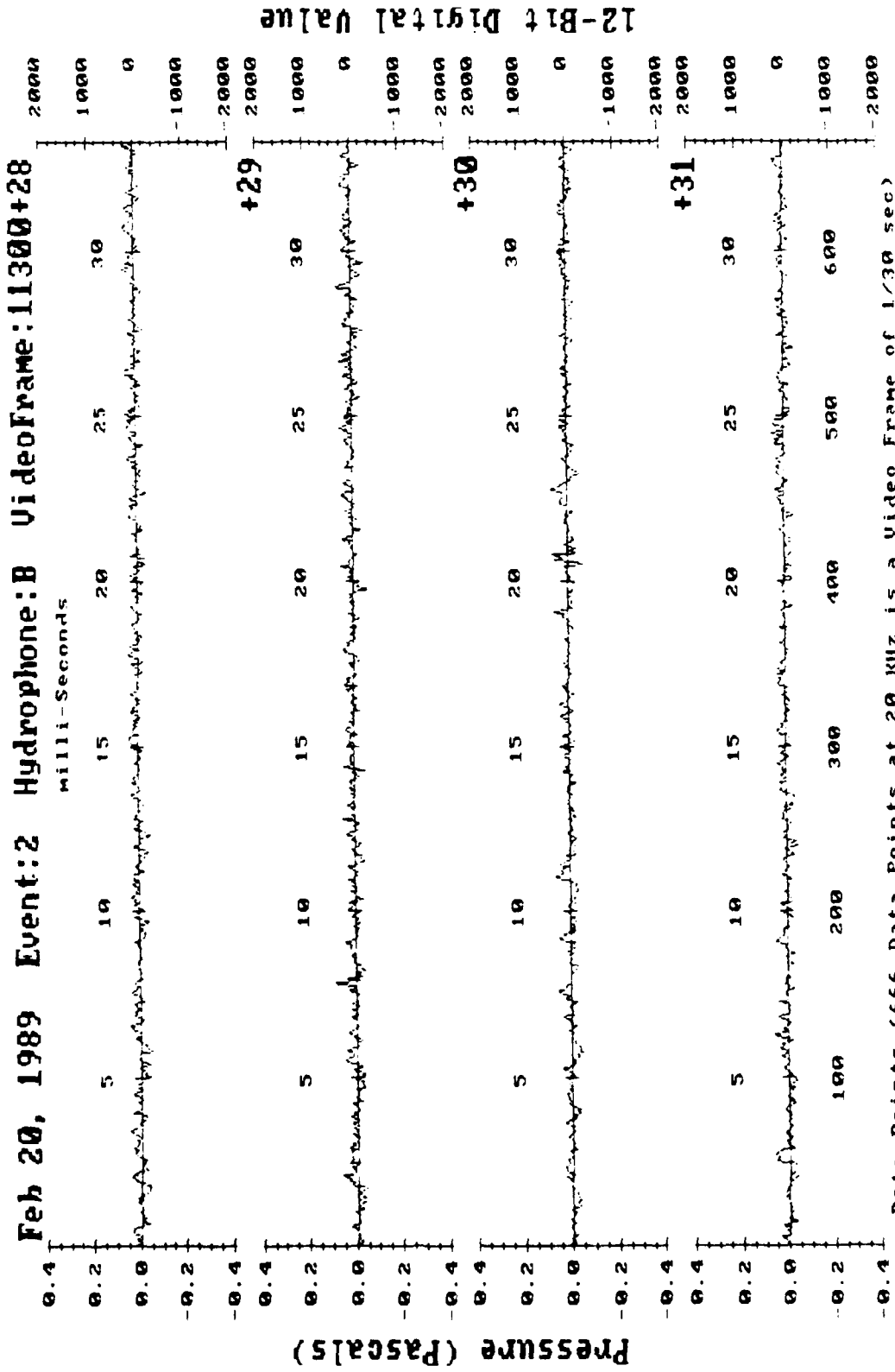
Chapter 3, Figure 2e: Video Frames 11316 to 11319.



Chapter 3, Figure 2f: Video Frames 11320 to 11323.

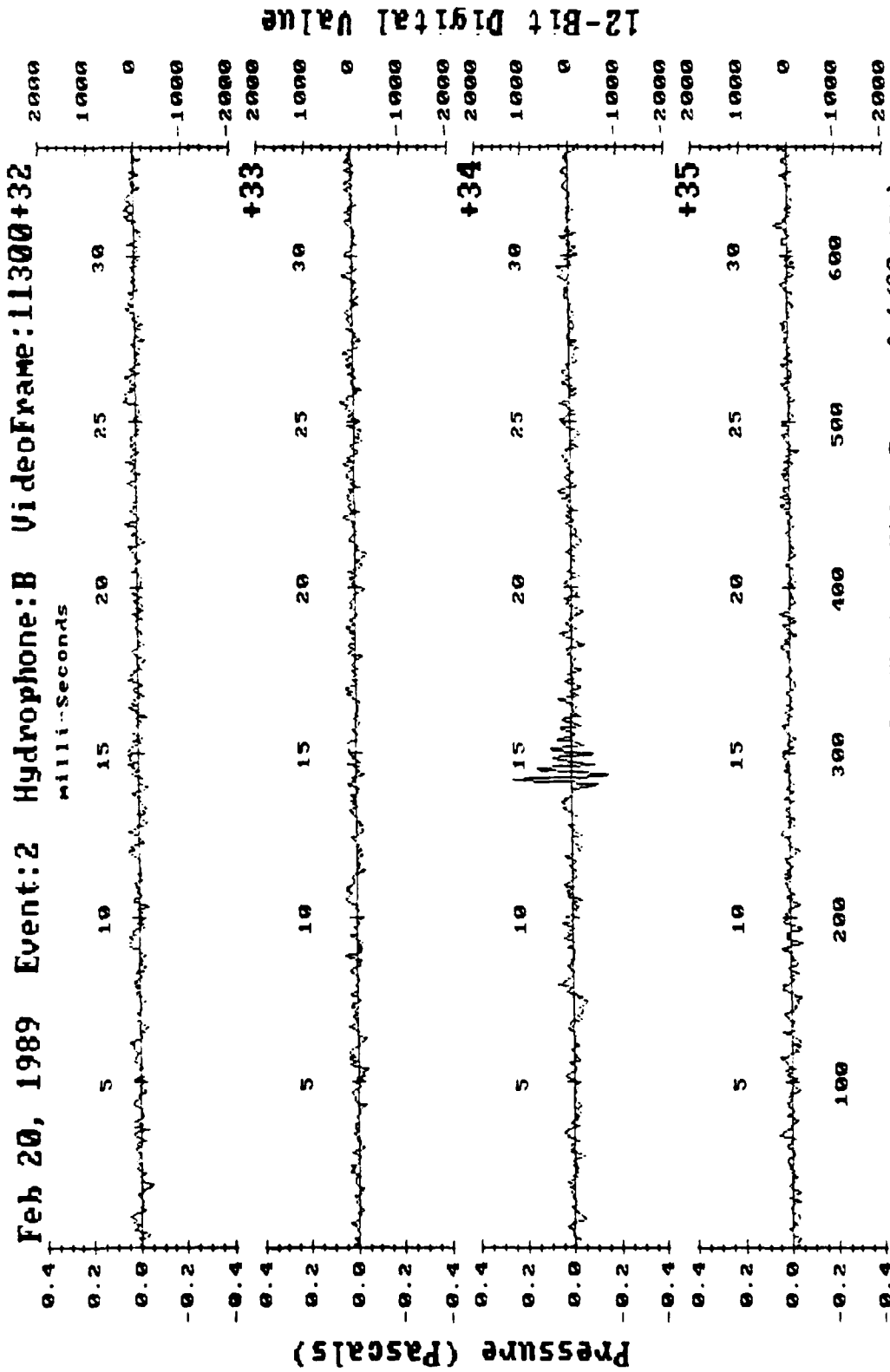


Chapter 3, Figure 2g: Video Frames 11324 to 11327.



Data Points (666 Data Points at 20 KHz is a Video Frame of 1/30 sec)

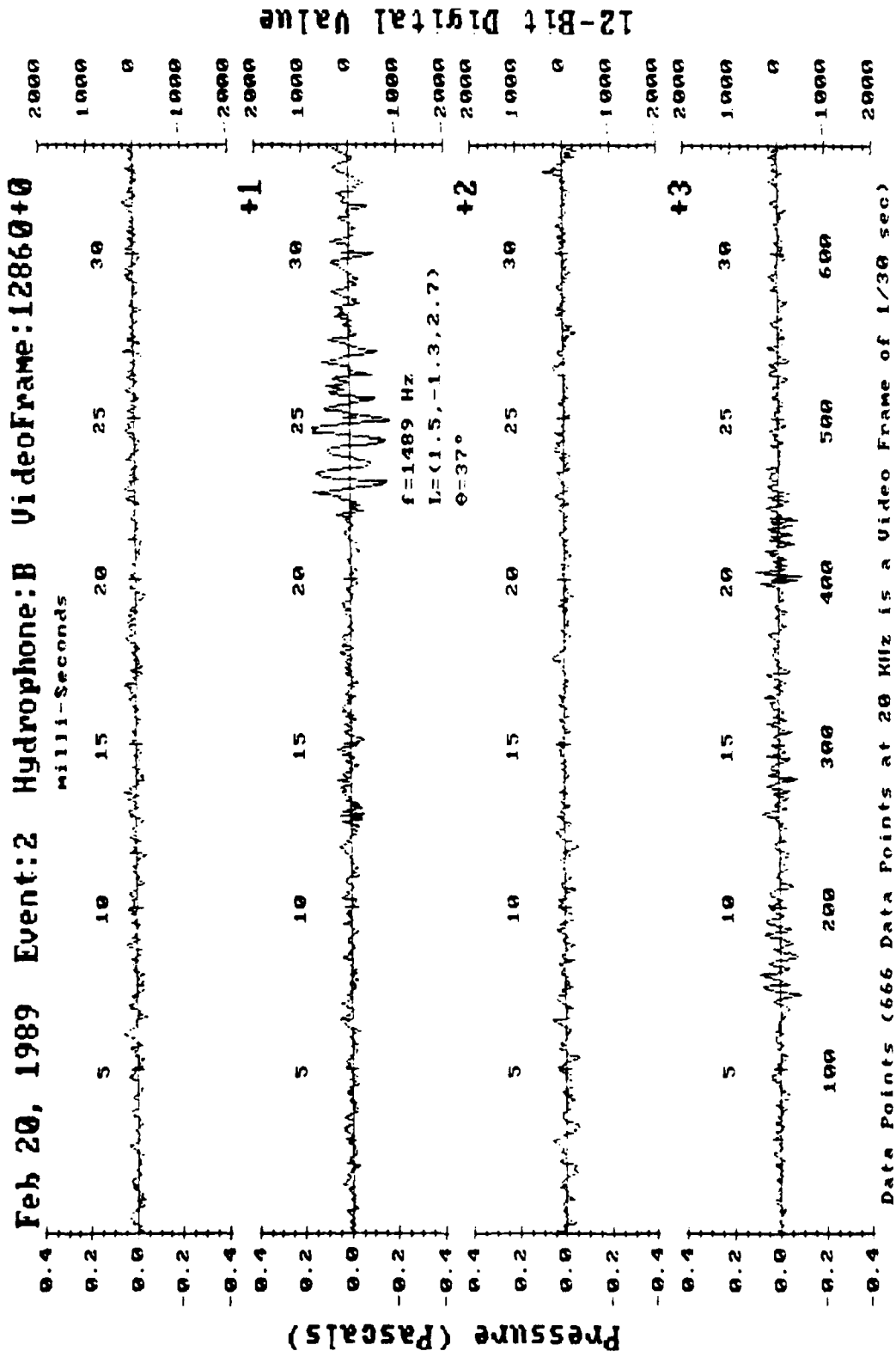
Chapter 3, Figure 2h: Video Frames 11328 to 11331.



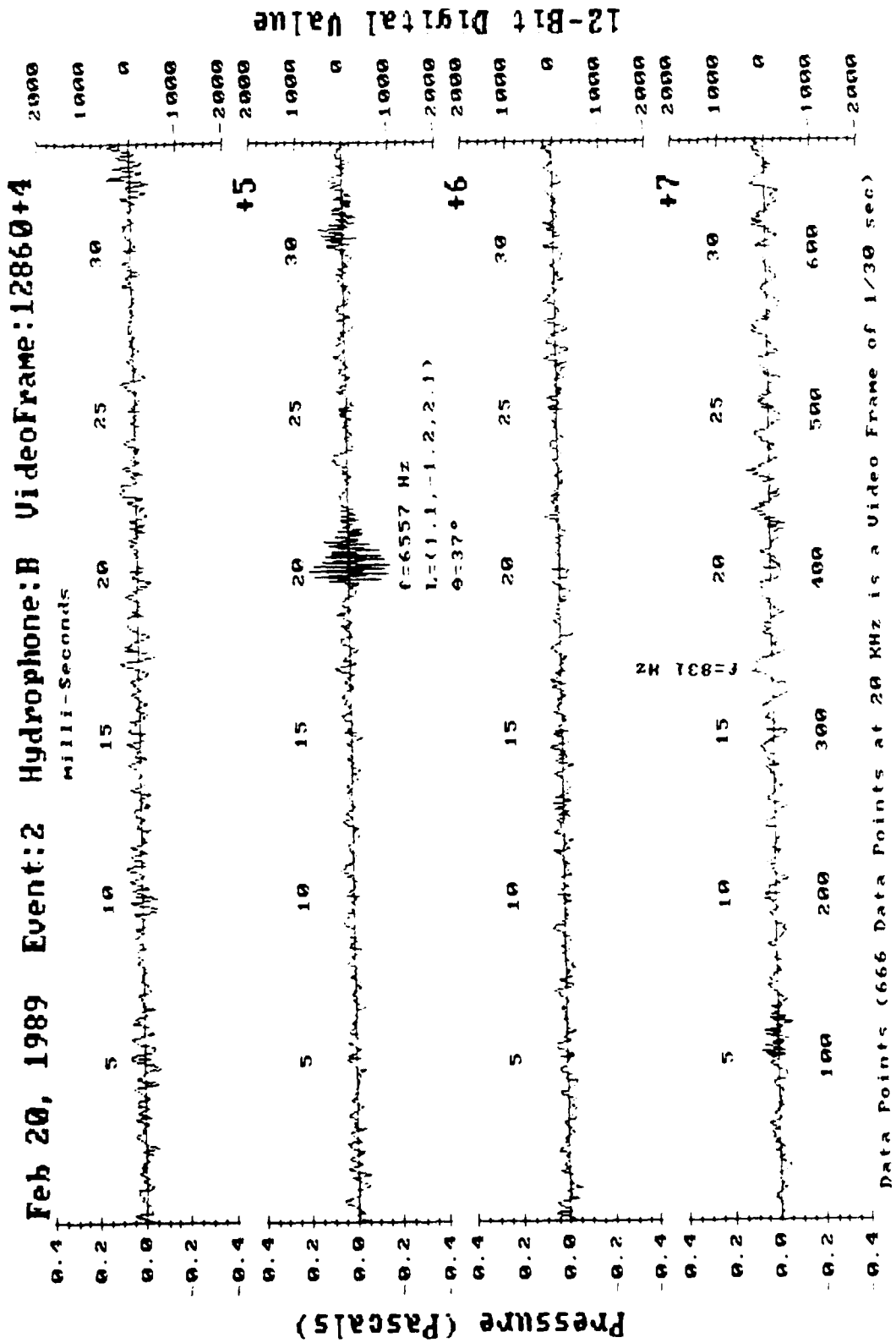
Data Points (666 Data Points at 20 KHz is a Video Frame of 1/30 sec)

Chapter 3, Figure 2i: Video Frames 11332 to 11335.

**Chapter 3, Figures 3a to 3k: Energetic spill recorded one minute after
Chapter 3, Figure 2.**

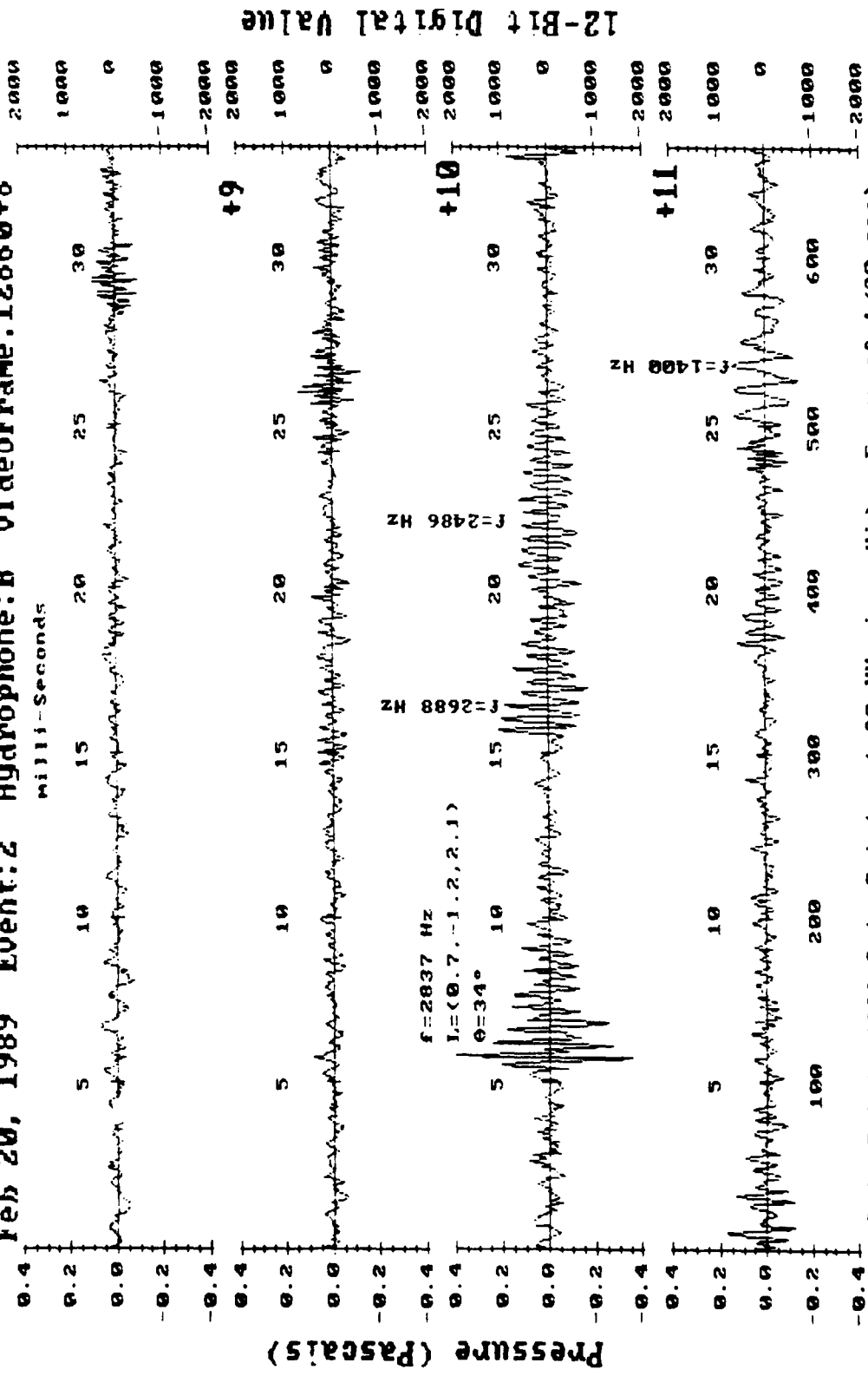


Chapter 3, Figure 3a: Video Frames 12860 to 12863.



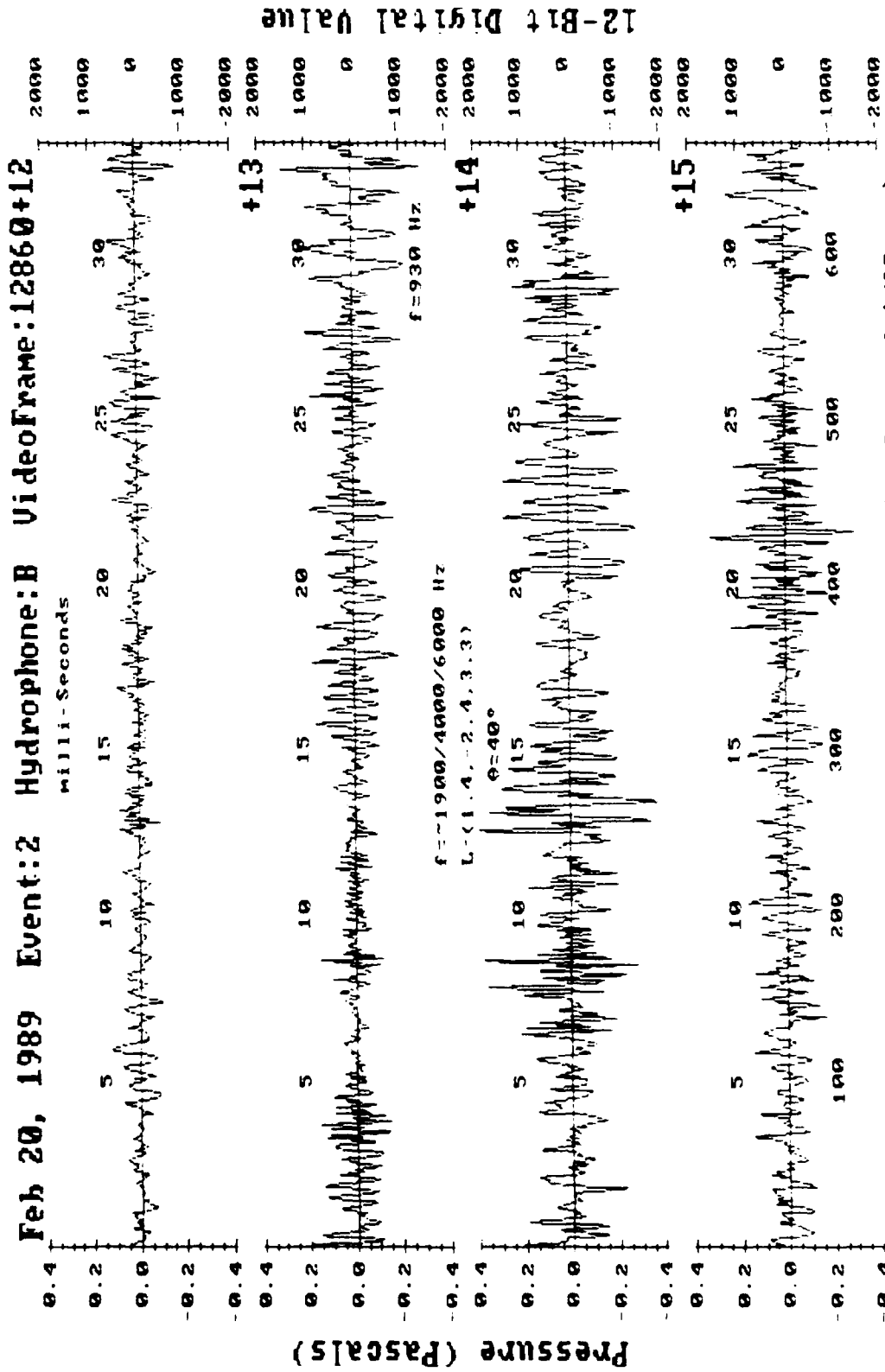
Chapter 3, Figure 3b: Video Frames 12864 to 12867.

Feb 20, 1989 Event:2 Hydrophone:B VideoFrame:12860+8

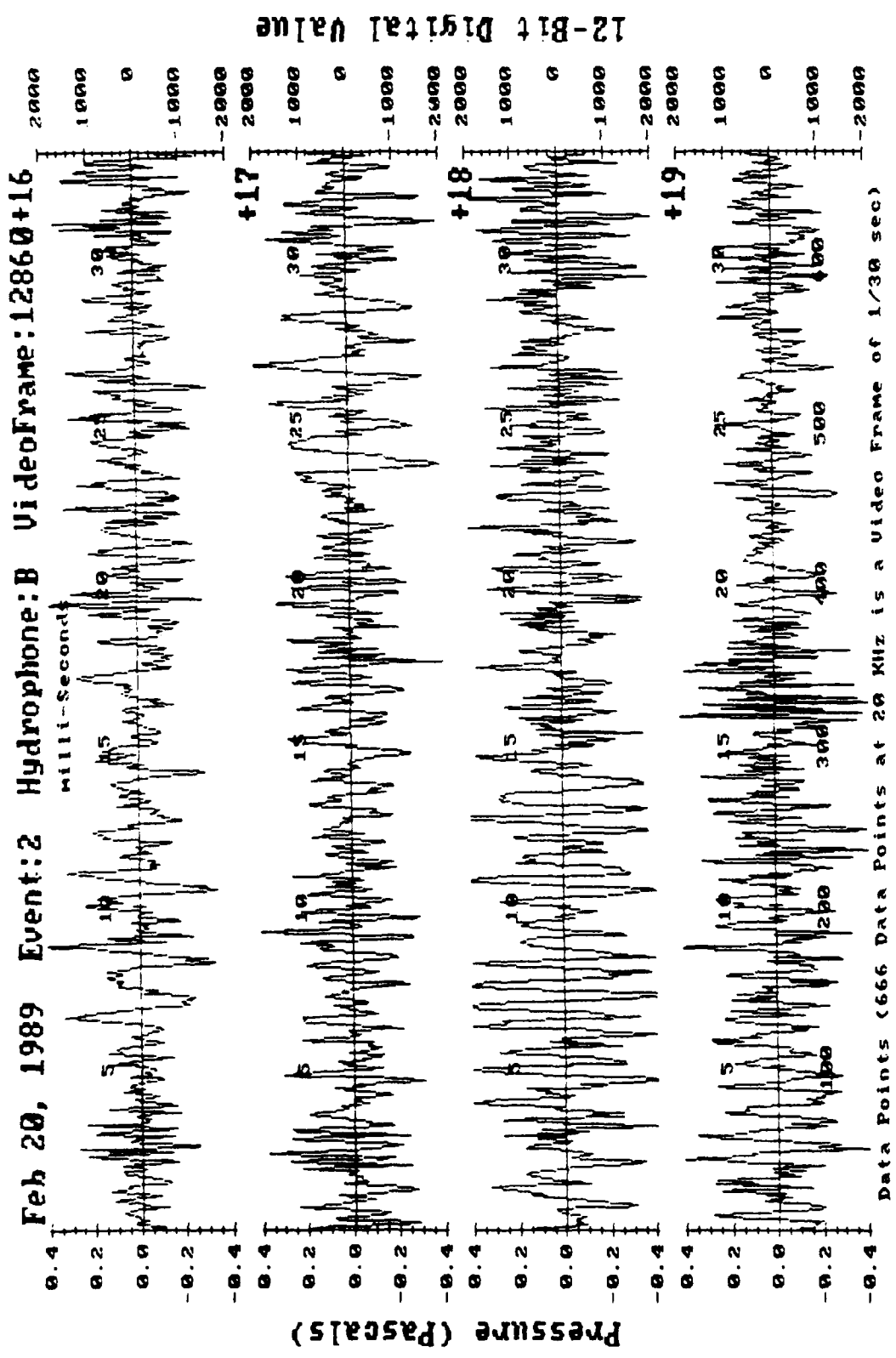


Data Points (666 Data Points at 20 KHz is a Video Frame of 1/30 sec)

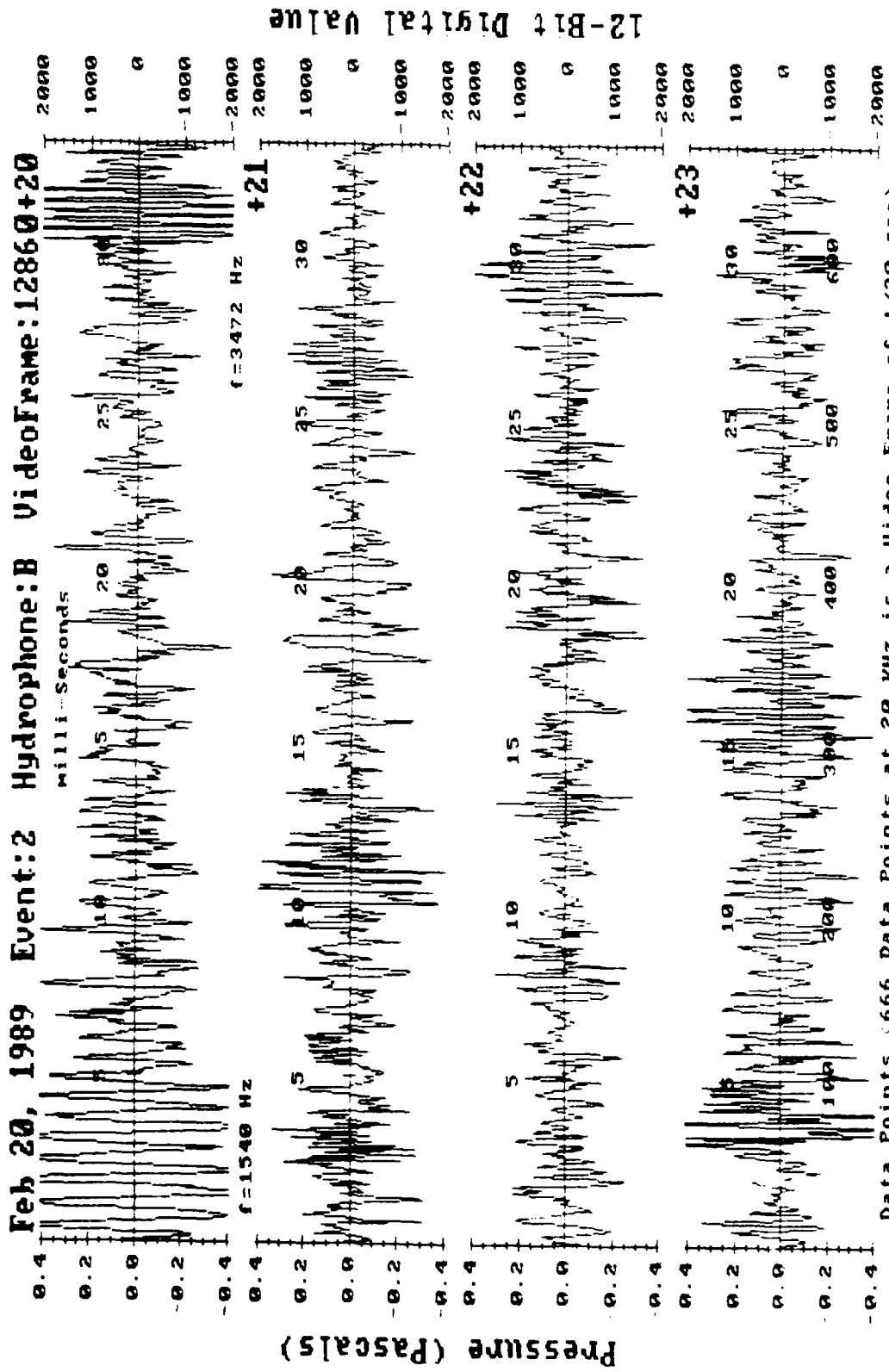
Chapter 3, Figure 3c: Video Frames 12868 to 12871.



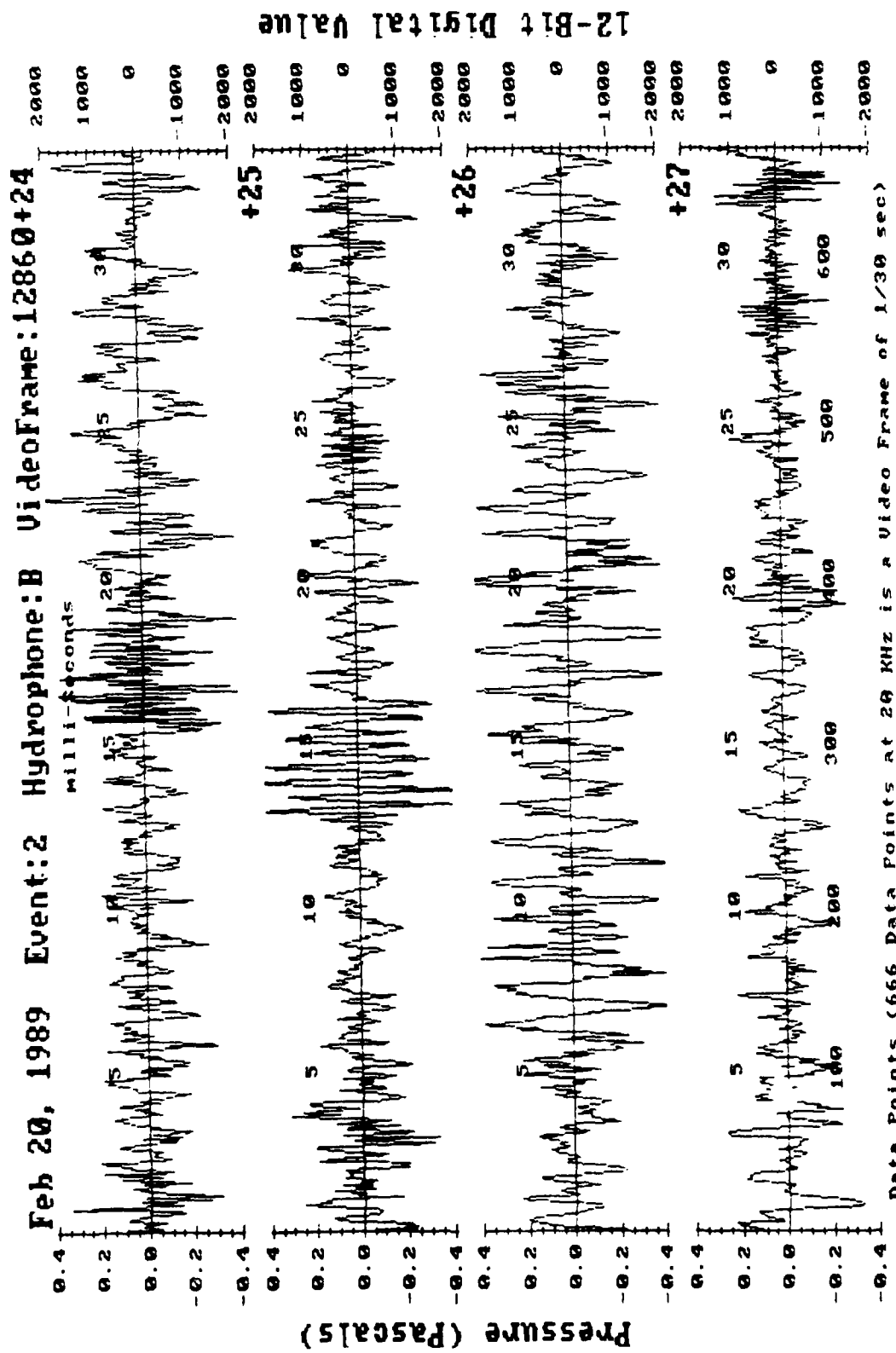
Chapter 3, Figure 3d: Video Frames 12872 to 12875.



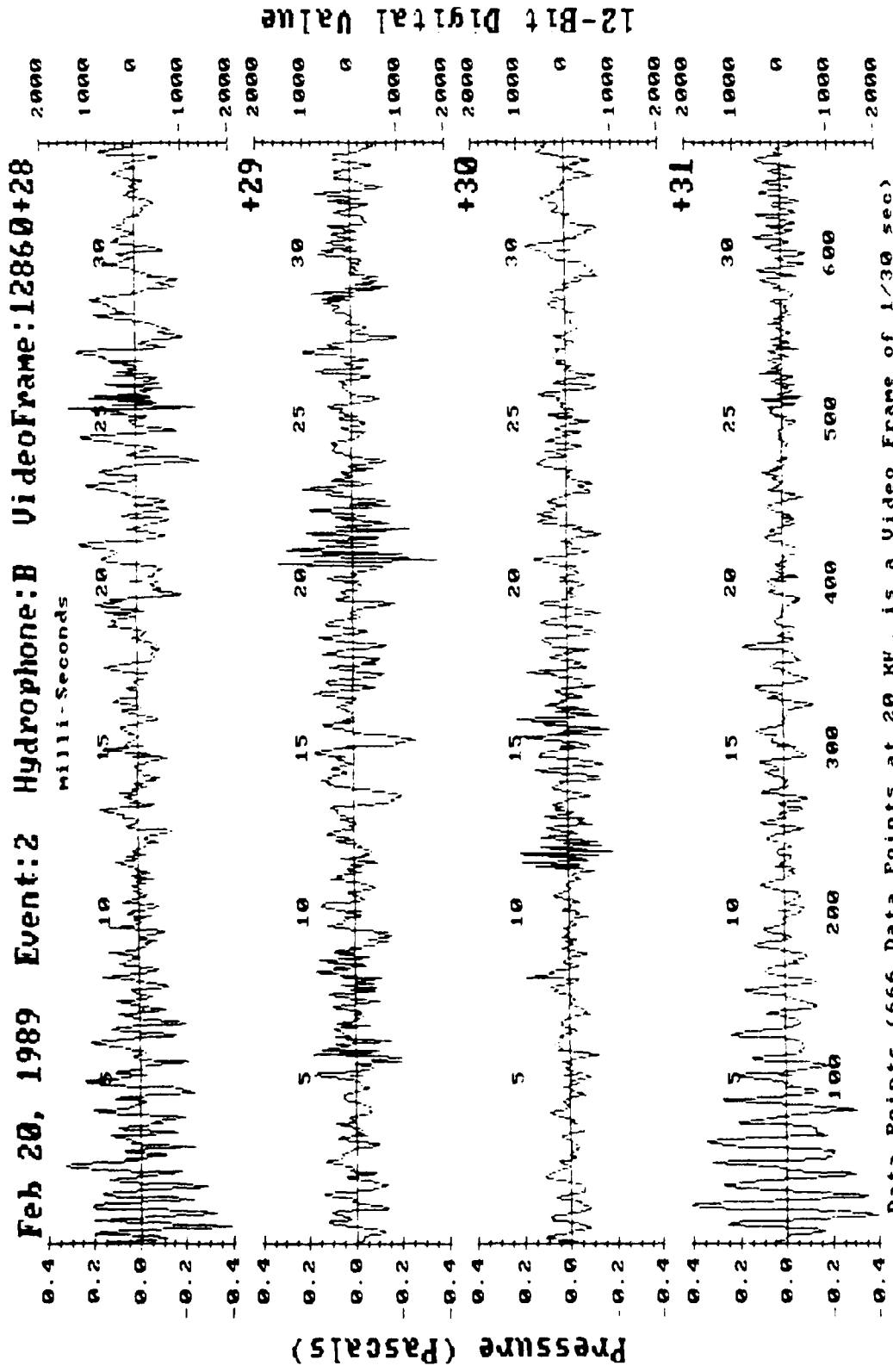
Chapter 3, Figure 3e: Video Frames 12876 to 12879.



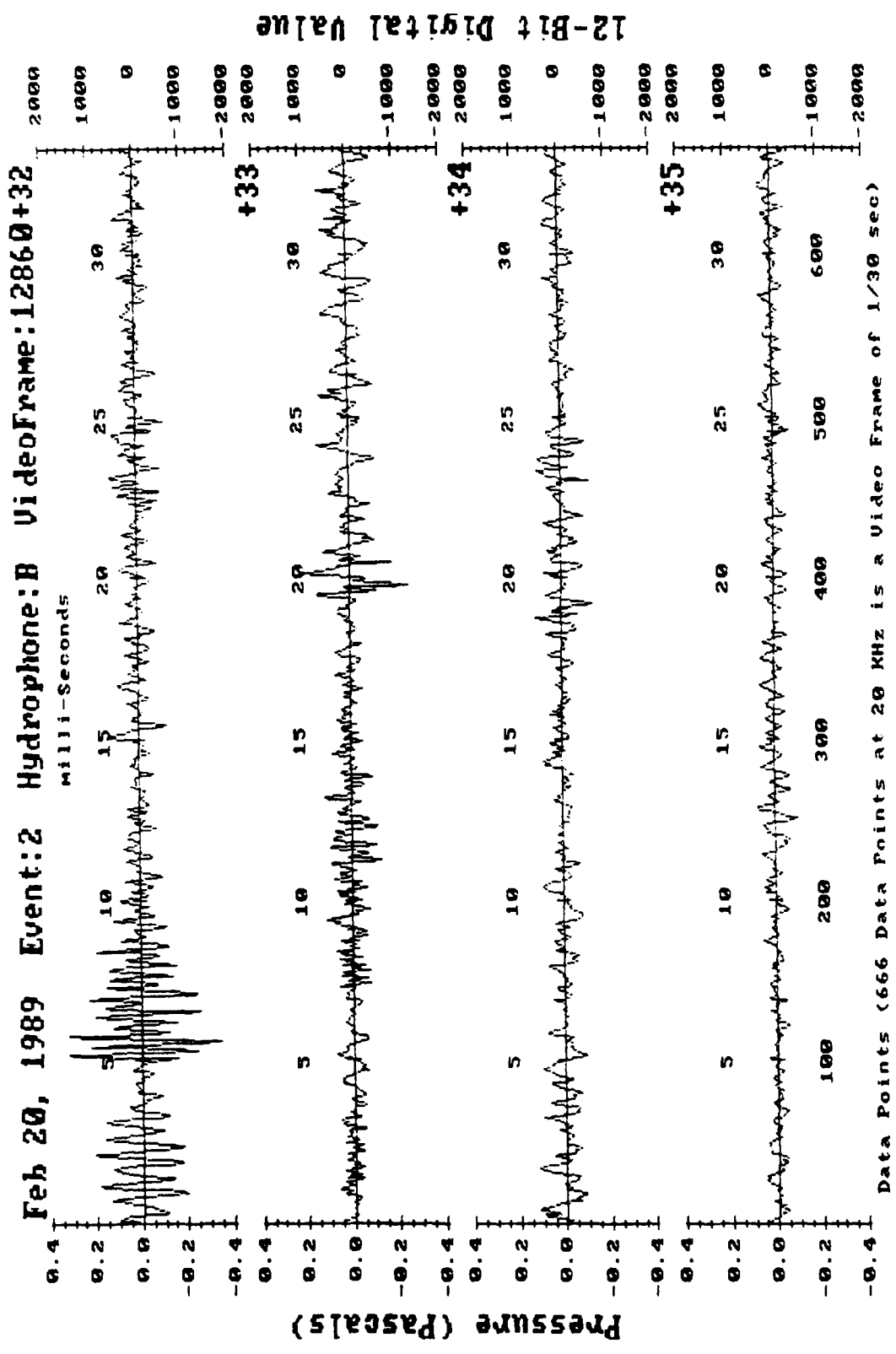
Chapter 3, Figure 3f: Video Frames 12880 to 12883.



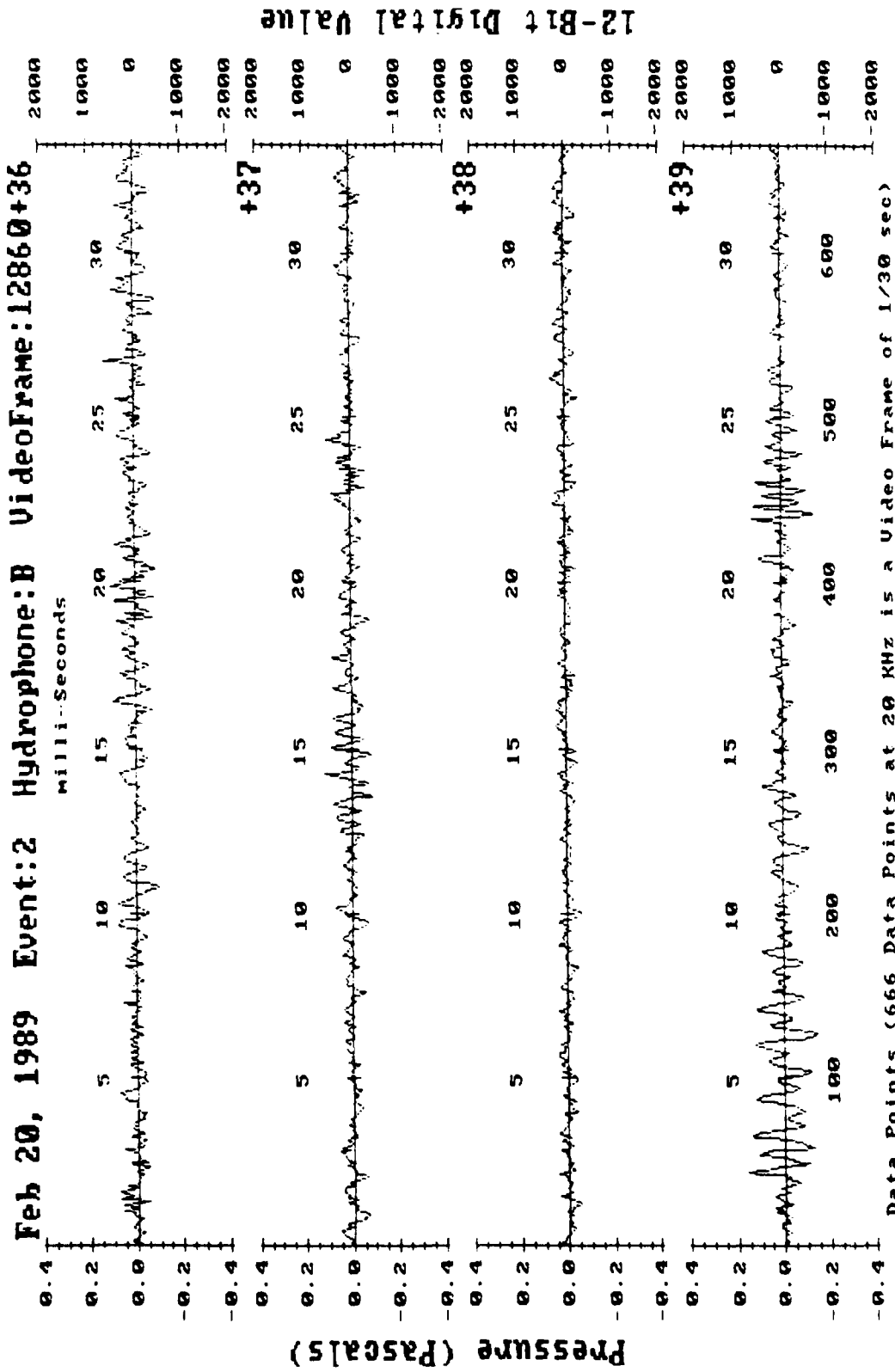
Chapter 3, Figure 3g: Video Frames 12884 to 12887.



Chapter 3, Figure 3h: Video Frames 12888 to 12891.



Chapter 3, Figure 3i: Video Frames 12892 to 12895.

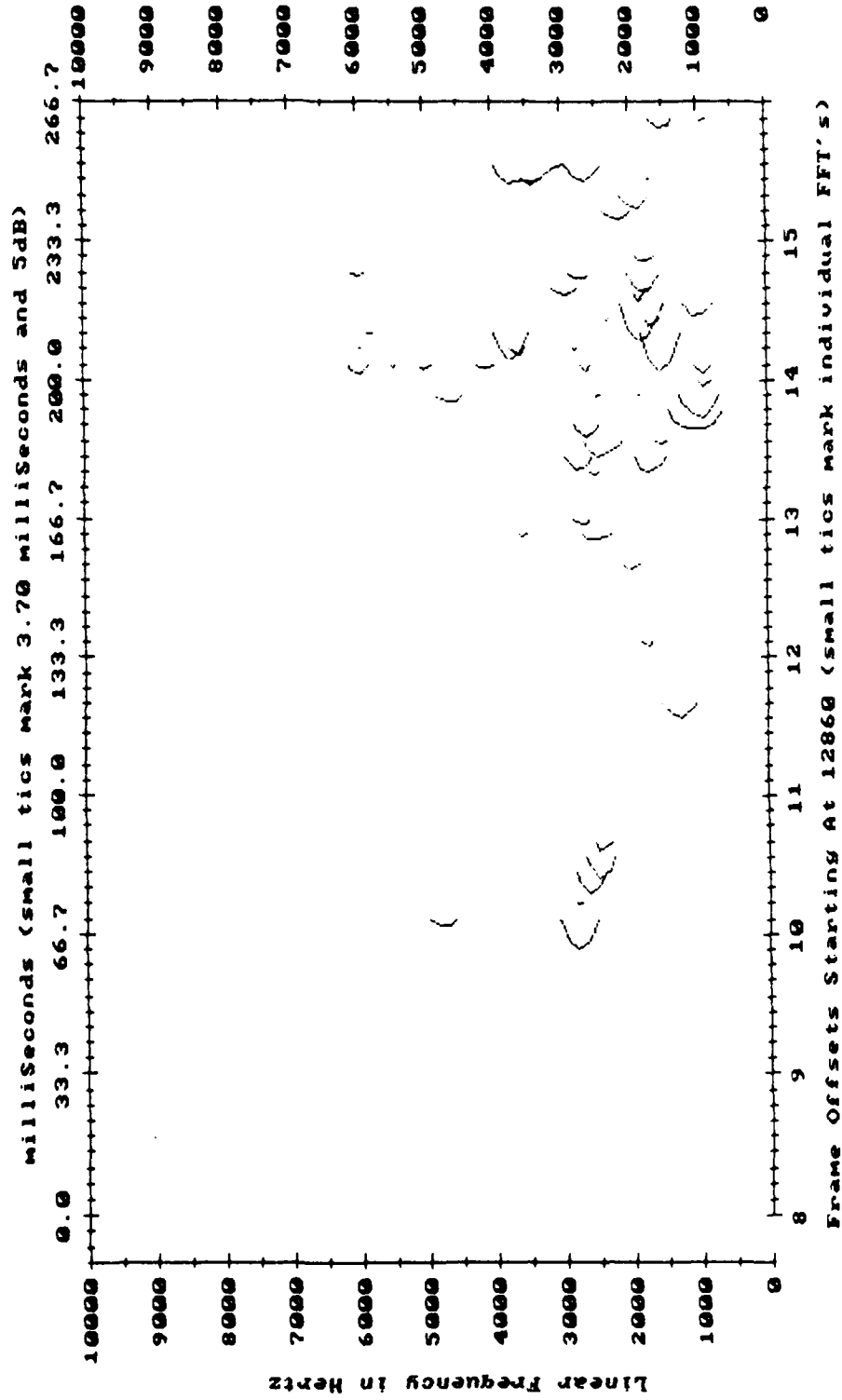


Chapter 3, Figure 3j: Video Frames 12896 to 12899.

Chapter 3, Figures 4a to 4e: Waterfall plot consisting of peaks from individual FFT's of time-series shown in Figure 3.

Feb 20, 1989 Event:2 Hydrophone:B VideoFrames 12860+8 thru +15

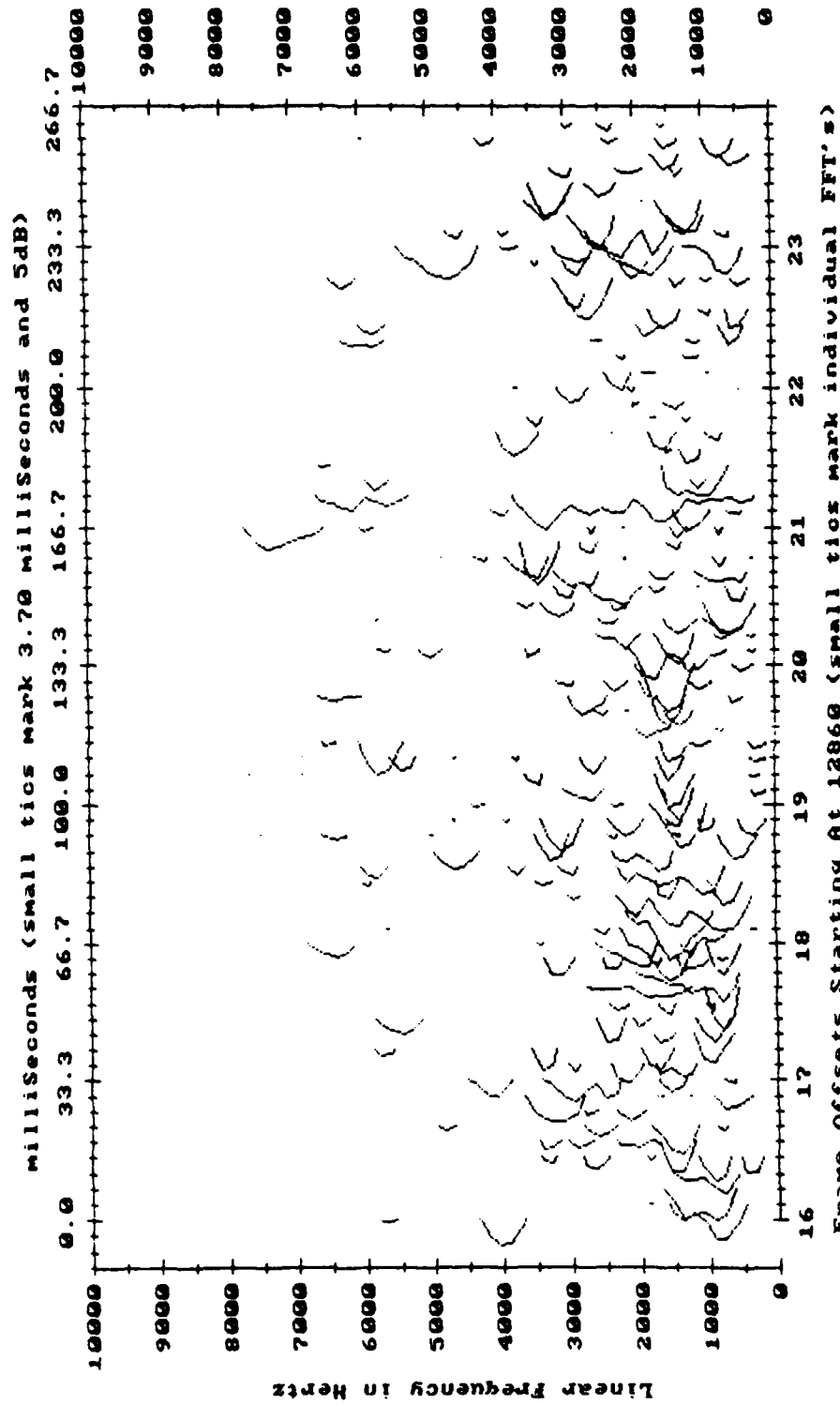
Waterfall Series From Overlapping 128-Point FFT's, 9 Per Frame
Minimum Threshold = 65 dB re 1 μ Pa-squared per Hertz



Chapter 3, Figure 4b: Video Frames 12868 to 12875.

Feb 20, 1989 Event:2 Hydrophone:B VideoFrames 12860+16 thru +23

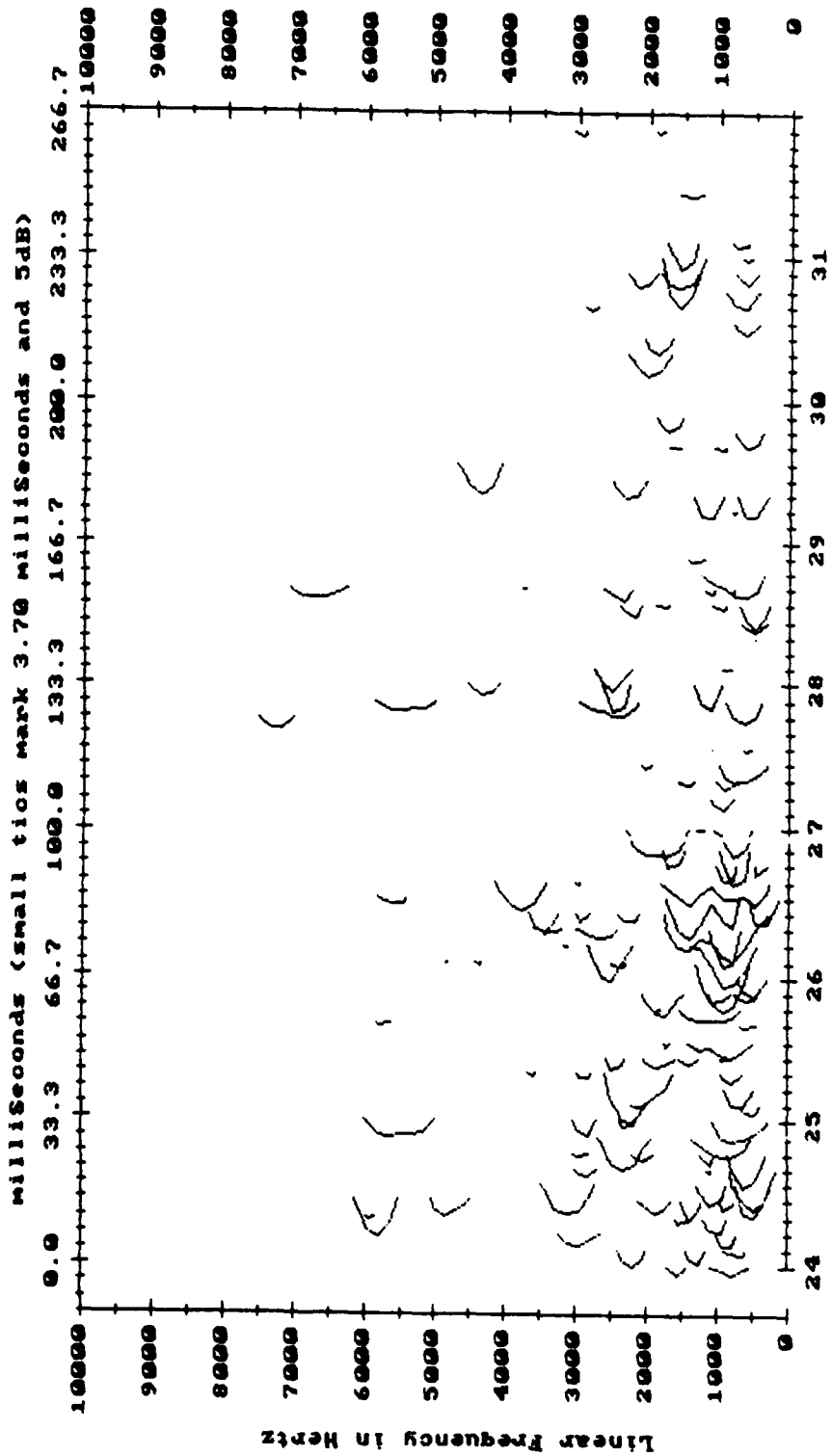
Waterfall Series From Overlapping 128-Point FFT's, 9 Per Frame
Minimum Threshold = 65 dB re 1 μ Pa-squared per Hertz



Chapter 3, Figure 4c: Video Frames 12876 to 12883.

Feb 20, 1989 Event:2 Hydrophone:B VideoFrames 12860+24 thru +31

Waterfall Series From Overlapping 128-Point FFT's, 9 Per Frame
Minimum Threshold = 65 dB re 1 μ Pa-squared per Hertz

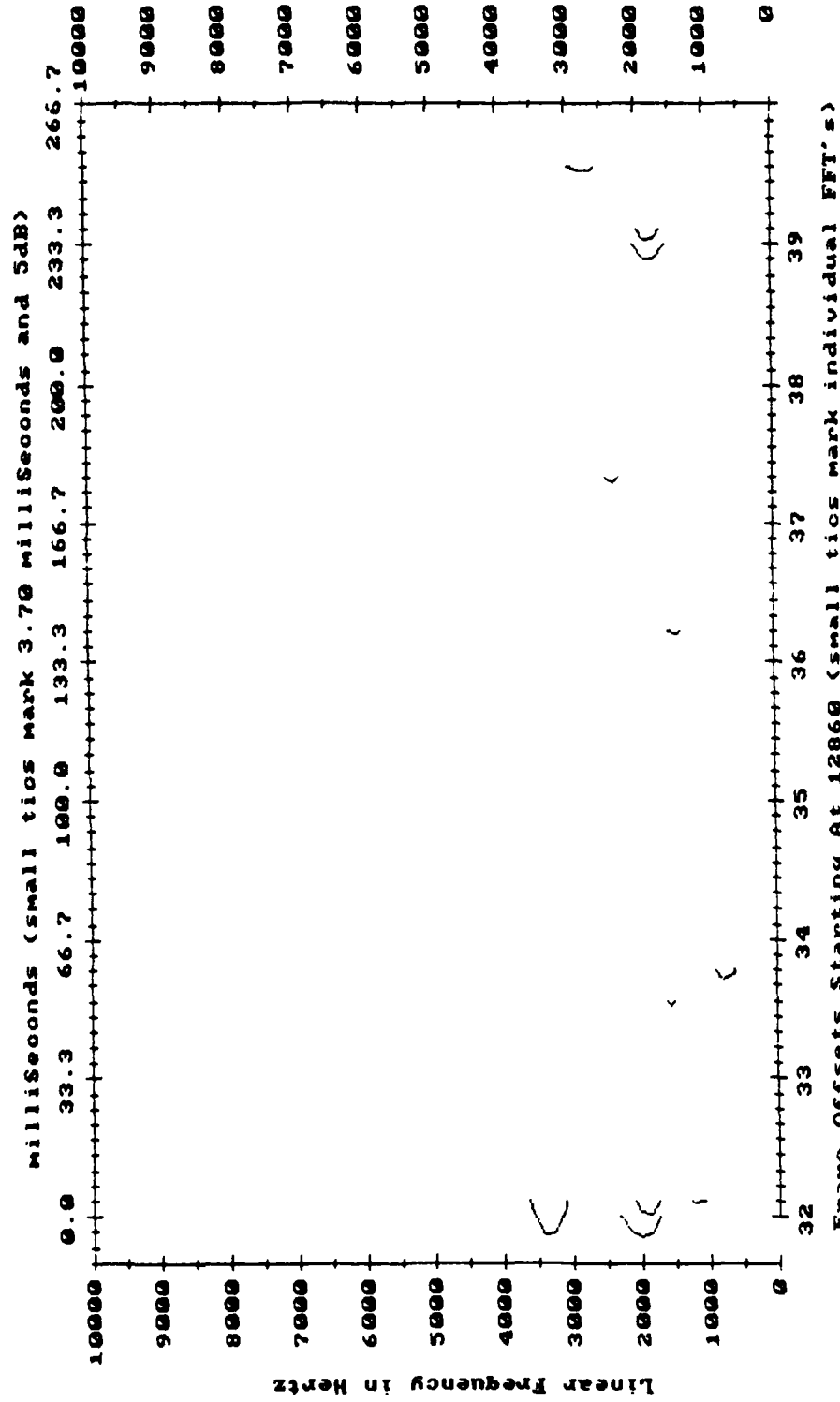


Frame Offsets Starting At 12860 (small ticks mark individual FFT's)

Chapter 3, Figure 4d: Video Frames 12884 to 12891.

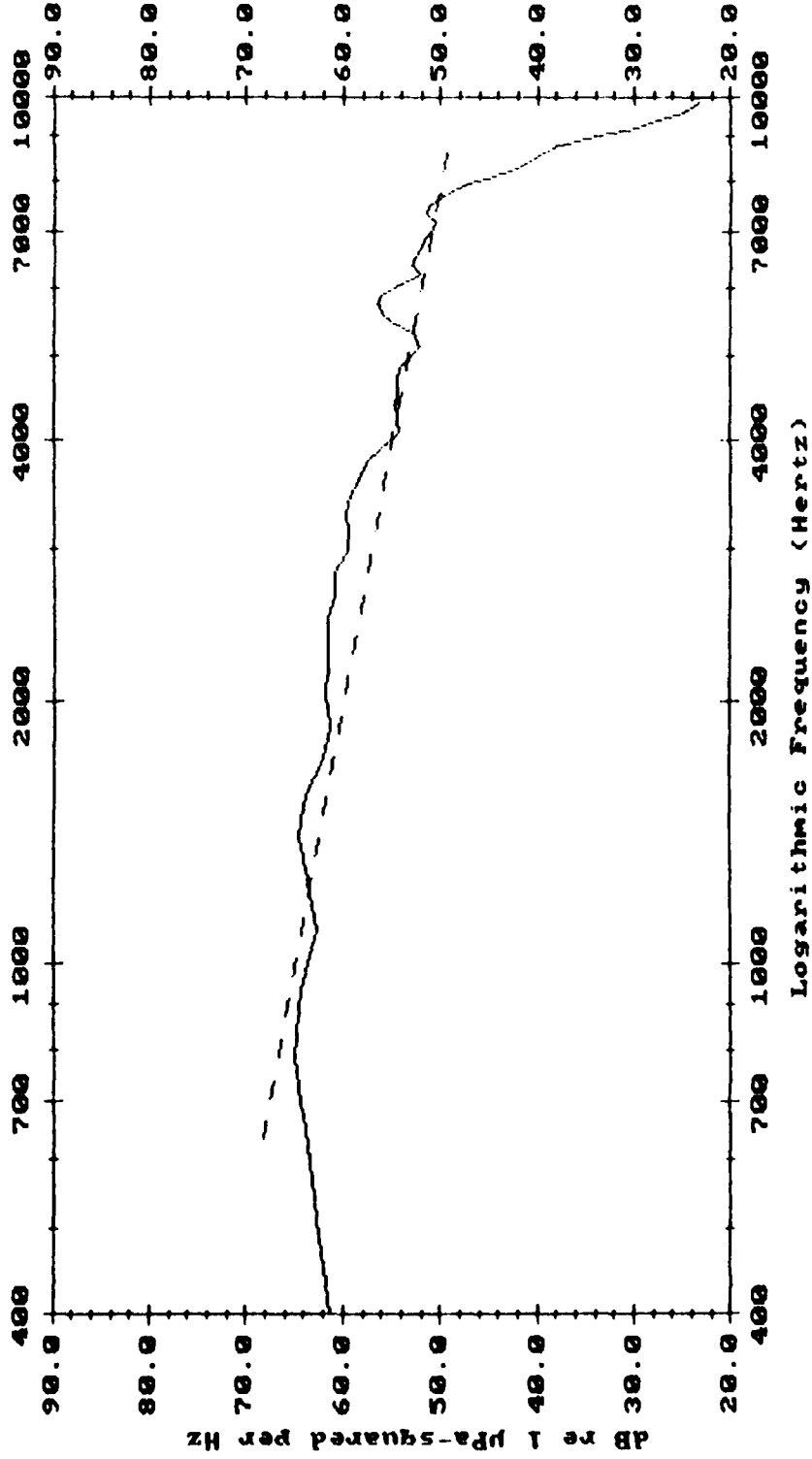
Feb 20, 1989 Event:2 Hydrophone:B VideoFrames 12860+32 thru +39

Waterfall Series From Overlapping 128-Point FFT's, 9 Per Frame
 Minimum Threshold = 65 dB re 1 μ Pa-squared per Hertz



Chapter 3, Figure 4e: Video Frames 12892 to 12899.

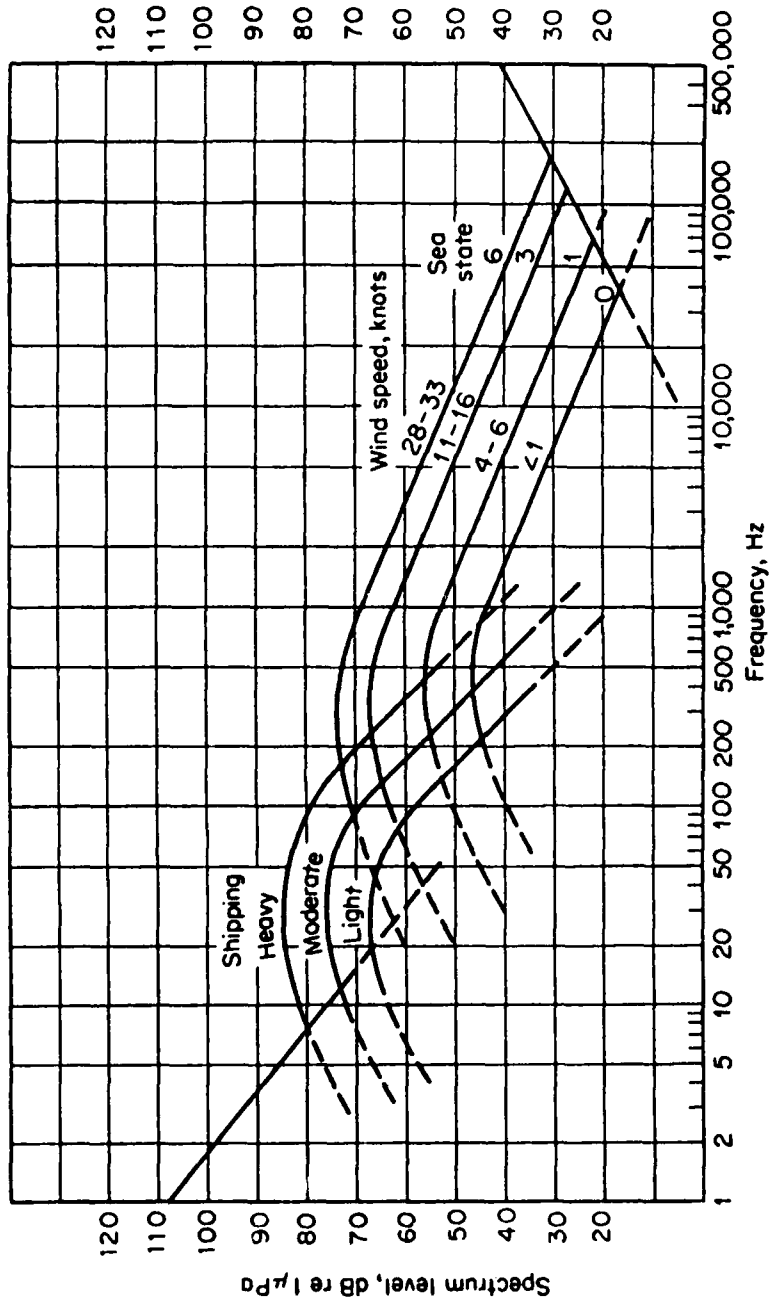
Feb 20, 1989 Event:2 Hydrophone:B VideoFrames: 12860+16 to +28



Average Of 117 128-Point FFT's With Kaiser-Bessel ($\alpha = 3$) Windowing

Chapter 3, Figure 5: Average of FFT's taken from energetic part of Figure 3. SSNI filters attenuated frequencies below 500 and

above 8000 Hertz. The dashed reference line represents -5 dB per octave.



Chapter 3, Figure 6 [from Urlick, 1983]: Average deep water ambient ocean noise spectra.

negative cycle, which could be the result of surface reflection reinforcement. Unfortunately, because the accuracy of our bubble position calculations is about 0.1 to 0.2 meters, we cannot confirm such a depth for the bubbles we have studied. Also, lacking an echo sounder, our instrument is incapable of measuring the surface height variation due to small swells. However, Medwin & Beaky's artificial waves contained bubbles with rise times extending over several cycles, and their Figure 10 plot shows a strong spectral dip between 5,500 and 6,500 Hz, followed by a peak at 7300 Hz, which is similar to our Figure 5 spectrum. They have stated that their bubbles all oscillated within microns to millimeters of the surface, which would be much too shallow to allow cancellations and reinforcements over narrow audible frequency bands. The similarity between their results and ours suggests that our bubbles are likewise ringing very close to the surface. Since their spectral dip takes place approximately 1,000 Hz higher than our valley, perhaps it represents some sort of signature which is indicative of the type and energy of a breaking surface wave.

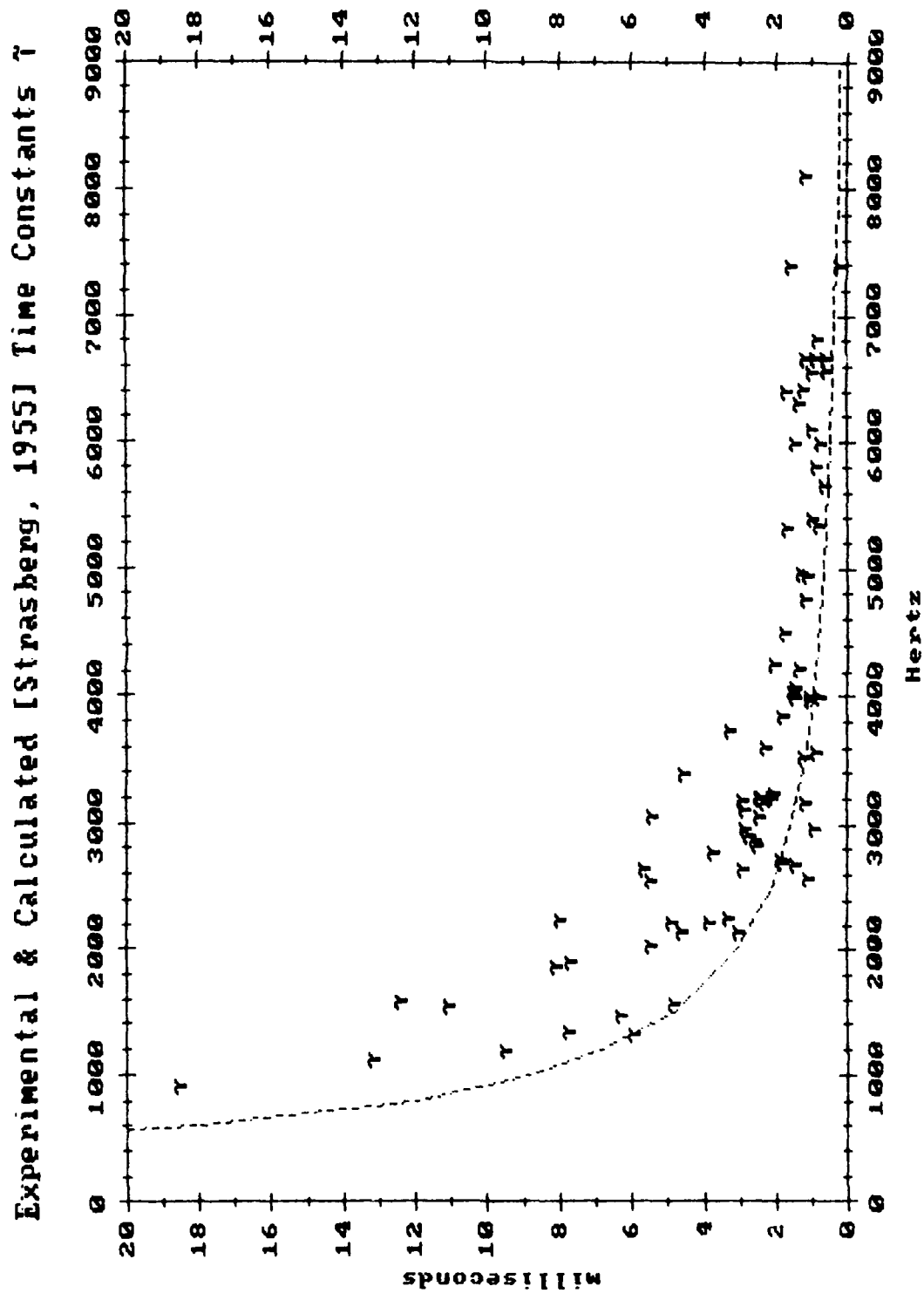
Another explanation for the multiple cycles required for bubble oscillations to reach their peaks is suggested by the dipole effect of Longuet-Higgins, mentioned in Section I, in which bubbles formed at the surface are swept millimeters deeper while ringing, thereby increasing the signal strength at the sensing instrument.

III. INDIVIDUAL OSCILLATION STATISTICS

Since most of the surface spills recorded on February 20, 1989, were composed of distinct bubble oscillations, we have been able to characterize a number of these bubble events from various wavelet breaks as to their relative locations, peak pressures, time-integrated pressures, and exponential decay rates. In all, 81 oscillations were analyzed over 14 breaks during the first 11.5 minutes of the deployment. It should be noted that, in general, only isolated oscillations were analyzed. Overlapping oscillations, or cases in which bubble locations could not be calculated for lack of a distinct start or sufficient amplitude at all four hydrophones, had to be excluded. These restrictions most affected oscillations of less than 1,000 Hertz, where overlaps were more common because of their longer lifetimes.

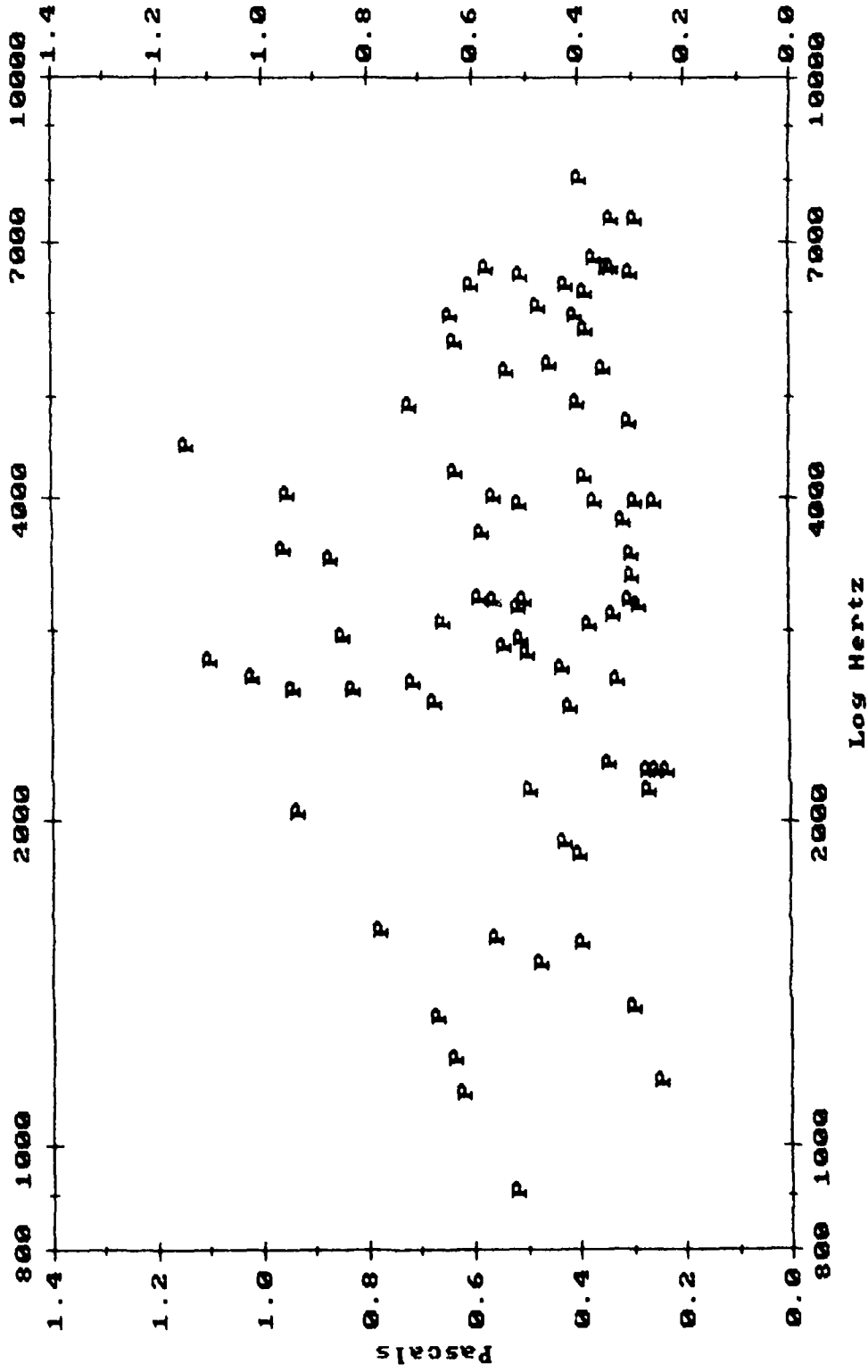
The frequency versus lifetime relationship for these oscillations is displayed as a scatter plot in Figure 7. Each exponential decay time constant τ has been calculated by measuring the average decrement of successive oscillation peaks. The dashed line represents an empirically derived formula by Strasberg [1956] for resonating bubble decay rates. The reasonable match between SSNI data points and the Strasberg curve confirms that the oscillations are bubbles freely oscillating at their resonant frequency. The slightly higher lifetimes of the SSNI data points are probably the result of the measurement technique; steady background noise from the support ship contributed disproportionately to the smaller amplitudes at the end of each oscillation. Another factor may be Longuet-Higgins' dipole effect, described in Section I, in which acoustic damping is reduced for bubbles close to the surface, thereby resulting in longer lifetimes.

Figure 8 shows a scatter plot of the peak source pressures from the 81 oscillations, compensated for spherical spreading to a source distance of 1 meter. Note that the values are well scattered, with no universal trend toward higher pressures at lower frequencies, although there does appear to be a falloff in the highest peaks for frequencies below 3,000 Hz and above 4,000 Hz. We might expect some reduction in acoustic pressures at the higher frequencies due to the gradual shift in the oscillation damping mechanism, as reported by Prosperetti [1988], from mostly acoustic radiation damping for bubbles oscillating lower than 1,000 Hertz, to mostly thermal damping for bubbles oscillating higher than 1,000 Hertz. In any case, the slight difference shown here is obviously insufficient to contribute to the -5 dB per octave falloff of the Knudsen curves.



Chapter 3, Figure 7: Scatter plot of oscillation decay rates versus frequency. The dashed reference line is based on Strasberg's [1955] empirical formulas.

Peak Oscillation Source Pressures For Hydrophone B



Chapter 3, Figure 8: Scatter plot of the peak oscillation pressures from 81 bubble oscillations recorded during 14 small wave breaks.

Oscillation locations have been used to calculate the peak pressures at a distance of 1 meter based on spherical spreading losses.

However, if we consider the overall energy contribution of each bubble, by integrating the square of its pressure over the life of its oscillations, the resulting plot, pictured in Figure 9, shows a fair match with a -5 dB per octave reference line. Thus, rather than a difference in *peak* oscillation pressures, it is the difference in oscillation *lifetimes* for variously sized bubbles that contributes to the observed -5 dB per octave slopes. We can take this analysis a step further by considering an oscillating bubble to be a simple damped sinusoid of resonant frequency f , radiating a pressure at time t :

$$p(t, f) = p_0 \sin(2\pi f t) e^{-t/\tau(f)}$$

p_0 is the peak pressure, and τ is the oscillation decay constant experimentally calculated by Strasberg [1956] to be:

$$\tau(f) = \frac{91,000}{\pi f (f + 1300)} \text{ seconds .}$$

By integrating p^2 from $t = 0$ to infinity, we obtain

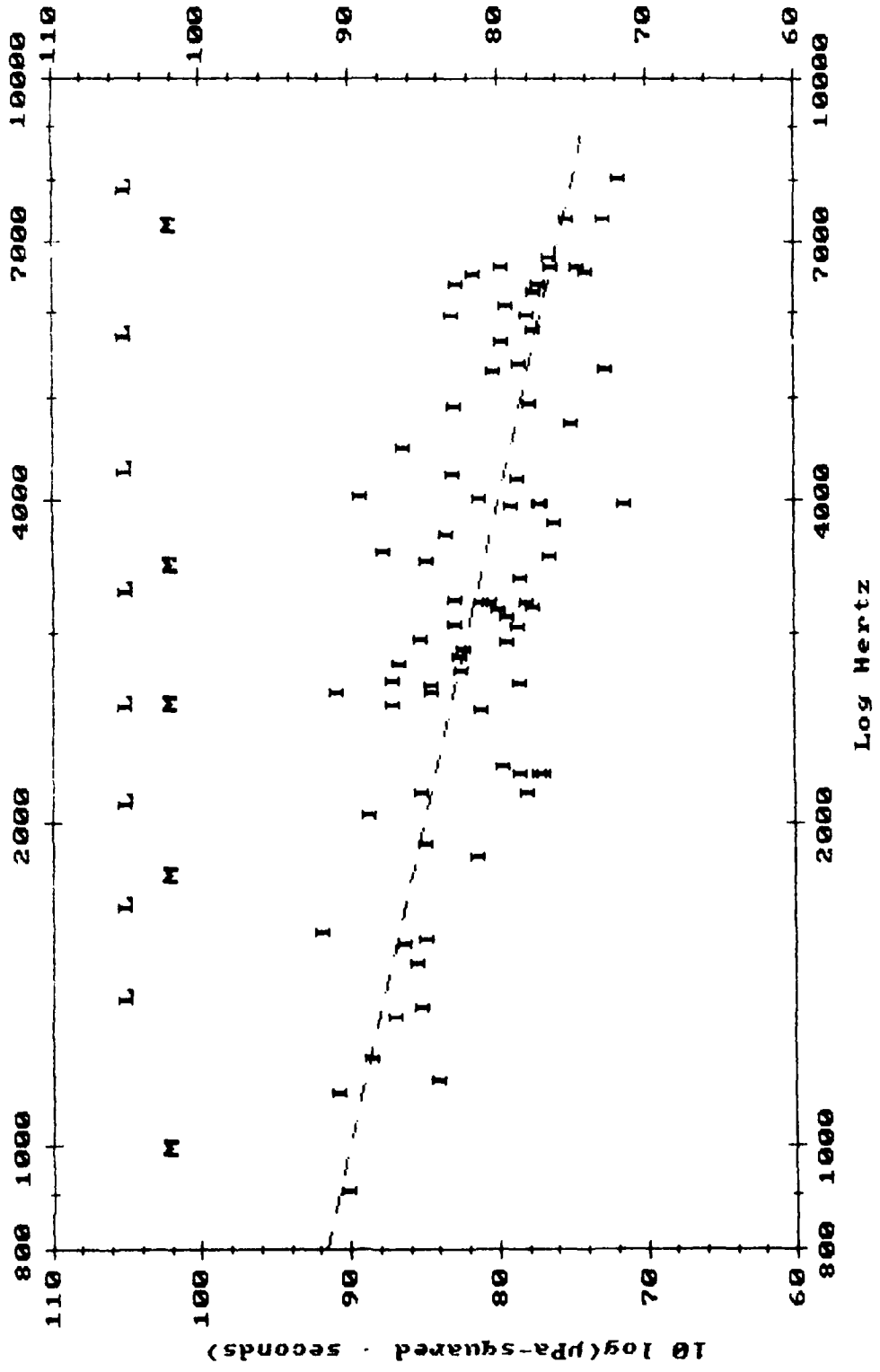
$$I(f) = \frac{p_0^2 \pi^2 f^2 \tau^3(f)}{4\pi^2 f^2 \tau^2(f) + 1}$$

$$\approx \frac{7200 p_0^2}{f(f + 1300)}$$

This is plotted against frequency as a solid line in Figure 10, where p_0 has been estimated at 0.5 Pascals. The dashed -5 dB per octave reference line is at the same level as in Figure 9. We see that the solid line maintains a -5 dB per octave slope for frequencies around 1300 Hz. Lower frequencies generate a slope of -3 dB per octave, while higher values produce a slope of -6 dB per octave. The match between observed data and these calculations, where the acoustic energy from bubbles of different sizes varies only by their oscillation lifetimes, implies that bubbles within wavelet spills are randomly produced on a logarithmic scale.

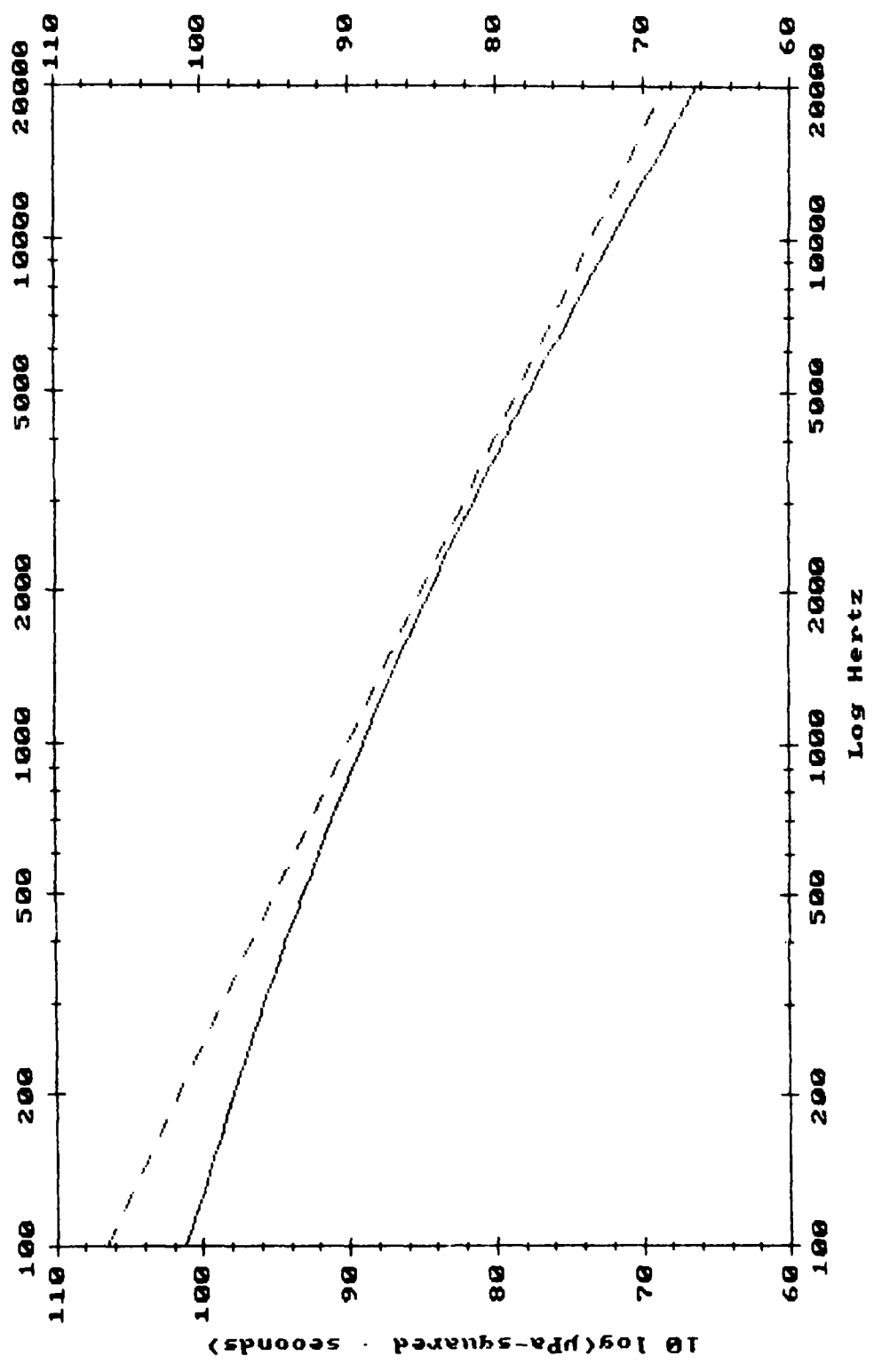
But what causes the bubbles to start ringing when initially entrained? Recently, Longuet-Higgins [1989a] has proposed a mechanism in which it is the non-linear effects of a bubble's distortion as it is pinched off that initiates the resonant frequency oscillations. His theory predicts specific peaks at certain frequencies, and these are marked with the letter "L" along the top of Figure 11. Different peaks were experienced by Medwin & Beaky [1989] for their experimental data, and these have been marked with "M"s. In general, our data does not provide much support for Longuet-Higgins' prediction. In contrast with Medwin & Beaky's results, our limited set of data points shows little consistent peakedness. Instead, most of the oscillations we have analyzed tend to cluster around certain frequencies. However, it should be noted that this apparent clustering may actually represent pressure peaks, with the lack of measured oscillations in between caused by pressure values too low for our analysis. In any case, the only frequencies of possibly common agreement occur at 2,600 Hz and in the neighborhood of 7,000 Hz.

Source Integrated Square-Pressures For Hydrophone B

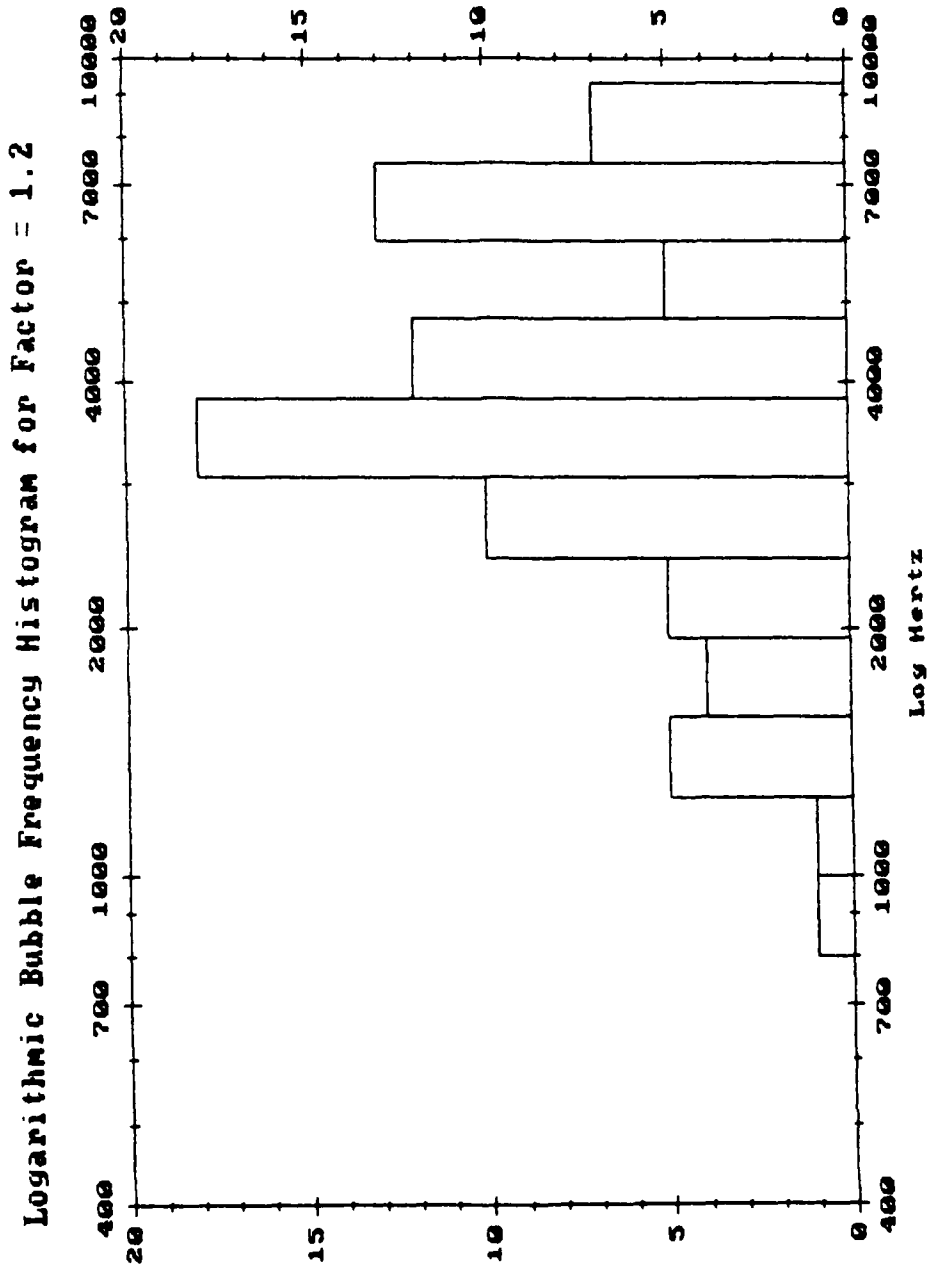


Chapter 3, Figure 9: Scatter plot in which the square pressure has been integrated over the life of each oscillation. The dashed reference line represents -5 dB per octave.

Theoretical Integrated Square-Pressure for Peak Pressures of 0.5 Pa



Chapter 3, Figure 10: Solid line -- Integrated square pressure over life of bubble modelled as simple exponentially decaying sinusoid plotted against resonant frequency. Dashed line -- same -5 dB per octave reference line used in Figure 9.



Chapter 3, Figure 11: Logarithmic histogram of bubble frequency distributions. Outer distributions have been affected by both the SSNI filters, which attenuated frequencies below 500 Hertz and above 8,000 Hertz, and by the rejection of overlapping oscillations, which occurred mostly for frequencies below 1,000 Hertz.

How significant is this clustering? With only 81 points, we are forced to work in broad strokes, but the logarithmic frequency histogram in Figure 11 shows obvious clumping. While noting that the long-lived oscillations below 1,000 Hz were discriminated against in selection, and frequencies below 500 and above 8,000 Hz were filtered out by the instrument, there are obvious octave peaks at 3,400 Hz and 6,800 Hz which are separated by a strong dip at 5,200 Hz. As a measure of consistency, splitting the data into halves based on early and late times within the deployment continues to show the same pattern in each half. Intriguingly, the histogram, which is based on oscillations from a number of wavelet breaks, roughly matches the peaks and valleys of the spectral average in Figure 5, which was based on the single energetic wave break in Figure 3

IV. ENVIRONMENTAL OBSERVATIONS

In addition to video and acoustical data, the SSNI also contains environmental sensors which are recorded 30 times per second. Figure 12 shows the instrument's depth and roll angle, along with the wind speed and direction recorded by the SSNI surface buoy, for a half-hour of data taken June 30, 1988, west of San Diego. The water depth during this deployment was 700 meters. In the plot, the roll sensor is assumed to reflect the instrument's tilt due to the wave trains of long-period swells. Readings from the instrument's pitch angle sensor have been omitted because it is affected by the occasional tug of the instrument's tether. All data in these plots has been averaged into 1-second intervals.

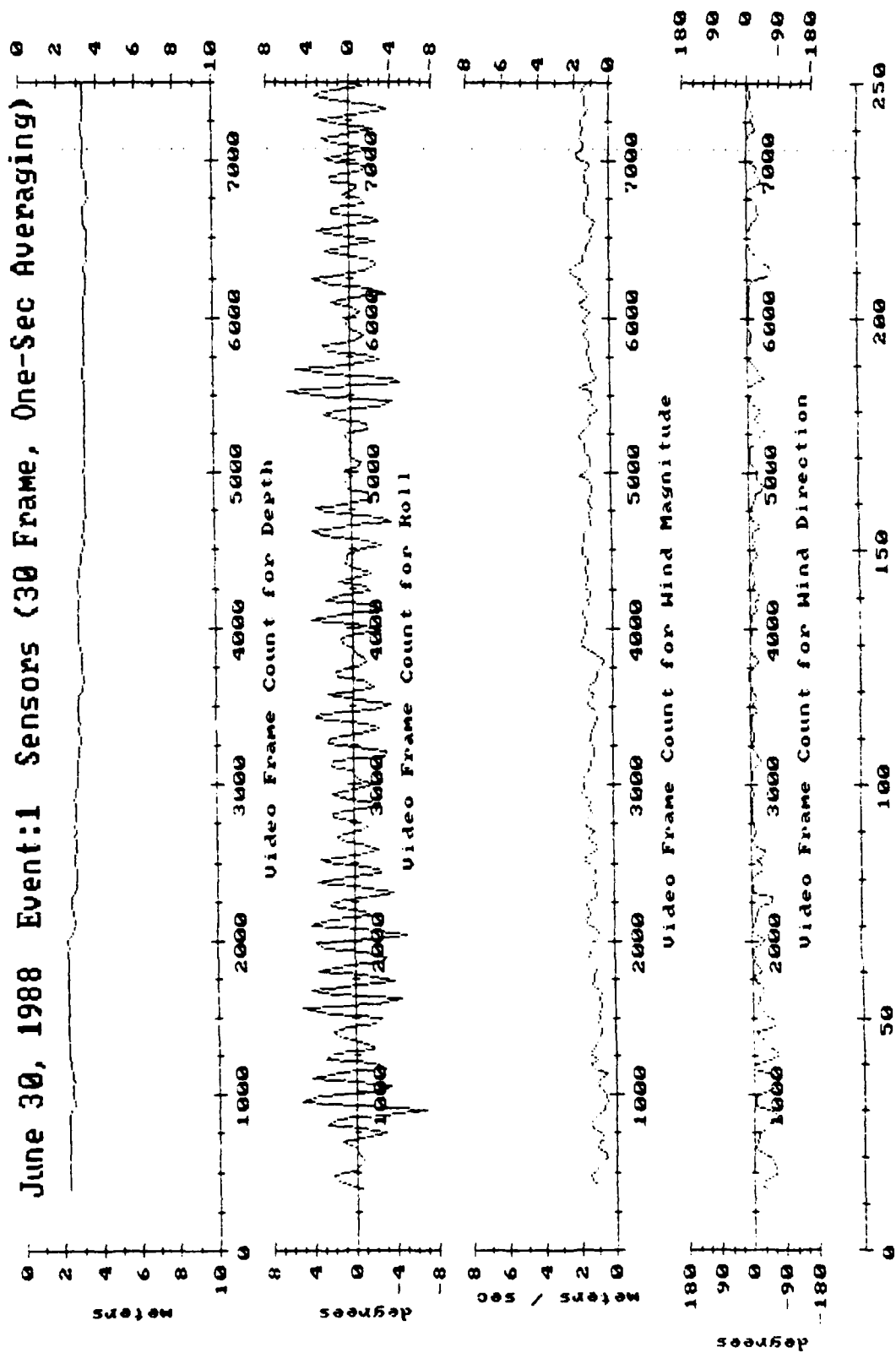
Breaking wavelets, identified by listening to the audio tracks recorded on videotape, have been marked by dashed vertical lines (unfortunately, loud occasional "clunk" noises caused by both instrument's tether attachment and the shifting anchor chain of the barge in this early deployment prevented the use of a more quantitative wave-break measure, such as RMS acoustic pressure). The presence of variable winds and large, 1.5 meter high, 5-second swells, illustrate a pair of observations noted in other SSNI records (see the appendices of Updegraff [1989]):

- 1) Abruptly higher winds do not immediately result in wave breaks.
- 2) The spills, which are associated with small, 1-second swells, do not correlate with the phases or amplitudes of the long-period swells recorded by the instrument's roll sensor.

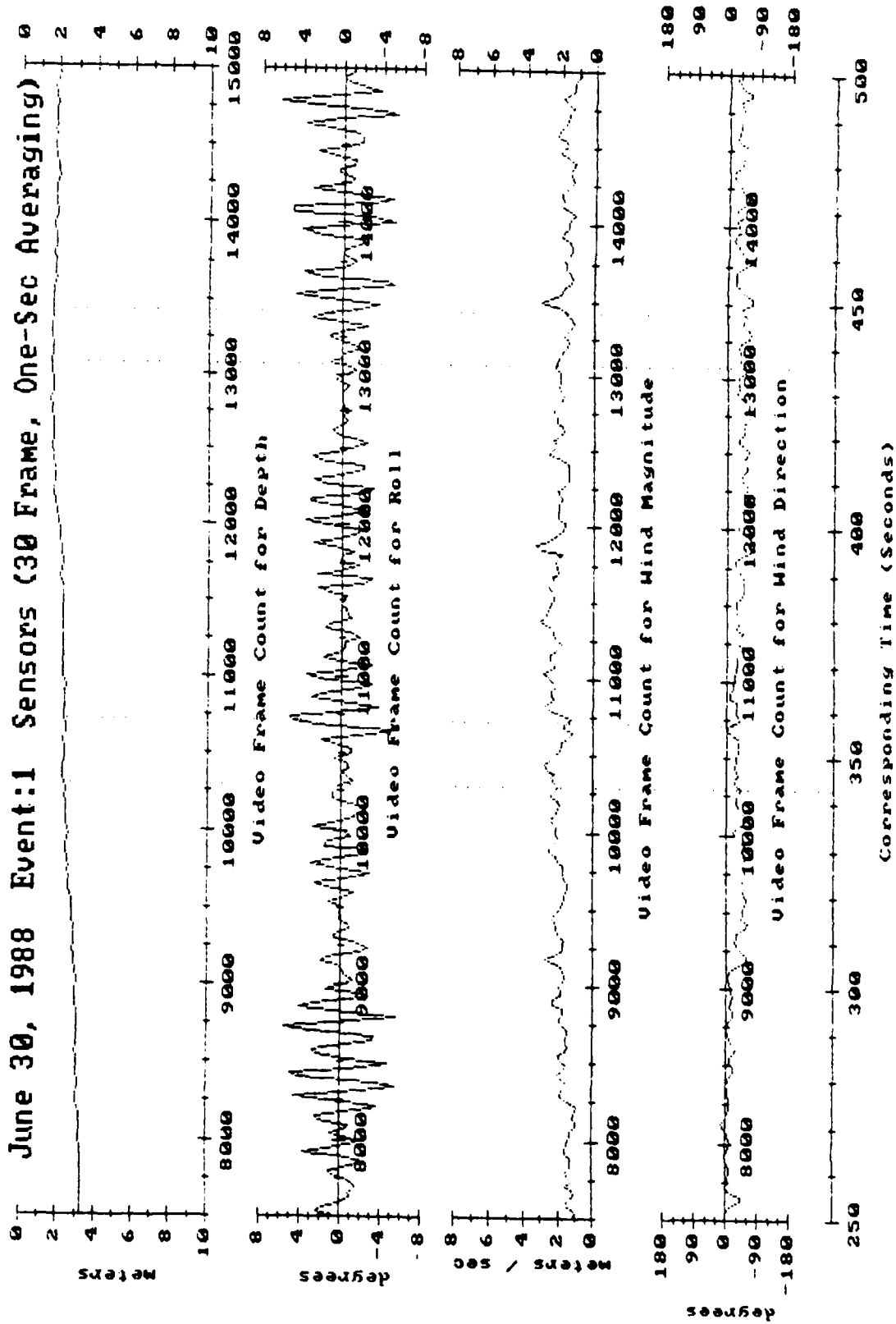
Item (1) suggests that, since there is no instant threshold wind speed that causes immediate wave breaking, winds do not *directly* produce breaks and spills at these low speeds. Rather, winds gradually create the small swells and capillary conditions that cause breaks to occur. Gradual changes in wind speed change the probability that a break will occur within a surface patch. However, while there is no instant wind speed threshold, data taken during the February 20, 1989 deployment *does* indicate a low wind limit for production of spill-causing conditions. During the deployment that included the data in Figures 2 and 3, when winds ranged from 1.5 to 2.1 meters/sec measured 1.5 meters over the water, over 40 wavelet spills were audible during the half-hour recording. One hour later, when a second recording showed winds starting at 1 meter/sec and slowly dropping to nothing over the course of the recording, there was only *one* spill at the very beginning of the deployment.

Given the indirect role that light winds appear to play in wavelet breaks, it is not surprising that Figures 2 and 3 resemble Medwin and Beaky's windless, artificially created wave breaks.

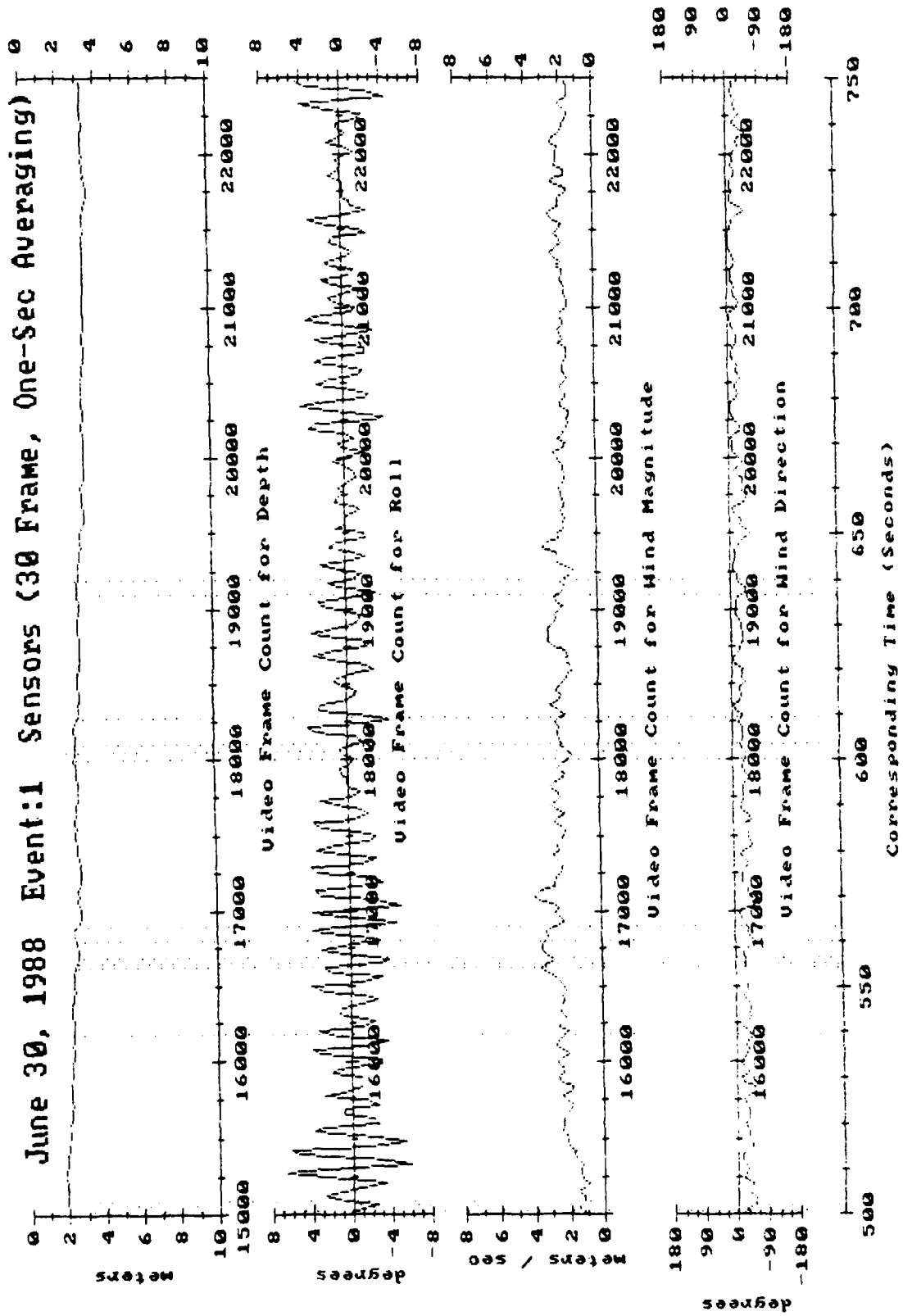
Chapter 3, Figure 12a to 12i: 30 minute time series of instrument environment during deployment on June 30, 1988. Instrument depth is plotted at the top of each page, followed by the instrument roll due to long swells, followed by the speed and direction of winds measured 1.5 meters over the oceans surface with the SSNI Surface Buoy. A time scale is plotted at the bottom. Vertical dashed lines mark wavelet breaks determined from audio playback of videotape.



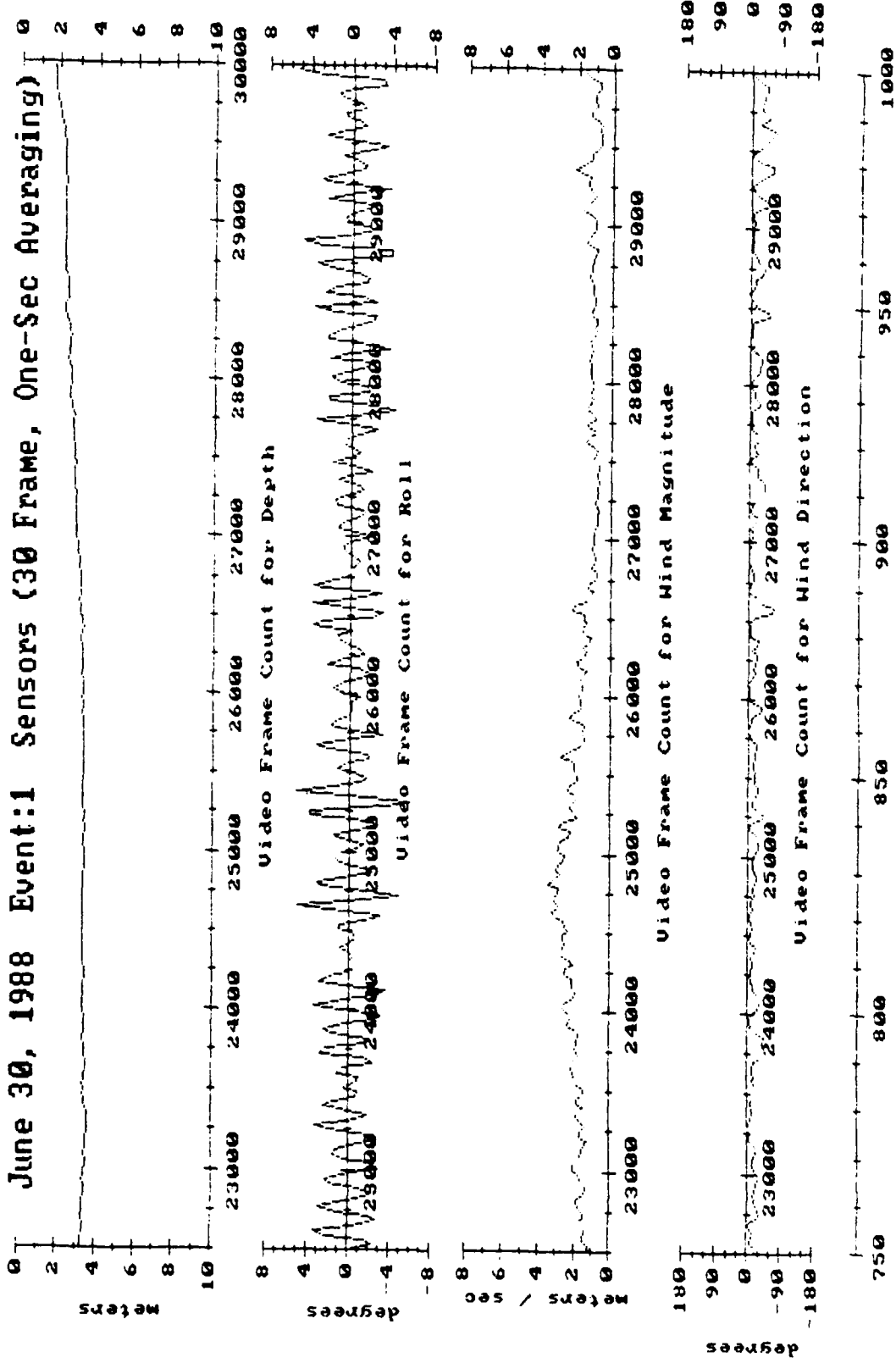
Chapter 3, Figure 12a: Instrument depth and roll, plus nearby wind speed and direction.



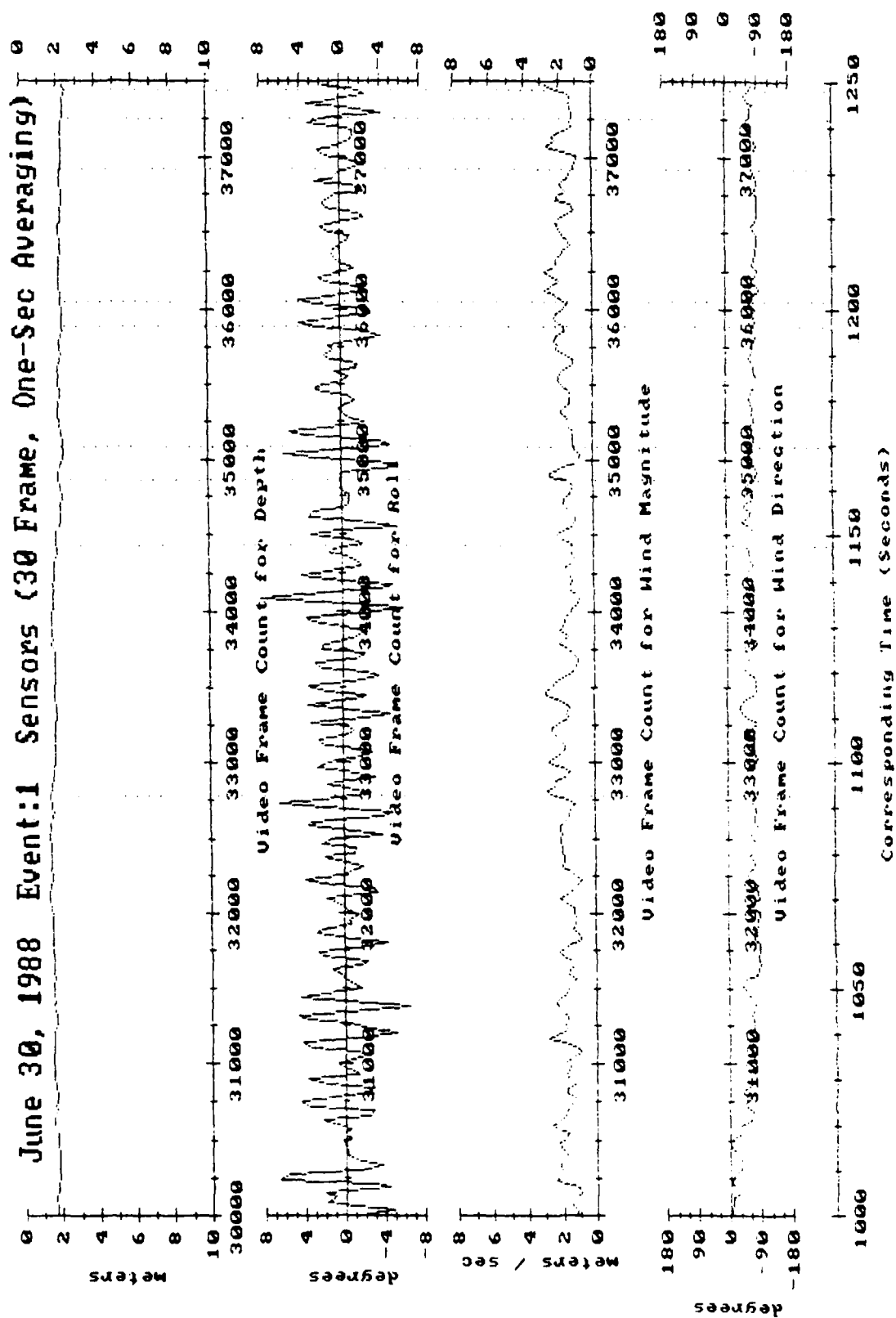
Chapter 3, Figure 12b: Instrument depth and roll, plus nearby wind speed and direction.



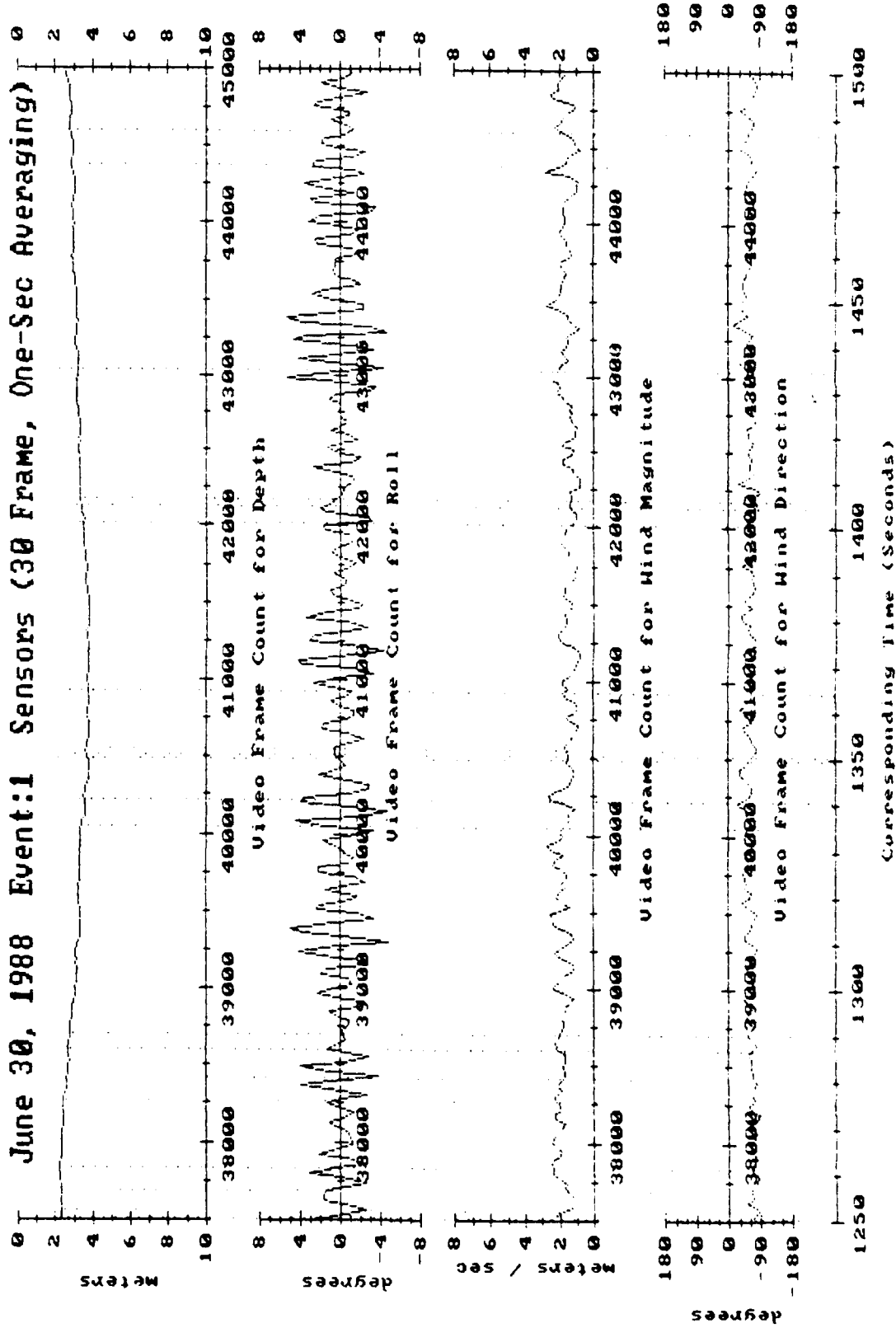
Chapter 3, Figure 12c: Instrument depth and roll, plus nearby wind speed and direction.



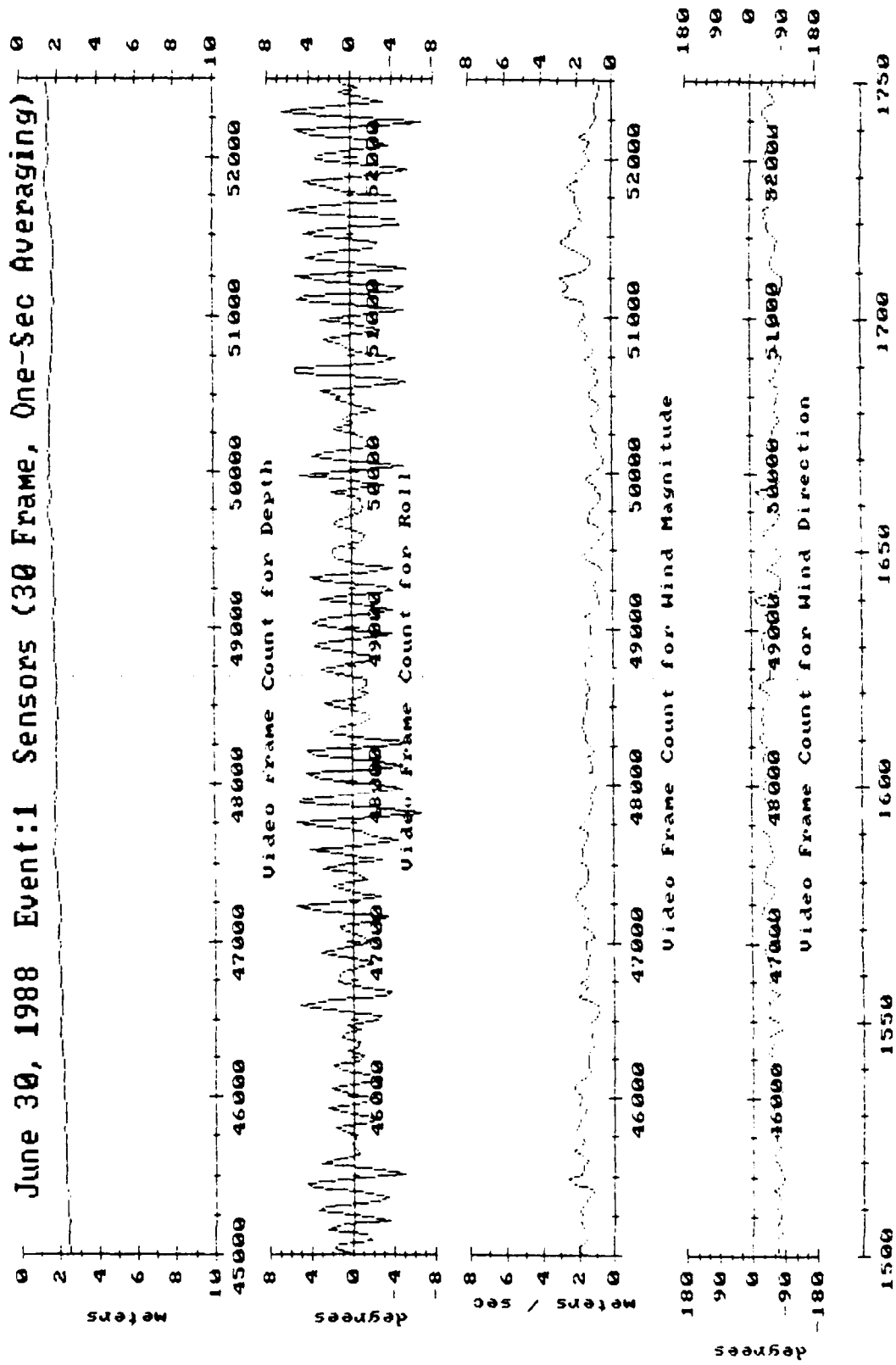
Chapter 3, Figure 12d: Instrument depth and roll, plus nearby wind speed and direction.



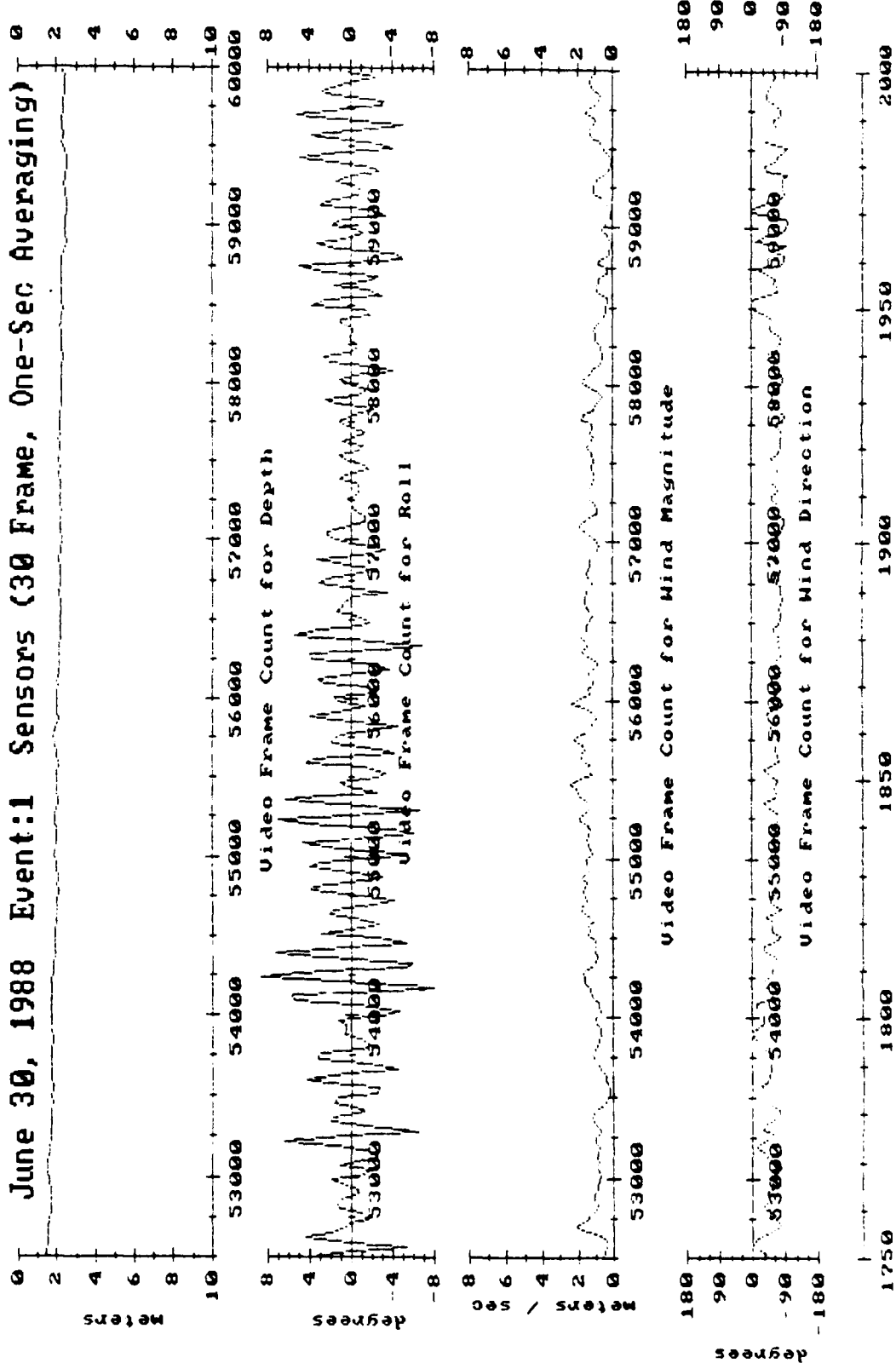
Chapter 3, Figure 12e: Instrument depth and roll, plus nearby wind speed and direction.



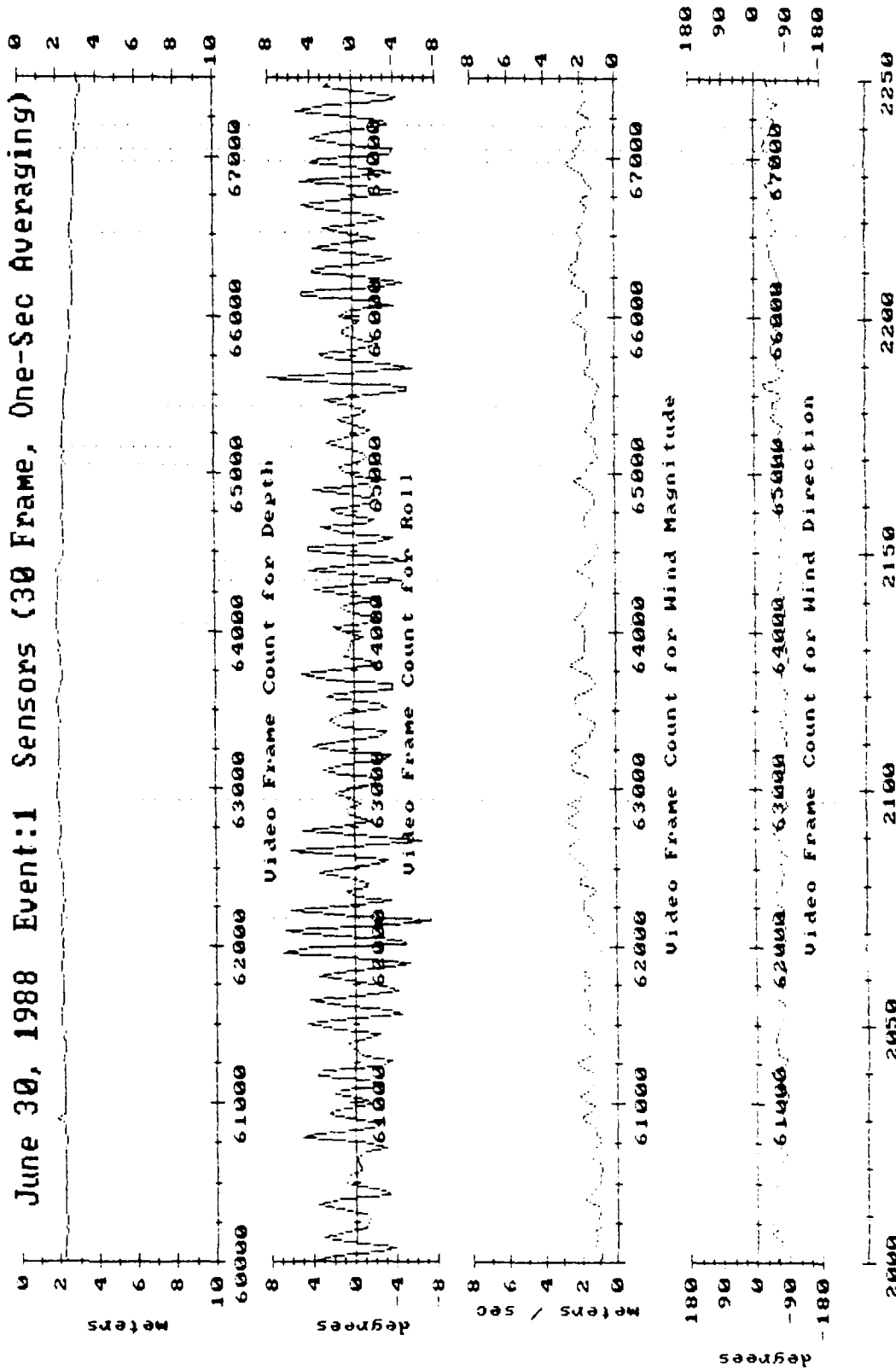
Chapter 3, Figure 12f: Instrument depth and roll, plus nearby wind speed and direction.



Chapter 3, Figure 12g: Instrument depth and roll, plus nearby wind speed and direction.



Chapter 3, Figure 12h: Instrument depth and roll, plus nearby wind speed and direction.



Chapter 3, Figure 12i: Instrument depth and roll, plus nearby wind speed and direction.

Item (2) above indicates that wave breaks in light winds do not couple with long, fast moving swells (in this case, 40 meter swells moving 8 meters per second -- much faster than the prevailing wind speed). Although small, slow swells are undetectable by the SSNI, their effect can be determined indirectly: Some of the wave breaks in Figure 12 occurred in short clusters with individual separations of approximately 1 second. The small, one meter long swells associated with this time period move at about 1.6 meters per second, very close to the prevailing winds measured by the SSNI over the ocean surface. The effect of higher winds was later recorded during a night-time deployment on July 4, 1988, when winds were measured at approximately 7.5 meters per second at the support ship (the SSNI wind buoy maximum speed is 6 meters/sec). At these higher speeds, the predominant long swells (36 meters long moving 7.5 meters per second) detected by the SSNI broke fairly often. Thus, it seems that swells contribute to wave breaks (and therefore to surface noise) only when accompanied by matching or faster moving wind speeds.

CONCLUSION

The SSNI has allowed us to characterize small wave spills in light winds from a depth of 1 to 2 meters. Our results may be summarized as follows:

Wind varying noise from the ocean's surface at low wind speeds is caused by small wavelet breaks and spills. These spills, which bear a striking acoustical resemblance to the artificial wave breaks described by Medwin & Beaky [1989], consist of a number of distinct, approximately millimeter-sized, highly tonal bubble oscillations, which behave like the freely ringing breathing-mode bubbles described by Strasberg [1956]. The bubbles apparently begin ringing during entrainment at peak pressures of roughly 1 Pascal, die out exponentially within milliseconds, and then disappear from the acoustic record. Unless they are somehow split, bubbles are not acoustically recycled. However, oscillation distortions at the end of one of our more energetic wave breaks may have been caused by the passive acoustic scattering of previously entrained bubbles.

The -5 dB per octave surface noise slope of the Knudsen curves is the result of the longer lifetimes of larger bubbles, which allows them to generate noise for longer periods than their high frequency brethren. Peak pressures of individual oscillations are well scattered and do not vary appreciably with bubble frequency over the range of the instrument. The spectral average of a single energetic break, measured from a distance of 2.5 to 3 meters and containing numerous overlapping oscillations, matched the Knudsen curves at the Sea State 4 or 5 level. However, because such surface breaks are widely scattered at low sea states, a hydrophone at great depth would record a much lower average value for a large sea surface area.

81 individual oscillations were analyzed. Integrating the square of the oscillation pressures over their lifetimes, as a measure of their energy contributions at their resonant frequencies, roughly matched the -5 dB per octave Knudsen curves. The integrated pressures provided little support for Longuet-Higgins' [1989a] theory concerning breathing mode oscillations caused by the non-linear effects of bubble distortion during initial formation. A histogram of the measured bubble frequencies indicated most measured bubbles tended to occur at 3,200 and 7,000 Hz (400 Hertz), while very few occurred around 5,200 Hz. These two peaks and the valley correlated well with the spectral average of the energetic wave break described in the previous paragraph. Medwin & Beaky's data showed a strong spectral dip at roughly 6,000 Hz, suggesting that the dip may be indicative of the energy and type of a breaking wave. This idea, however, requires additional investigation.

Long period swells, measured by a tilt sensor in the submerged instrument, showed no phase or amplitude correlation with wave breaks in light winds. In general, swells appear to contribute to wave

breaks only when moving at speeds equal to or less than the prevailing winds. An overall low wind limit for wavelet breaks is suggested by a half-hour deployment in winds equal to or less than 1.5 meters per second, where only one audible spill was generated. However, sudden increases in wind speed during other deployments at higher wind levels did not result in immediate increases in wave breaks. Apparently, moderate winds indirectly cause wave breaks by gradually generating the swells and capillary waves which cause small spills to occur.

Additional plots of wave breaks and environmental conditions are contained in the appendices of Updegraff [1989].

ACKNOWLEDGMENTS

This project was supported under Office of Naval Research Contract Number N00014-87-K-0010.

We wish to thank Jim Rohr of the Naval Ocean Systems Center (NOSC) for his assistance during deployments and analysis, and for his help in securing ship time for the data collected in February, 1989, through the Independent Research Program at NOSC. We would also like to thank Michael Longuet-Higgins of the University of Cambridge, currently at the Center for Studies of Nonlinear Dynamics, in La Jolla, California, for his analysis suggestions.

LIST OF REFERENCES IN CHAPTER 3

- Banner, M. L. and D. H. Cato, 1988. "Physical Mechanisms of Noise Generation by Breaking Waves -- A Laboratory Study", from *Sea Surface Sound*, 429-436, Kluwer Academic Publishers, edited by B. R. Kerman.
- Crighton, D. G. and J. E. Ffowcs Williams, 1969. "Sound Generation by Turbulent Two-Phase Flow", *J. Fluid Mech.* 36(3), 585-603.
- Franz, G. J., 1959. "Splashes as Sources of Sound in Liquids", *J. Acoust. Soc. Amer.* 31(8), 1080-1096.
- Harris, F. J., 1978. "On the Use of Windows for Harmonic Analysis with the Discrete Fourier Transform", *Proc. of the IEEE* 66(1), 51-83.
- Knudsen, V. O., R. S. Alford, and J. W. Emling, 1948. "Underwater Ambient Noise", *J. Mar. Res.* 7, 410-429.
- Longuet-Higgins, M. S., 1989a. "Monopole Emission of Sound by Asymmetric Bubble Oscillations", *J. Fluid Mech.* 201, 525-565.
- Longuet-Higgins, M. S., 1989b. "Bubble Noise Spectra", submitted to *J. Acoust. Soc. Amer.* in May, 1989.
- Minnaert, M., 1933. "On Musical Air-Bubbles and the Sounds of Running Water", *Phil. Mag.* 16, 235-248.
- Medwin, H. and M. M. Beaky, 1989. "Bubble Sources of the Knudsen Sea Noise Spectra", *J. Acoust. Soc. Amer.* 86(3), 1124-1130.
- Prosperetti, A., 1988. "Bubble Dynamics in Oceanic Ambient Noise", from *Sea Surface Sound*, Kluwer Academic Publishers, edited by B. R. Kerman.
- Pumphrey, H. C., L. A. Crum, L. Bjorno, 1988. "Underwater Sound Produced by Individual Drop Impacts and Rainfall", *J. Acoust. Soc. Amer.* 85(4), 1518-1526.
- Strasberg, M. 1956. "Gas Bubbles as Sources of Sound in Liquids", *J. Acoust. Soc. Amer.* 28(1), 20-26.
- Updegraff, G. E., 1989. "In Situ Investigation of Sea Surface Noise From a Depth of One Meter", Ph.D. dissertation, Scripps Institution of Oceanography, U.C. San Diego, CA 92093.
- Urick, R. J., 1983. *Principles of Underwater Sound for Engineers*, (3rd edition), McGraw-Hill, New York.
- Wenz, G. M., 1962. "Acoustic Ambient Noise in the Ocean: Spectra and Sources", *J. Acoust. Soc. Amer.* 34(12), 1936-1956.

Appendix A:

30-Minute Environmental Time Series

Each plot in this appendix displays approximately thirty minutes of one-second averages of the Synoptic Surface Noise Instrument's (SSNI) sensor values during a deployment. Among the sensors displayed are the SSNI's depth, roll angle, wind speed and direction, and the mean square acoustic pressure at Hydrophone B in decibels. The roll angle of the submerged instrument is assumed to represent the tilt of the instrument due to long swells. Swells with lengths of less than two meters do not tilt the instrument enough to be measured. The vertical tilt angle perpendicular to the roll, measured by the pitch sensor, is omitted because it is affected by the occasional tugs on the instrument's tether.

In some cases, only the wind speed in one direction is displayed because one of the two perpendicular wind sensors failed in the surface buoy. These records have been included to illustrate the non-correlation between long, fast moving swells and wavelet breaks.

During the deployments in June and July, 1988, the tether attachment cable and the barge anchor generated a number of spurious "clanks" and "clunks" which were recorded by the submerged instrument's hydrophones. For this reason, wavelet breaks have been marked in these plots with dashed vertical lines, based upon careful listening of the videotape stereo record. Although this offers no measure of the strength of a spill, it does provide a measure of the number of spills taking place for a given set of conditions.

Although a low steady background noise from the support ship was recorded during the deployments on February 20, 1989, the random clunk noises were virtually absent. Thus, these records contain more meaningful Mean Square Acoustic Pressure plots instead of dashed vertical lines, and the occasional non-water sounds are individually marked. Because the data during these deployments was not pre-whitened by the instrument, the wave breaks tend to show more energy than in the 1988 deployments.

I. ENVIRONMENTAL RECORD FROM JUNE 30, 1988

This record is displayed in Chapter 5, Figure 12, pages 102-111.

The data was recorded at 12:55 pm, PST, at latitude 32° 29' and longitude 118° 29', west of San Diego. The surface conditions were about Sea State 1. The wind was blowing from roughly 180 degrees at approximately 1 to 3 meters per second, as measured 1.5 meters over the sea surface by the SSNI wind buoy. Swells with a period of 6 seconds and height of 1.5 meters were moving roughly towards 90 degrees.

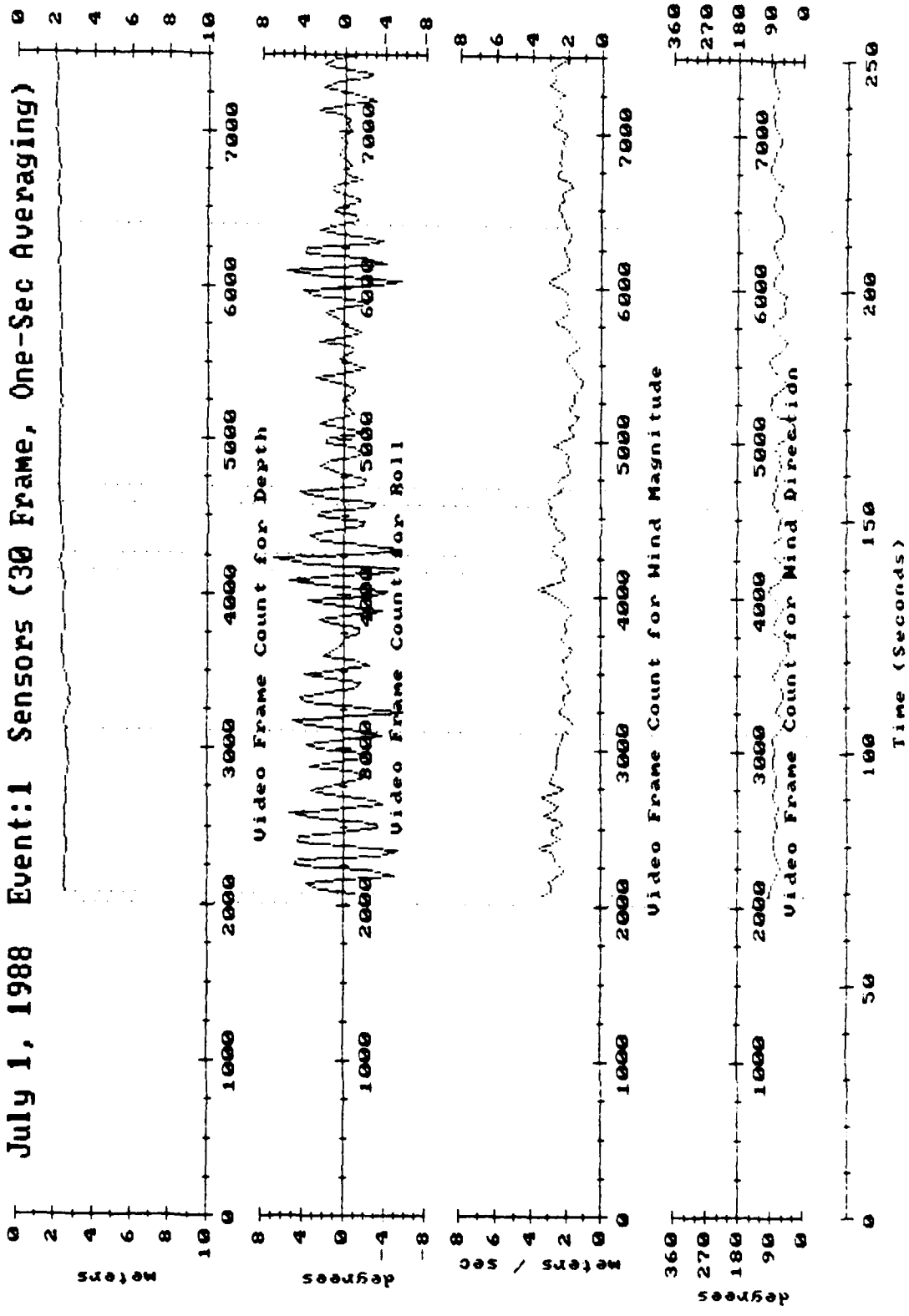
Due to the number and intensity of spurious background noises from the instrument's attachment tether, the mean square acoustic pressure has not been plotted. Wavelet breaks have been marked by dashed vertical lines.

II. ENVIRONMENTAL RECORD FROM JULY 1, 1988

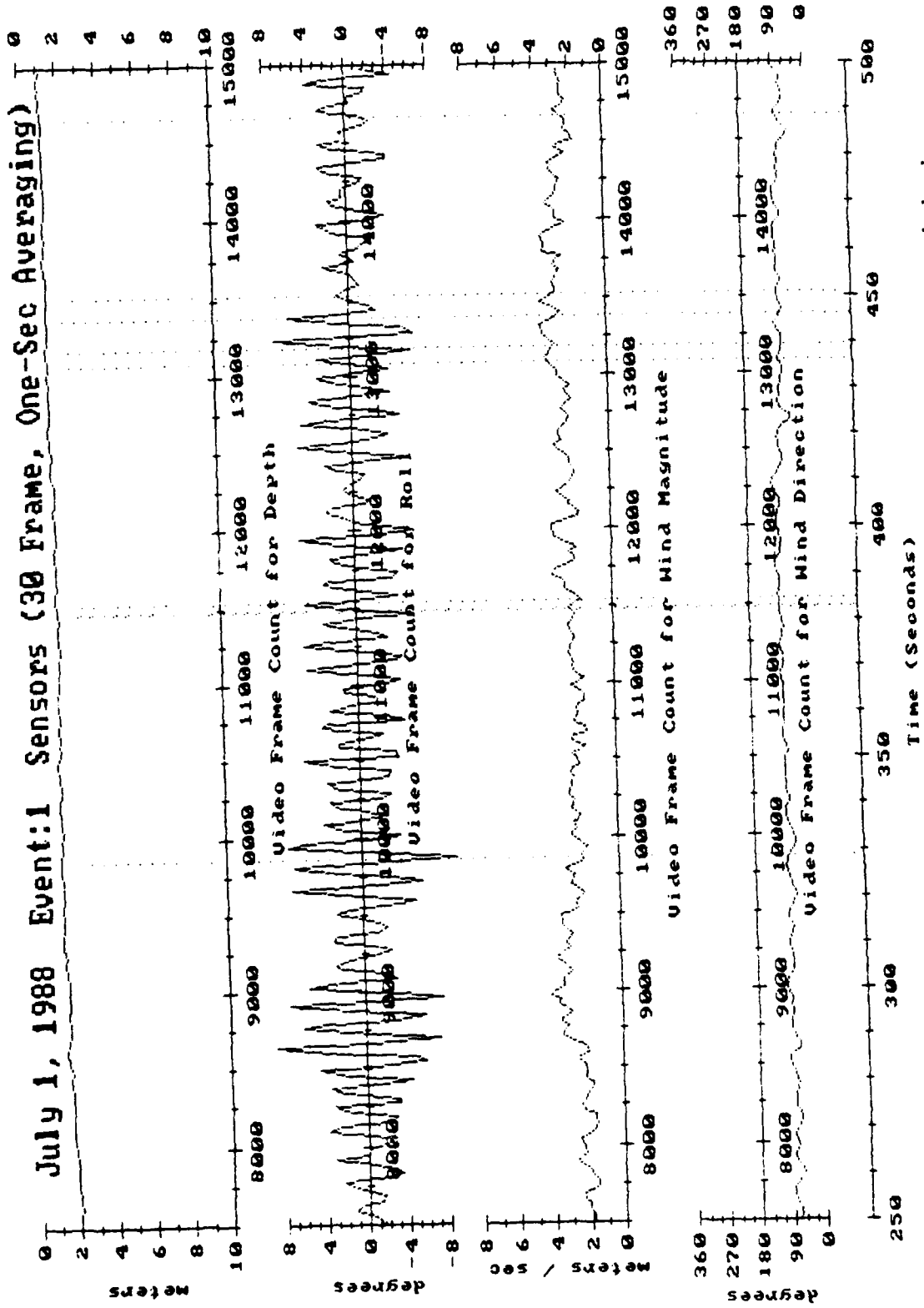
This record is plotted starting on the next page.

The data was recorded at 1:57 pm, PST, at latitude 32° 29' and longitude 118° 29', west of San Diego. The surface conditions ranged from Sea State 0 to 1. The wind was blowing from roughly 250 degrees at approximately 2 to 3.5 meters per second, as measured 1.5 meters over the sea surface by the SSNI wind buoy. Swells with a period of 7 seconds and height of 0.8 meters were moving roughly towards 50 degrees.

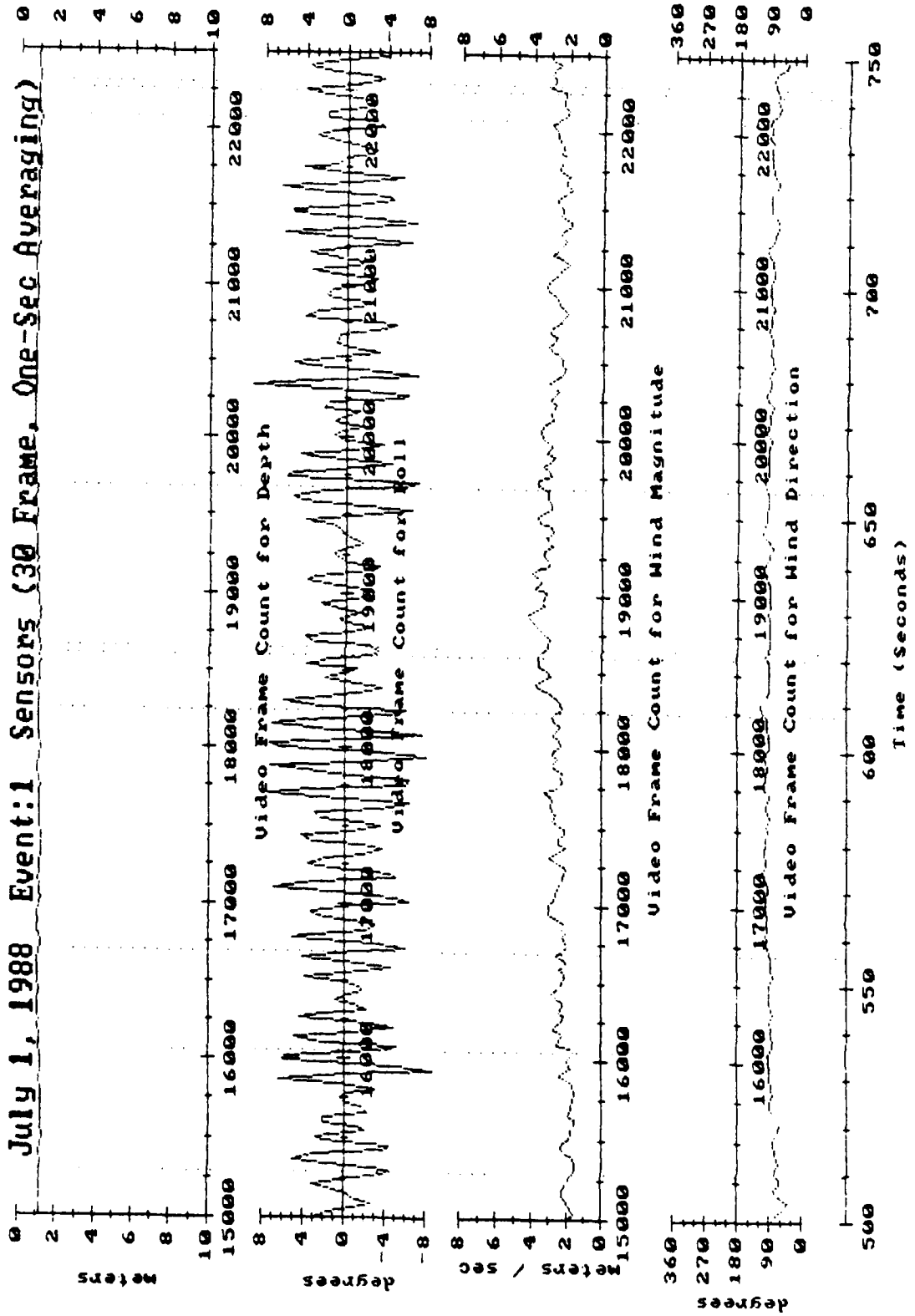
Due to the number and intensity of spurious background noises from the instrument's attachment tether, the mean square acoustic pressure has not been plotted. Wavelet breaks have been marked by dashed vertical lines.



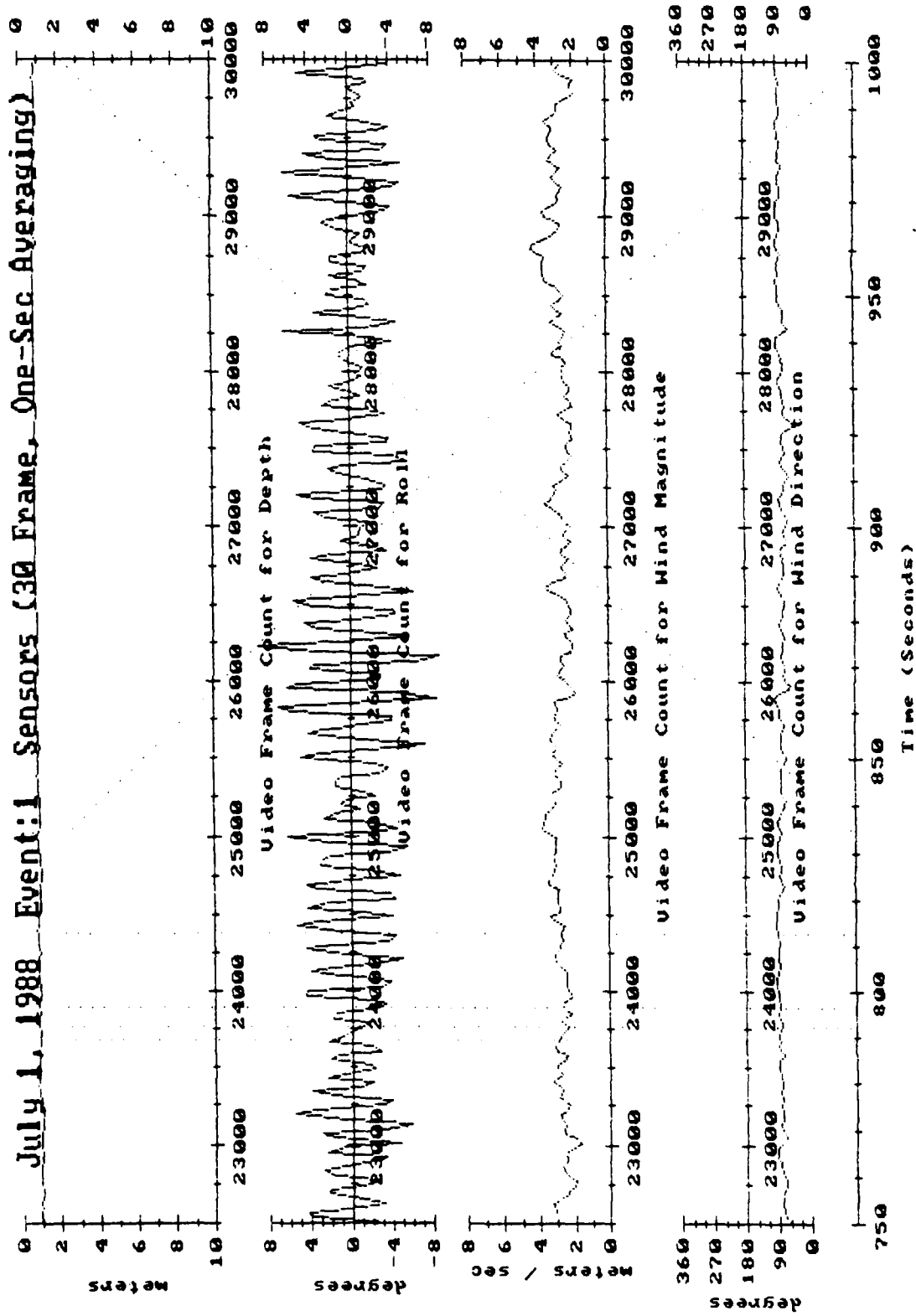
Appendix A, Figure 1a: Instrument depth and roll, plus nearby wind speed and dir. Vertical dashed lines mark wavelet breaks.



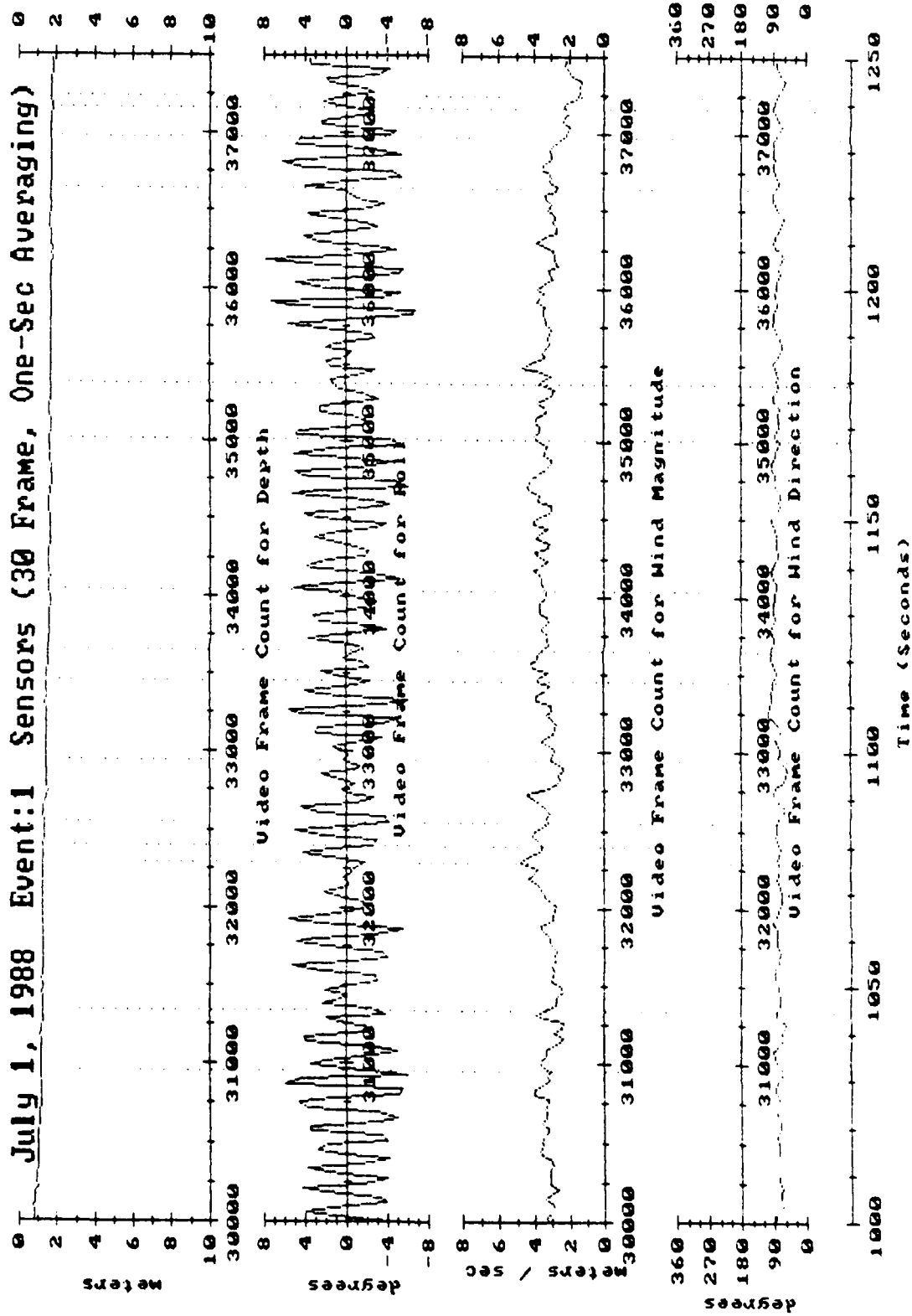
Appendix A, Figure 1b: Instrument depth and roll, plus nearby wind speed and dir. Vertical dashed lines mark wavelet breaks.



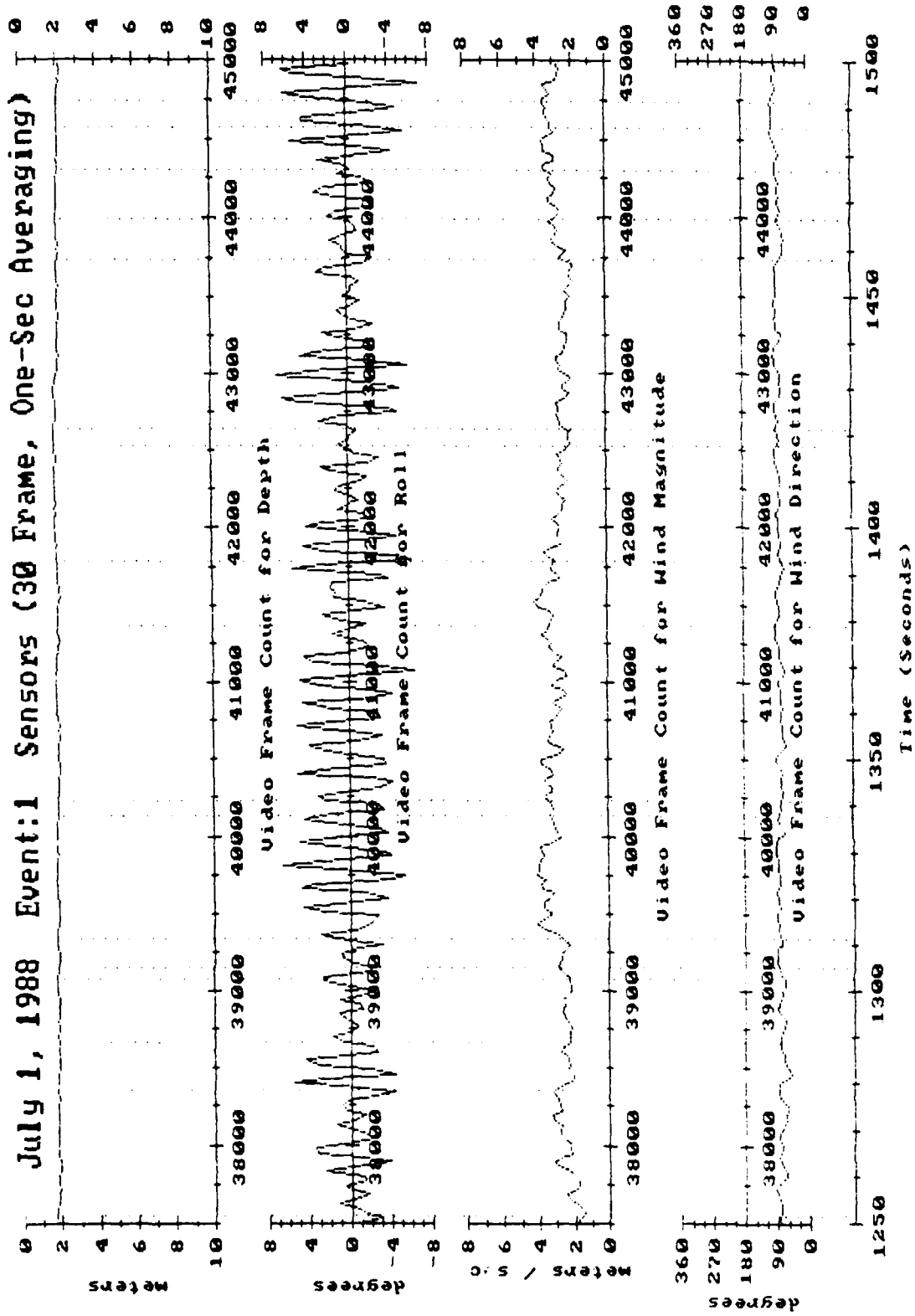
Appendix A, Figure 1c: Instrument depth and roll, plus nearby wind speed and dir. Vertical dashed lines mark wavelet breaks.



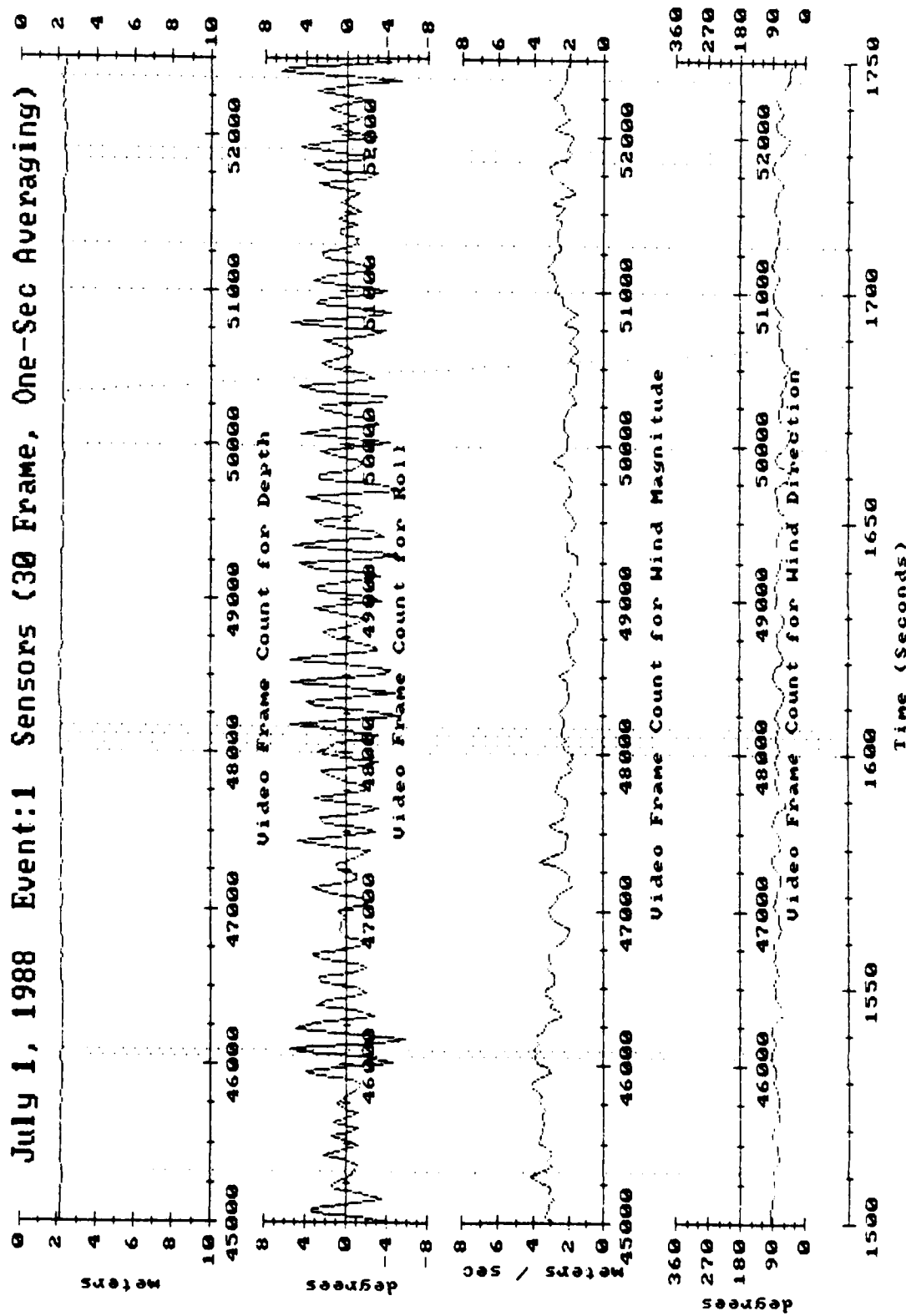
Appendix A, Figure 1d: Instrument depth and roll, plus nearby wind speed and dir. Vertical dashed lines mark wavelet breaks.



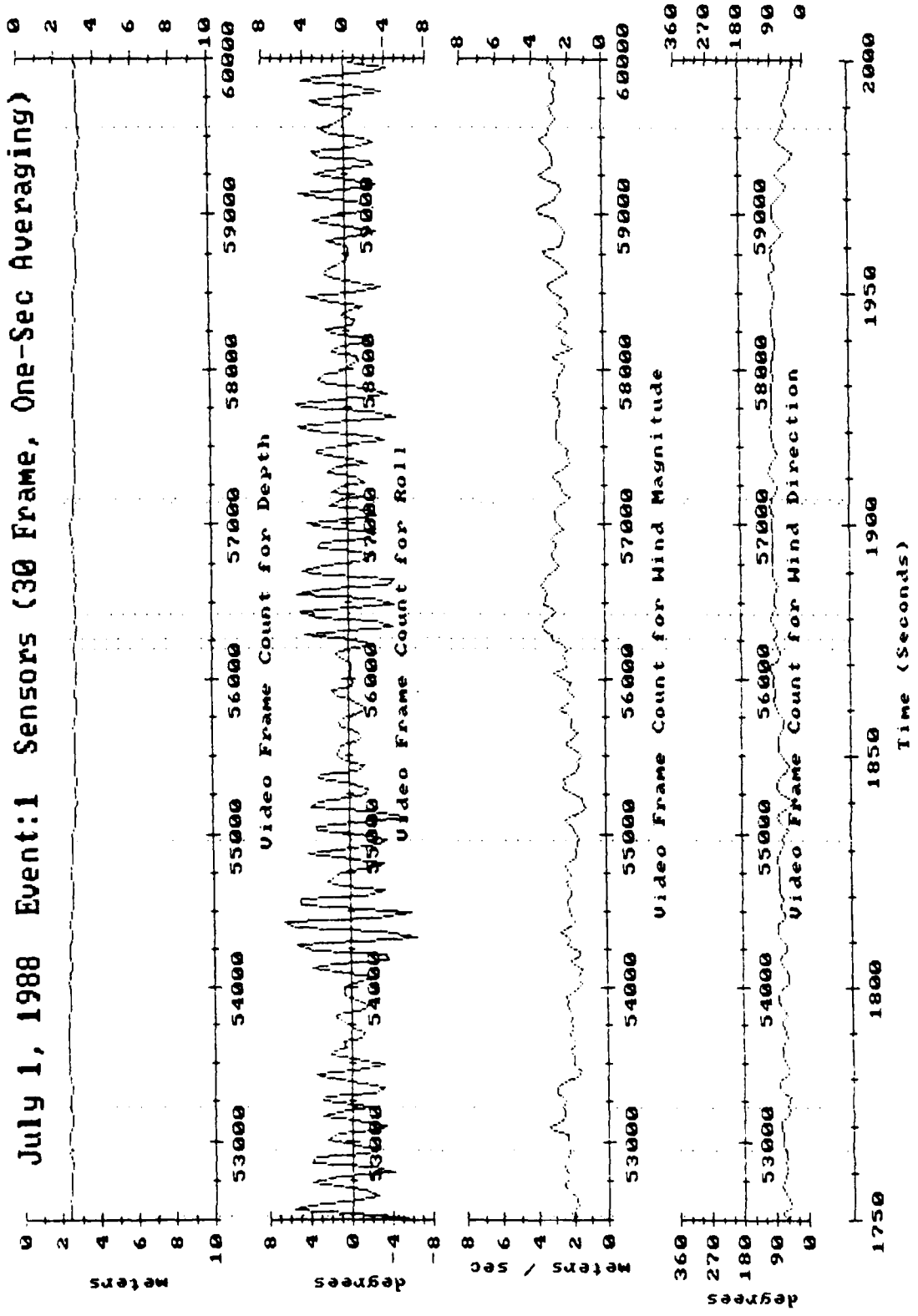
Appendix A, Figure 1e: Instrument depth and roll, plus nearby wind speed and dir. Vertical dashed lines mark wavelet breaks.



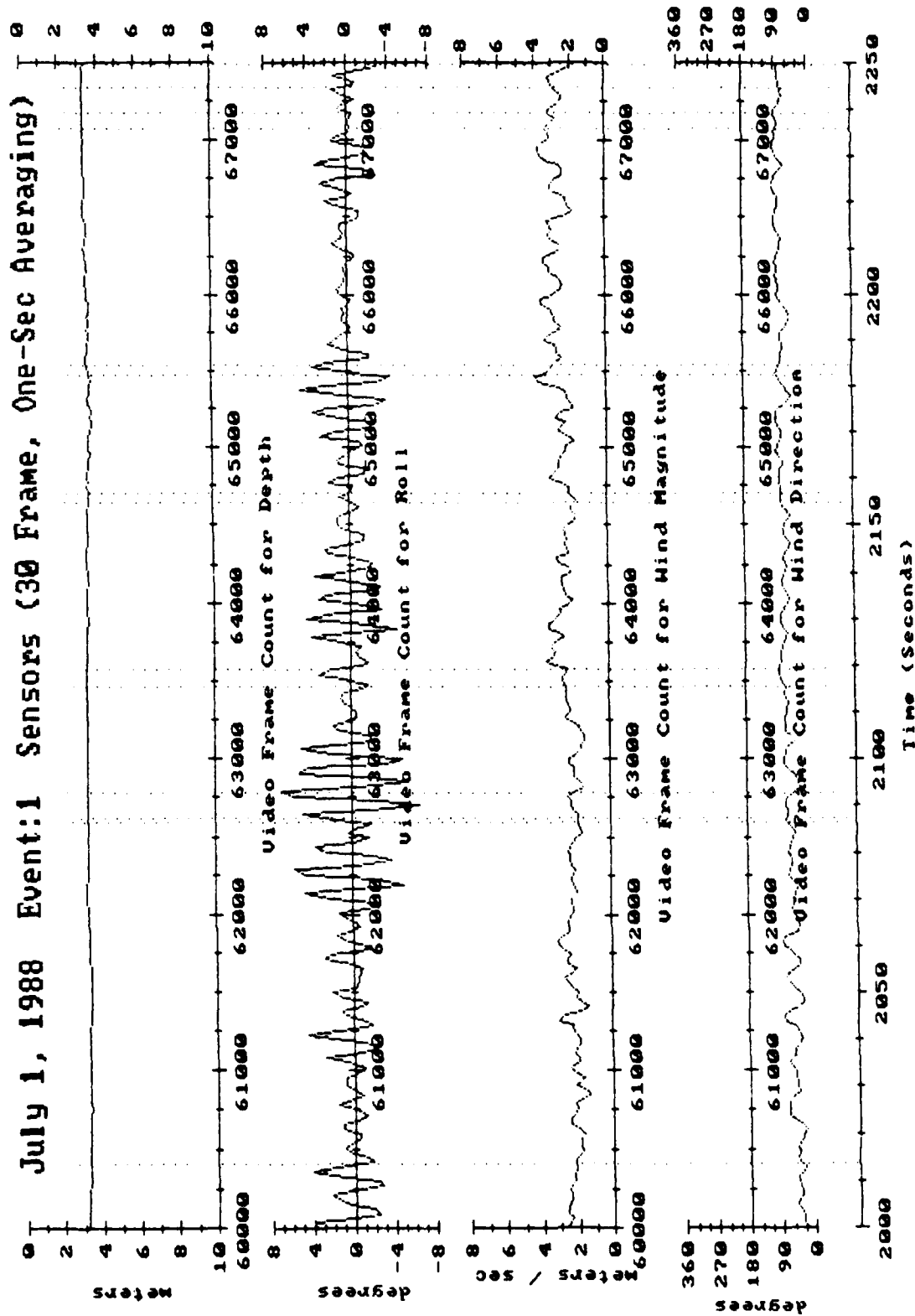
Appendix A, Figure 1f: Instrument depth and roll, plus nearby wind speed and dir. Vertical dashed lines mark wavelet breaks.



Appendix A, Figure 1g: Instrument depth and roll, plus nearby wind speed and dir. Vertical dashed lines mark wavelet breaks.



Appendix A, Figure 1h: Instrument depth and roll, plus nearby wind speed and dir. Vertical dashed lines mark wavelet breaks.



Appendix A, Figure 1i: Instrument depth and roll, plus nearby wind speed and dir. Vertical dashed lines mark wavelet breaks.

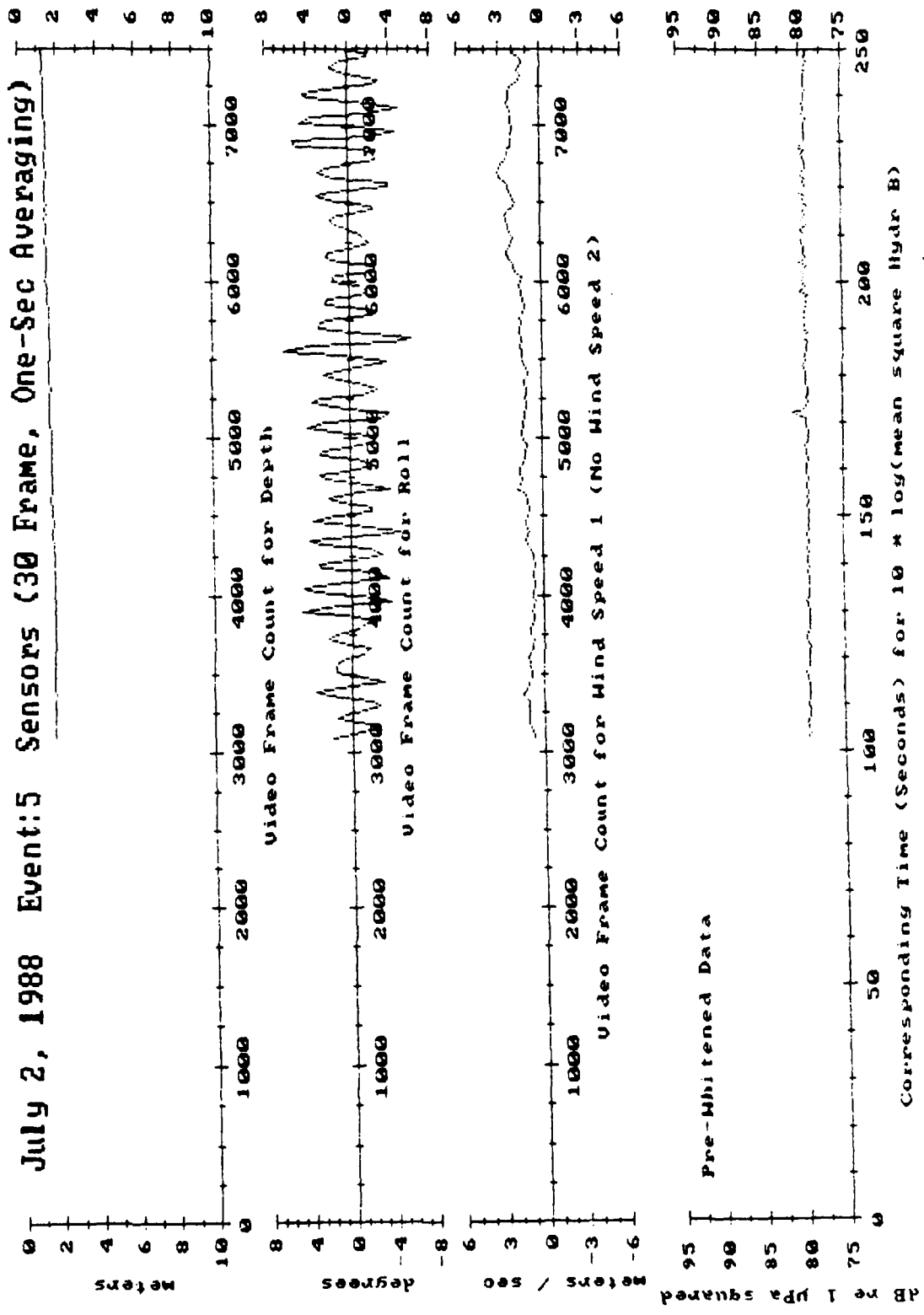
III. ENVIRONMENTAL RECORD 5 FROM JULY 2, 1988

This record is plotted starting on the next page.

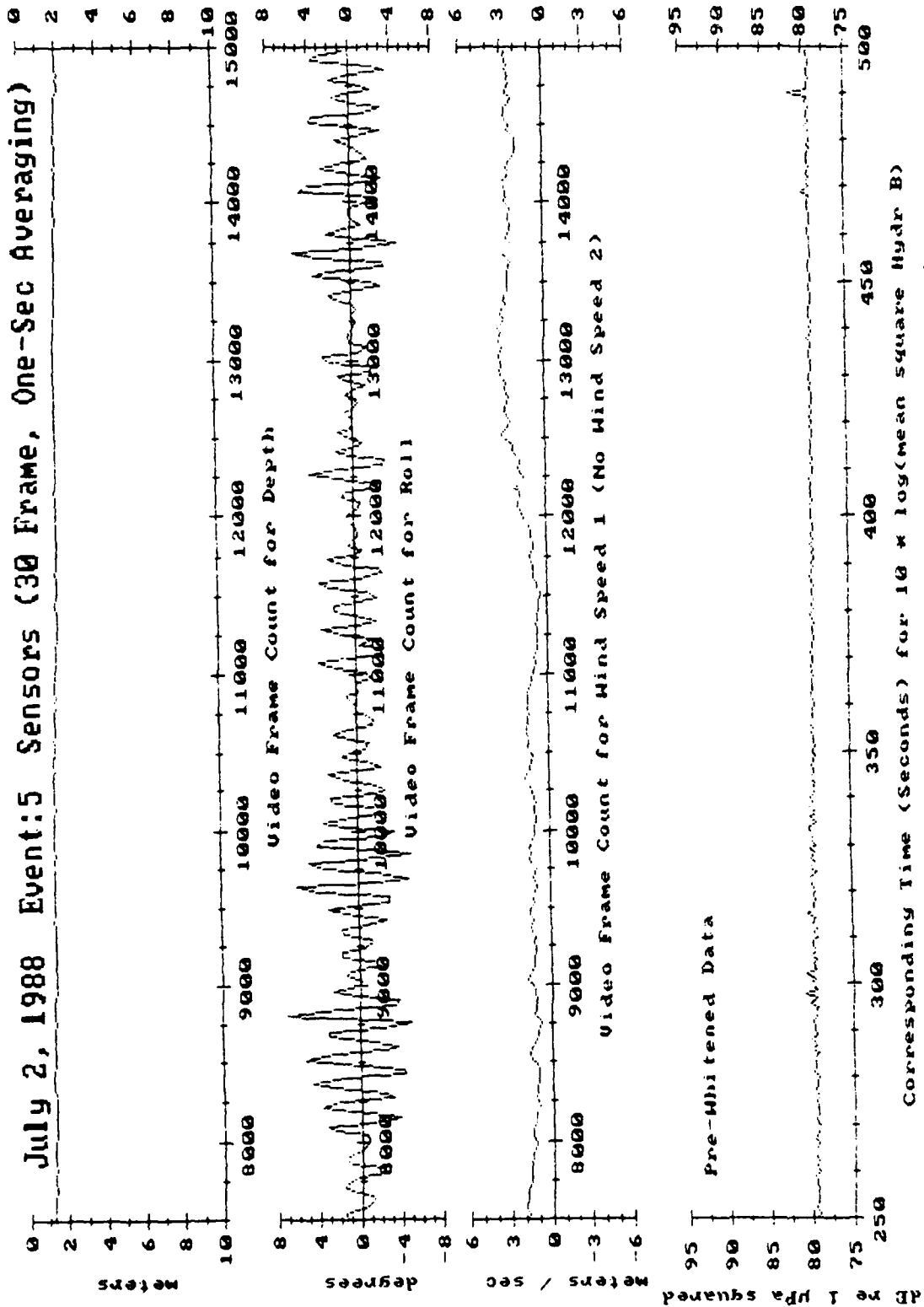
The data was recorded at 4:57 pm, PST, at latitude 32° 29' and longitude 118° 29', west of San Diego. The surface conditions were about Sea State 1. The wind was blowing from roughly 240 degrees at approximately 2.5 meters per second, as measured by an uncalibrated anemometer over the support barge. Swells with a period of 5 seconds and height of 0.3 meters were moving roughly towards 80 degrees.

Due to the number and intensity of spurious background noises from the instrument's attachment tether, wavelet breaks have been marked by dashed vertical lines in the plots which follow. Note when referencing the Mean Square Acoustic Pressure plots that the low acoustic frequencies were attenuated at the instrument by a pre-whitening filter of 6 dB per octave. Also, echo sounder pings from an unrelated device beneath the support barge caused a rather high mean square background noise level.

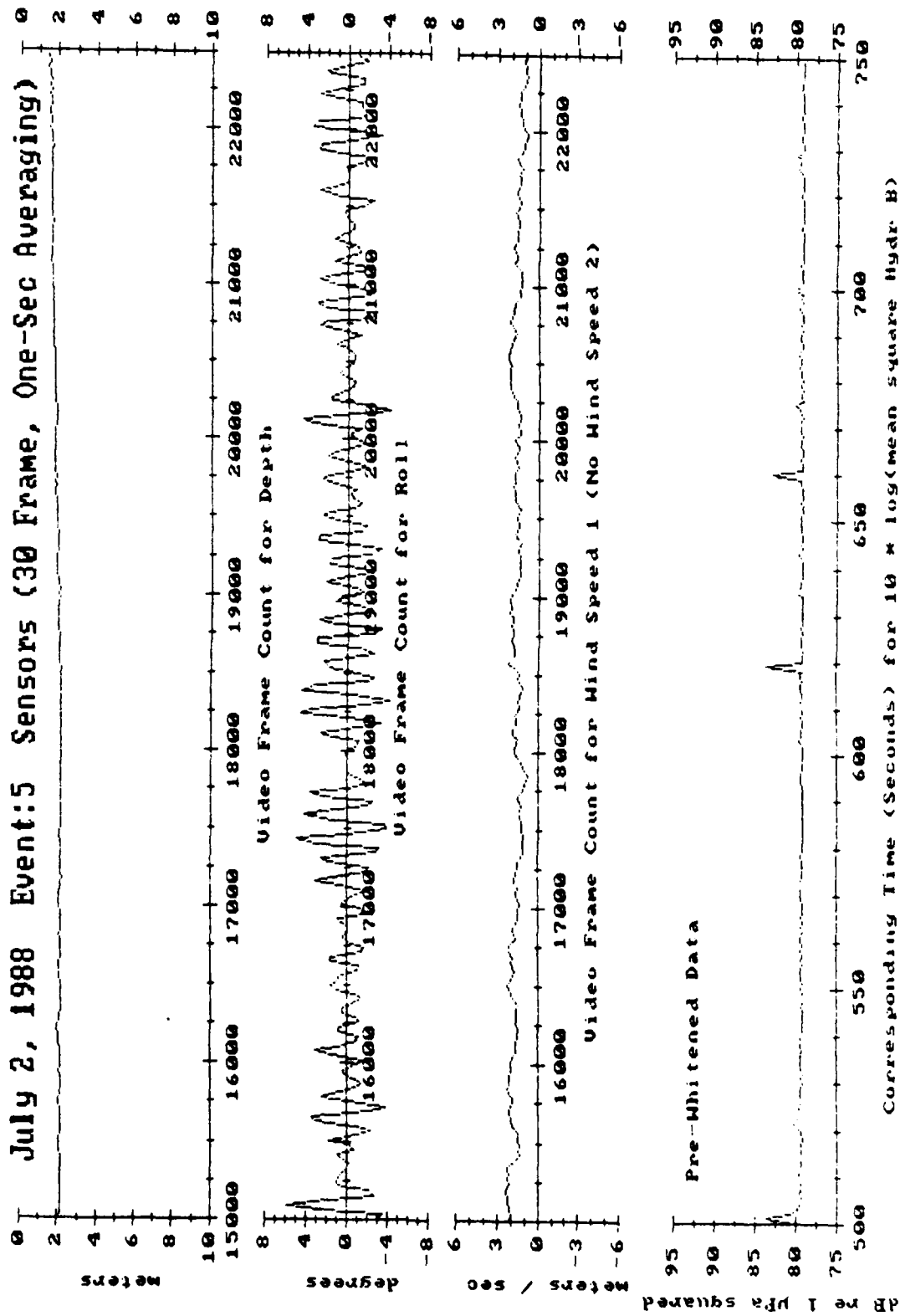
Only one of two perpendicular wind sensors was working, so wind direction has not been plotted.



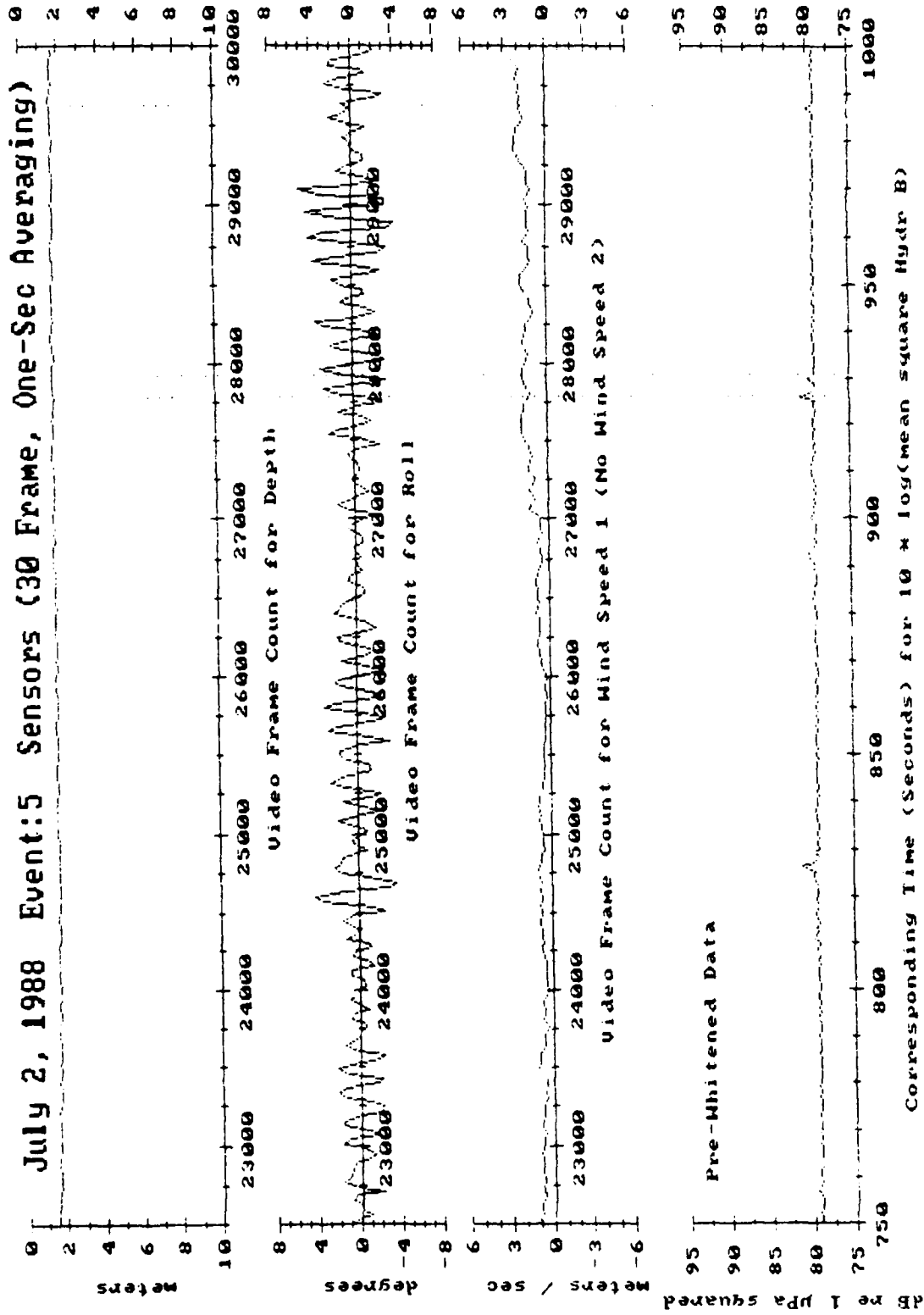
Appendix A, Figure 2a: Instrument depth and roll, plus nearby wind in one direction and the mean square acoustic pressure at Hydrophone B. Vertical dashed lines mark wavelet breaks.



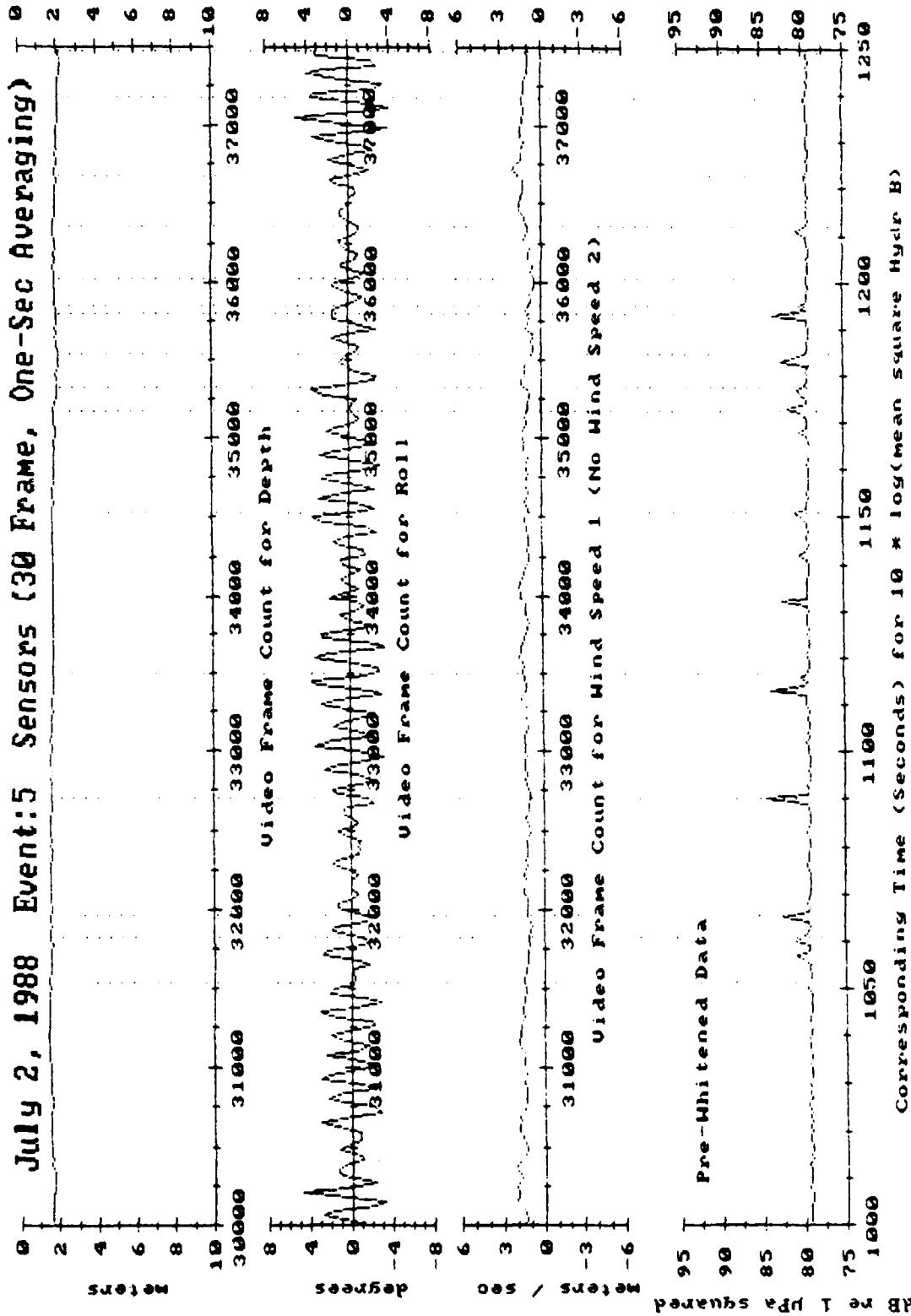
Appendix A, Figure 2b: Instrument depth and roll, plus nearby wind in one direction and the mean square acoustic pressure at Hydrophone B. Vertical dashed lines mark wavelet breaks.



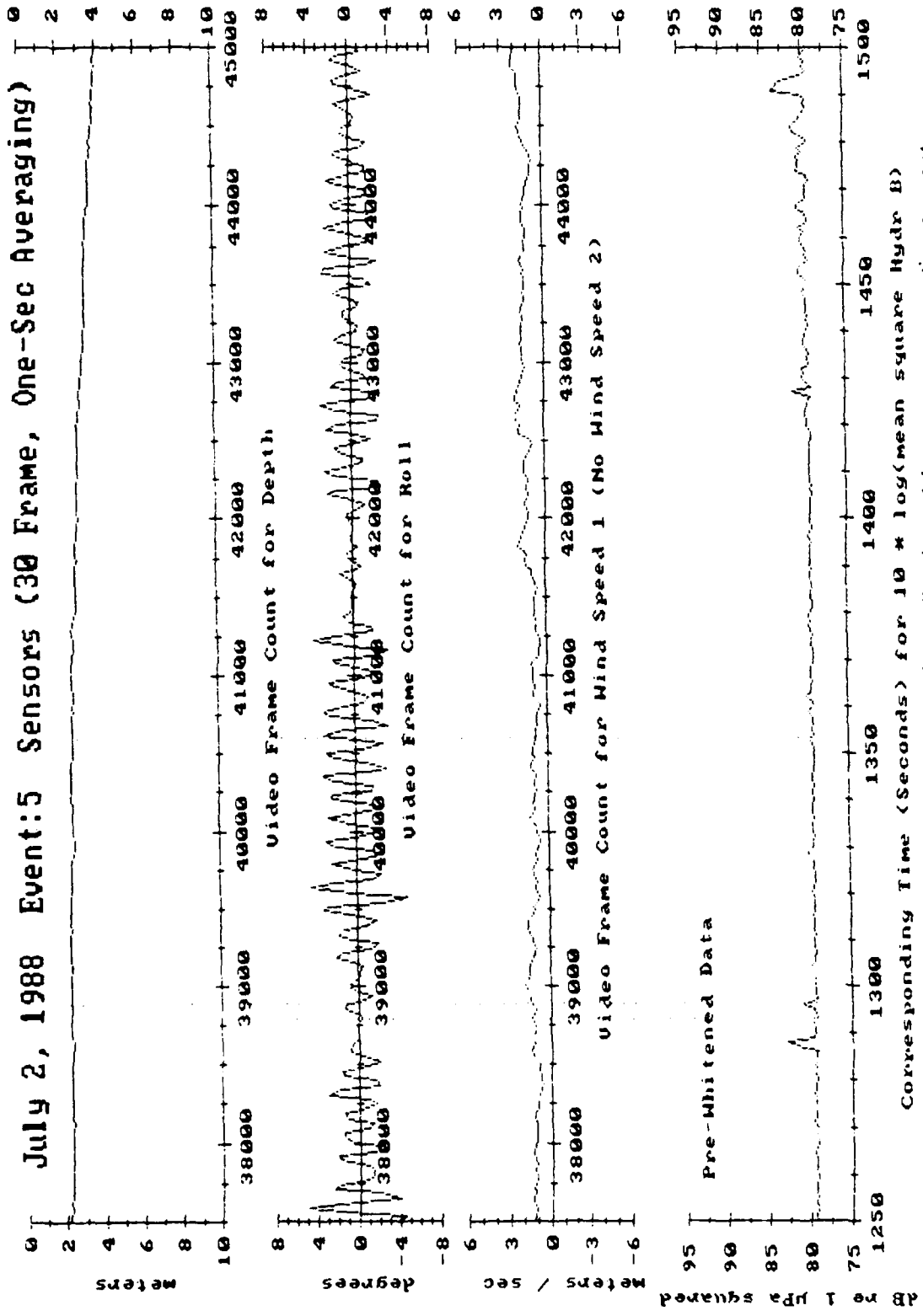
Appendix A, Figure 2c: Instrument depth and roll, plus nearby wind in one direction and the mean square acoustic pressure at Hydrophone B. Vertical dashed lines mark wavelet breaks.



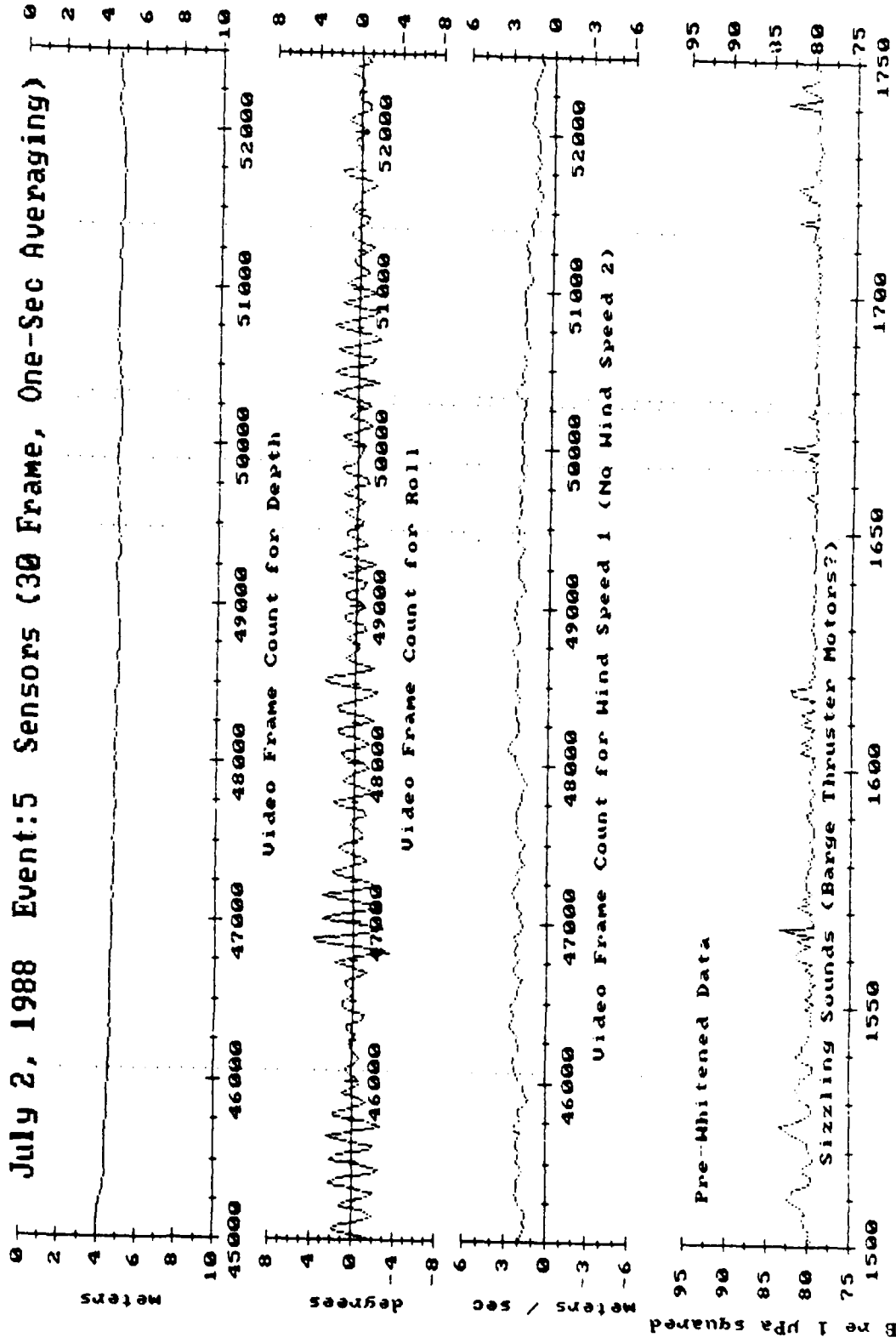
Appendix A, Figure 2d: Instrument depth and roll, plus nearby wind in one direction and the mean square acoustic pressure at Hydrophone B. Vertical dashed lines mark wavelet breaks.



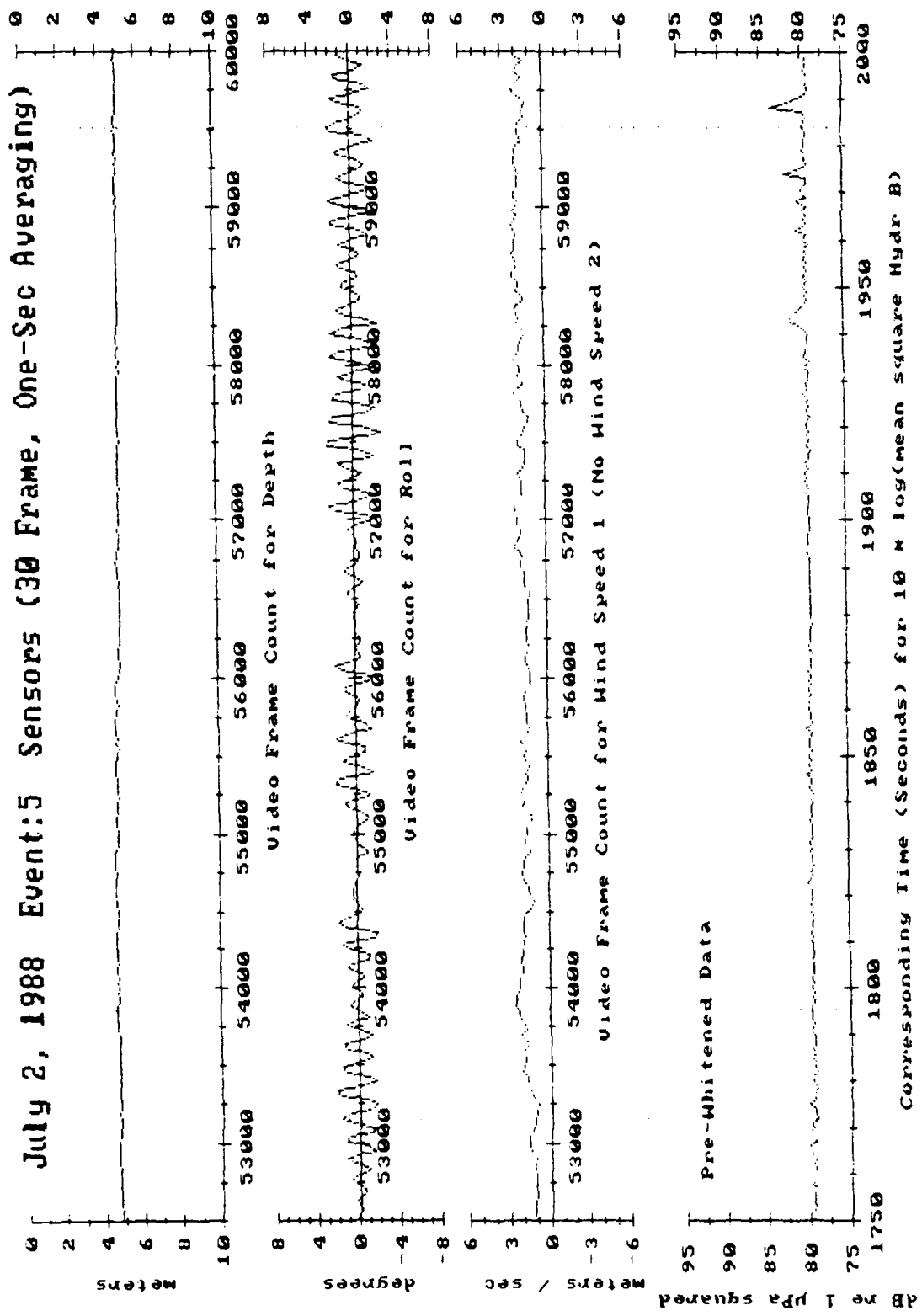
Appendix A, Figure 2e: Instrument depth and roll, plus nearby wind in one direction and the mean square acoustic pressure at Hydrophone B. Vertical dashed lines mark wavelet breaks.



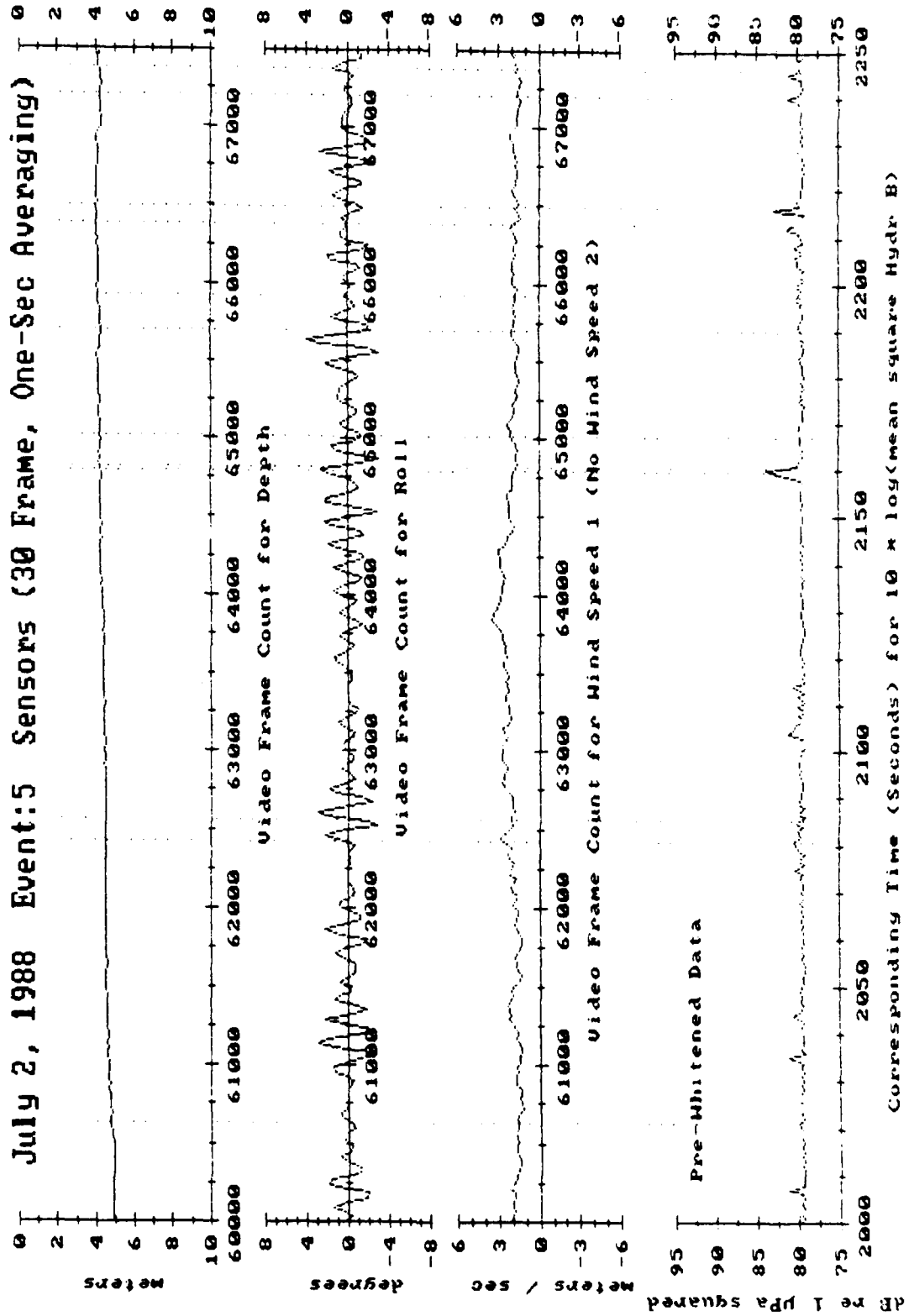
Appendix A, Figure 2f: Instrument depth and roll, plus nearby wind in one direction and the mean square acoustic pressure at Hydrophone B. Vertical dashed lines mark wavelet breaks.



Appendix A, Figure 2g: Instrument depth and roll, plus nearby wind in one direction and the mean square acoustic pressure at Hydrophone B. Vertical dashed lines mark wavelet breaks.



Appendix A, Figure 2h: Instrument depth and roll, plus nearby wind in one direction and the mean square acoustic pressure at Hydrophone B. Vertical dashed lines mark wavelet breaks.



Appendix A, Figure 2i: Instrument depth and roll, plus nearby wind in one direction and the mean square acoustic pressure at Hydrophone B. Vertical dashed lines mark wavelet breaks.

IV. ENVIRONMENTAL RECORD 8 FROM JULY 2, 1988

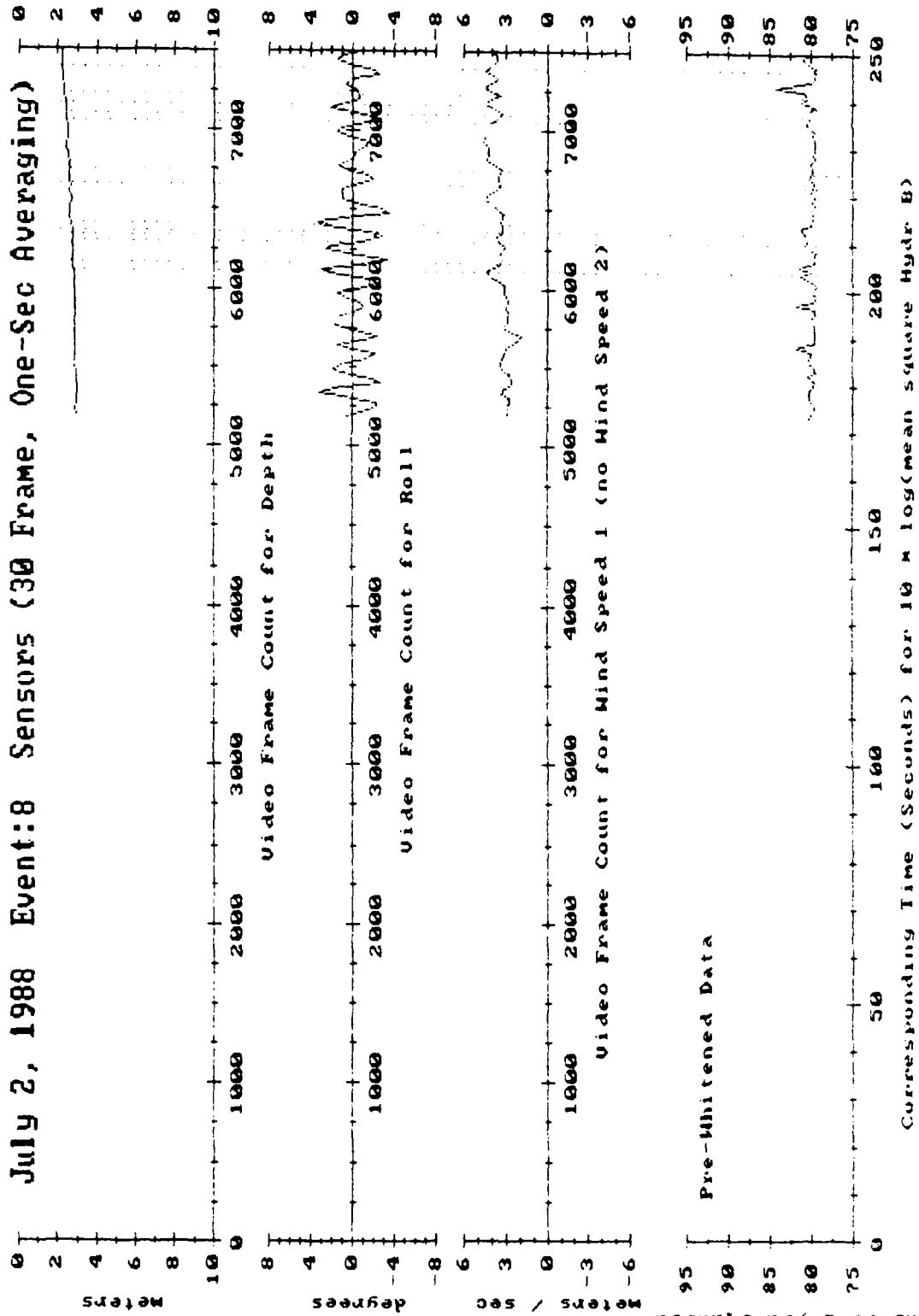
This record is plotted starting on the next page.

The data was recorded at 6:27 pm, PST, at latitude 32° 29' and longitude 118° 29', west of San Diego. The surface conditions were about Sea State 1. The wind was blowing from roughly 200 degrees at approximately 2 meters per second, as measured by an uncalibrated anemometer over the support barge, and increased during the recording. Swells with a period of 4 seconds and height of 0.2 meters were moving roughly towards 110 degrees.

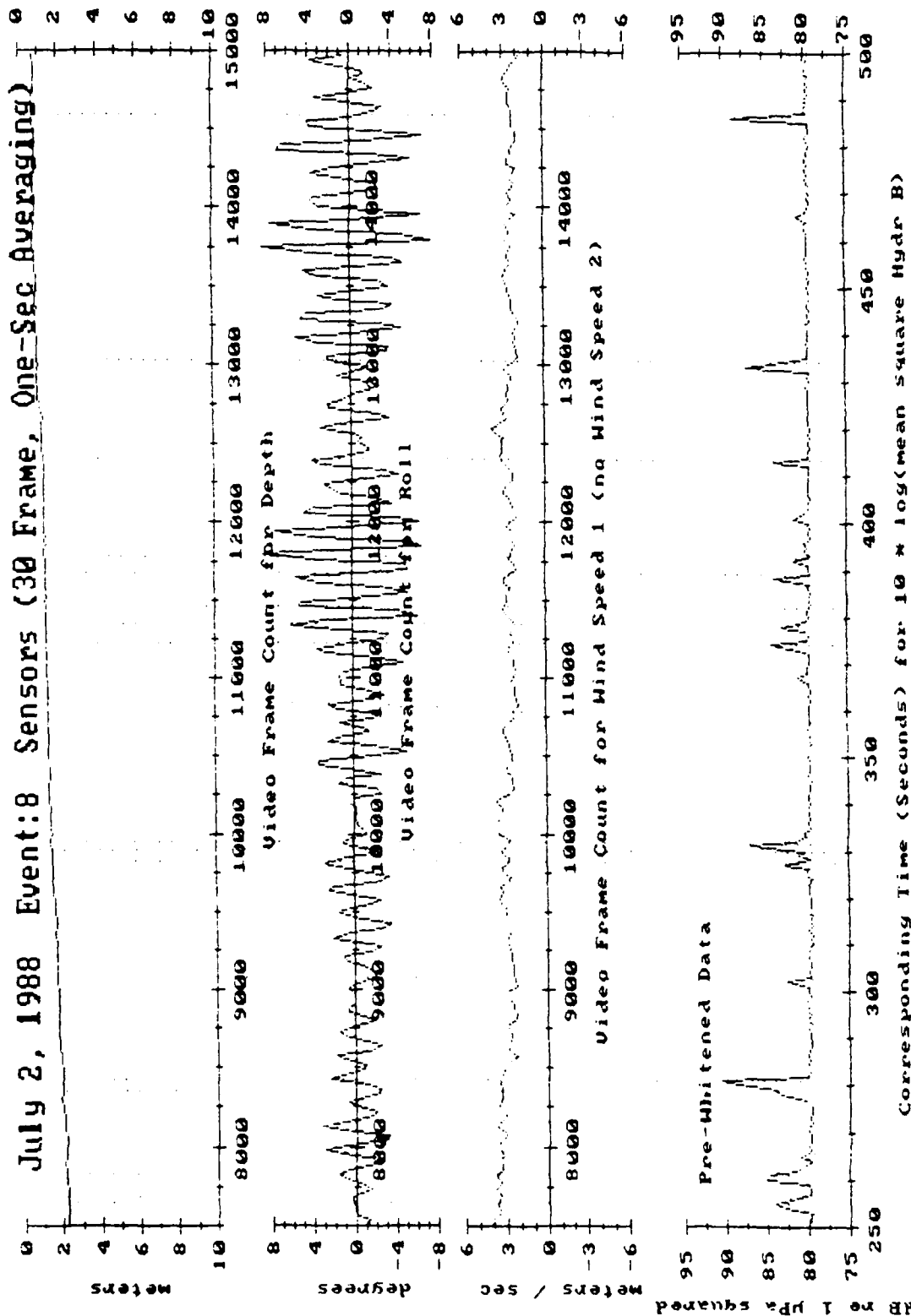
Due to the number and intensity of spurious background noises from the instrument's attachment tether, wavelet breaks have been marked by dashed vertical lines in the plots which follow. Note when referencing the Mean Square Acoustic Pressure plots that the low acoustic frequencies were attenuated at the instrument by a pre-whitening filter of 6 dB per octave. Also, echo sounder pings from an unrelated device beneath the support barge caused a rather high mean square background noise level.

Only one of two perpendicular wind sensors was working, so wind direction has not been plotted.

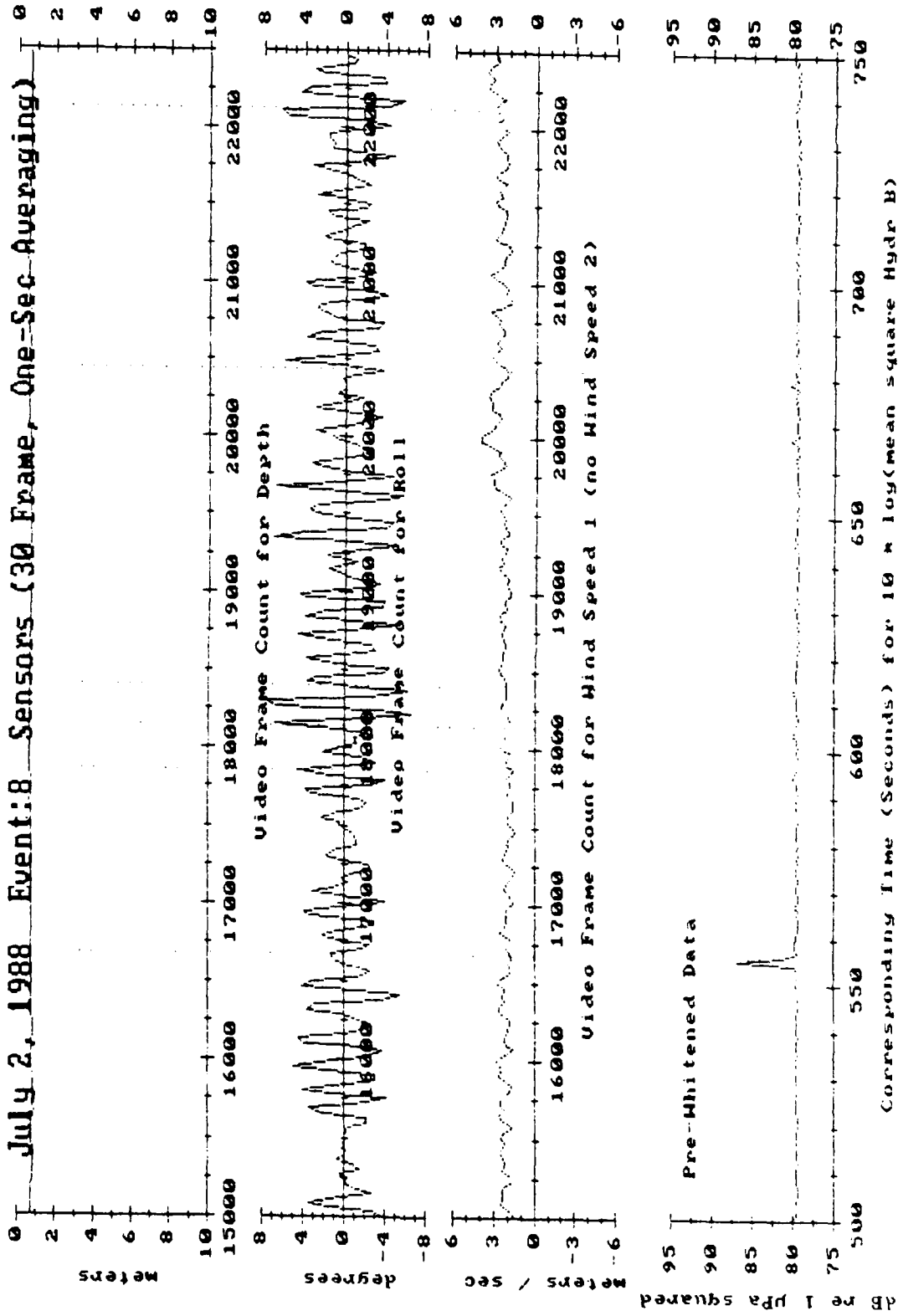
The submerged instrument temporarily breaks the surface at about frame 40,000.



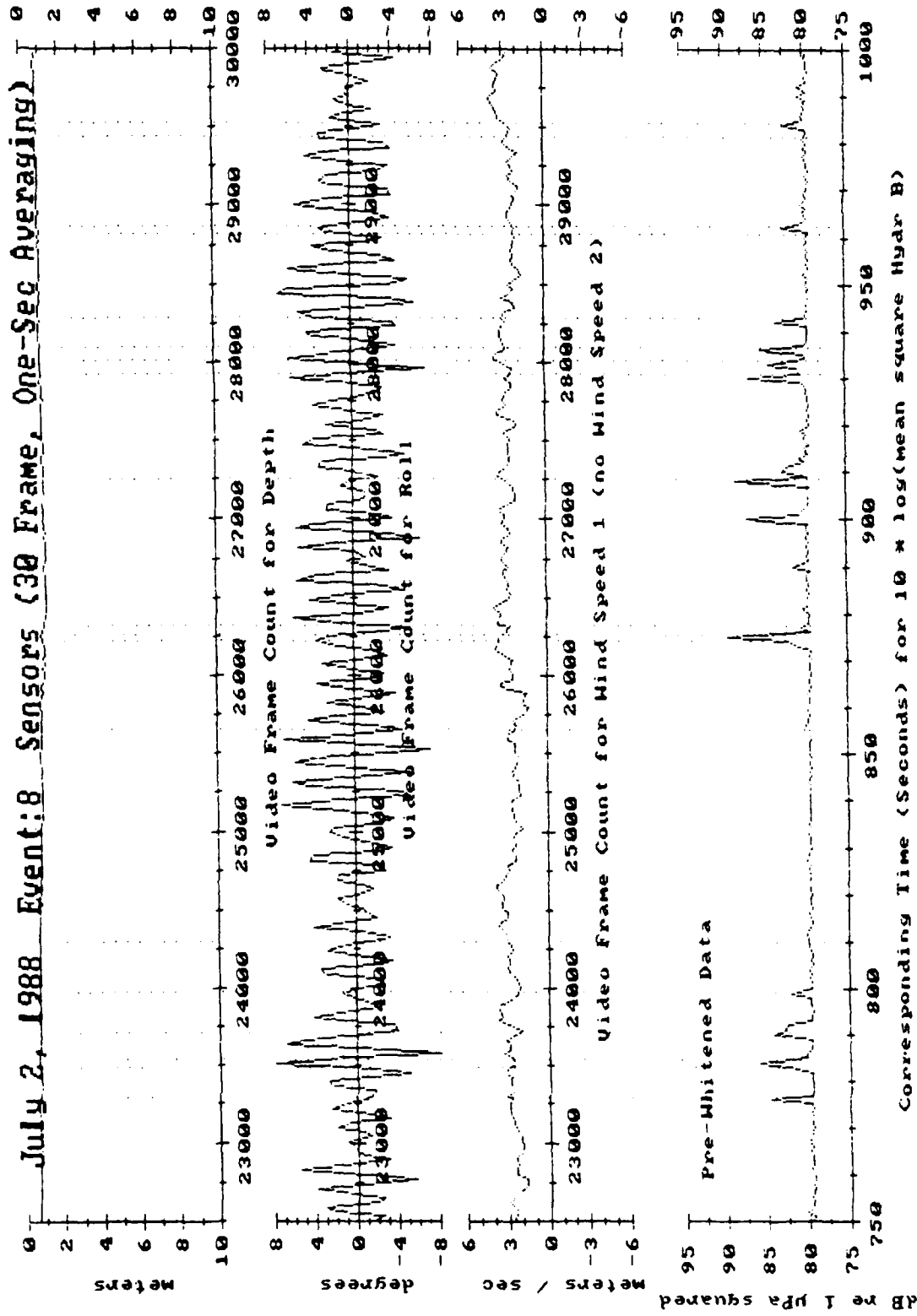
Appendix A, Figure 3a: Instrument depth and roll, plus nearby wind in one direction and the mean square acoustic pressure at Hydrophone B. Vertical dashed lines mark wavelet breaks.



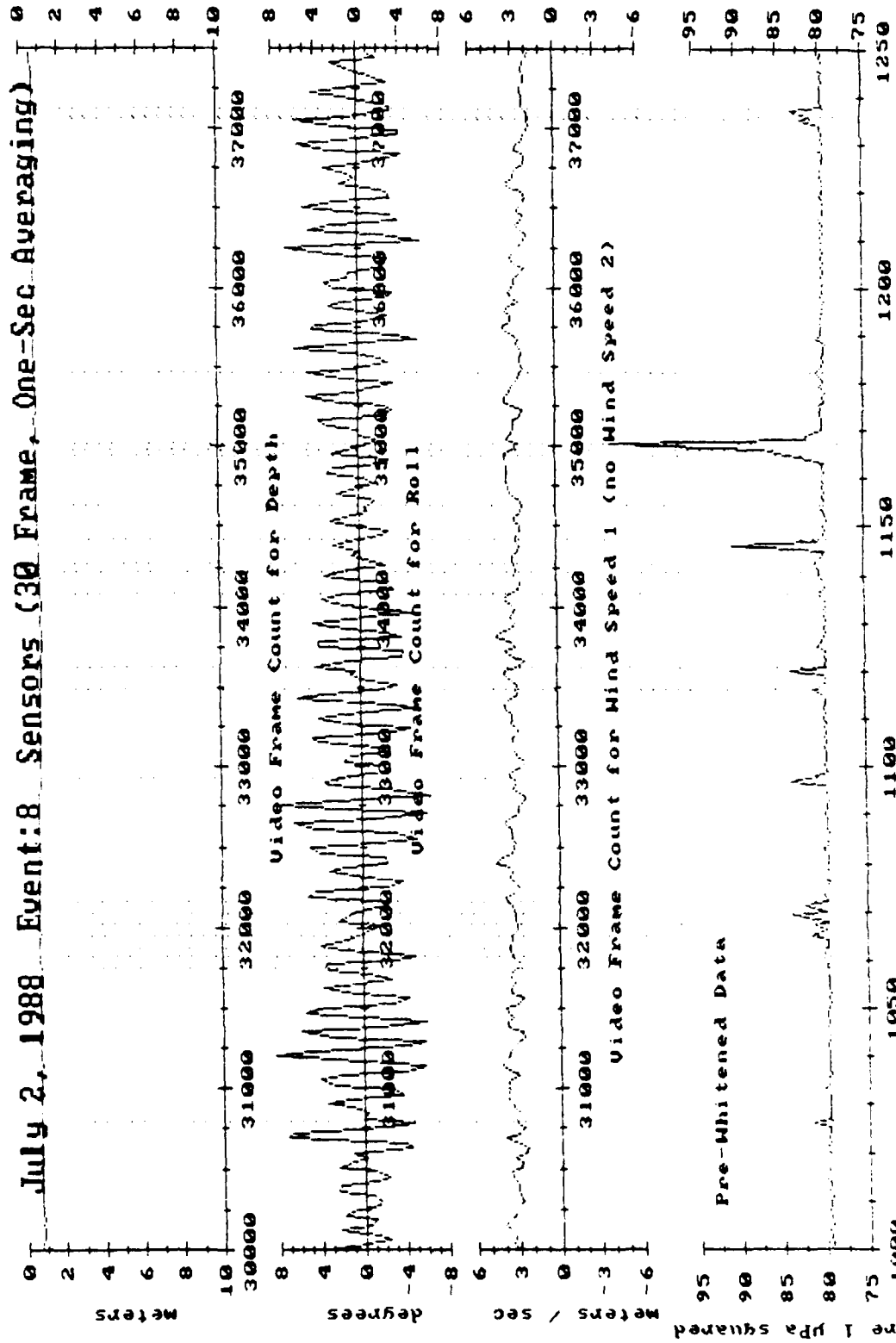
Appendix A, Figure 3b: Instrument depth and roll, plus nearby wind in one direction and the mean square acoustic pressure at Hydrophone B. Vertical dashed lines mark wavelet breaks.



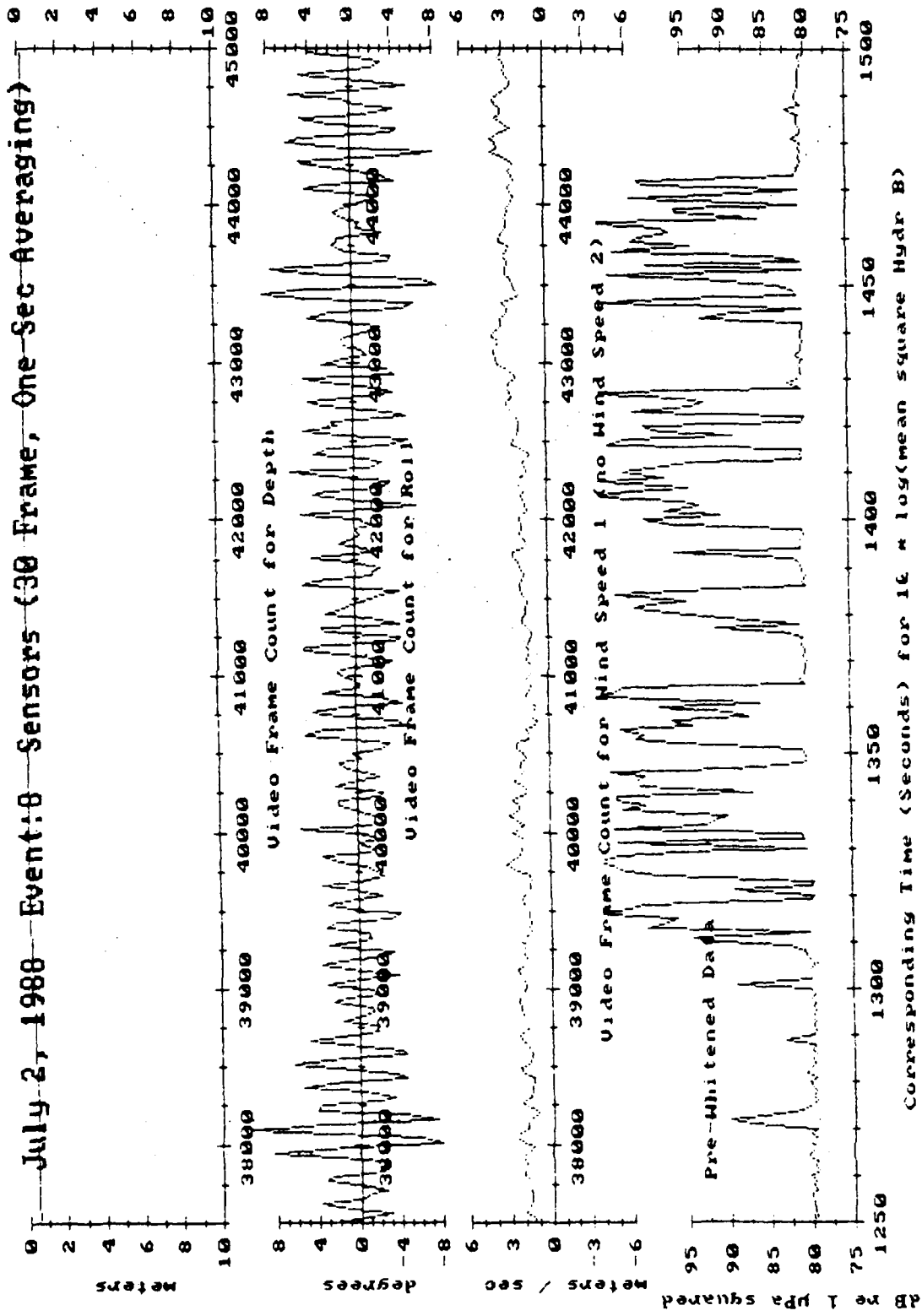
Appendix A, Figure 3c: Instrument depth and roll, plus nearby wind in one direction and the mean square acoustic pressure at Hydrophone B. Vertical dashed lines mark wavelet breaks.



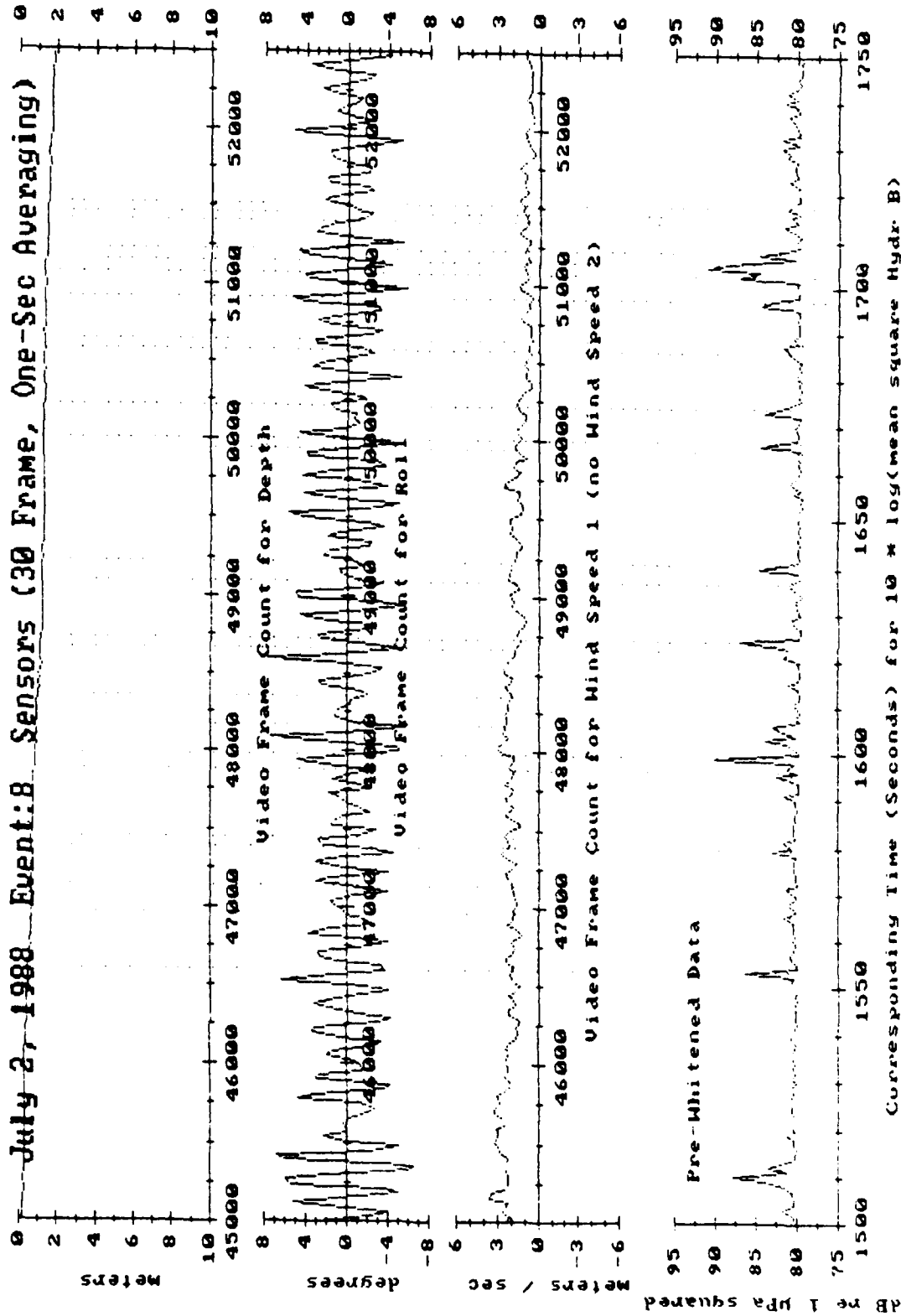
Appendix A, Figure 3d: Instrument depth and roll, plus nearby wind in one direction and the mean square acoustic pressure at Hydrophone B. Vertical dashed lines mark wavelet breaks.



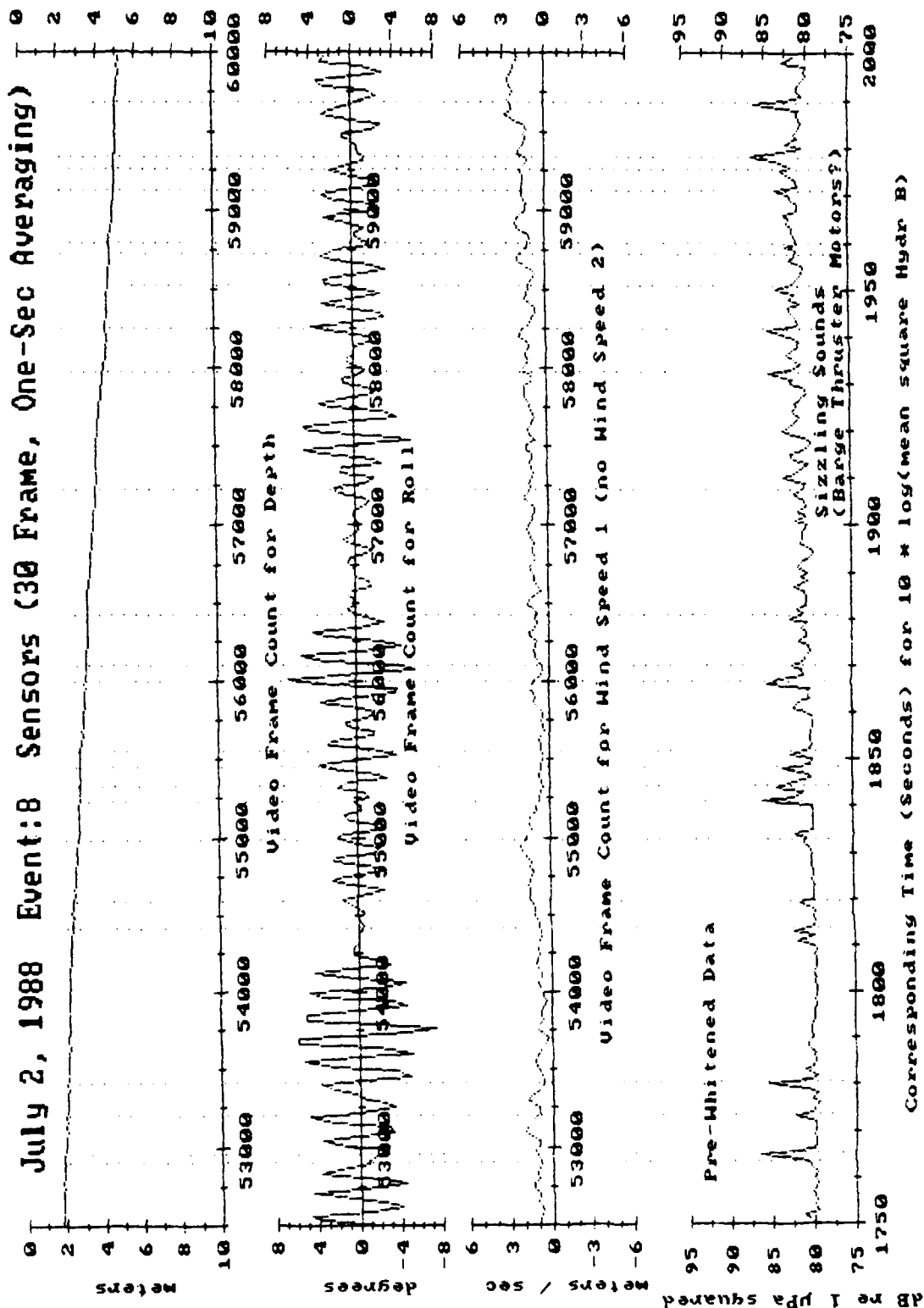
Appendix A, Figure 3e: Instrument depth and roll, plus nearby wind in one direction and the mean square acoustic pressure at Hydrophone B. Vertical dashed lines mark wavelet breaks.



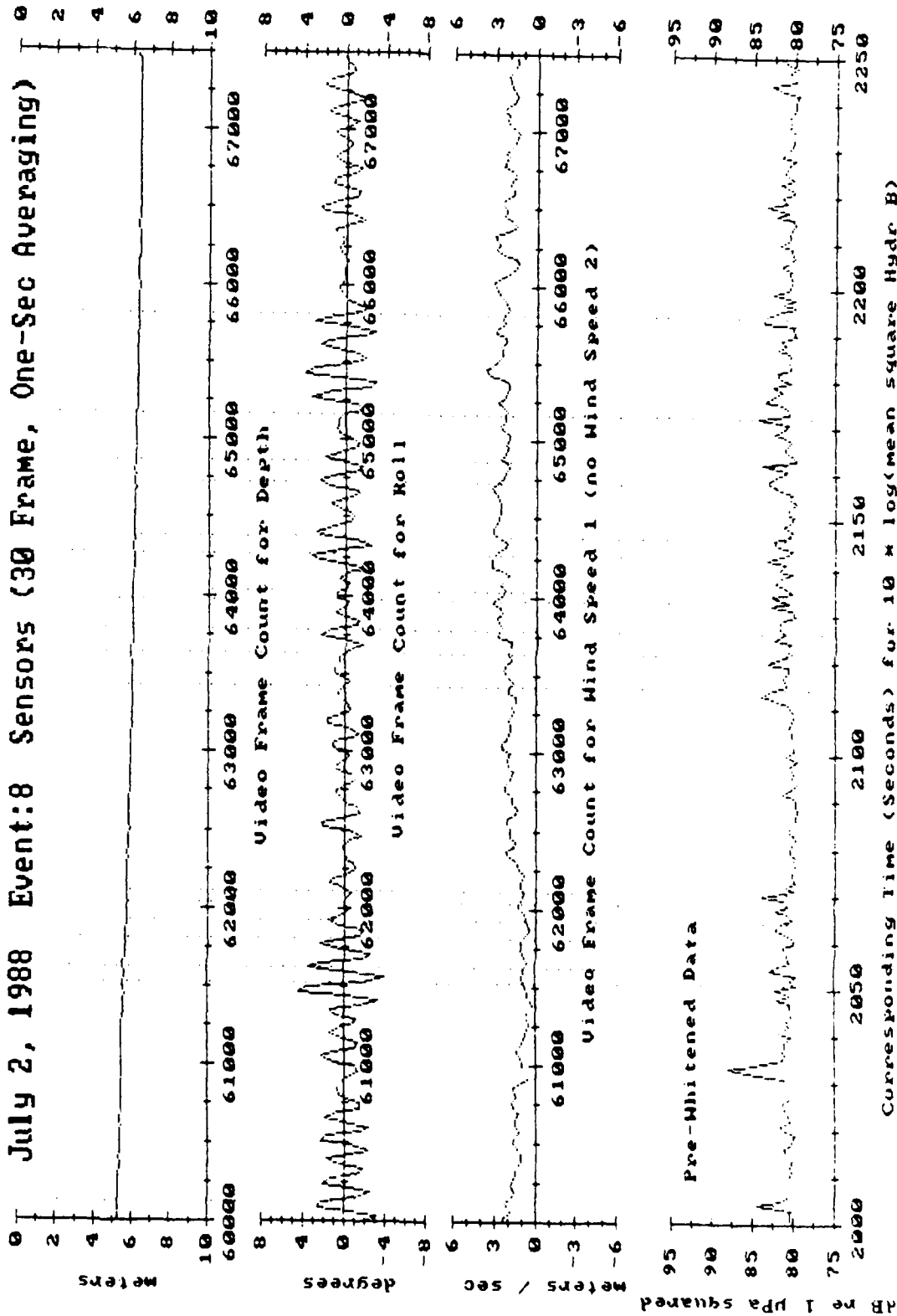
Appendix A, Figure 3f: Instrument depth and roll, plus nearby wind in one direction and the mean square acoustic pressure at Hydrophone B. Vertical dashed lines mark wavelet breaks.



Appendix A, Figure 3g: Instrument depth and roll, plus nearby wind in one direction and the mean square acoustic pressure at Hydrophone B. Vertical dashed lines mark wavelet breaks.



Appendix A, Figure 3h: Instrument depth and roll, plus nearby wind in one direction and the mean square acoustic pressure at Hydrophone B. Vertical dashed lines mark wavelet breaks.



Appendix A, Figure 3i: Instrument depth and roll, plus nearby wind in one direction and the mean square acoustic pressure at Hydrophone B. Vertical dashed lines mark wavelet breaks.

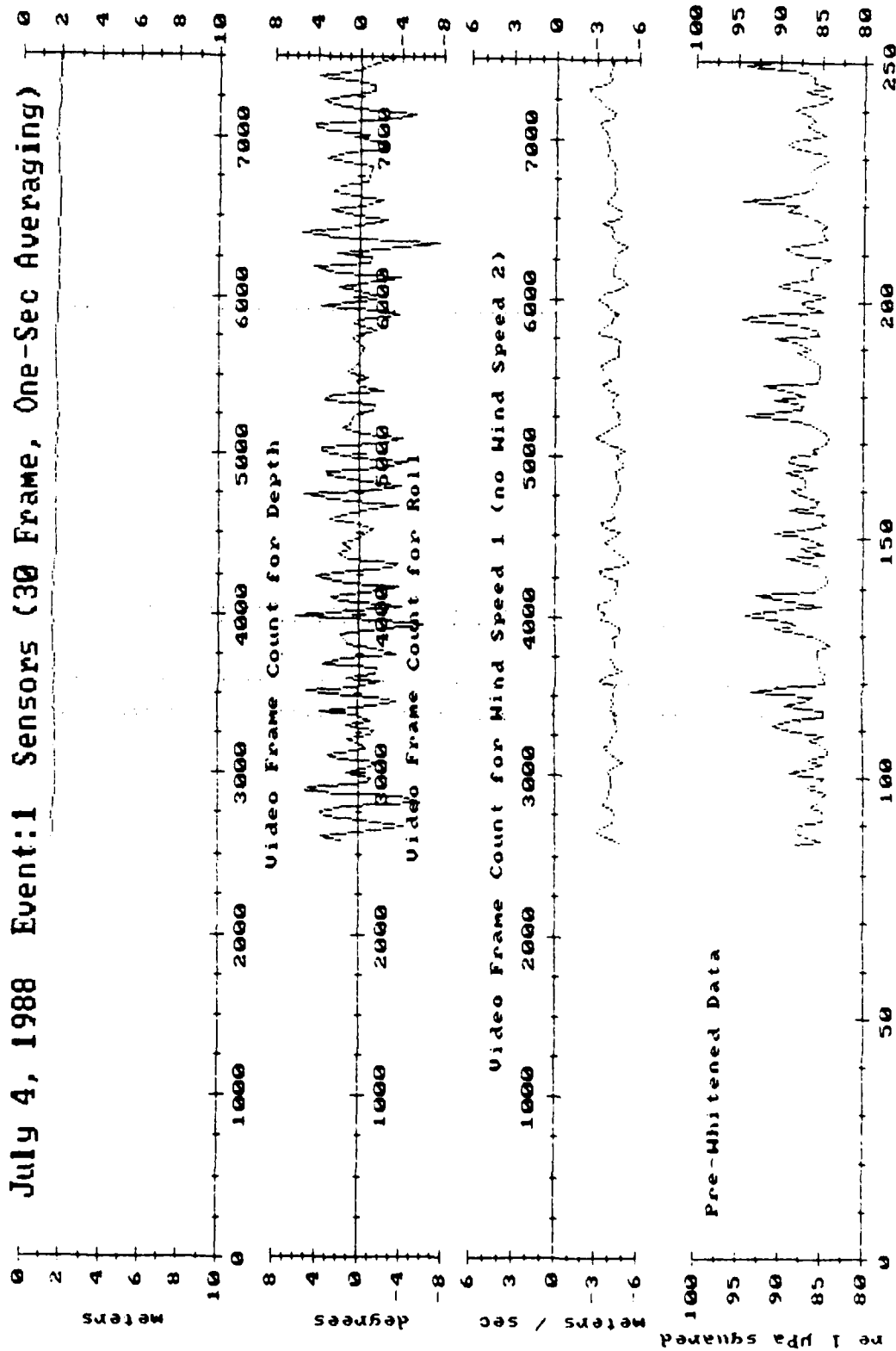
V. ENVIRONMENTAL RECORD FROM JULY 4, 1988

This record is plotted starting on the next page.

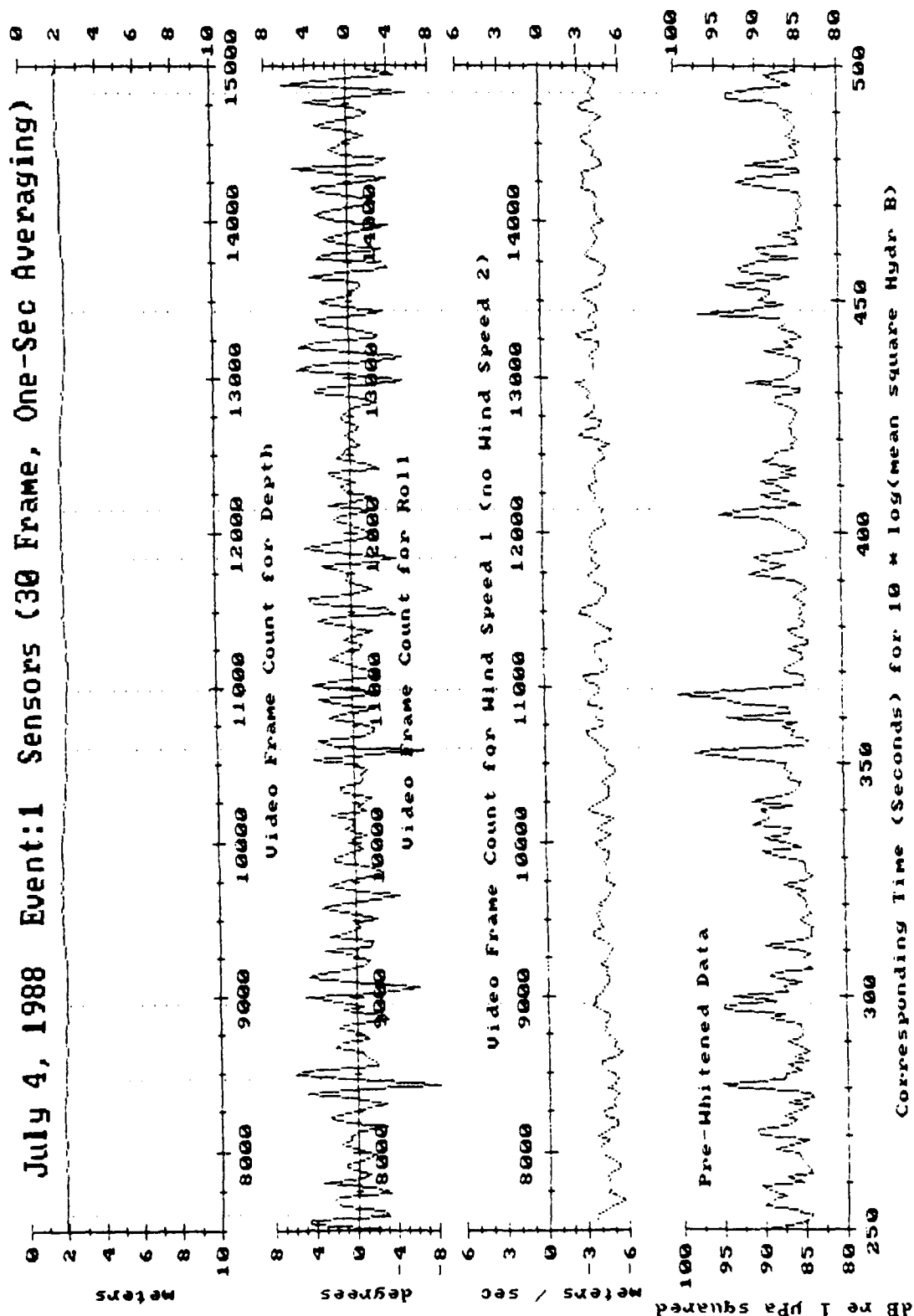
The data was recorded at 8:54 pm, PST, at latitude 32° 29' and longitude 118° 29', west of San Diego. The surface conditions were about Sea State 3. The wind blew at approximately 7 meters per second, as measured by an uncalibrated anemometer over the support barge. Swells had a period of 4 to 5 seconds and a height of about 1 meter. Neither the swell nor wind directions were properly recorded.

Due to the number and intensity of spurious background noises from the instrument's attachment tether, the larger wave breaks have been marked by dashed vertical lines in the plots which follow. Small wavelet breaks were too indistinct to mark. Note when referencing the Mean Square Acoustic Pressure plots that the low acoustic frequencies were attenuated at the instrument by a pre-whitening filter of 6 dB per octave. Also, echo sounder pings from an unrelated device beneath the support barge caused a rather high mean square background noise level until approximately Frame 40,000, when it was shut down.

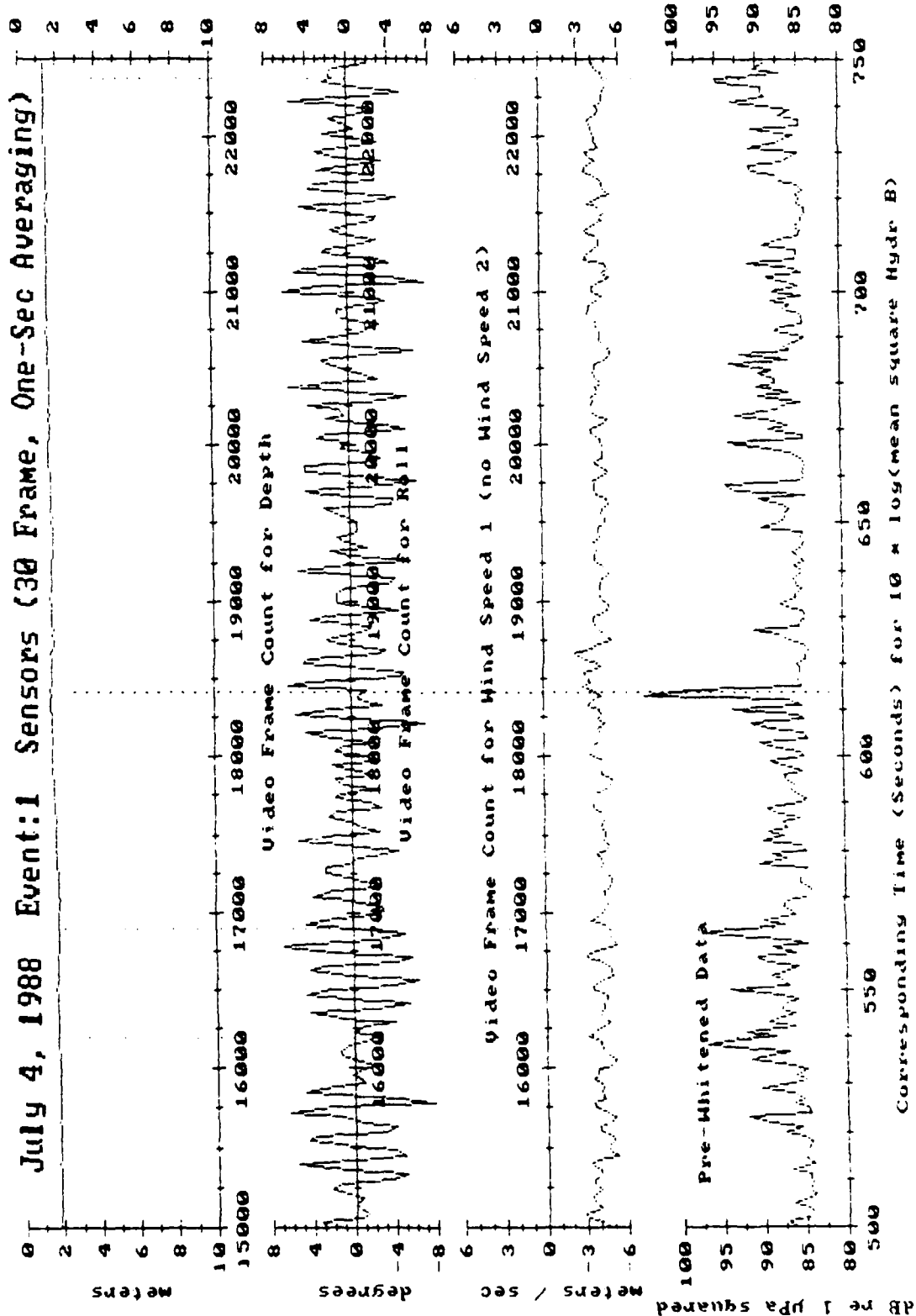
Only one of two perpendicular wind sensors was working, so wind direction has not been plotted.



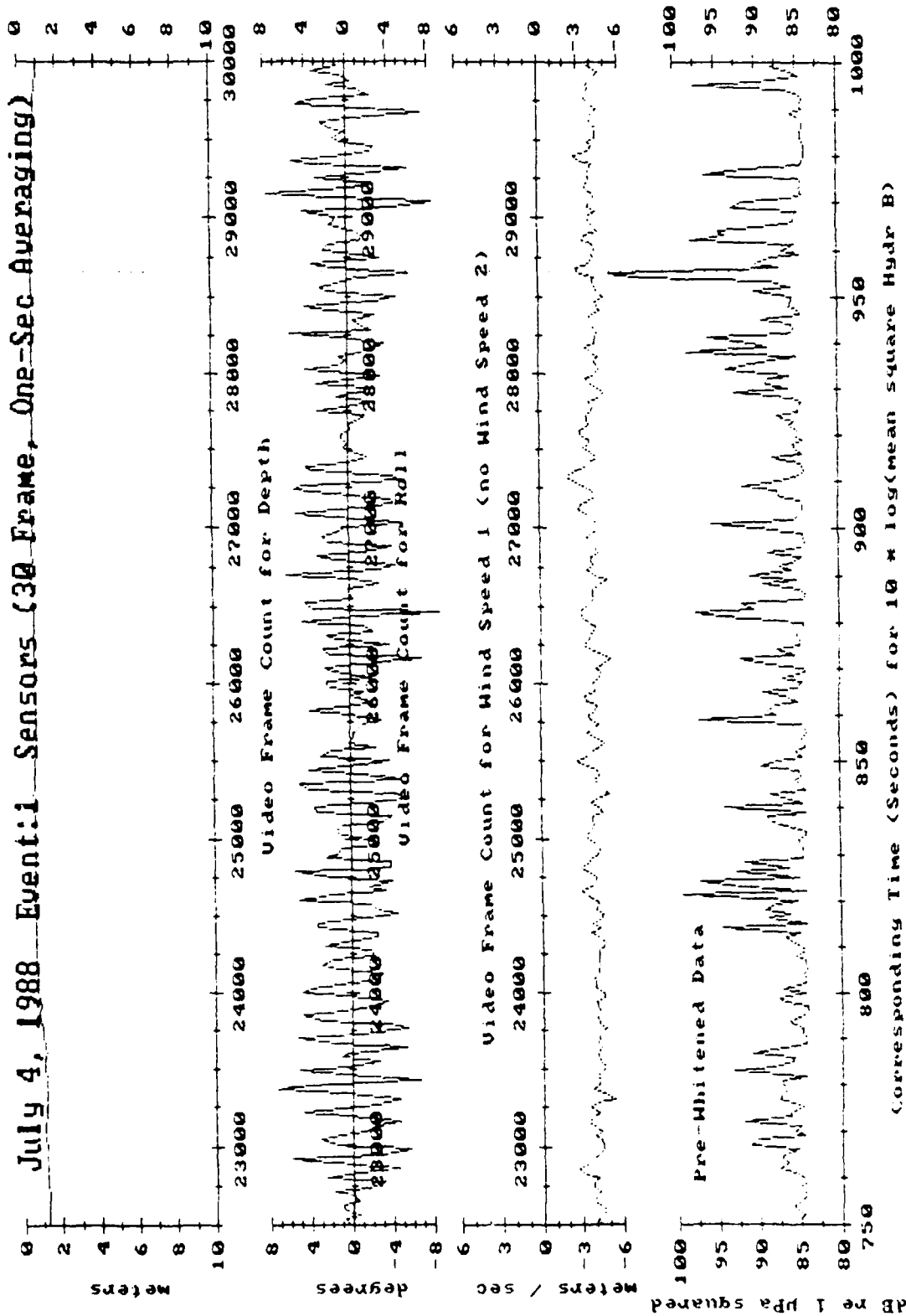
Appendix A. Figure 4a: Instrument depth and roll, plus nearby wind in one direction and the mean square acoustic pressure at Hydrophone B. Vertical dashed lines mark wavelet breaks.



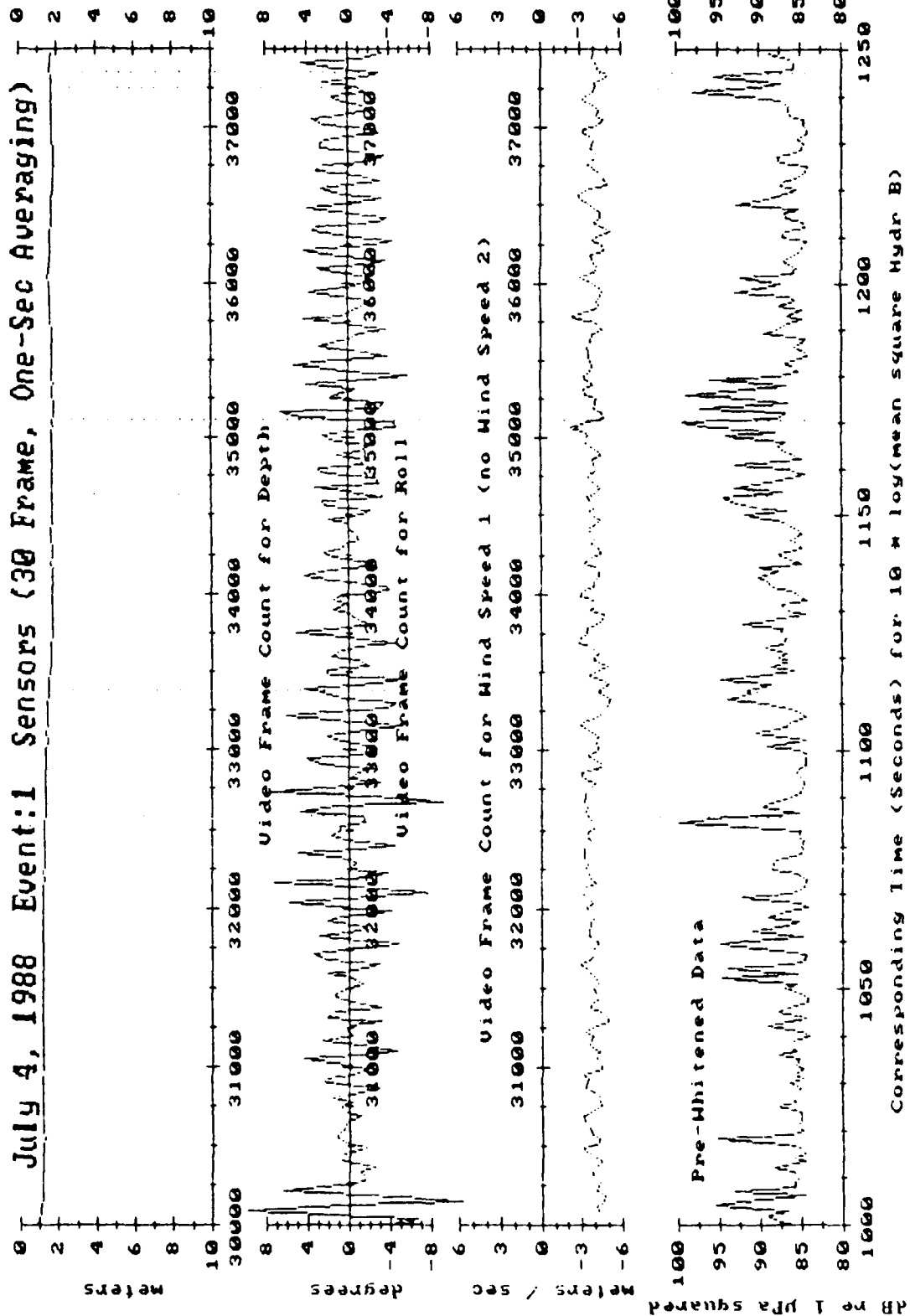
Appendix A, Figure 4b: Instrument depth and roll, plus nearby wind in one direction and the mean square acoustic pressure at Hydrophone B. Vertical dashed lines mark wavelet breaks.



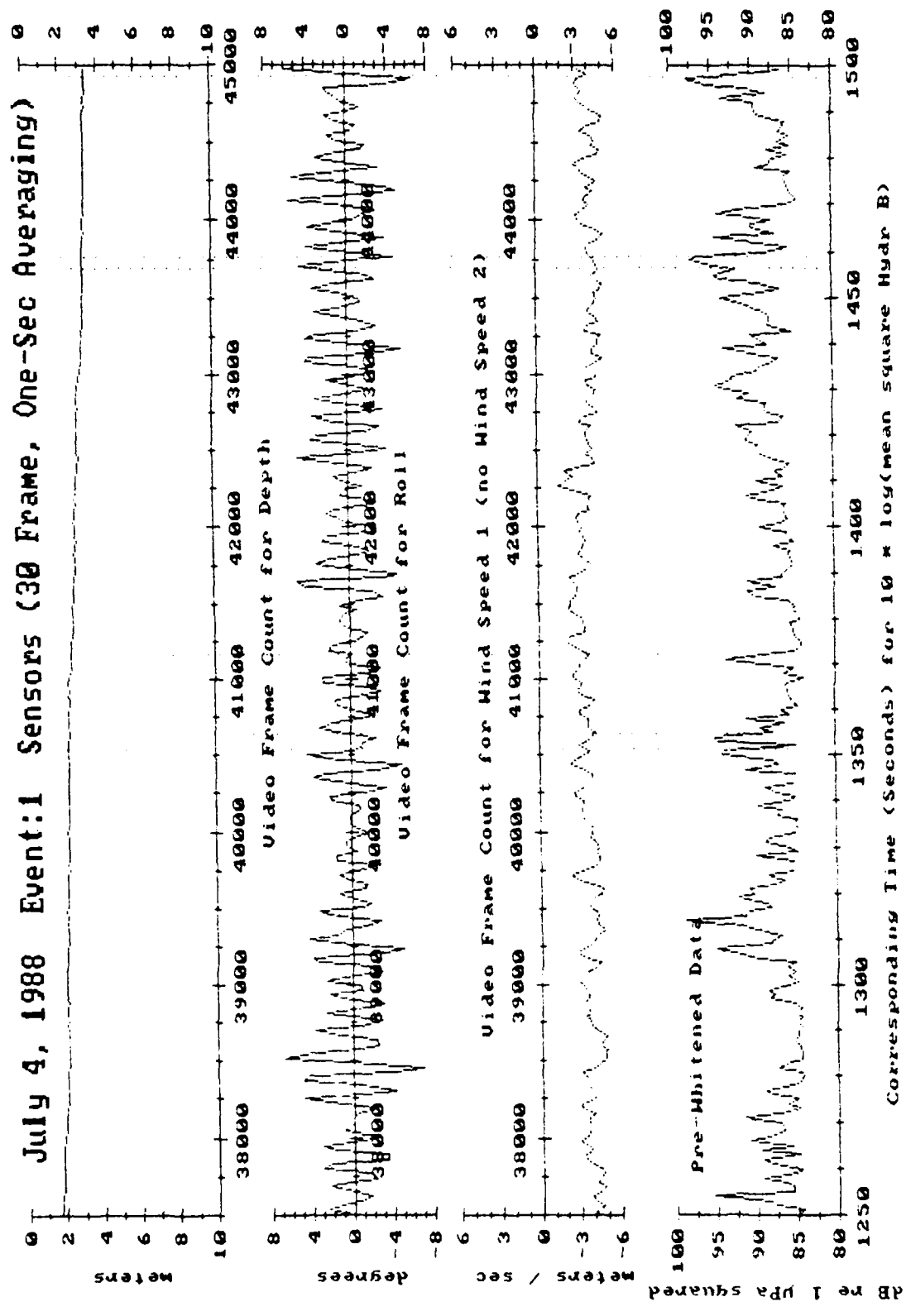
Appendix A, Figure 4c: Instrument depth and roll, plus nearby wind in one direction and the mean square acoustic pressure at Hydrophone B. Vertical dashed lines mark wavelet breaks.



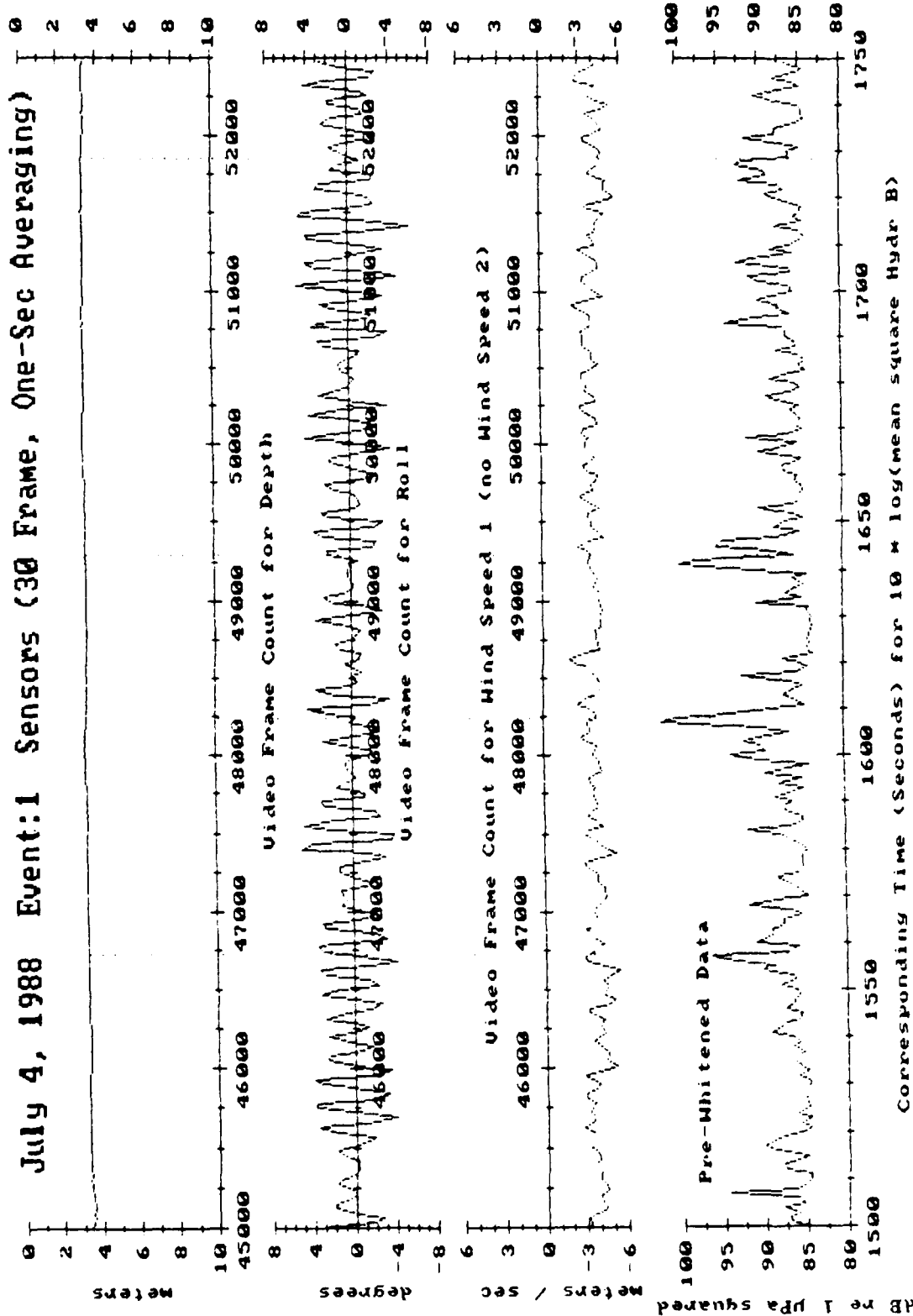
Appendix A, Figure 4d: Instrument depth and roll, plus nearby wind in one direction and the mean square acoustic pressure at Hydrophone B. Vertical dashed lines mark wavelet breaks.



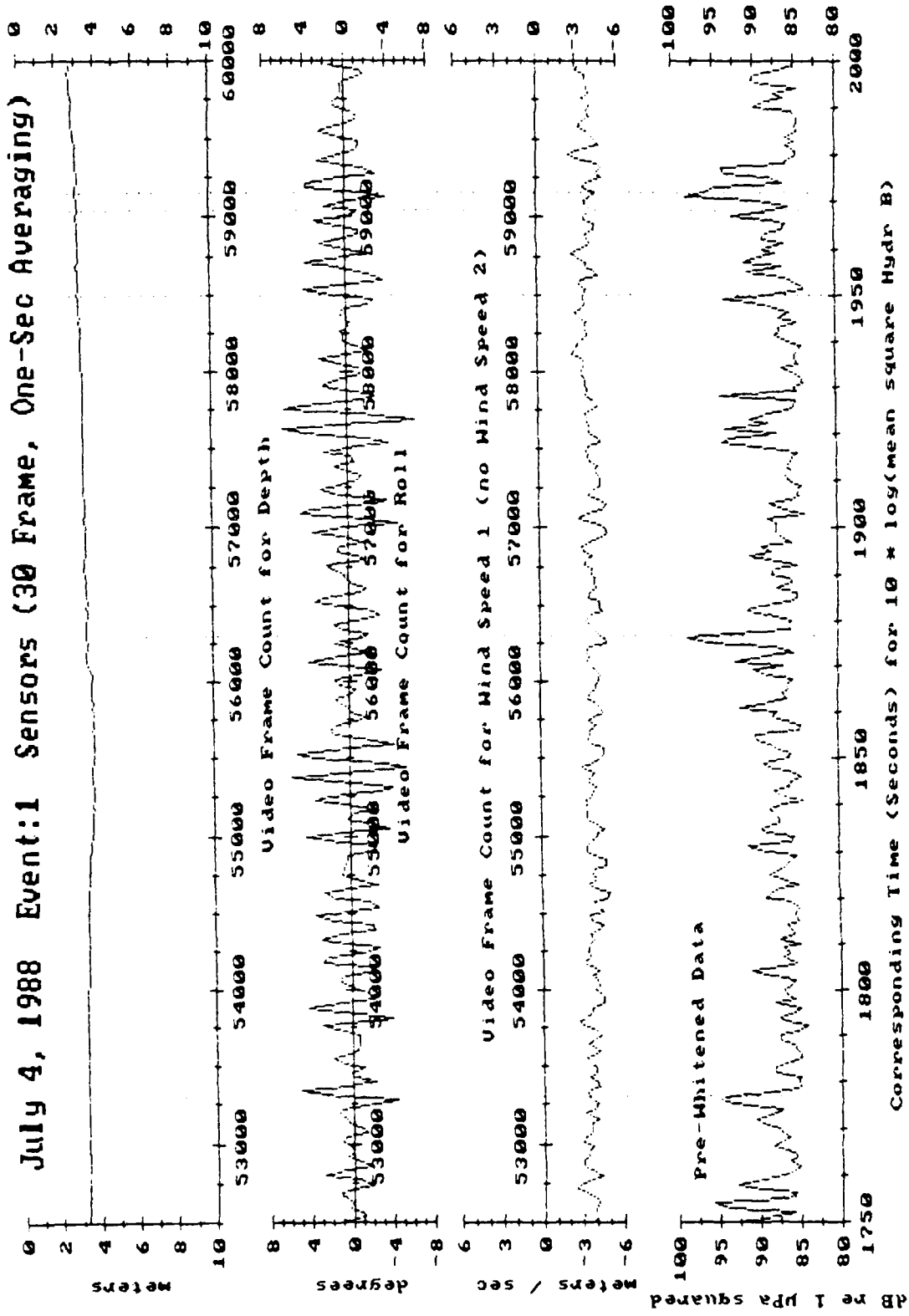
Appendix A, Figure 4e: Instrument depth and roll, plus nearby wind in one direction and the mean square acoustic pressure at Hydrophone B. Vertical dashed lines mark wavelet breaks.



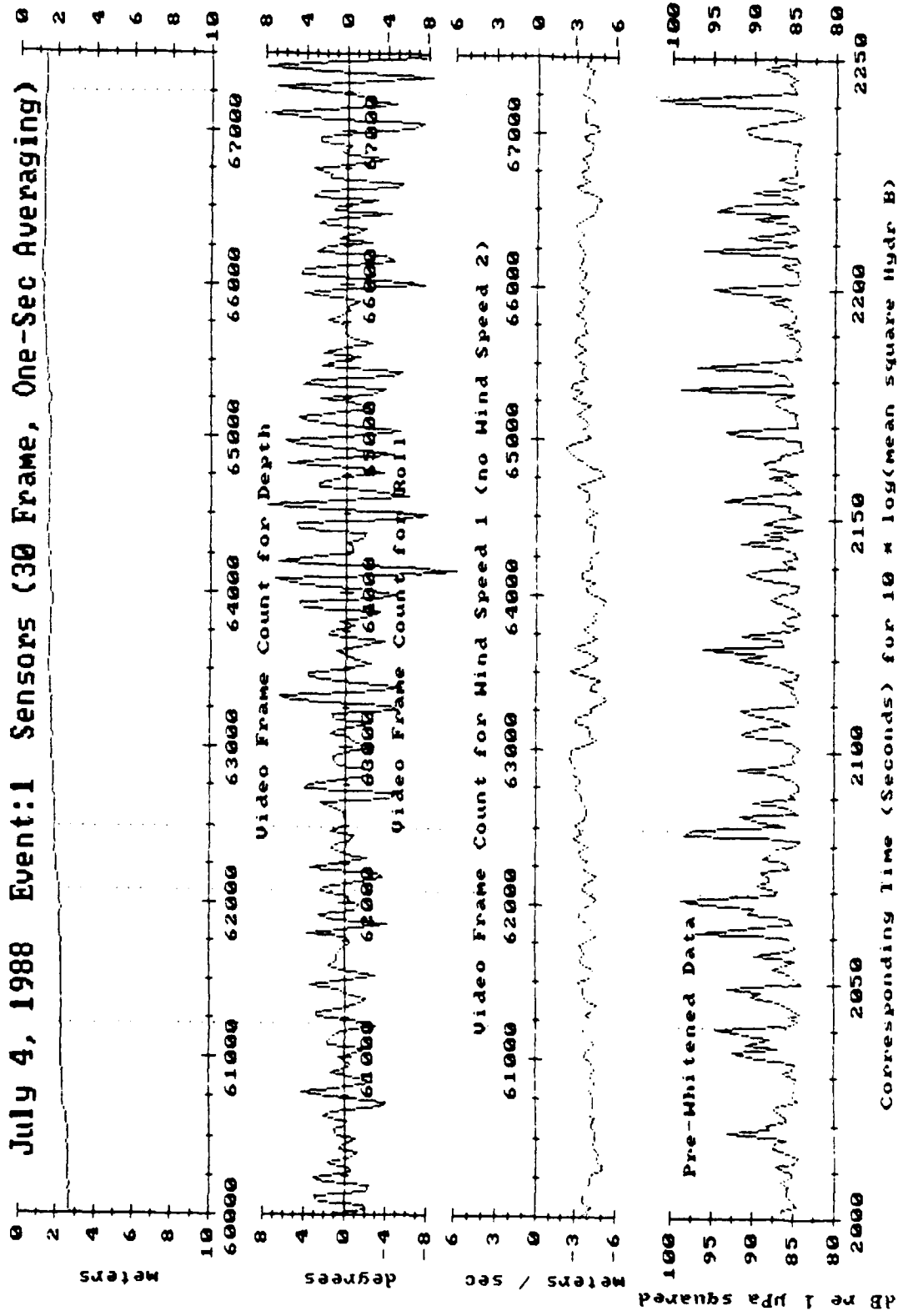
Appendix A, Figure 4f: Instrument depth and roll, plus nearby wind in one direction and the mean square acoustic pressure at Hydrophone B. Vertical dashed lines mark wavelet breaks.



Appendix A, Figure 4g: Instrument depth and roll, plus nearby wind in one direction and the mean square acoustic pressure at Hydrophone B. Vertical dashed lines mark wavelet breaks.



Appendix A, Figure 4h: Instrument depth and roll, plus nearby wind in one direction and the mean square acoustic pressure at Hydrophone B. Vertical dashed lines mark wavelet breaks.



Appendix A. Figure 4i: Instrument depth and roll, plus nearby wind in one direction and the mean square acoustic pressure at Hydrophone B. Vertical dashed lines mark wavelet breaks.

VI. ENVIRONMENTAL RECORD 2 FROM FEBRUARY 20, 1989

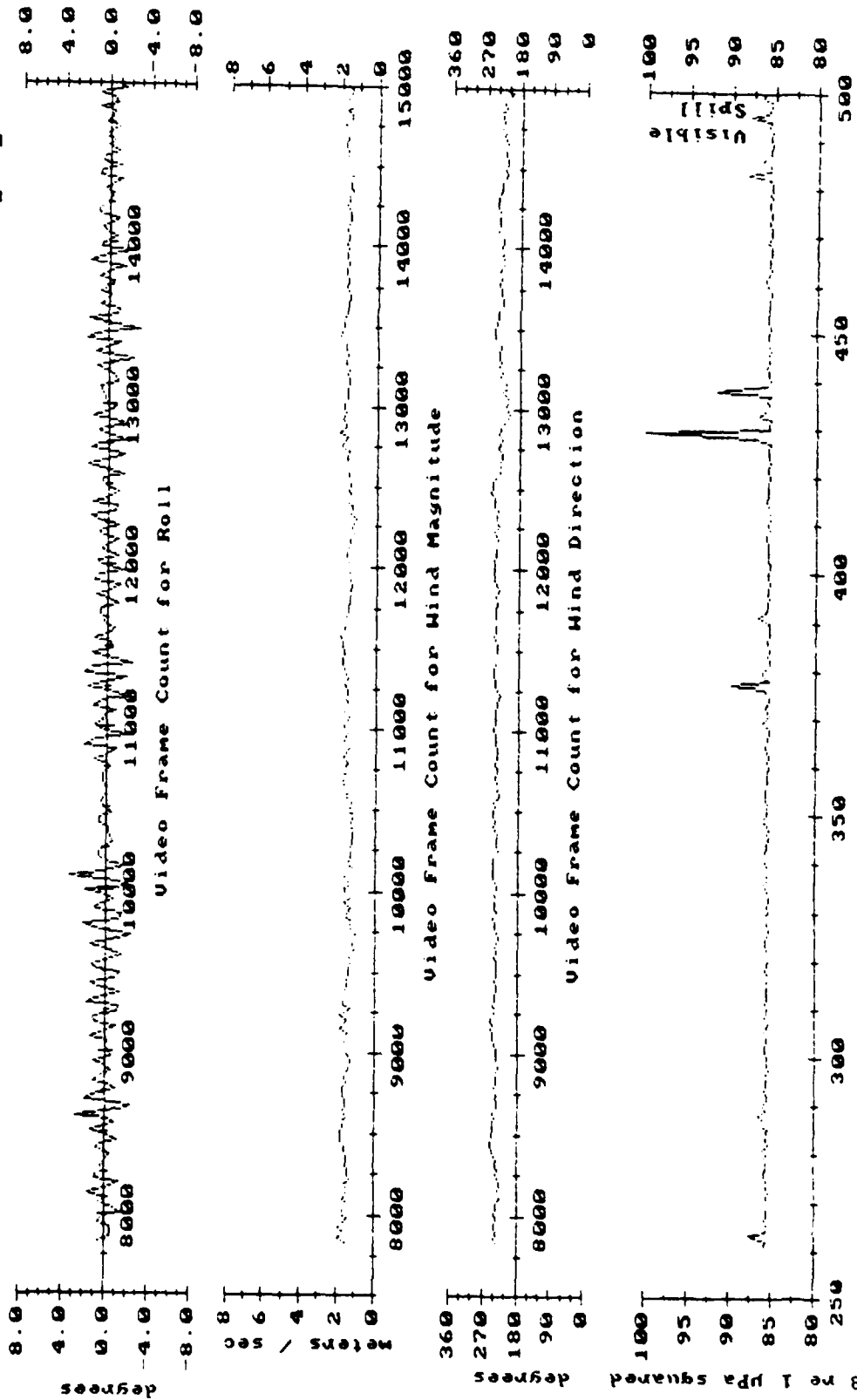
This record is plotted starting on the next page.

The data was recorded at 10:41 am, PST, at latitude 27° 38' and longitude 111° 38', in the Gulf of California. The surface conditions were about Sea State 1/2. The wind was blowing from 82 degrees at approximately 1.6 meters per second, as measured 1.5 meters over the sea surface by the SSNI wind buoy. Long period swell height was negligible.

Wavelet breaks are represented by peaks in the Mean Square Acoustic Pressure plot, unless marked otherwise in the plots. Data was not pre-whitened.

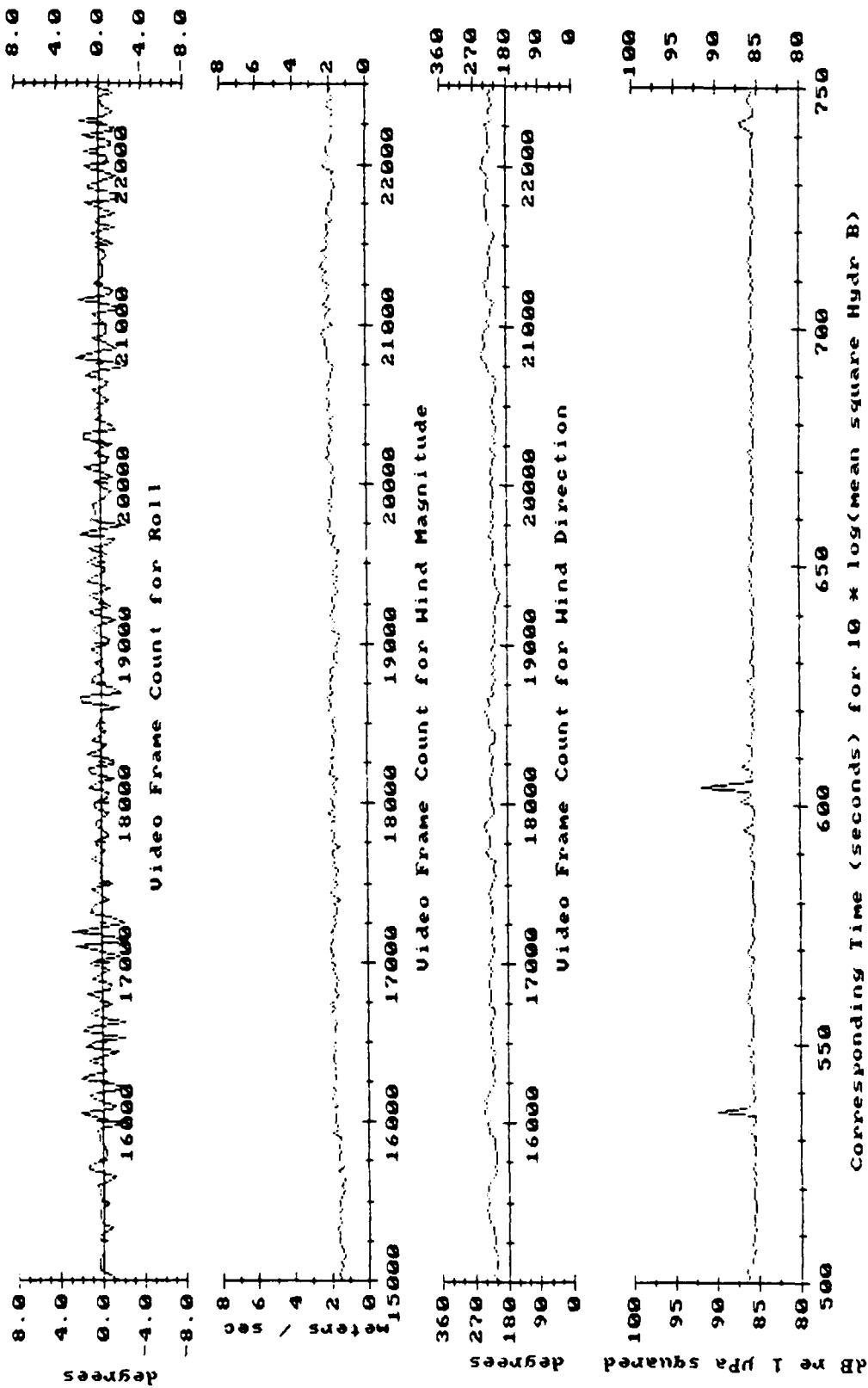
The depth sensor was not working during this deployment and has not been plotted.

Feb 20, 1989 Event:2 Sensors (30 Frame, One-Sec Averaging)



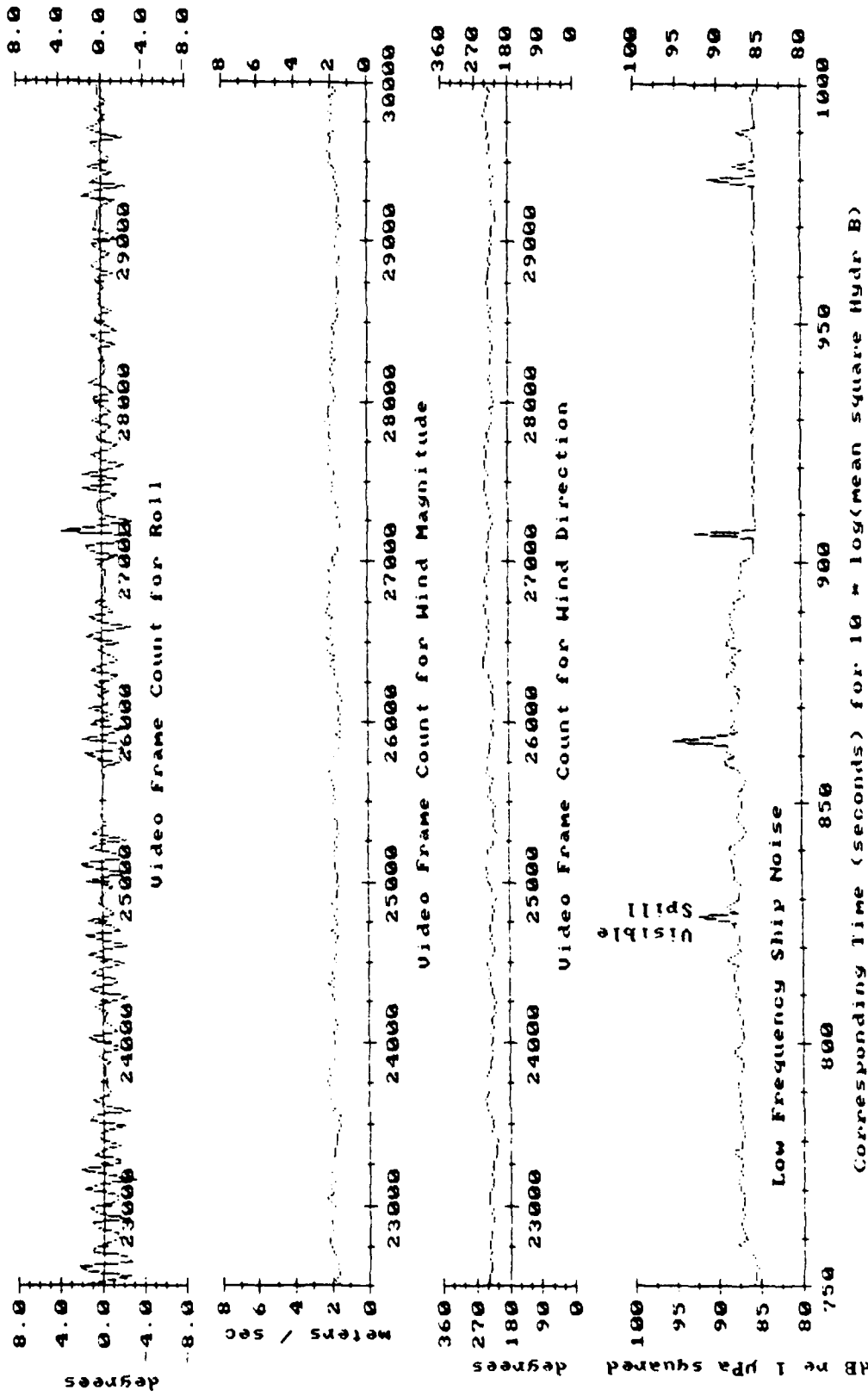
Appendix A, Figure 5a: Instrument roll, plus nearby wind speed and direction, and the mean square acoustic pressure at Hydrophone B.

Feb 20, 1989 Event:2 Sensors (30 Frame, One-Sec Averaging)



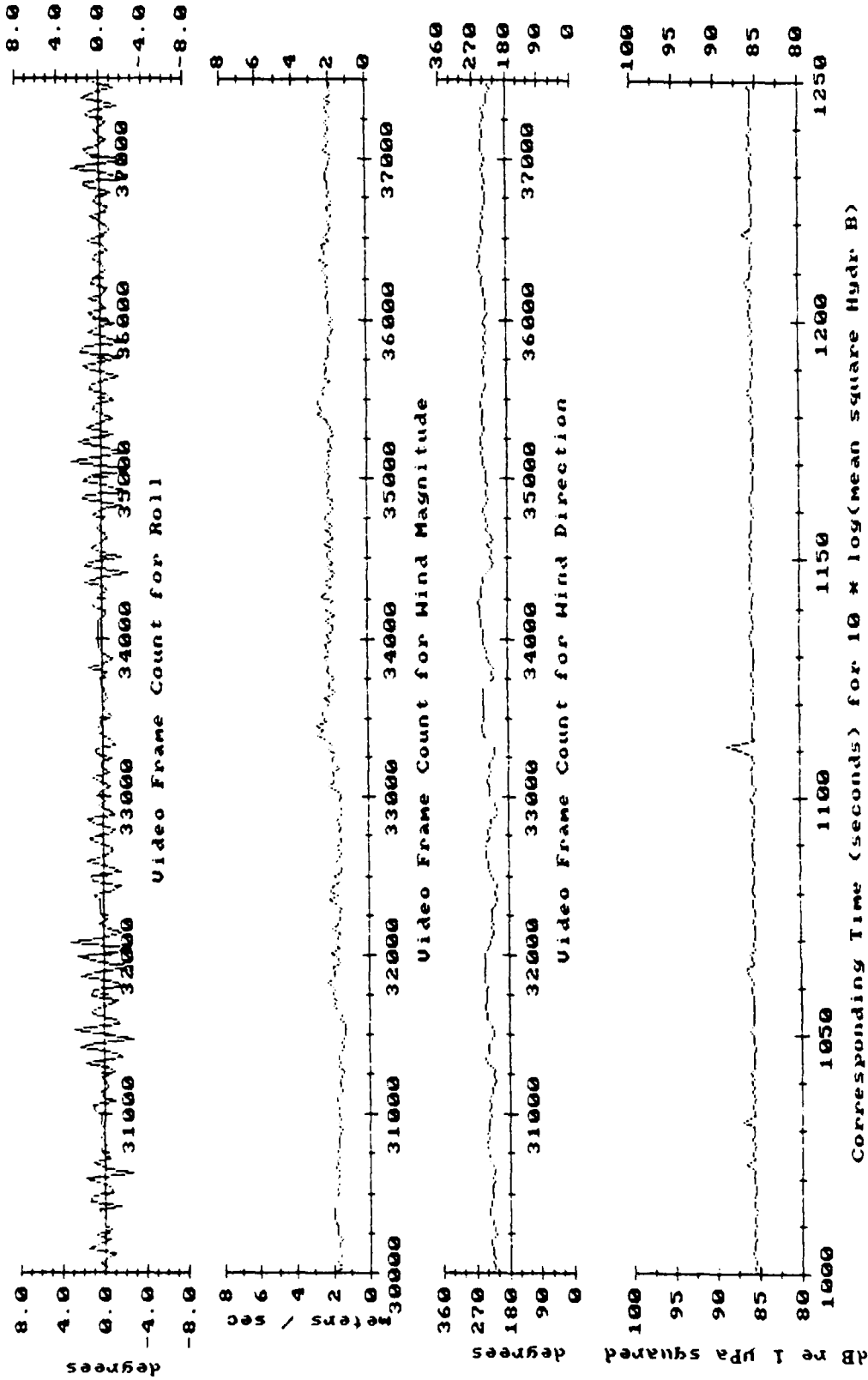
Appendix A, Figure 5b: Instrument roll, plus nearby wind speed and direction, and the mean square acoustic pressure at Hydrophone B.

Feb 20, 1989 Event:2 Sensors (30 Frame, One-Sec Averaging)



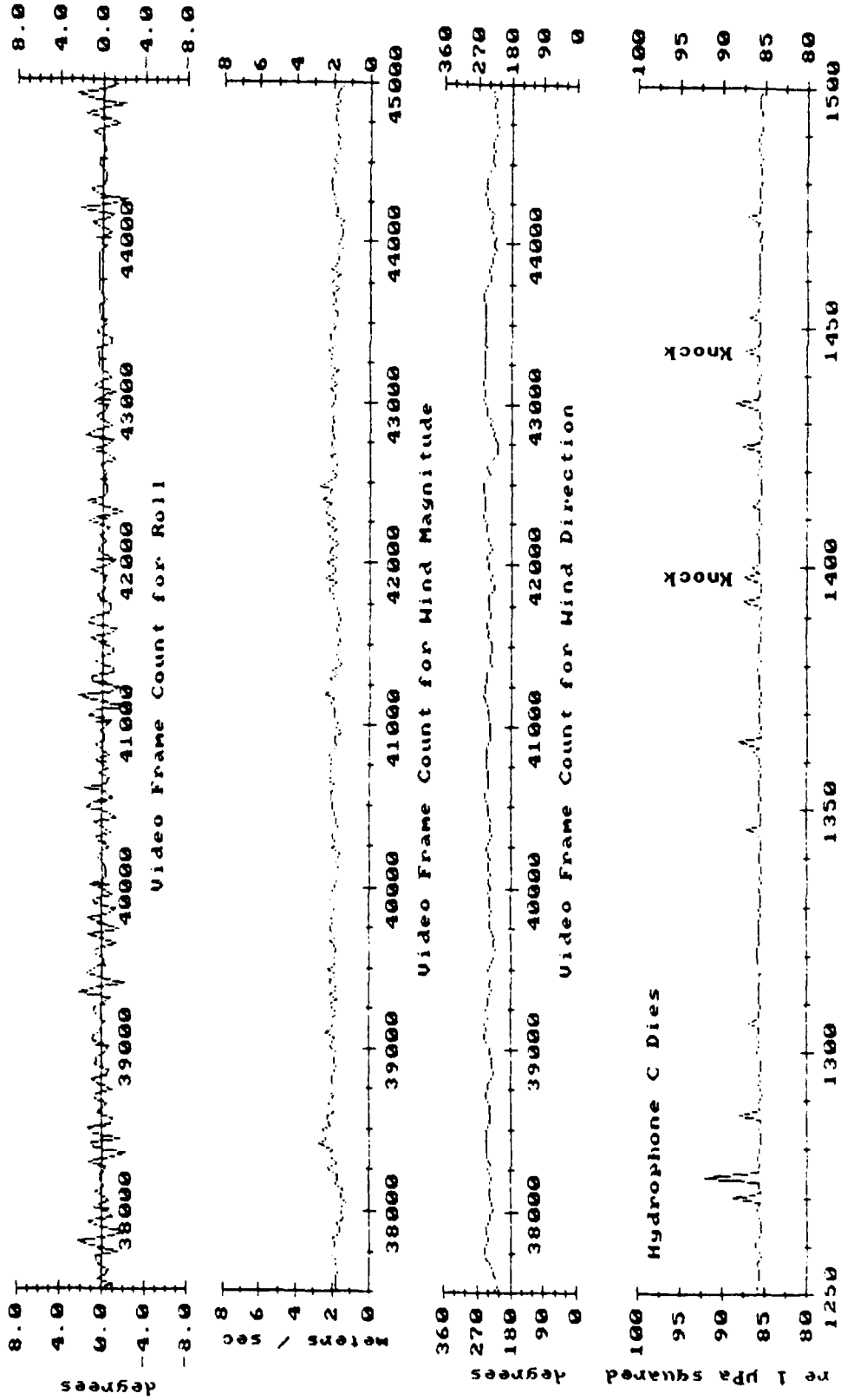
Appendix A, Figure 5c: Instrument roll, plus nearby wind speed and direction, and the mean square acoustic pressure at Hydrophone B.

Feb 20, 1989 Event:2 Sensors (30 Frame, One-Sec Averaging)



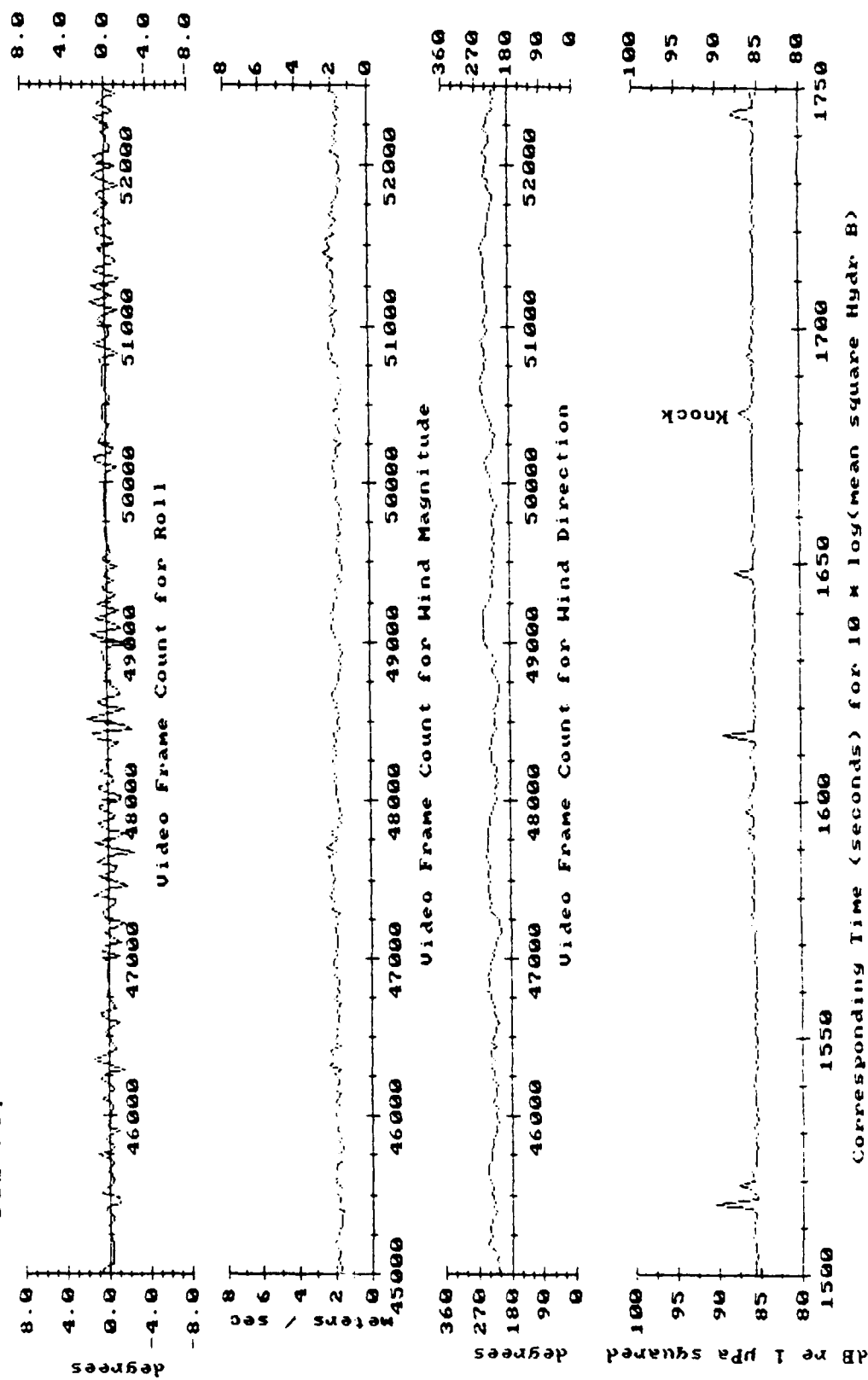
Appendix A, Figure 5d: Instrument roll, plus nearby wind speed and direction, and the mean square acoustic pressure at Hydrophone B.

Feb 20, 1989 Event:2 Sensors (30 Frame, One-Sec Averaging)



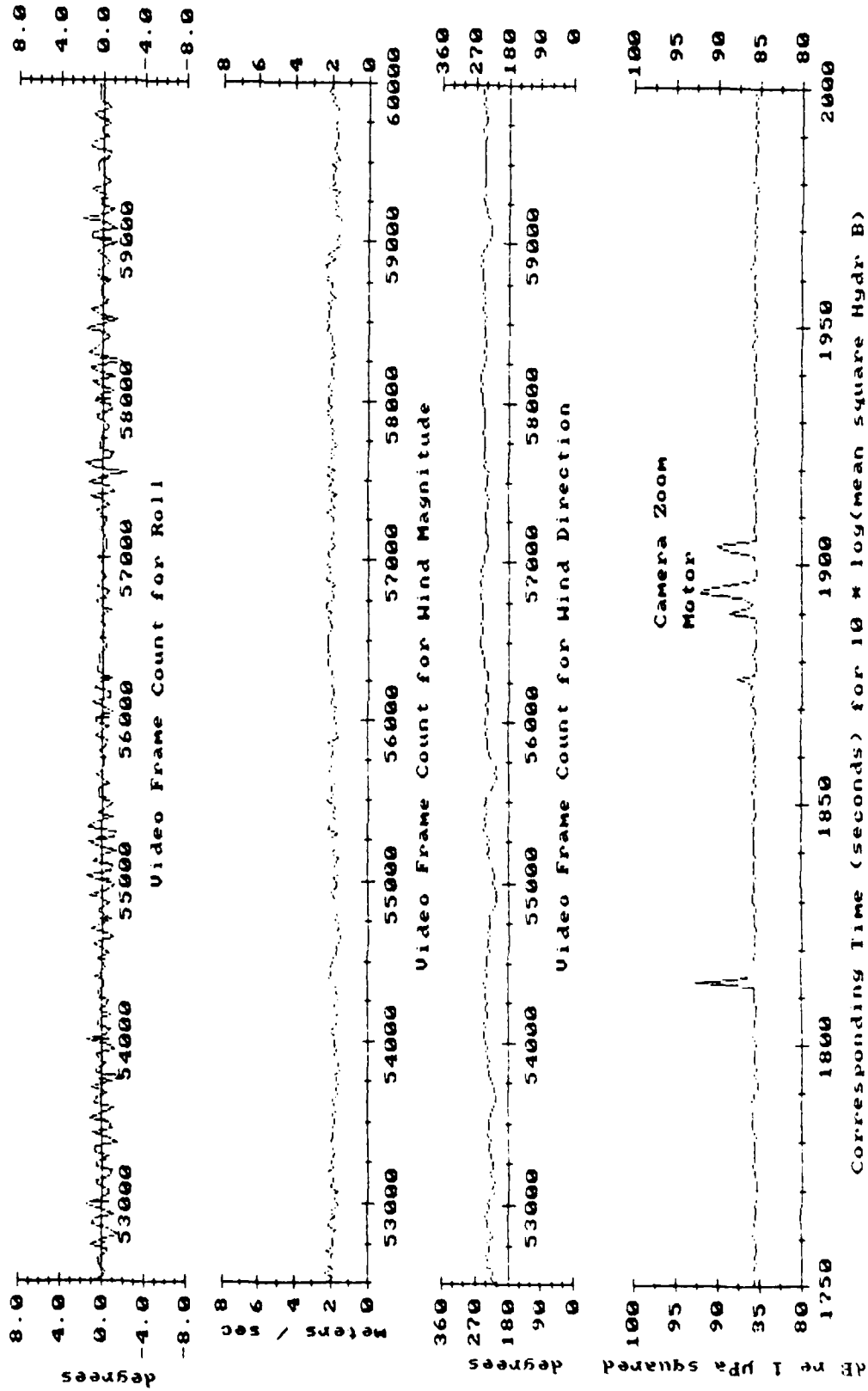
Appendix A, Figure 5e: Instrument roll, plus nearby wind speed and direction, and the mean square acoustic pressure at Hydrophone B.

Feb 20, 1989 Event:2 Sensors (30 Frame, One-Sec Averaging)



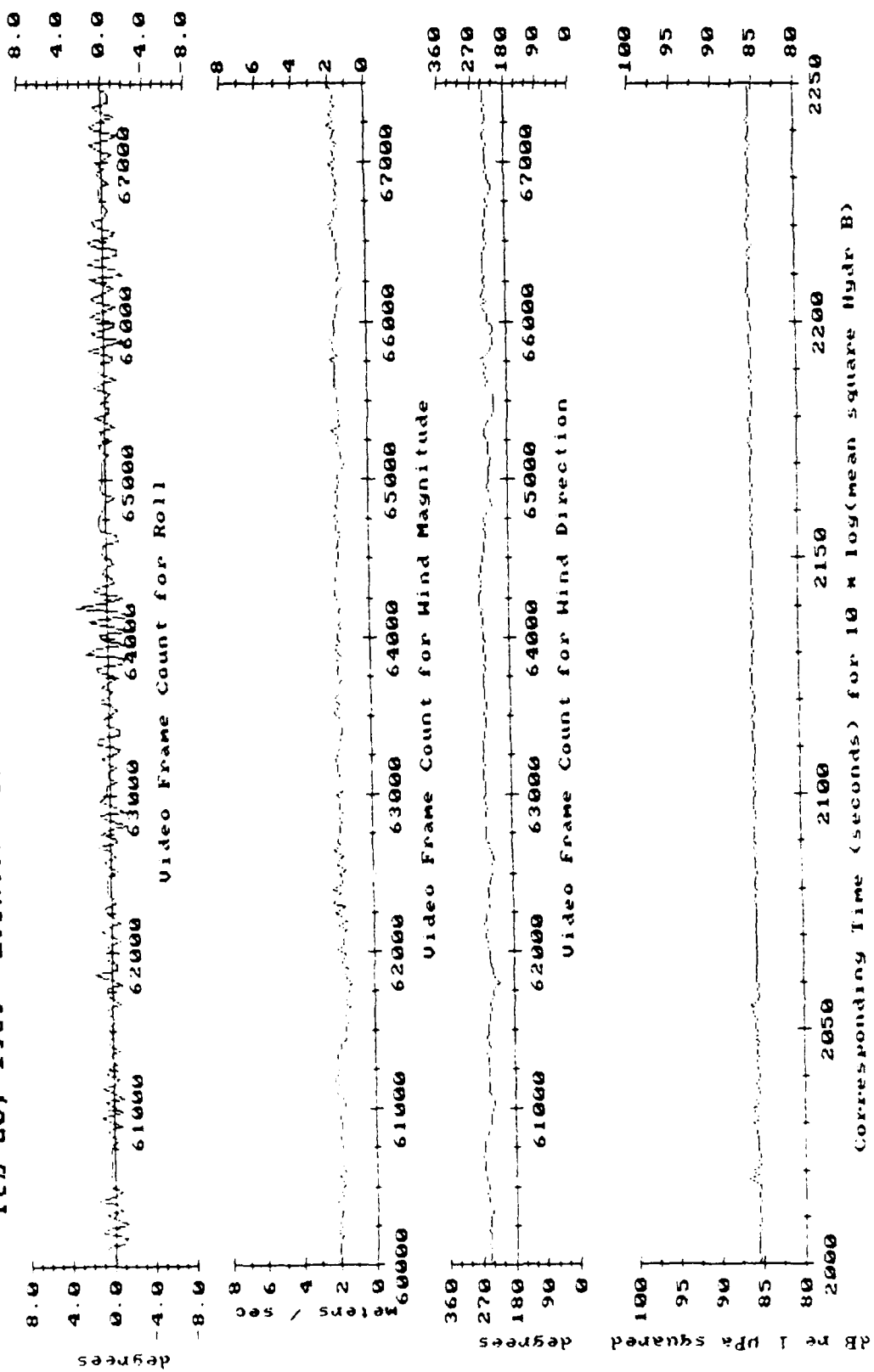
Appendix A, Figure 5f: Instrument roll, plus nearby wind speed and direction, and the mean square acoustic pressure at Hydrophone B.

Feb 20, 1989 Event:2 Sensors (30 Frame, One-Sec Averaging)



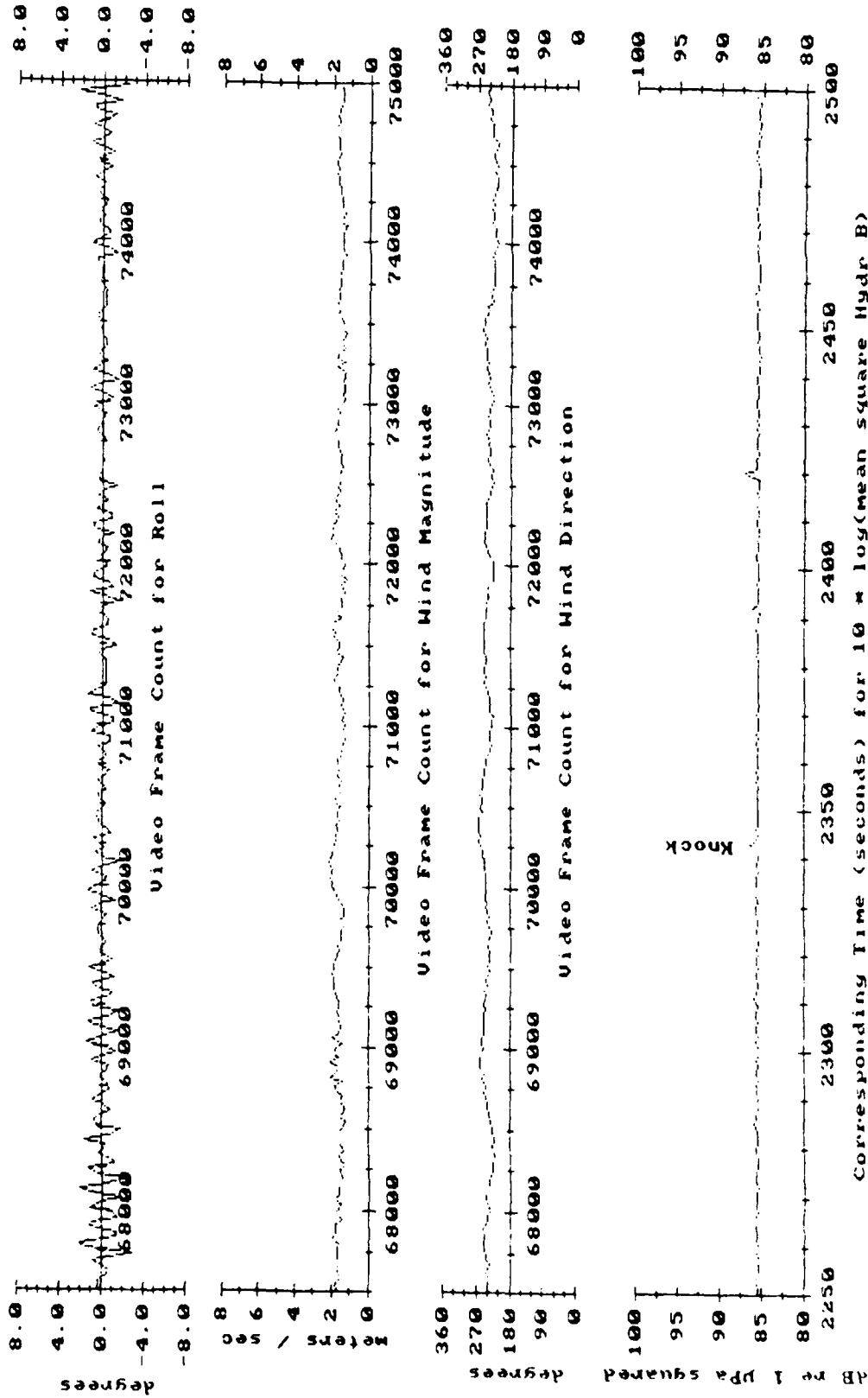
Appendix A, Figure 5g: Instrument roll, plus nearby wind speed and direction, and the mean square acoustic pressure at Hydrophone B.

Feb 20, 1989 Event:2 Sensors (30 Frame, One-Sec Averaging)



Appendix A, Figure 5h: Instrument roll, plus nearby wind speed and direction, and the mean square acoustic pressure at Hydrophone B.

Feb 20, 1989 Event:2 Sensors (30 Frame, One-Sec Averaging)



Appendix A, Figure 5i: Instrument roll, plus nearby wind speed and direction, and the mean square acoustic pressure at Hydrophone B.

VII. ENVIRONMENTAL RECORD 4 FROM FEBRUARY 20, 1989

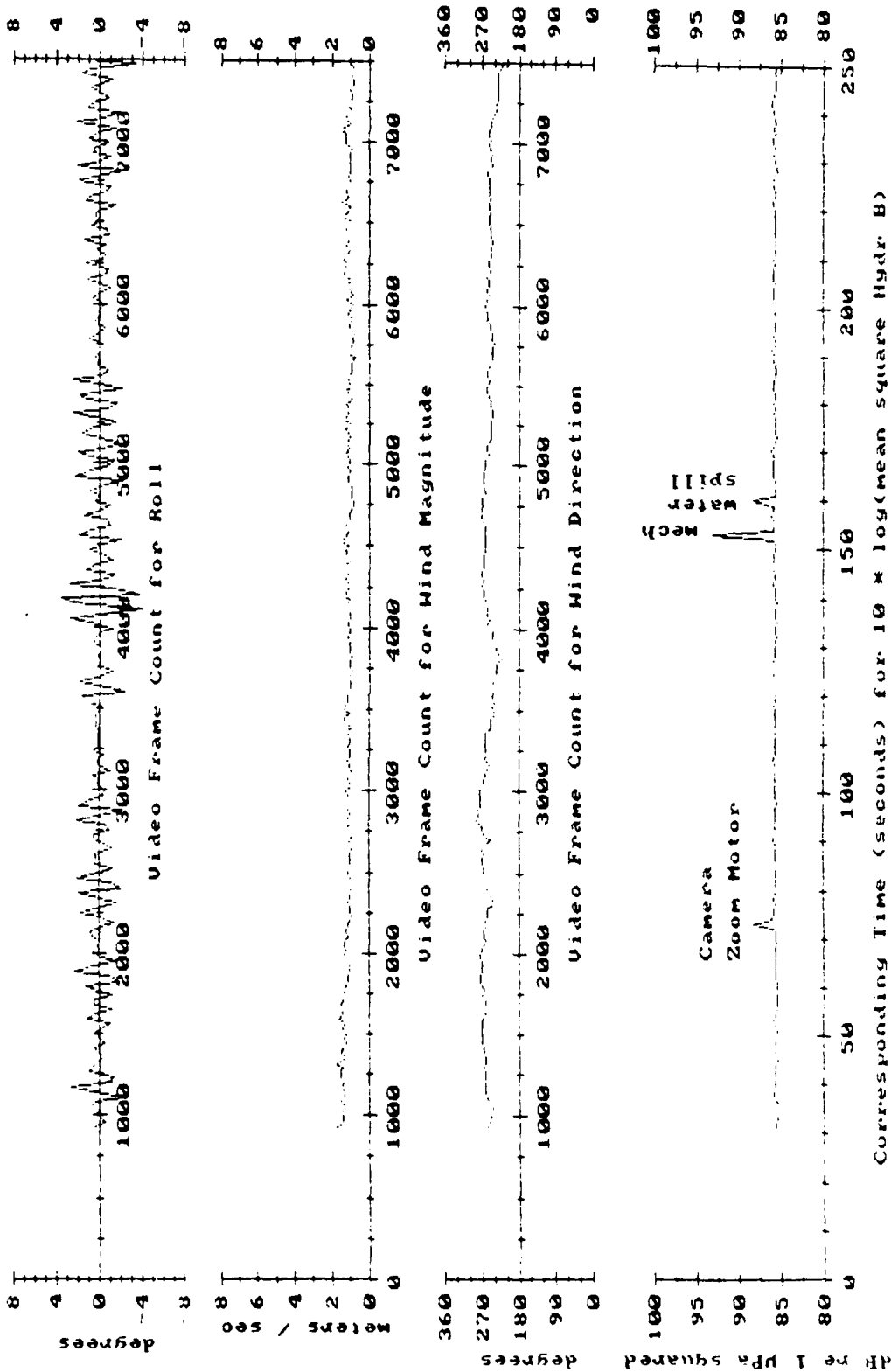
This record is plotted starting on the next page.

The data was recorded at 11:59 am, PST, at latitude 27° 37' and longitude 111° 40', in the Gulf of California. The surface conditions were about Sea State 1/2. The wind was blowing from 90 degrees at approximately 1.3 meters per second, as measured 1.5 meters over the sea surface by the SSNI wind buoy. Long period swell height was negligible.

Only one wavelet break was noted during the entire recording. Data was not pre-whitened.

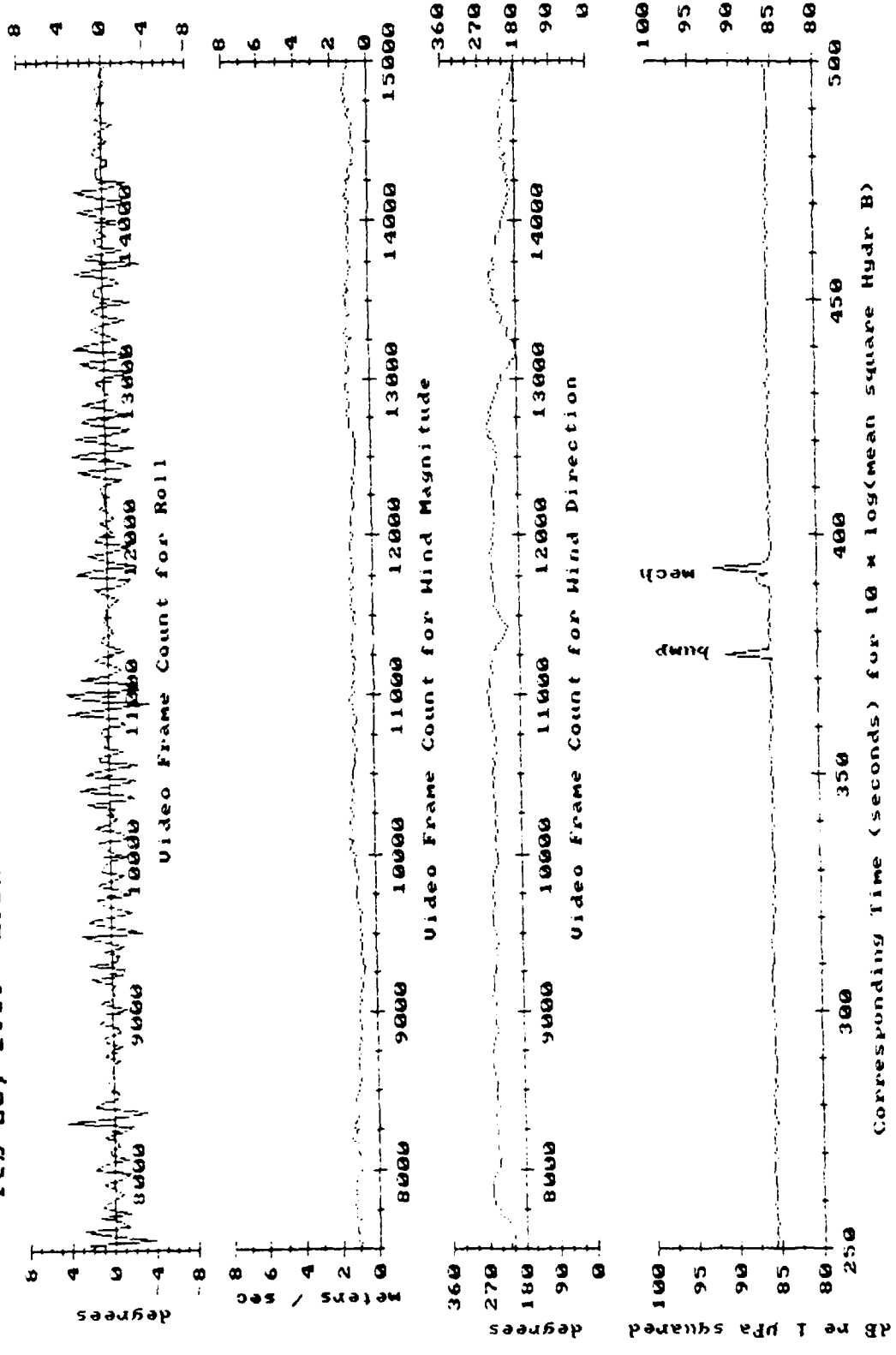
The depth sensor was not working during this deployment and has not been plotted.

Feb 20, 1989 Event:4 Sensors (30 Frame, One-Sec Averaging)



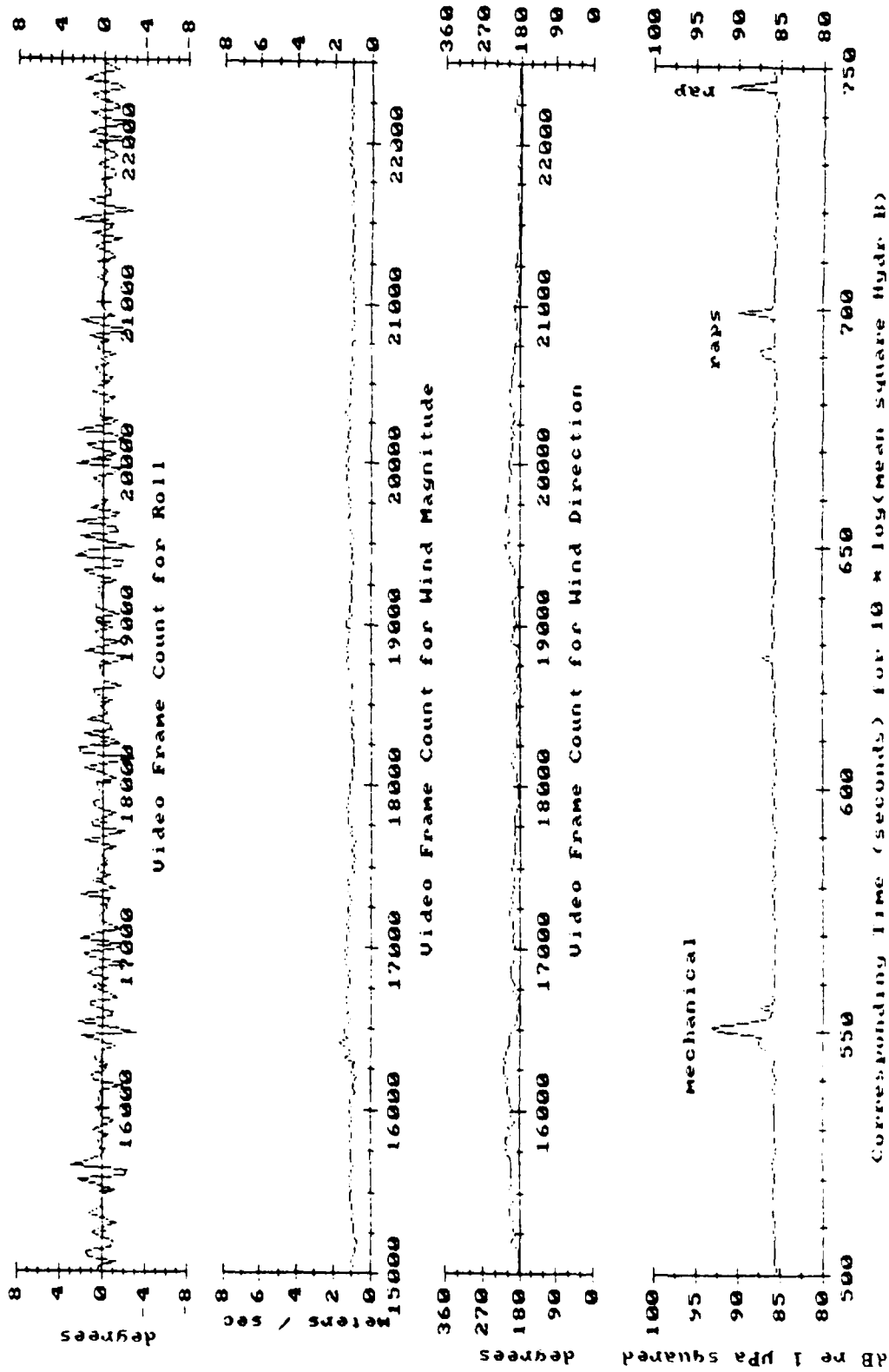
Appendix A, Figure 6a: Instrument roll, plus nearby wind speed and direction, and the mean square acoustic pressure at Hydrophone B.

Feb 20, 1989 Event: 4 Sensors (30 Frame, One-Sec Averaging)



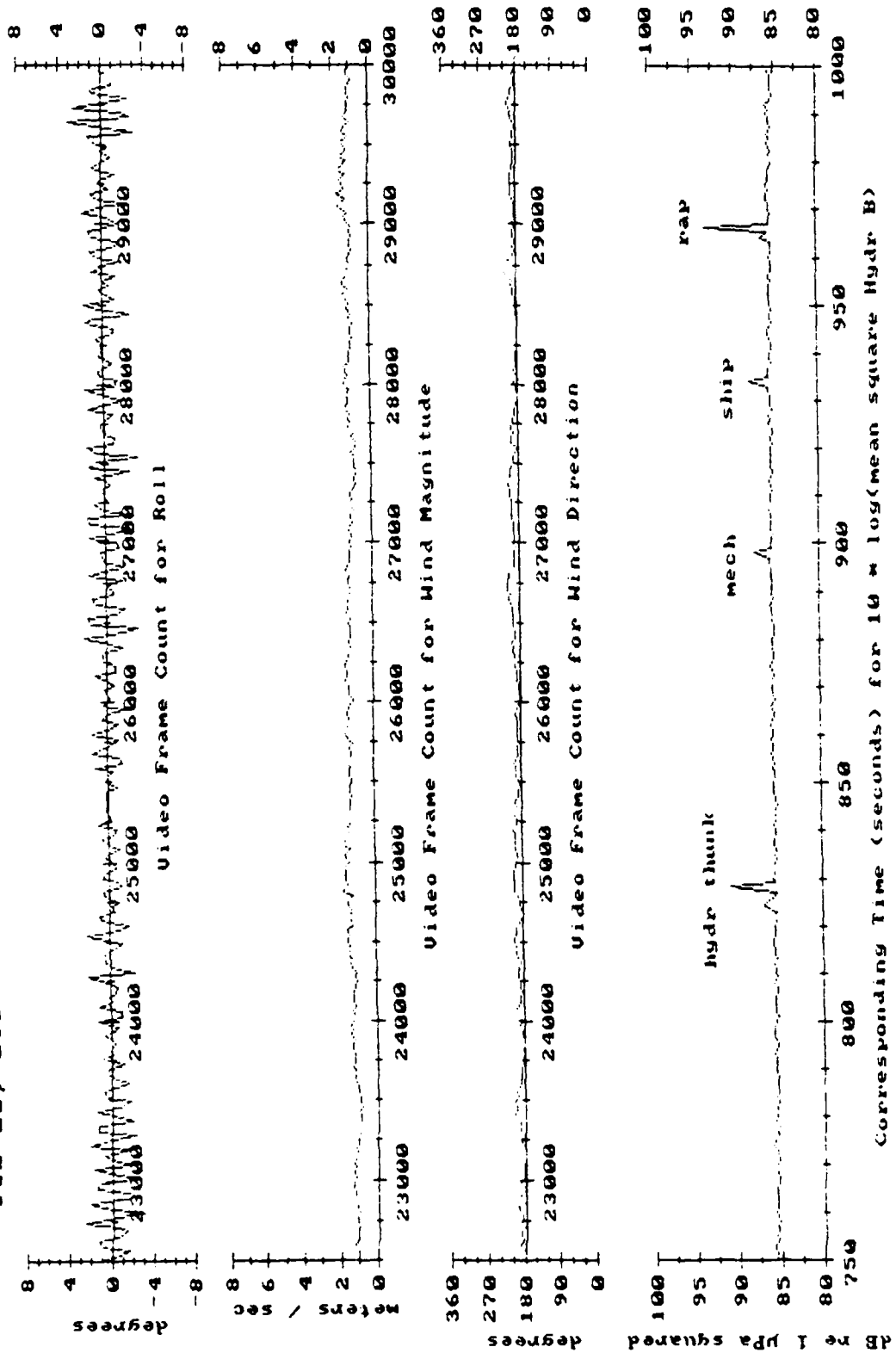
Appendix A, Figure 6b: Instrument roll, plus nearby wind speed and direction, and the mean square acoustic pressure at Hydrophone B.

Feb 20, 1989 Event: 4 Sensors (30 Frame, One-Sec Averaging)



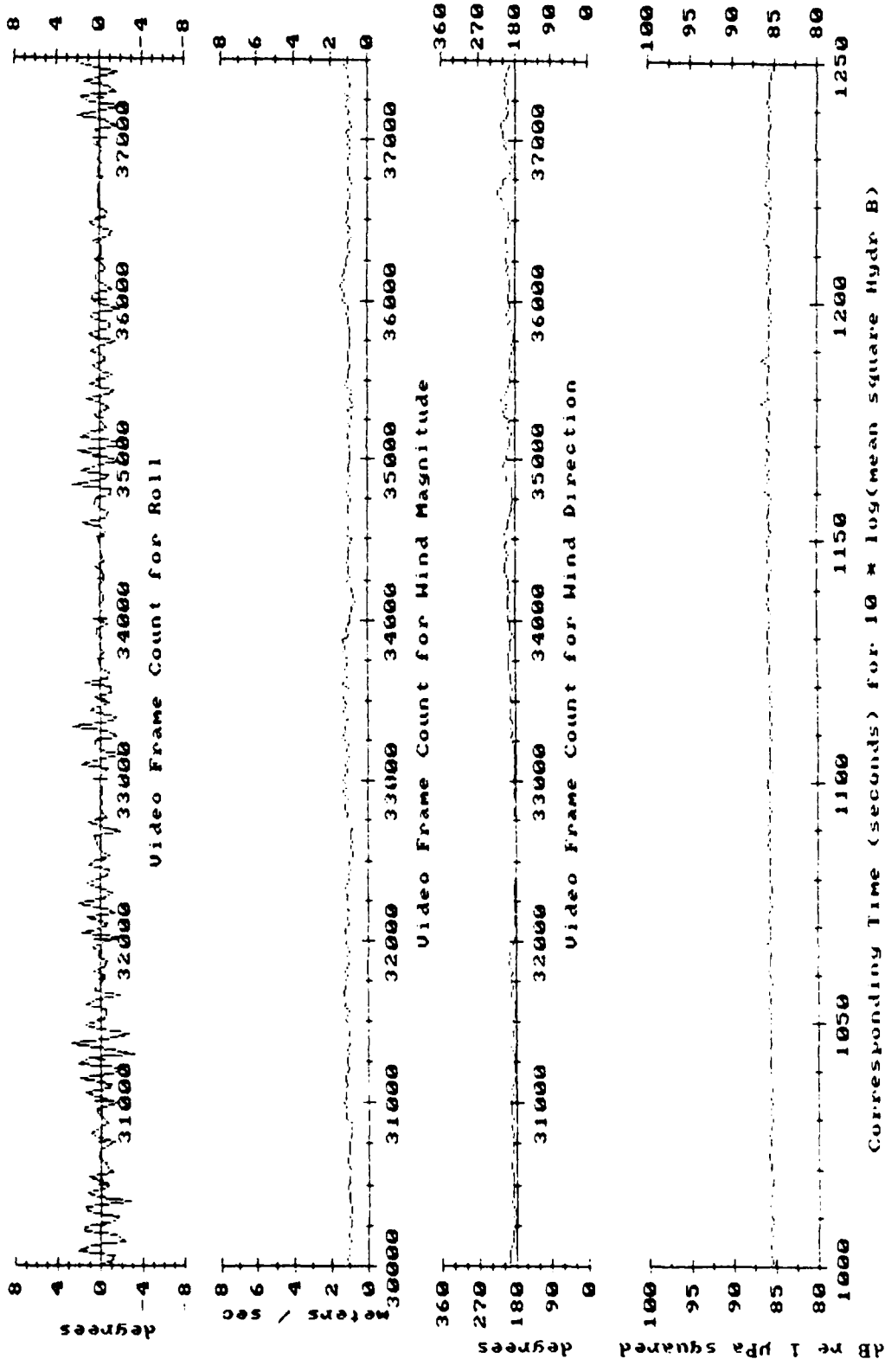
Appendix A, Figure 6c: Instrument roll, plus nearby wind speed and direction, and the mean square acoustic pressure at Hydrophone B.

Feb 20, 1989 Event: 4 Sensors (30 Frame, One-Sec Averaging)



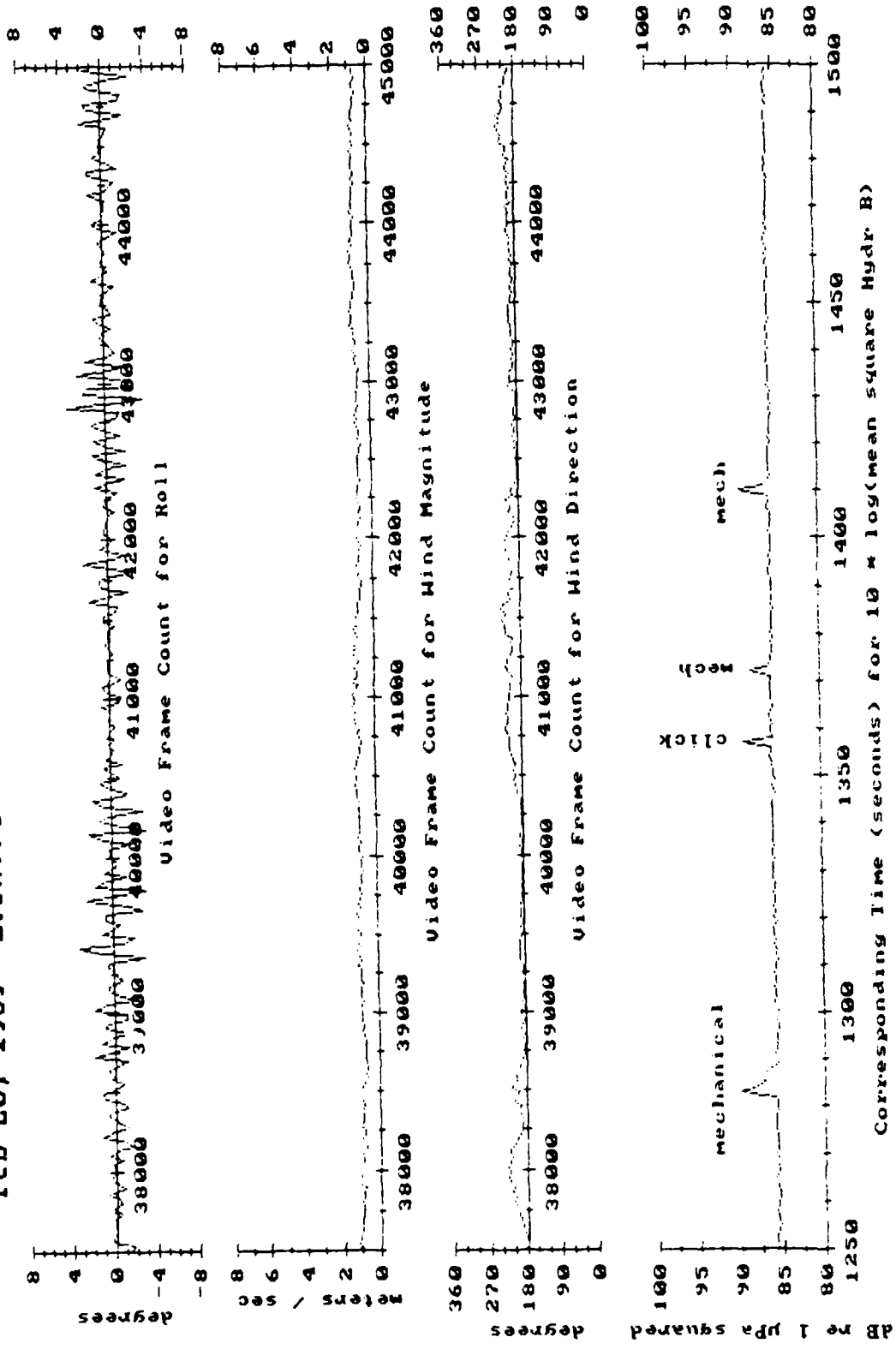
Corresponding Time (seconds) for 10 * log(mean square Hydr B)
 Appendix A, Figure 6d: Instrument roll, plus nearby wind speed and direction, and the mean square acoustic pressure at Hydrophone B.

Feb 20, 1989 Event: 4 Sensors (30 Frame, One-Sec Averaging)



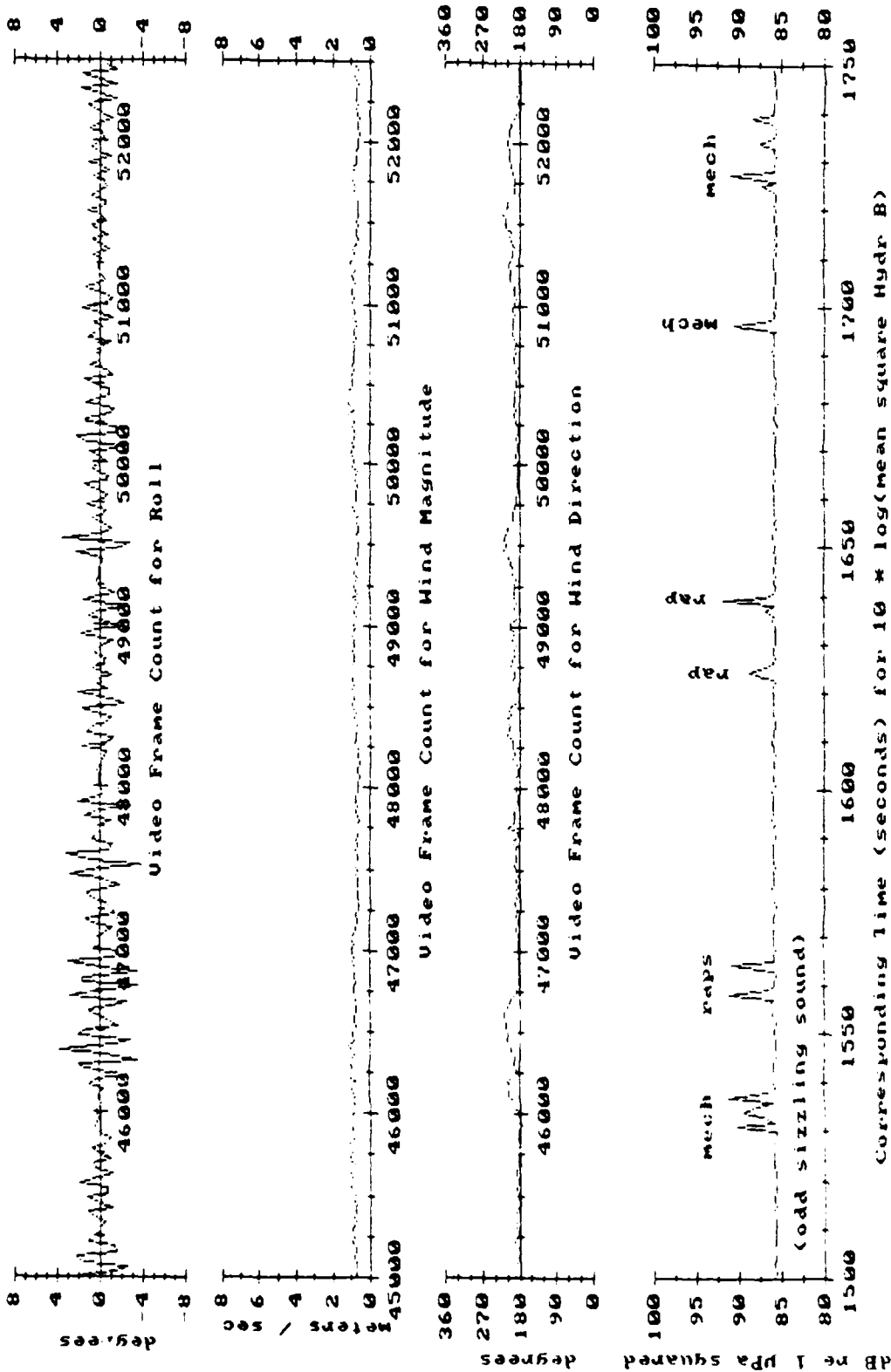
Appendix A, Figure 6e: Instrument roll, plus nearby wind speed and direction, and the mean square acoustic pressure at Hydrophone B.

Feb 20, 1989 Event: 4 Sensors (30 Frame, One-Sec Averaging)



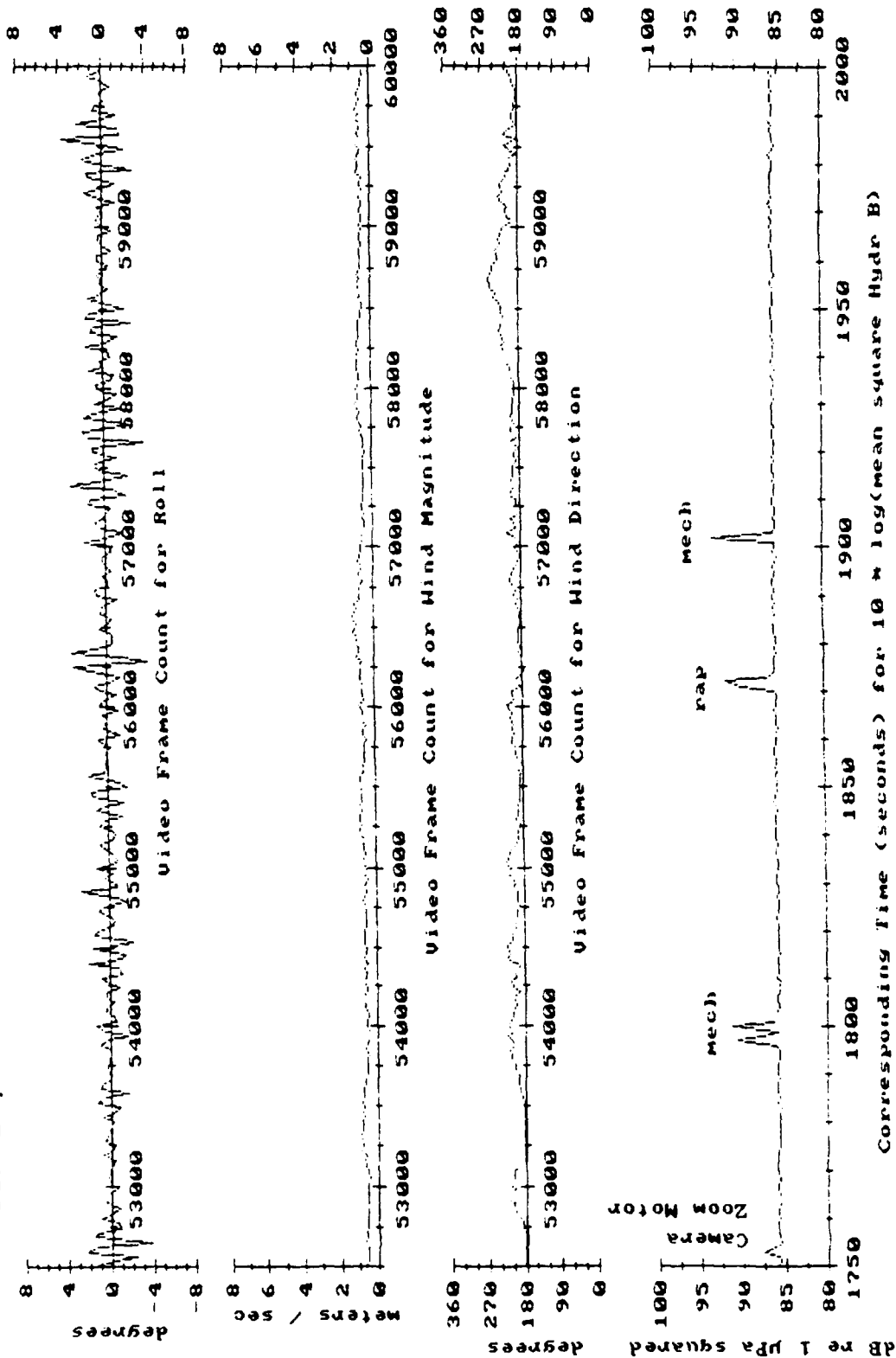
Appendix A, Figure 6f: Instrument roll, plus nearby wind speed and direction, and the mean square acoustic pressure at hydrophone B.

Feb 20, 1989 Event: 4 Sensors (30 Frame, One-Sec Averaging)



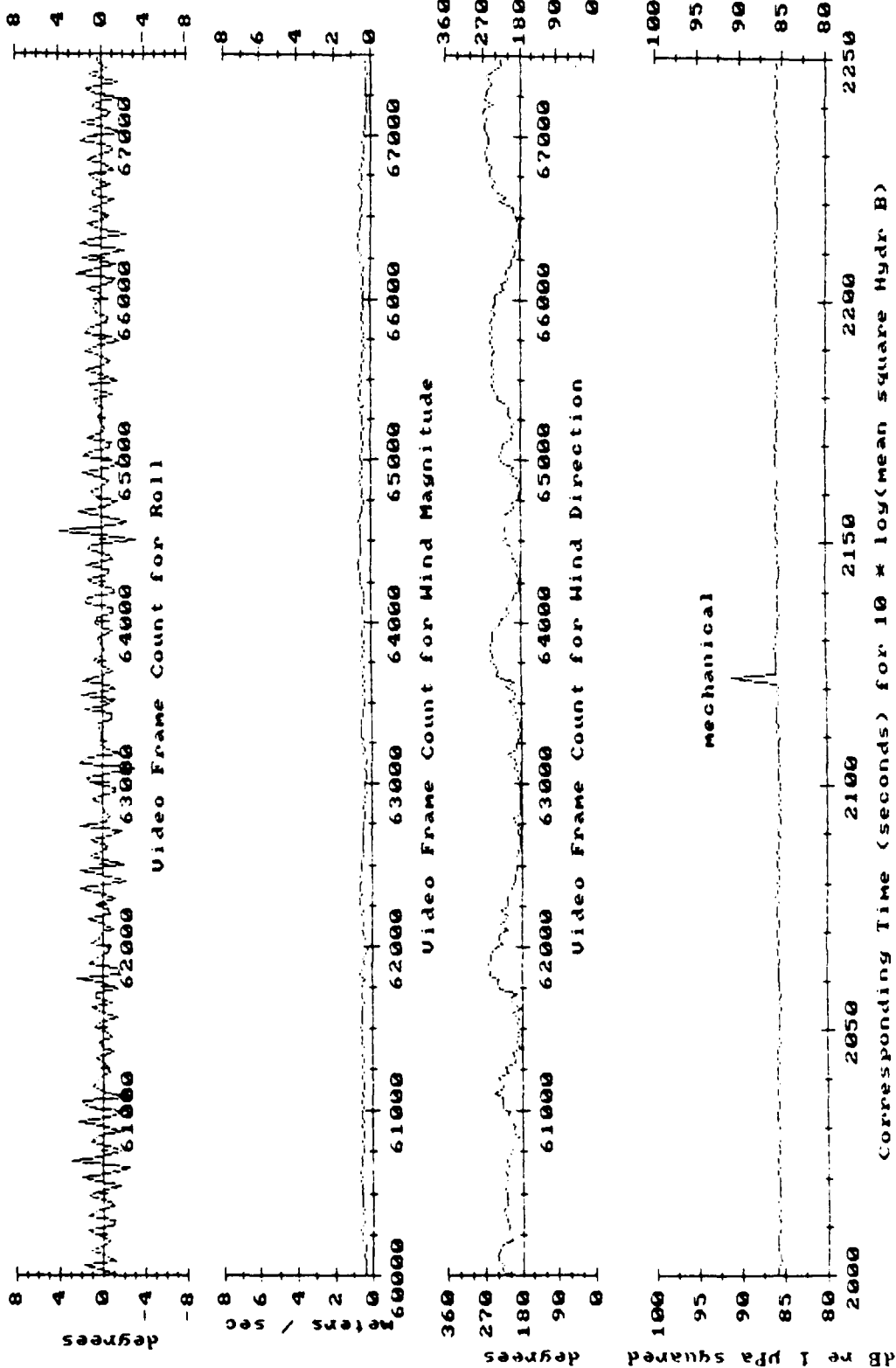
Appendix A, Figure 6g: Instrument roll, plus nearby wind speed and direction, and the mean square acoustic pressure at Hydrophone B.

Feb 20, 1989 Event: 4 Sensors (30 Frame, One-Sec Averaging)



Appendix A, Figure 6h: Instrument roll, plus nearby wind speed and direction, and the mean square acoustic pressure at Hydrophone B.

Feb 20, 1989 Event:4 Sensors (30 Frame, One-Sec Averaging)



Appendix A, Figure 6i: Instrument roll, plus nearby wind speed and direction, and the mean square acoustic pressure at Hydrophone B.

Appendix B:

Acoustic Time Series Samples From February 20, 1989, Record 2

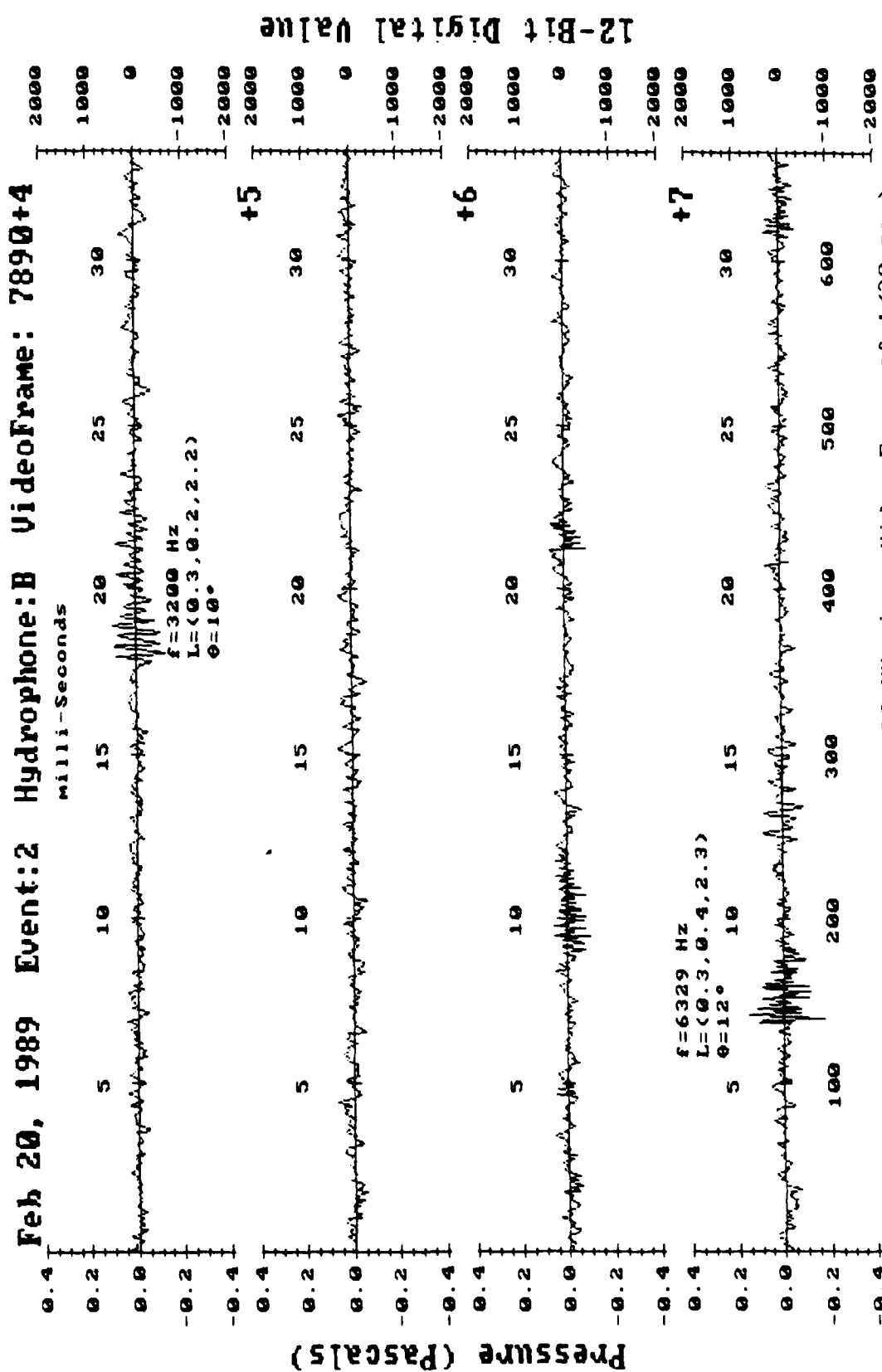
With a considerable amount of acoustic data recorded by the SSNI, and yet with few samples displayed in the rest of this dissertation, I have utilized this appendix to include additional time series samples from small wavelet spills. Each section that follows contains plot pages covering the entirety of a wavelet break, as recorded by Hydrophone B of the SSNI on February 20, 1989. The sound from each spill generally takes place within one second. The environmental conditions during these spills can be obtained from Appendix A, Figures 5a to 5i, pages 158 to 166, by matching Video Frame numbers.

Spills from this particular deployment have been selected because the pre-whitening filter, utilized in earlier deployments, was removed. Thus the frequency response is fairly flat from 800 to 8,000 Hertz. Unfortunately, the SSNI depth sensor was not working at this time. However, in previous deployments the calculated position of recorded bubble oscillations, accurate to $\pm 10\%$ (at a depth of approximately 2 meters), has been at the surface. Cartesian coordinates, relative to Hydrophone B and calculated using the signals from all four hydrophones, have been listed for most of the oscillations in these plots.

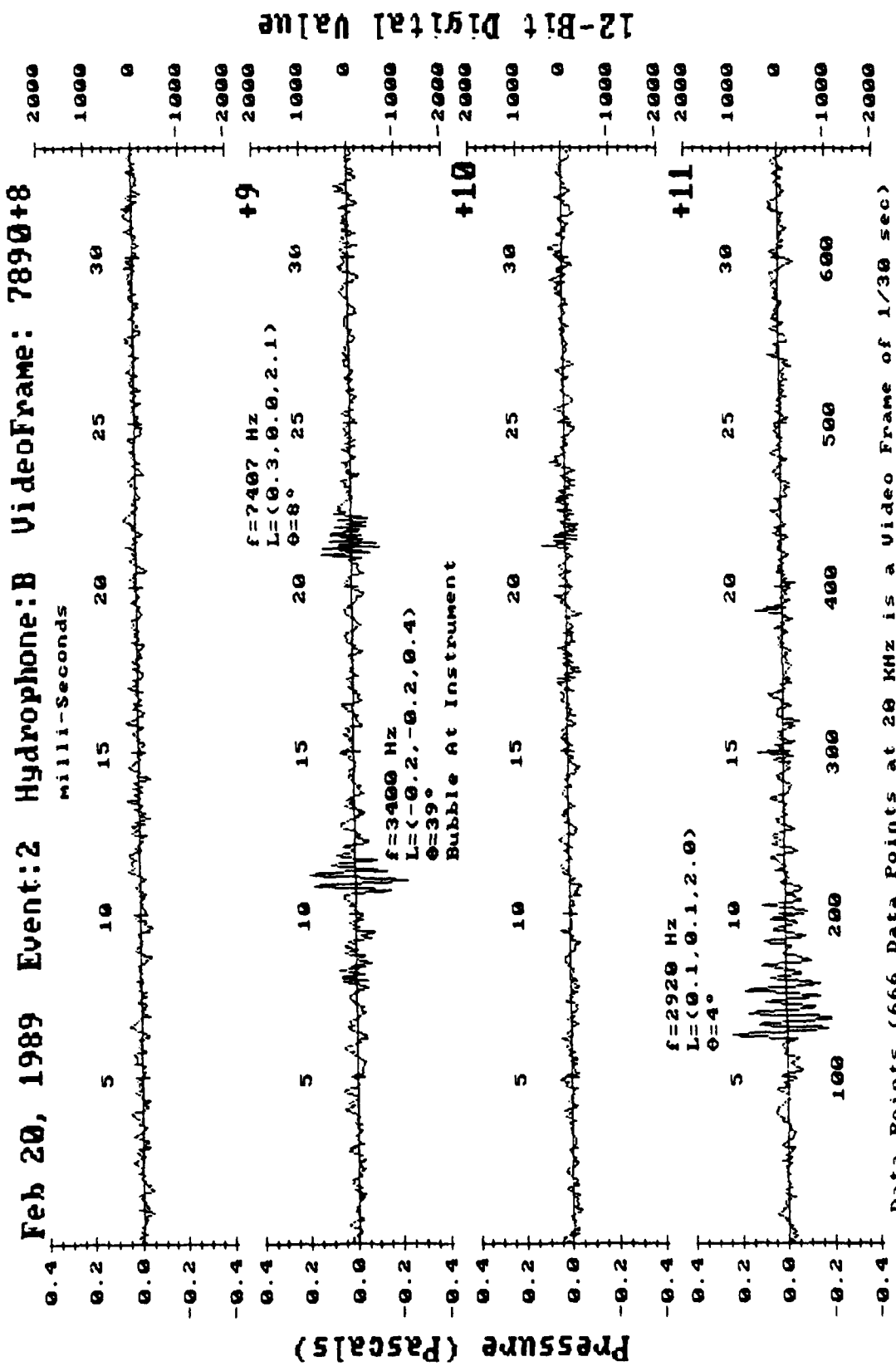
I. WAVELET BREAK AT VIDEO FRAME 7890

Within each of the contiguous plot pages which follow are four contiguous 1/30-second sections of data, each of which matches one video frame picture. Each plot line is labeled with an offset from the base reference Frame 7890.

Where possible, larger oscillations have been labeled as to frequency, locations relative to Hydrophone B, and angle from vertical over Hydrophone B. Bubble positions are accurate to +/- 10%.

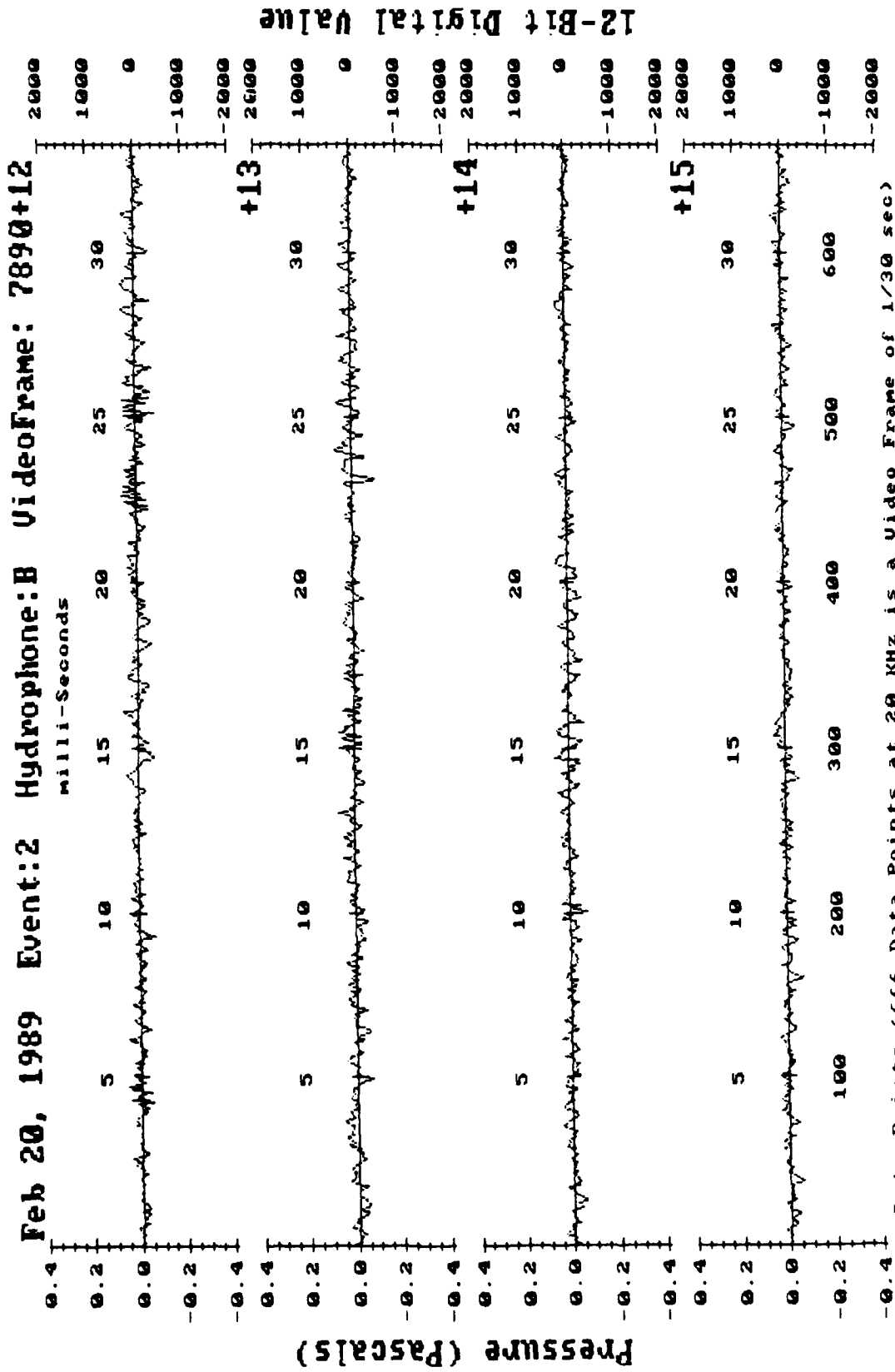


Data Points (666 Data Points at 20 KHz is a Video Frame of 1/30 sec)
 Appendix B, Figure 1b: Acoustic time Series, Frames 7894 to 7897.



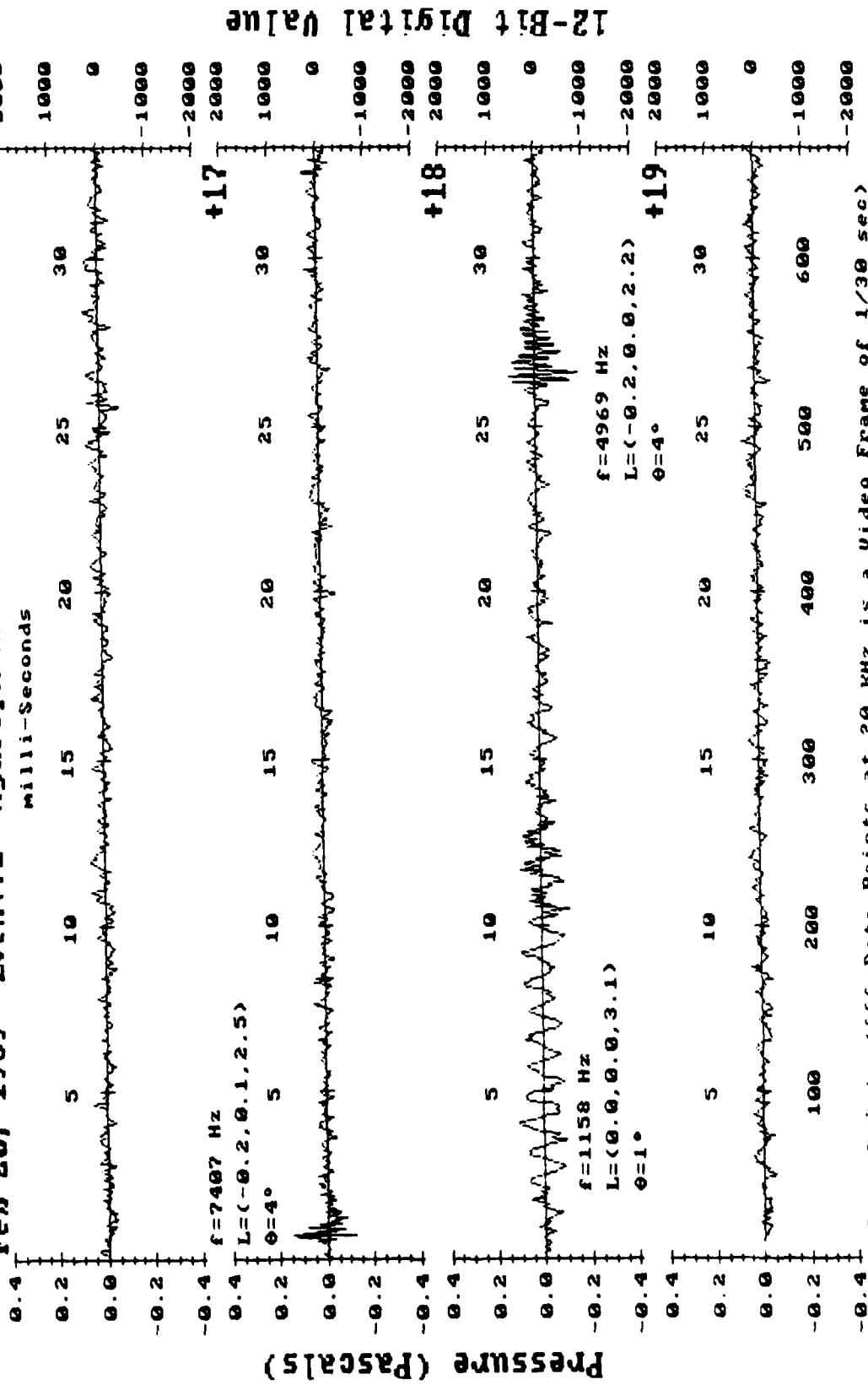
Data Points (666 Data Points at 20 KHz is a Video Frame of 1/30 sec)

Appendix B, Figure 1c: Acoustic time Series, Frames 7898 to 7901.



Appendix B, Figure 1d: Acoustic time Series, Frames 7902 to 7905.

Feb 20, 1989 Event:2 Hydrophone:B VideoFrame: 7890+16



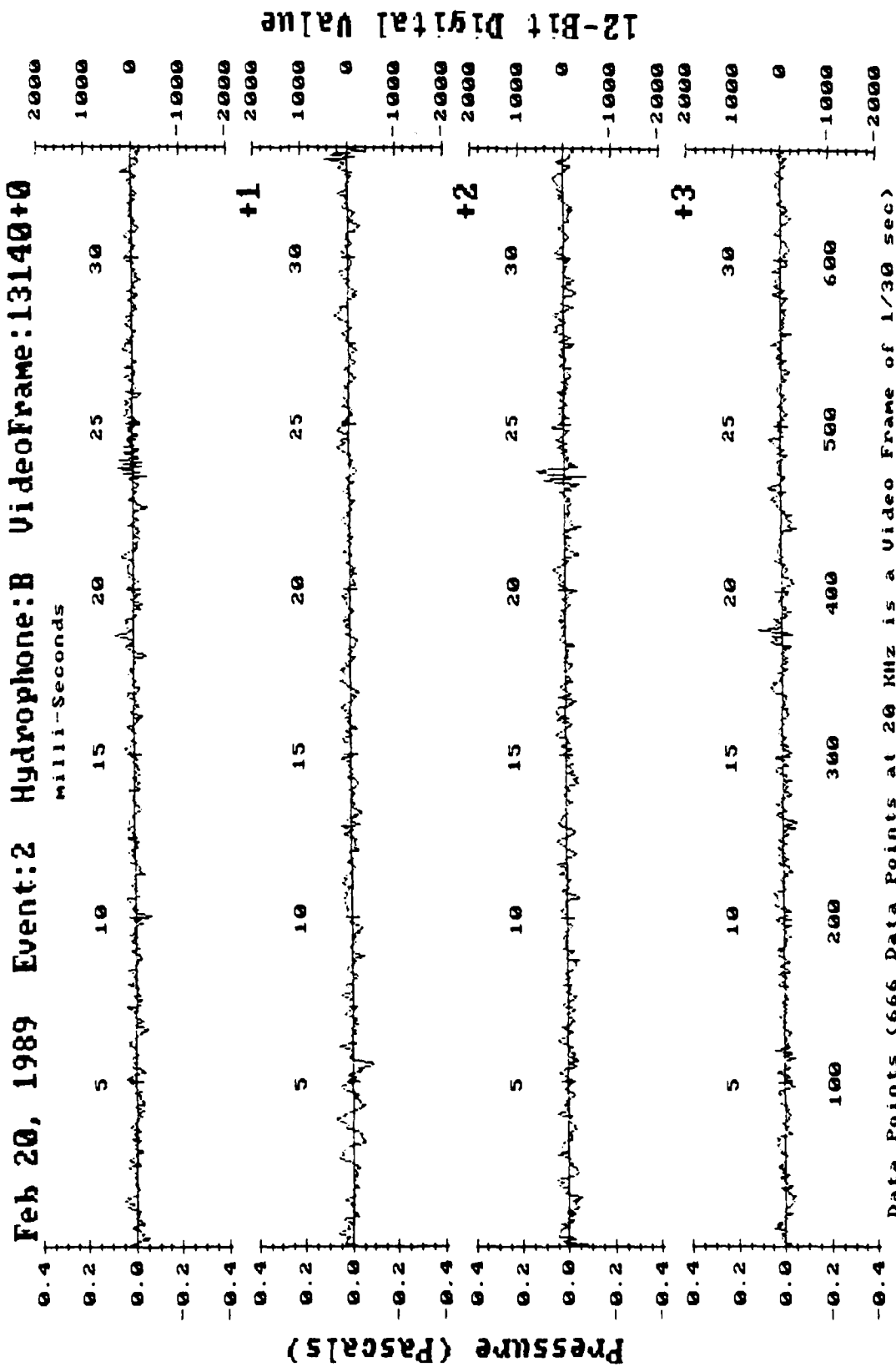
Data Points (666 Data Points at 20 KHz is a Video Frame of 1/30 sec)

Appendix B, Figure 1e: Acoustic time Series, Frames 7906 to 7909.

II. WAVELET BREAK AT VIDEO FRAME 13140

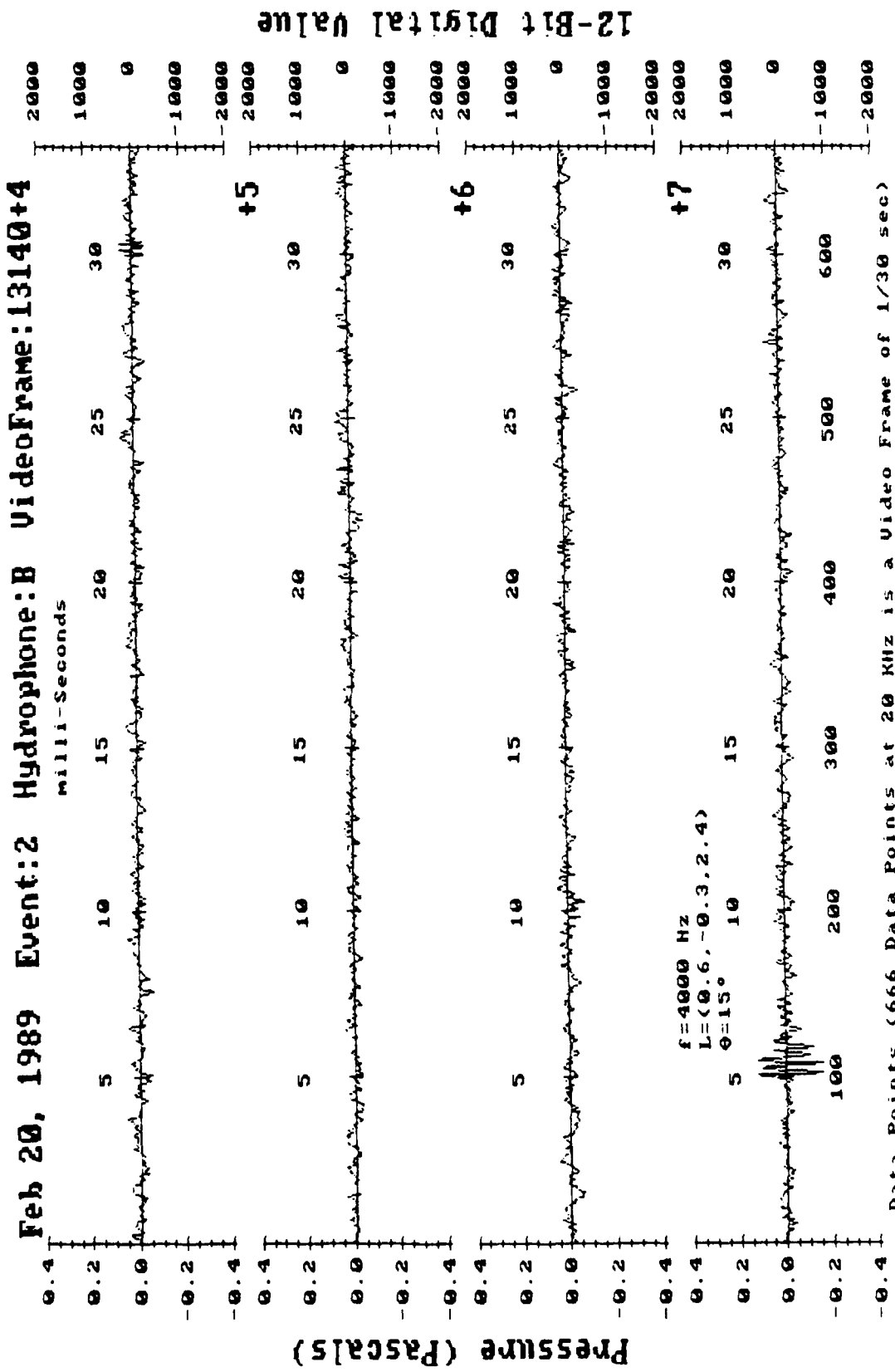
Within each of the contiguous plot pages which follow are four contiguous 1/30-second sections of data, each of which matches one video frame picture. Each plot line is labeled with an offset from the base reference Frame 13140.

Where possible, larger oscillations have been labeled as to frequency, locations relative to Hydrophone B, and angle from vertical over Hydrophone B. Bubble positions are accurate to +/- 10%.

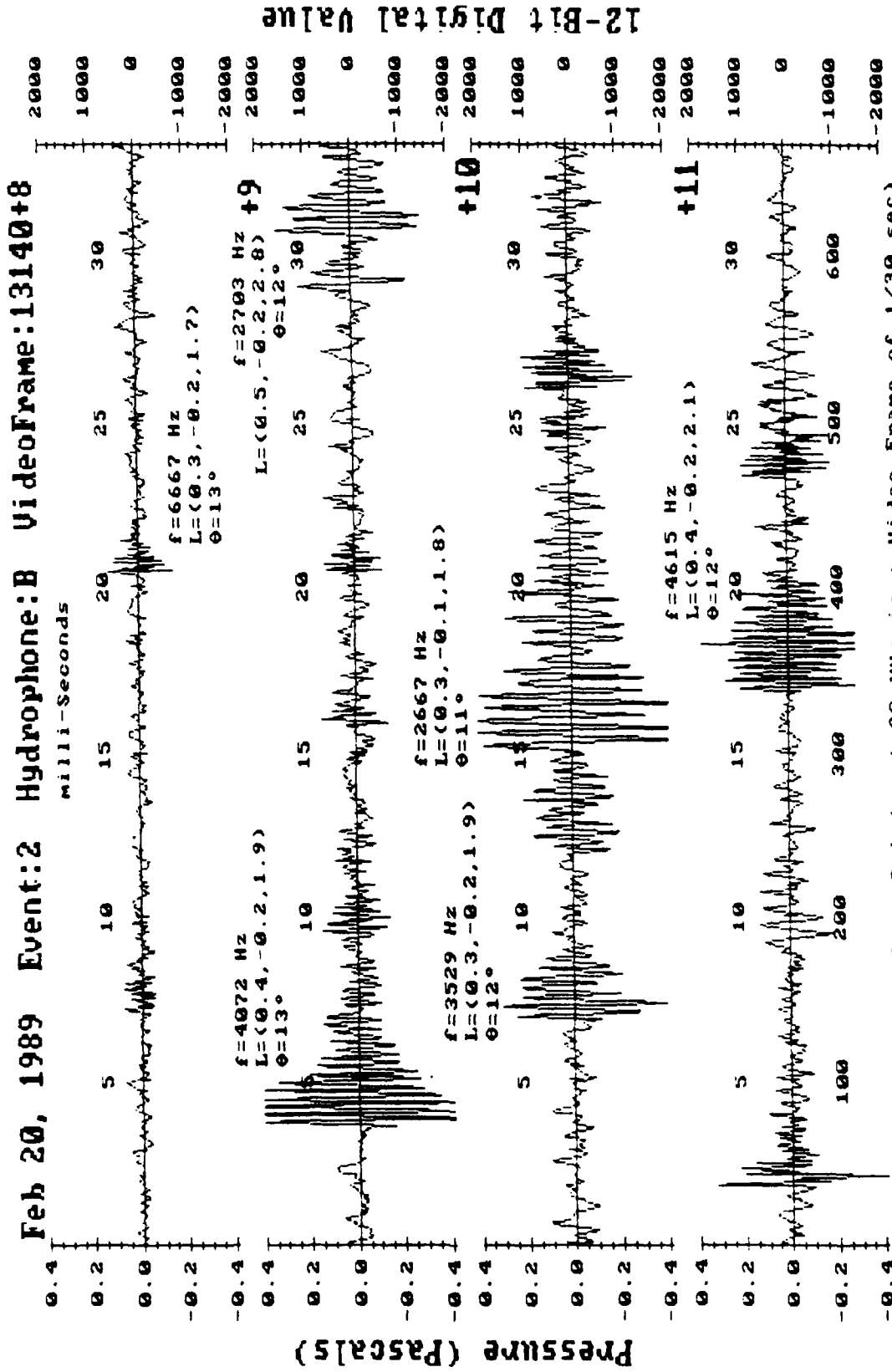


Data Points (666 Data Points at 20 KHz is a Video Frame of 1/30 sec)

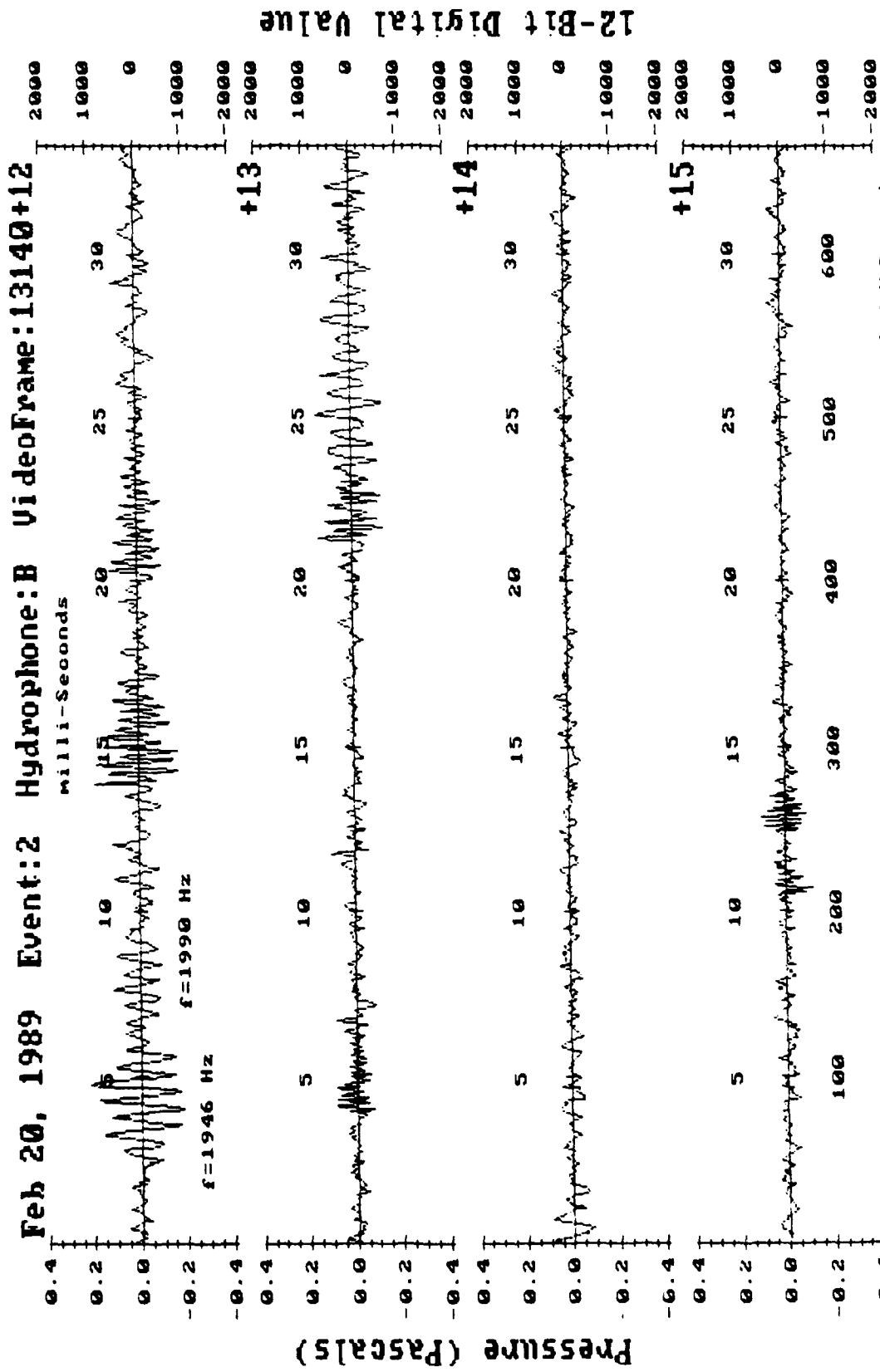
Appendix B, Figure 2a: Acoustic time Series, Frames 13140 to 13143.



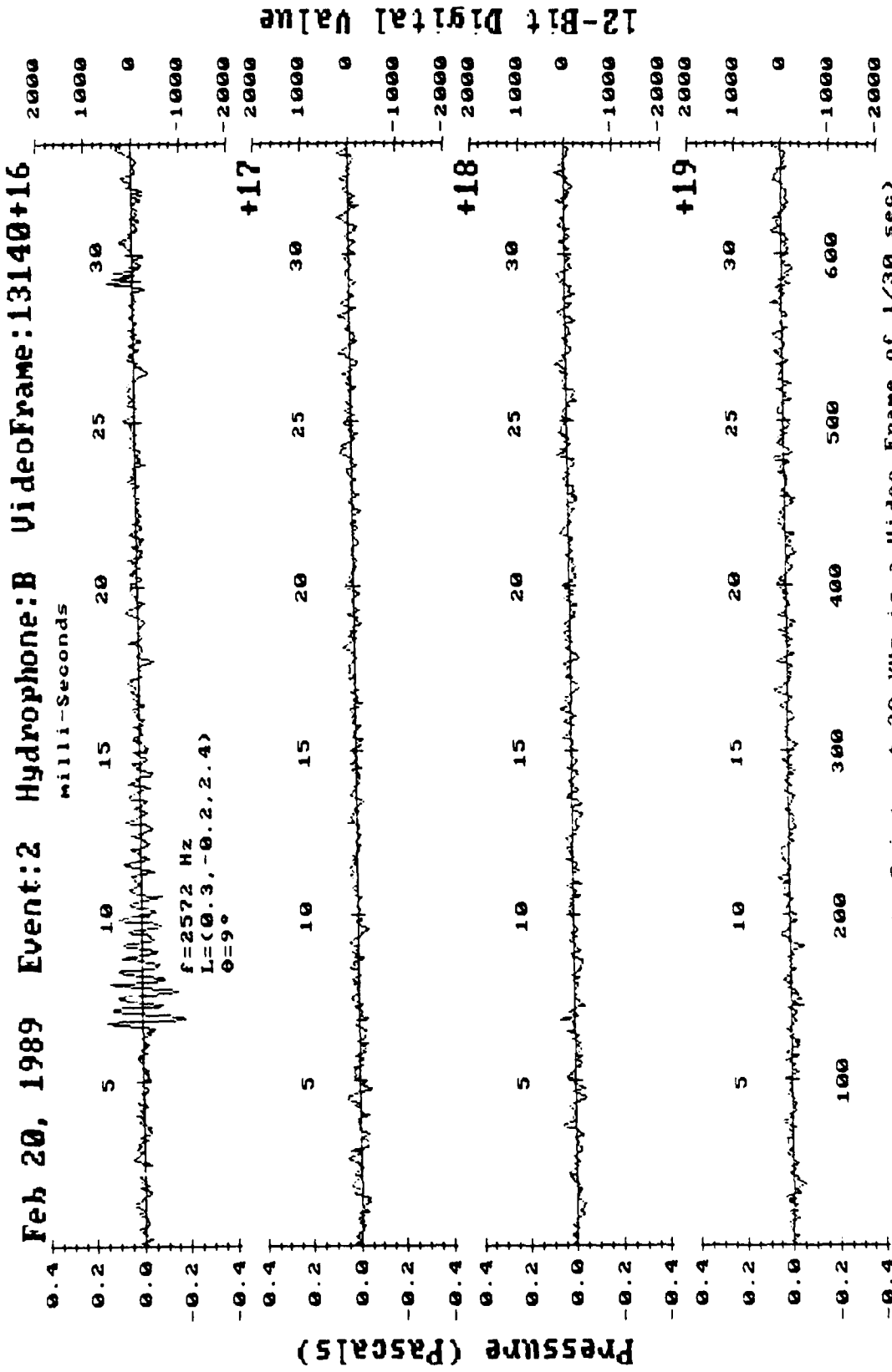
Appendix B, Figure 2b: Acoustic time Series, Frames 13144 to 13147.

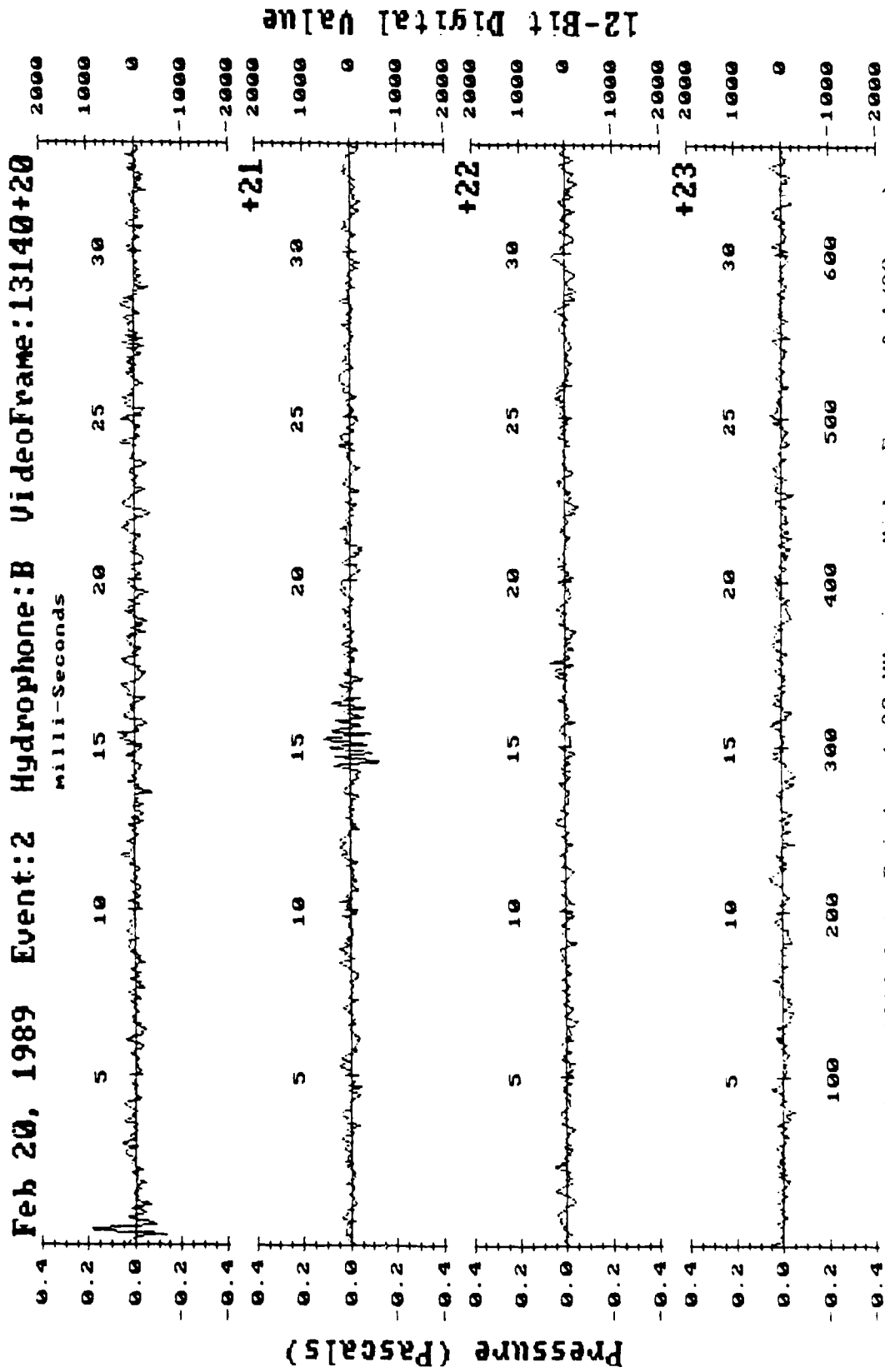


Data Points (666 Data Points at 20 KHz is a Video Frame of 1/30 sec)
 Appendix B, Figure 2c: Acoustic time Series, Frames 13148 to 13151.

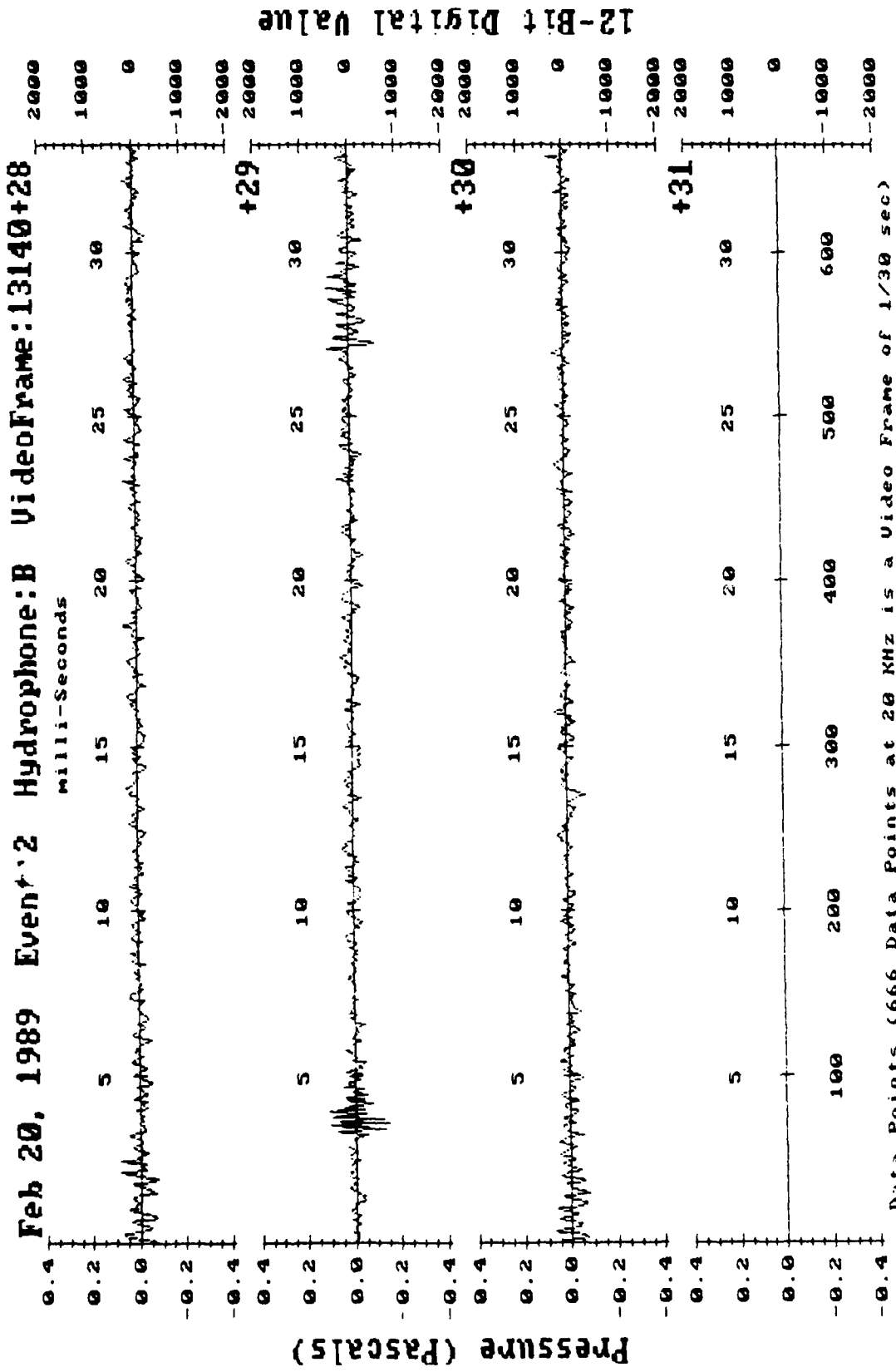


Data Points (666 Data Points at 20 KHz is a Video Frame of 1/30 sec)
Appendix B, Figure 2d: Acoustic time Series, Frames 13152 to 13155.





Data Points (666 Data Points at 20 KHz is a Video Frame of 1/30 sec)
Appendix B, Figure 2f: Acoustic time Series, Frames 13160 to 13163.

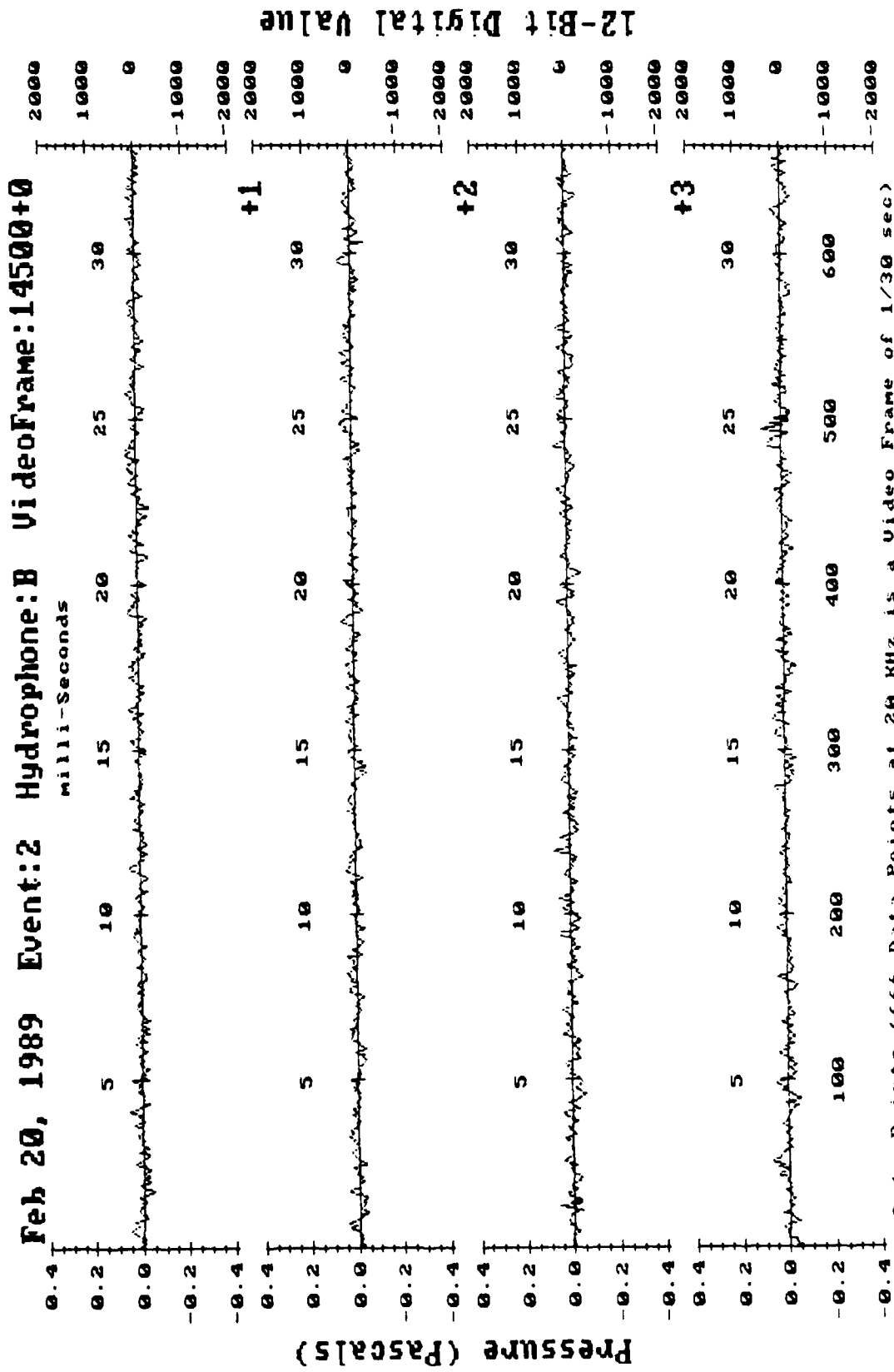


Data Points (666 Data Points at 20 KHz is a Video Frame of 1/30 sec)
 Appendix B, Figure 2h: Acoustic time Series, Frames 13168 to 13171.

III. WAVELET BREAK AT VIDEO FRAME 14500

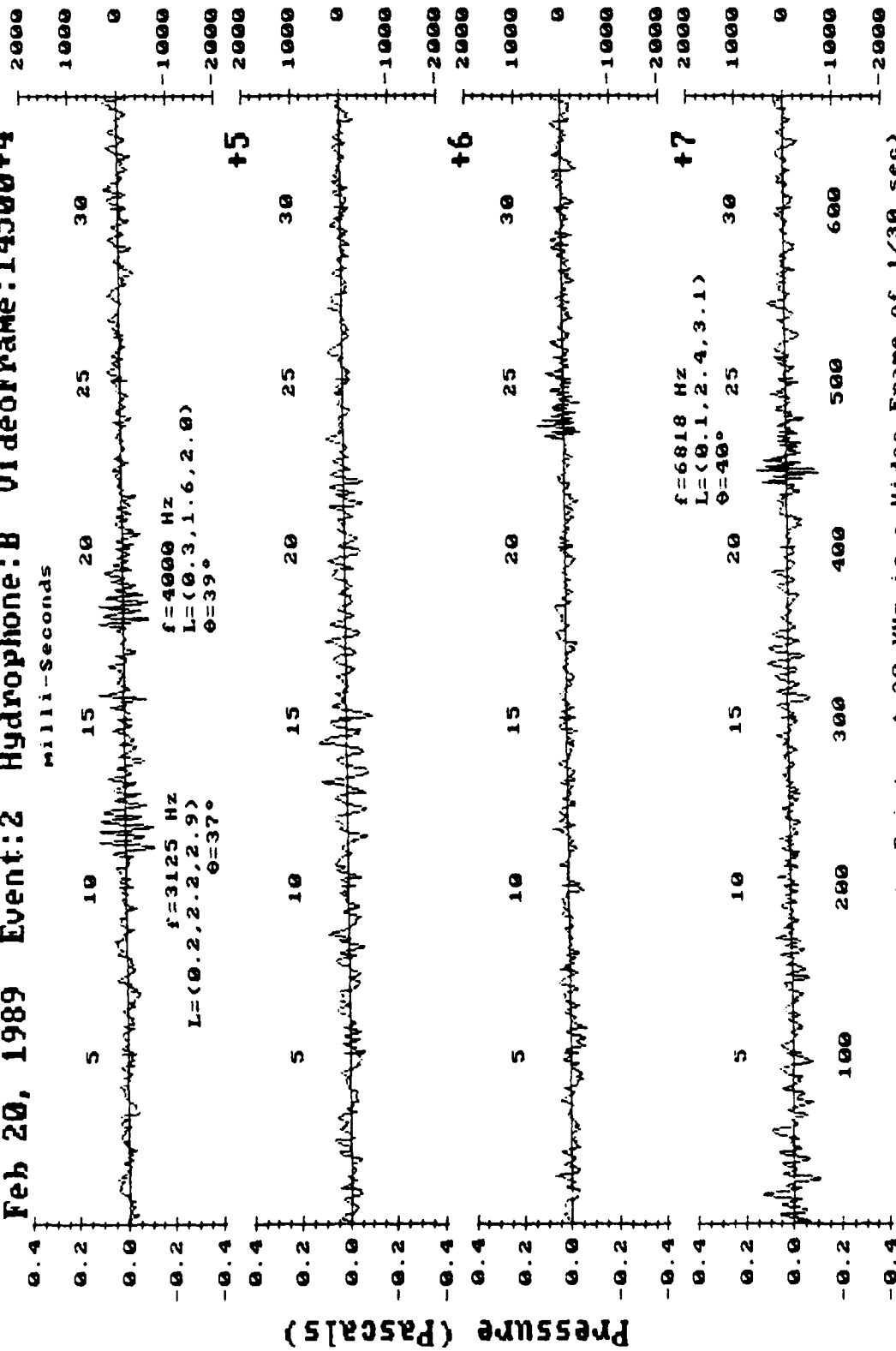
Within each of the contiguous plot pages which follow are four contiguous 1/30-second sections of data, each of which matches one video frame picture. Each plot line is labeled with an offset from the base reference Frame 14500.

Where possible, larger oscillations have been labeled as to frequency, locations relative to Hydrophone B, and angle from vertical over Hydrophone B. Bubble positions are accurate to +/- 10%.

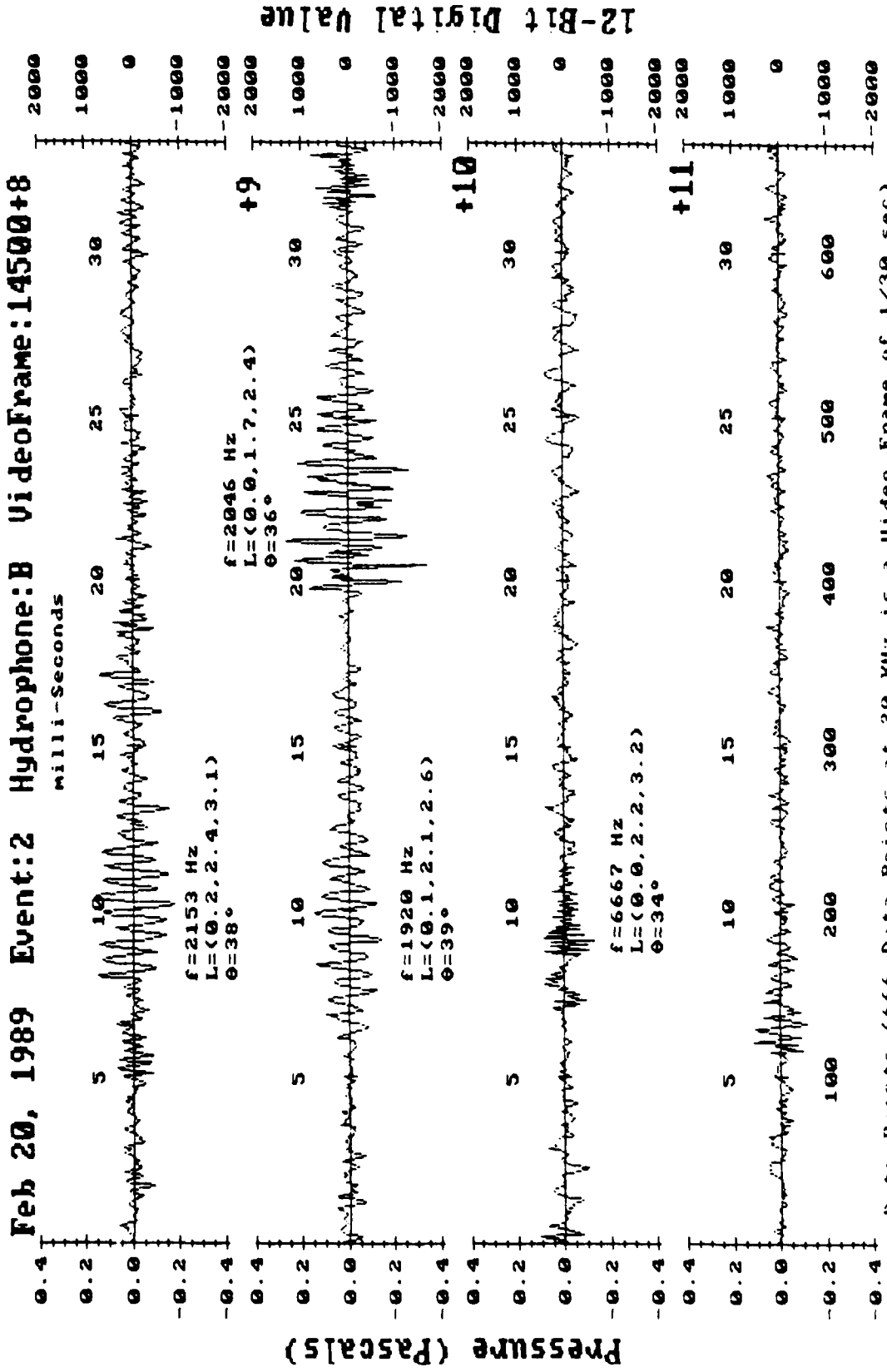


Data Points (666 Data Points at 20 KHz is a Video Frame of 1/30 sec)
Appendix B, Figure 3a: Acoustic time Series, Frames 14500 to 14503.

Feb 20, 1989 Event:2 Hydrophone:B VideoFrame:14500+4



Data Points (666 Data Points at 20 KHz is a Video Frame of 1/30 sec)
 Appendix B, Figure 3b: Acoustic time Series, Frames 14504 to 14507.



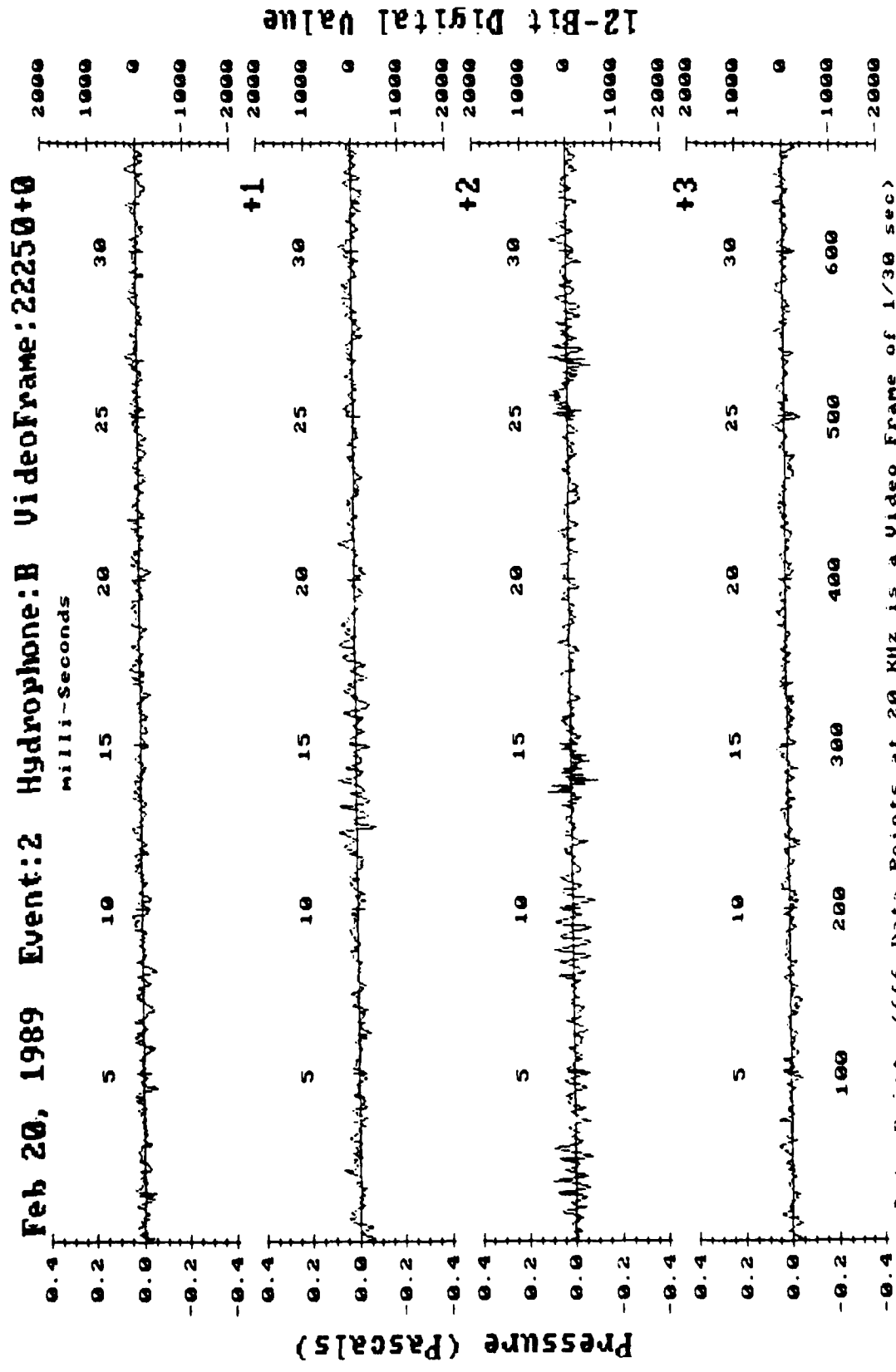
Appendix B, Figure 3c: Acoustic time Series, Frames 14508 to 14511.

IV. WAVELET BREAK AT VIDEO FRAME 22250

Within each of the contiguous plot pages which follow are four contiguous 1/30-second sections of data, each of which matches one video frame picture. Each plot line is labeled with an offset from the base reference Frame 22250.

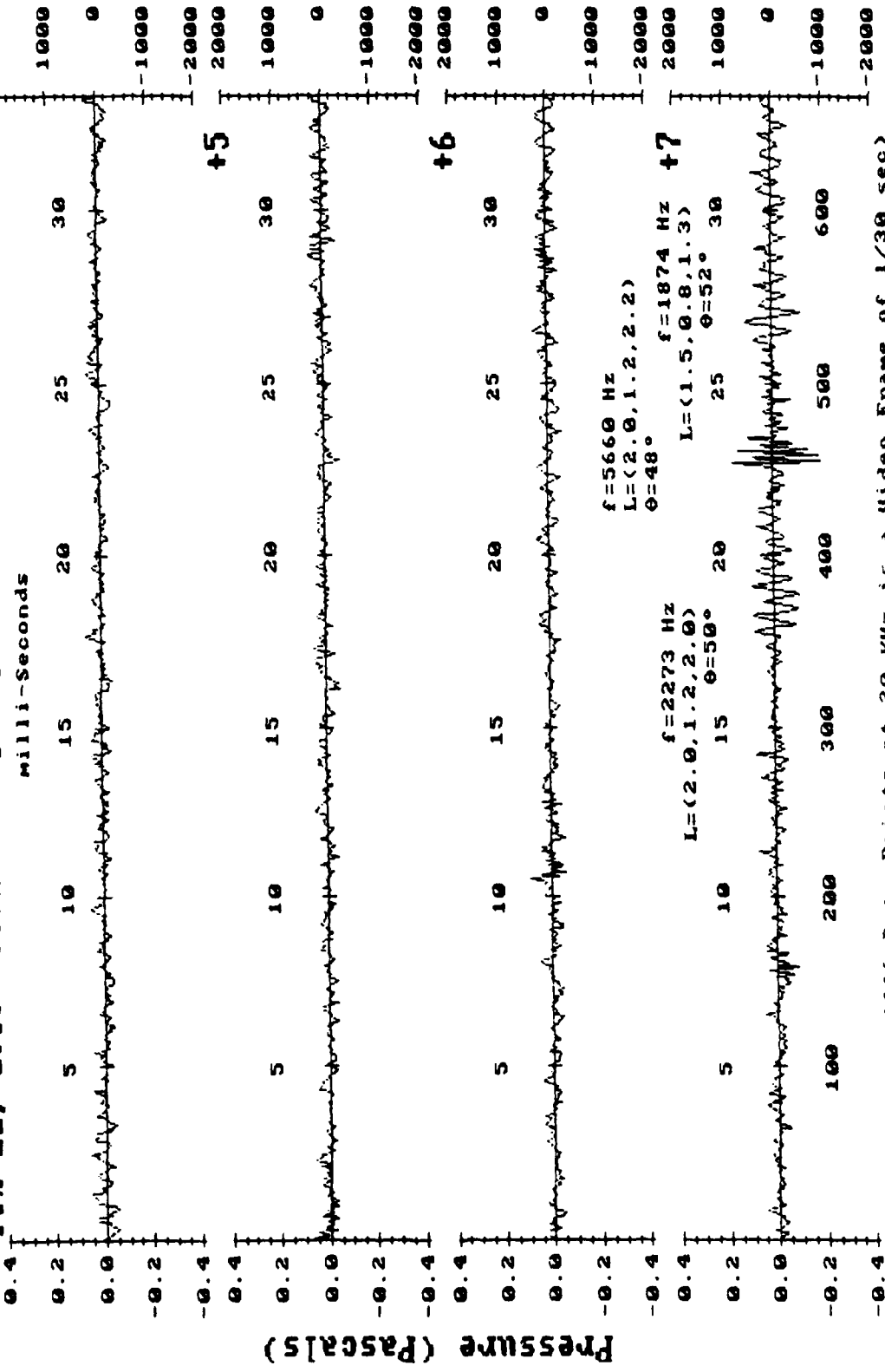
Where possible, larger oscillations have been labeled as to frequency, locations relative to Hydrophone B, and angle from vertical over Hydrophone B. Bubble positions are accurate to +/- 10%.

Positions of some of the low frequency oscillations were too difficult to calculate.



Data Points (666 Data Points at 20 KHz is a Video Frame of 1/30 sec)
Appendix B, Figure 4a: Acoustic time Series, Frames 22250 to 22253.

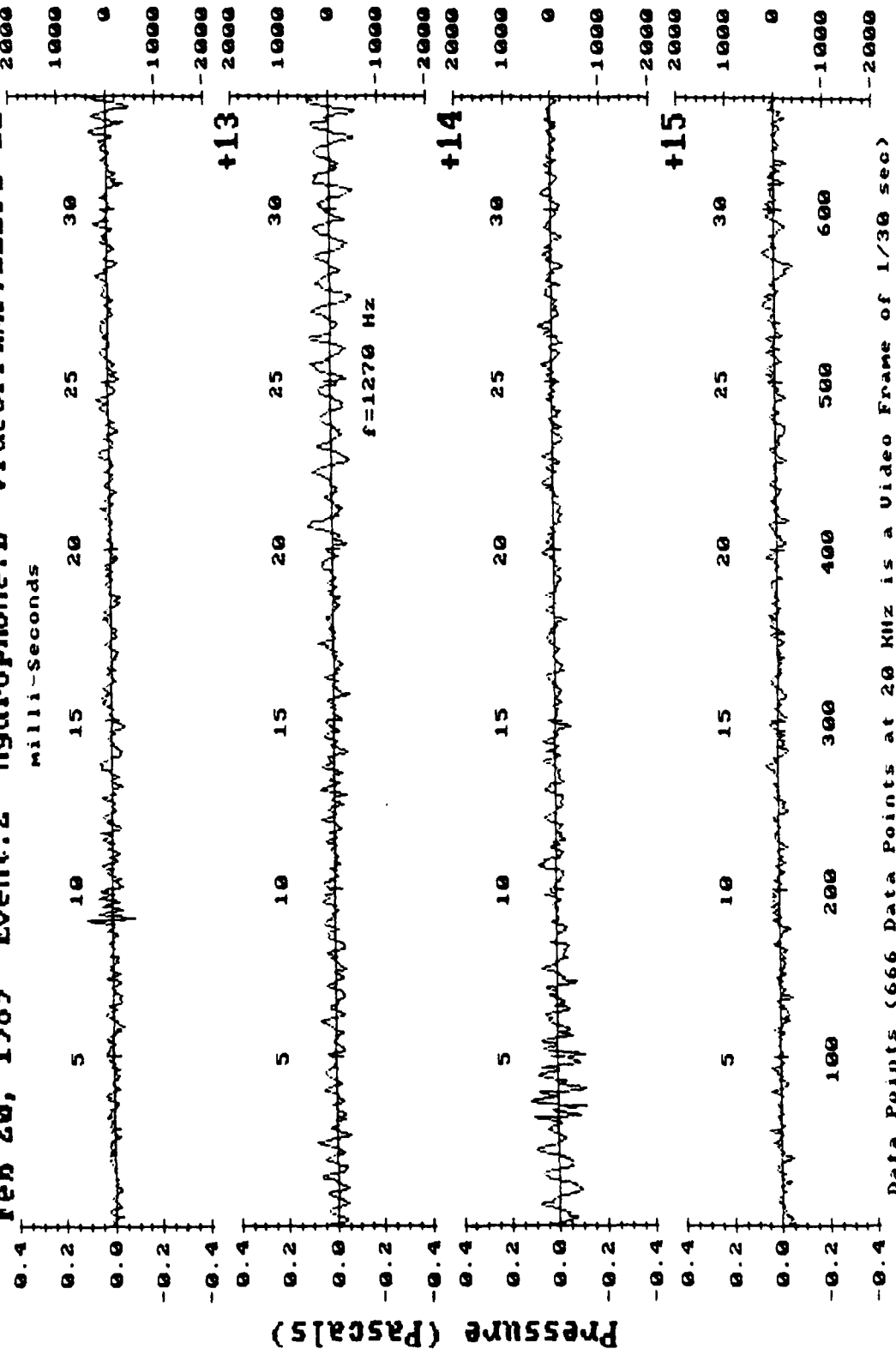
Feb 20, 1989 Event:2 Hydrophone:B VideoFrame:22250+4



Data Points (666 Data Points at 20 KHZ is a Video Frame of 1/30 sec)

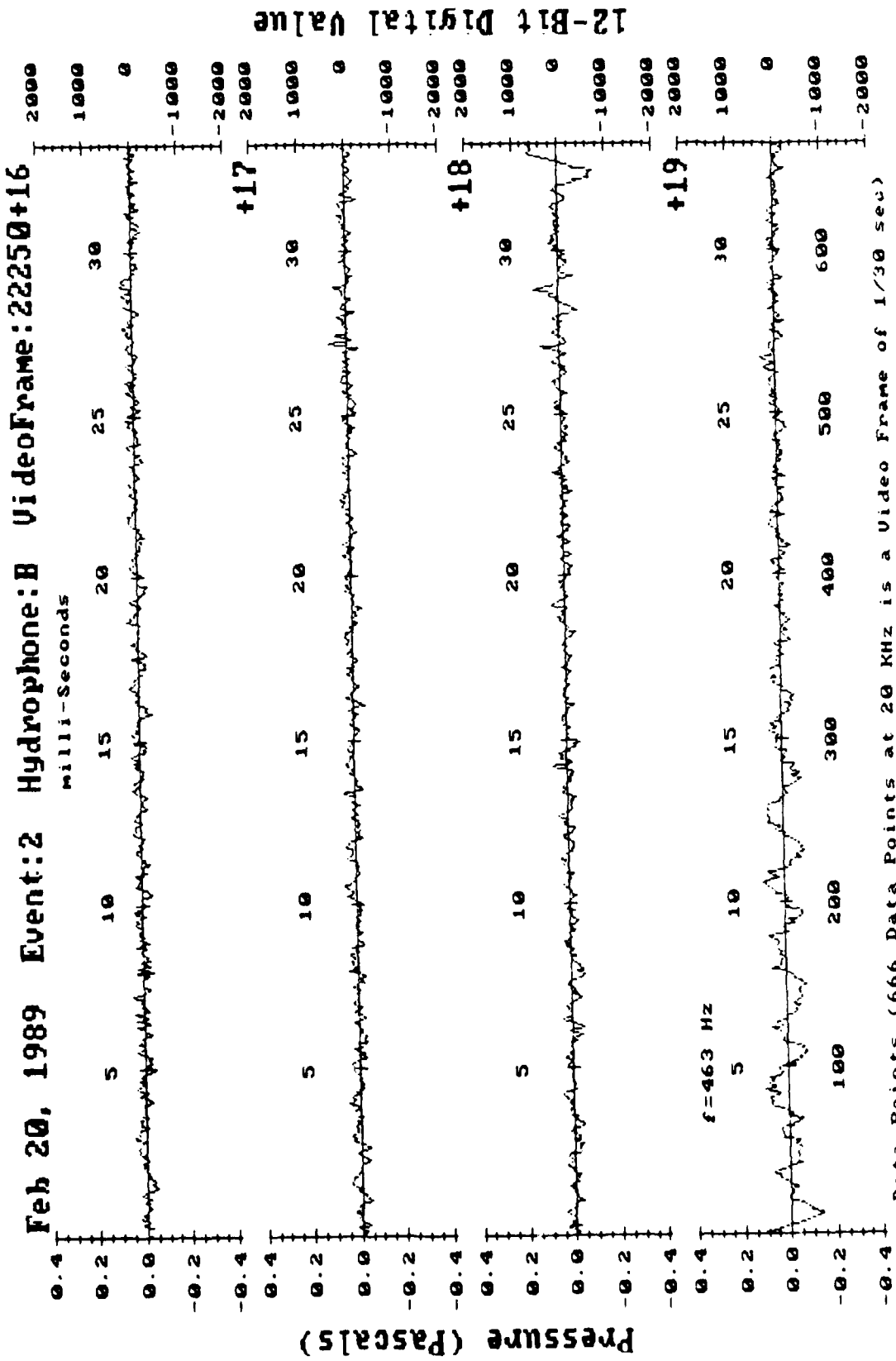
Appendix B, Figure 4b: Acoustic time Series, Frames 22254 to 22257.

Feb 20, 1989 Event:2 Hydrophone:B VideoFrame:22250+12



Data Points (666 Data Points at 20 KHz is a Video Frame of 1/30 sec)

Appendix B, Figure 4d: Acoustic time Series, Frames 22262 to 22265.

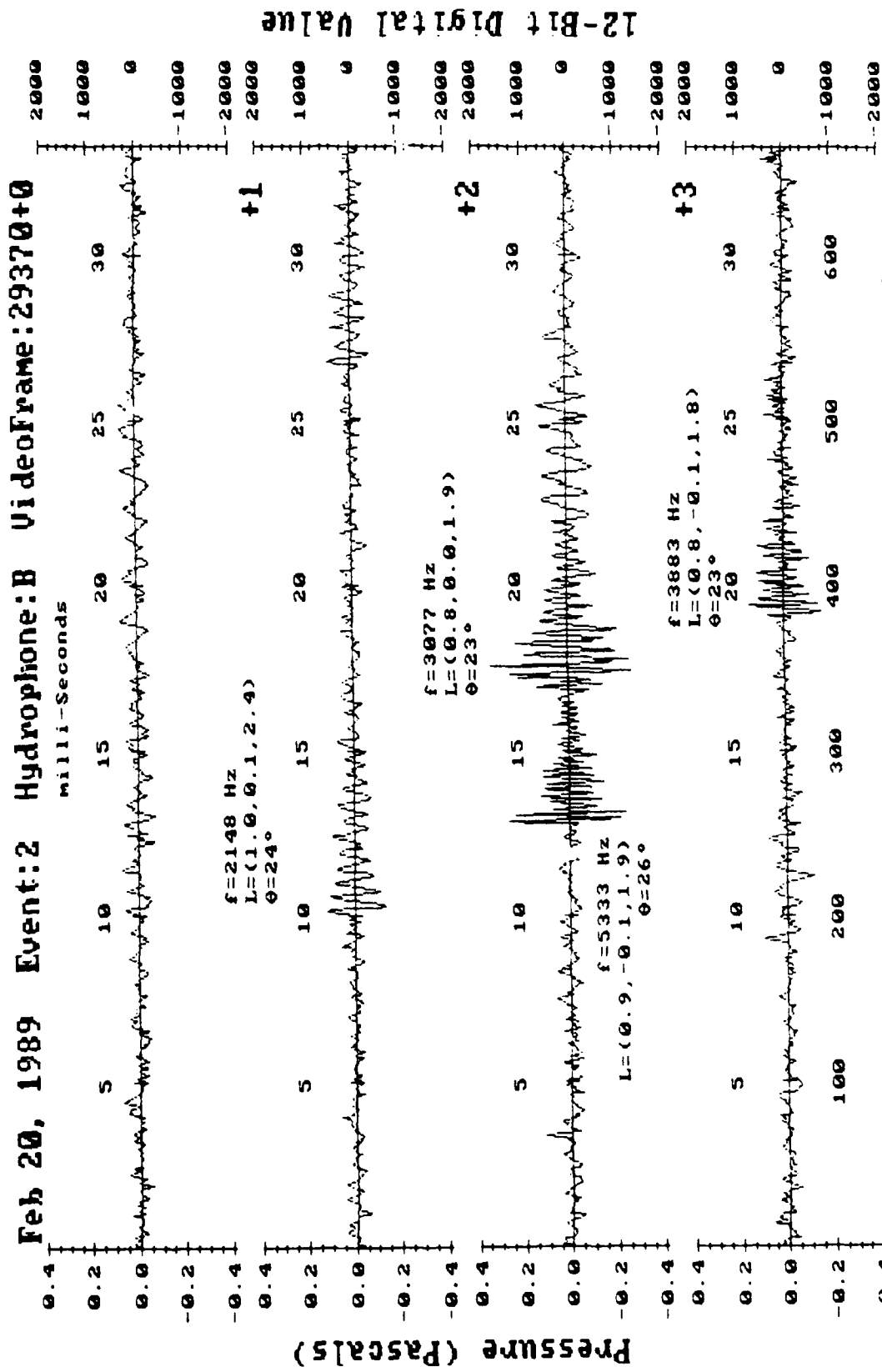


Appendix B, Figure 4e: Acoustic time Series, Frames 22266 to 22269.

V. WAVELET BREAK AT VIDEO FRAME 29370

Within each of the contiguous plot pages which follow are four contiguous 1/30-second sections of data, each of which matches one video frame picture. Each plot line is labeled with an offset from the base reference Frame 29370.

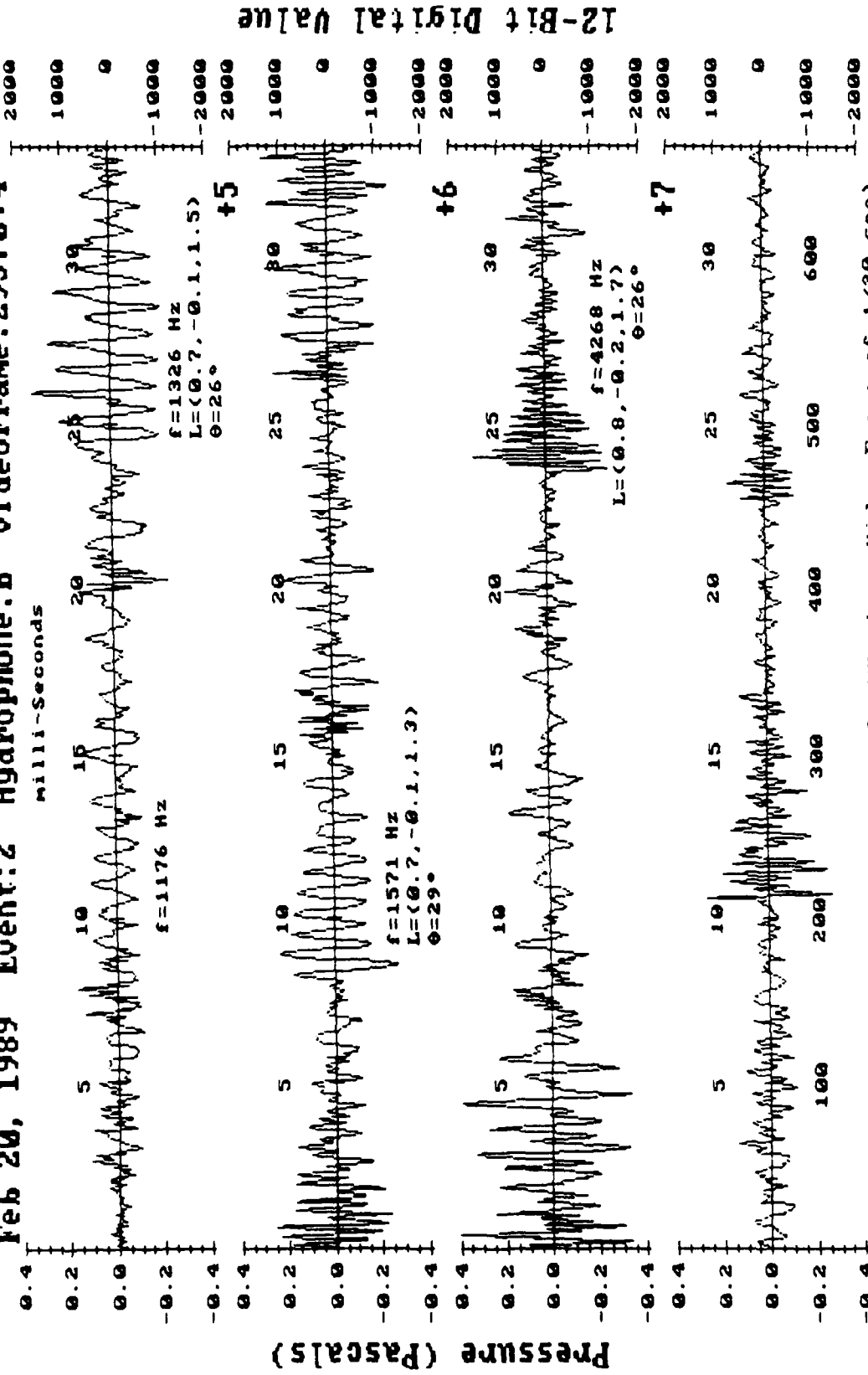
Where possible, larger oscillations have been labeled as to frequency, locations relative to Hydrophone B, and angle from vertical over Hydrophone B. Bubble positions are accurate to +/- 10%.



Data Points (666 Data Points at 20 KHz is a Video Frame of 1/30 sec)

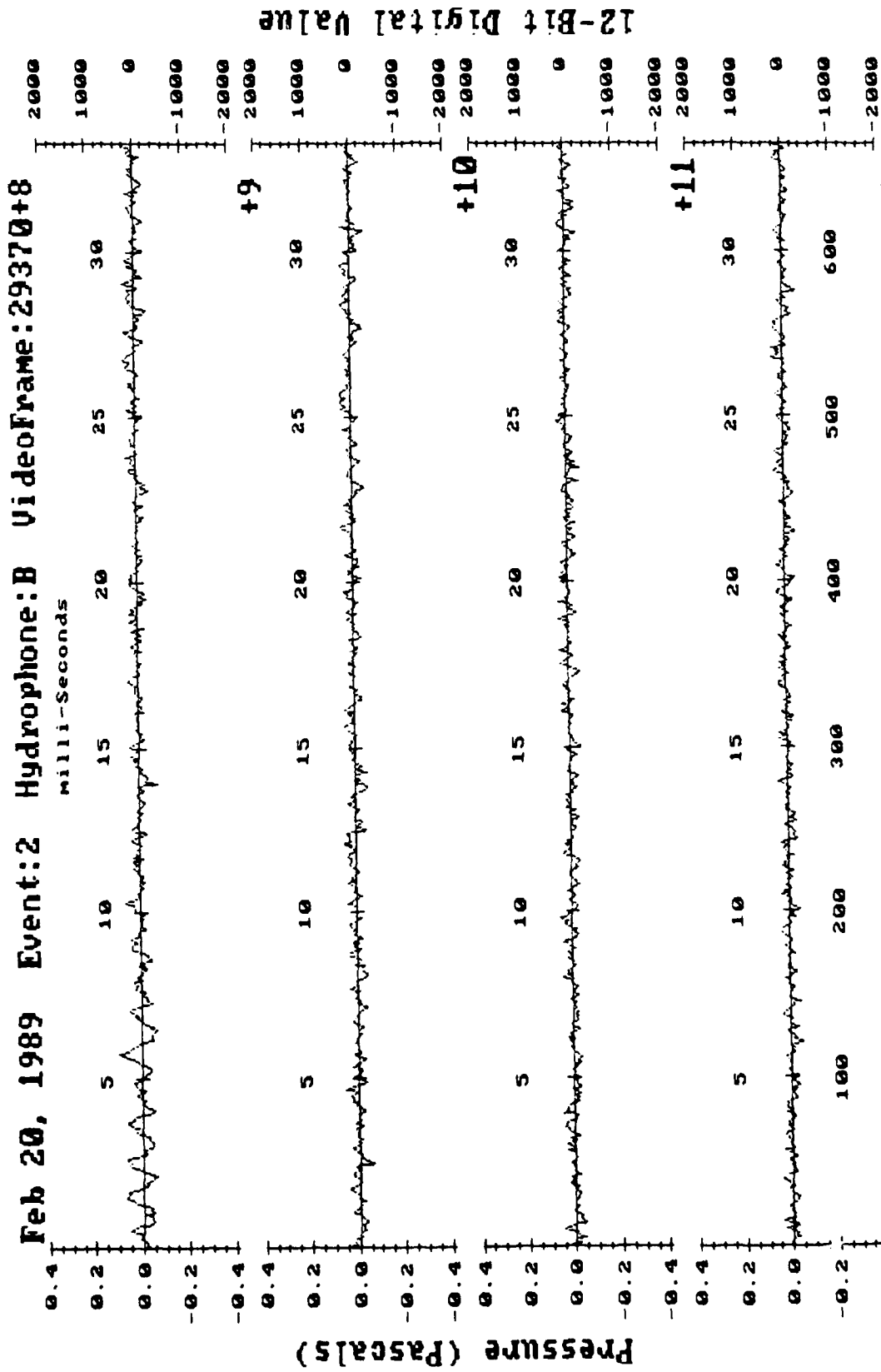
Appendix B, Figure 5a: Acoustic time Series, Frames 29370 to 29373.

Feb 20, 1989 Event:2 Hydrophone:B VideoFrame:29370+4



Data Points (666 Data Points at 20 KHz is a Video Frame of 1/30 sec)

Appendix B, Figure 5b: Acoustic time Series, Frames 29374 to 29377.



Data Points (666 Data Points at 20 KHz is a Video Frame of 1/30 sec)
Appendix B, Figure 5c: Acoustic time Series, Frames 29378 to 29381.

ONR/MPL GENERAL DISTRIBUTION LIST

Chief of Naval Research
 Department of the Navy
 Arlington, Virginia 22217-5000
 Code 12, 122(2), 125
 1121, 112, 1122,
 1123, 1125, 1125 OA,
 1125 GG, 23

ONRDET
 Stennis Space Center
 Ray St. Louis, Mississippi 39529-5004
 Code 125

Commander
 Naval Sea Systems Command
 Washington, D. C. 20362
 Code 63DB, 933A

Commanding Officer
 Naval Ocean Research and
 Development Activity
 Stennis Space Center
 Bay St. Louis, Mississippi 39529-5004
 Code 100, 110, 300, 330,
 200, 220, 240, 250, 270,
 320, 360, 350

Commander
 U.S. Naval Oceanographic Office
 NSTL Station
 Bay St. Louis, Mississippi 39522-5004
 Attn: Bill Jobst

Assistant Secretary of the Navy
 (Research Engineering & Systems)
 Department of the Navy
 Washington, D. C. 20350

Defense Advanced Res. Proj. Agency
 TTO - Tactical Technology Office
 1400 Wilson Boulevard
 Arlington, Virginia 22209-2308
 Attn: John N. Entzminger

National Oceanic & Atmospheric
Administration
 Ocean Engineering Office
 6001 Executive Boulevard
 Rockville, Maryland 20852

Commander
 Space and Naval Warfare
 Systems Command
 Washington, D. C. 20360-5100
 Code PMW-180T, PMW-180-S

Commander
 Naval Ship Res. & Dev. Center
 Bethesda, Maryland 20084

Executive Secretary
 Naval Studies Board
 National Academy of Sciences
 2101 Constitution Avenue, N.W.
 Washington, D.C. 20418

Director
 Strategic Systems Proj. Ofc.
 Department of the Navy
 Washington, D. C. 20361
 Code NSP-20

Commander
 Naval Ocean Systems Center
 San Diego, California 92152
 Code 00, 01, 16, 94,
 54, 541, 605, 71, 72, 701

Commander
 Submarine Development Group ONE
 139 Sylvester Road
 San Diego, California 92106

Commanding Officer
 Civil Engineering Laboratory
 Naval Construction Battalion Center
 Port Hueneme, California 93043
 Code L40, L42

Commanding Officer
 Naval Underwater Systems Center
 Newport, Rhode Island 02844
 Attn: E.L. Sullivan

Officer in Charge
 Naval Underwater Systems Center
 New London Laboratory
 New London, Connecticut 06320
 Code 900, 905, 910, 930, 960

Director of Research
 U.S. Naval Research Laboratory
 Washington, D. C. 20375
 Code 2620, 2627, 5000, 5100, 5800

Officer in Charge
 Naval Surface Warfare Center
 10901 New Hampshire Avenue
 White Oak Laboratory Detachment
 Silver Spring, Maryland 20903-5000
 Attn: E232 Tech Library

Commanding Officer
 Naval Coastal Systems Laboratory
 Panama City, Florida 32401

STOICAC
 Battelle Columbus Laboratories
 505 King Avenue
 Columbus, Ohio 43201

Commander
 Naval Air Systems Command
 Washington, D. C. 20361
 Code 370

Commanding Officer
 U.S. Naval Air Development Center
 Attention: Bruce Steinberg
 Warminster, Pennsylvania 18974

Director
 Defense Documentation Center
 (TIMA), Cameron Station
 5010 Duke Street
 Alexandria, Virginia 22314

Institute for Defense Analyses
 1801 North Beaupard Street
 Arlington, Virginia 22311

Superintendent
 U.S. Naval Postgraduate School
 Monterey, California 93940

Chief Scientist
 Navy Underwater Sound Reference Div.
 U.S. Naval Research Laboratory
 P.O. Box 8337
 Orlando, Florida 32806

Supreme Allied Commander
 U.S. Atlantic Fleet
 ASW Research Center, APO
 New York, New York 09019
 Via: ONR 100 M, CNO OP092D1,
 Secretariat of Military,
 Information Control, Committee

Director
 Institute of Marine Science
 University of Alaska
 Fairbanks, Alaska 99701

Director
 Applied Physics Laboratory
 Johns Hopkins University
 Johns Hopkins Road
 Laurel, Maryland 20810
 Attn: J. R. Austin

Director
 College of Engineering
 Department of Ocean Engineering
 Florida Atlantic University
 Boca Raton, Florida 33431

Director
 Marine Research Laboratories
 c/o Marine Studies Center
 University of Wisconsin
 Madison, Wisconsin 53706

Director
 Applied Research Laboratory
 Pennsylvania State University
 P.O. Box 30
 State College, Pennsylvania 16802

Director
 Applied Physics Laboratory
 University of Washington
 1013 NE 40th Street
 Seattle, Washington 98195

Director
 The Univ. of Texas at Austin
 Applied Research Laboratory
 P.O. Box 8029
 Austin, Texas 78712

Director
 Lamont-Doherty Geological Observatory
 Torrey Cliff
 Palisades New York 10964

Director
 Woods Hole Oceanographic Institution
 Woods Hole, Massachusetts 02543

Director
 Inst. of Ocean Science Engineering
 Catholic University of America
 Washington, D.C. 20017

National Science Foundation
 Ocean Sciences Division
 Washington, D. C. 20550

Office of Naval Research
 Resident Representative
 c/o Univ. of California, San Diego
 Mail Code 0023
 La Jolla, California 92093

University of California, San Diego
 Marine Physical Laboratory
 Branch Office
 La Jolla, California 92093